

**THE EFFECTS OF TEMPERATURE ON THE GEOMECHANICAL
RESPONSE OF AXIALLY LOADED FULLY GROUTED ROCK BOLTS
UTILIZING DISTRIBUTED FIBER OPTIC TECHNOLOGY**

**LES EFFETS DE LA TEMPÉRATURE SUR LA RÉPONSE
GÉOMÉCANIQUE DES BOULONS D'ANCRAGE ENTIÈREMENT
SCELLÉS CHARGÉS AXIALEMENT UTILISANT LA TECHNOLOGIE
DE FIBRE OPTIQUE DISTRIBUÉE**

A Thesis Submitted to the Division of Graduate Studies
of the Royal Military College of Canada

by

Chuyue Guo
Captain

In Partial Fulfillment of the Requirements for the Degree of
Masters of Applied Science

April 2024

© This thesis may be used within the Department of National Defence but
copyright for open publication remains the property of the author

Acknowledgements

This thesis project could not be completed without the support and contributions of numerous people and organizations. I would like to express my sincere gratitude and appreciation for all who have made this research possible and a valuable learning experience. Firstly, I would like to thank my thesis supervisors Dr. Nicholas Vlachopoulos and Captain Kieran Moore for their guidance, knowledge, and assistance through the whole journey. Their motivation and steadfast support has allowed me to take full advantage of various opportunities and achieve academic success. As well, the expertise and guidance of past graduate student Dr. Bradley Forbes was vital to the conceptualization and development of this project. The support of the Royal Military College of Canada (RMC) Civil Engineering Department, Canadian Military Geoworks Lab, and the RMC Green Team was instrumental in the completion of my studies. Thank you to 1 Engineering Support Unit as the sponsor of my studies.

I would like to acknowledge Mr. Vincent Trinidad, Mr. Dexter Gaskin, Mrs. Kristine Mattson, Mr. John Shaw, and Mr. Steve Vanvolkingburgh for their invaluable support and feedback in the laboratory, without which this project could not have been completed. Thank you for going out of your way to support me and enable this project, all your efforts are genuinely appreciated.

I would like to extend my appreciation for Sika Canada for contributing grout material samples for this project. The Tunnelling Association of Canada for the Eisenstein Memorial Scholarship award that contributed to the success of this research endeavour. The Ottawa Geotechnical Group and CGS Kingston Section for organizing the 48th Annual Michael Bozozuk Student Forum providing the opportunity to present my research and being selected as the winner of the competition. The recognition and support from external organizations and professionals in the field has been extraordinary and encouraging.

Finally, I would like to thank my family and friends for all their support throughout this journey. My parents, Jian and Yangsheng, for their unconditional love and advice that helped drive me to return and complete my graduate studies. All my friends for their constant motivation and Friday Coffee Time Girl Group for the weekly morale boost and sitting through so many practice presentations. And lastly, Pickles the best thesis writing companion.

Abstract

Fully grouted rock bolts (FGRB) are one of the most widely employed types of rock bolting in underground mining and civil engineering projects. Rock bolts create a zone of reinforcement and transfer the unstable rock load near the excavation boundary to the more stable rock mass (or ground) at depth. The design of ground support systems is a non-trivial pursuit as potential risks include loss of material, equipment, investments, and even human life. As underground operations have expanded globally, ground conditions and temperatures at the extremes become more prevalent which can potentially affect the bonding and performance of FGRBs. A multitude of global research endeavours have investigated FGRB performance and behaviour through field monitoring, laboratory and in situ testing, analytical methods, and numerical modelling to better understand their properties, mechanisms, and component interactions. However, limited existing literature has investigated the effects of temperature on these composite systems. In addition, a full range understanding of FGRBs is still yet to be achieved, due in part to a lack of spatial resolution in traditional test monitoring setups.

A series of laboratory pull-out tests were conducted on 24 FGRB specimens cured in a specific temperature range and for different durations in order to study the effects of temperature on their behaviour and capacity development. Two Canadian scenarios were considered in the conceptualization of this project: 1. Northern conditions (permafrost) as found in Northern Canada; and, 2. Nuclear waste repository (geothermally active) as per the requirements of the Nuclear Waste Management Organization. The temperature range chosen for the study included -20°C to $+45^{\circ}\text{C}$ and curing duration ranged from 3 days to 90 days. The specimens were assembled with 20M rebar at 1.3 m embedment length and two types of commercially available cement grouts. This project utilized the distributed fiber optic technique developed by the research group at the Royal Military College of Canada that leverages Rayleigh Optical Frequency Domain Reflectometry achieving an unprecedented spatial resolution of 0.65 mm. Modifications to the methodology have permitted the capture of both strain profiles and internal specimen temperature during testing. Results provide performance trends of the composite system and considerations for their loading and capacity development in these curing environments. Understanding behaviour changes due to extreme environments will be vital for safe and optimized designs of ground support.

Résumé

Les boulons d'ancrage entièrement scellés (BES) sont l'un des types de boulons d'ancrage plus utilisés dans le domaine de l'exploitation minière et des projets de génie civil souterrain. Les boulons d'ancrage créent une zone de renfort et transfèrent la charge de roche instable près du front de l'excavation aux masses plus stables derrière. La conception du soutènement au sol est une poursuite non triviale ainsi que les risques potentiels comprennent la perte des matériaux, équipements, investissements, et même la vie. À mesure que les opérations souterraines se développent globalement, les conditions de sol et les températures aux extrêmes deviendront plus fréquentes, ce qui peut potentiellement affecter l'adhérence et les performances des BES. Plusieurs des efforts de recherche mondiaux ont étudié les comportements des BES in-situ et en laboratoire, et aussi des plusieurs modèles analytiques et numériques ont été développés. Mais, la littérature existante explorant les effets de la température sur ces systèmes est limitée. Une gamme complète de compréhension des BES n'a pas encore été atteint. Les limites pratiques et technologiques ont toujours posé un défi à l'étude.

Une enquête de laboratoire détaillée est menée avec 24 spécimens de BES qui durcissent dans un régime de température spécifique avec des différentes durées pour évaluer les effets de la température sur le comportement et le développement des capacités. Deux scénarios canadiens ont été considérés dans la conceptualisation de ce projet : 1. Les conditions nordiques (pergélisol) trouvés dans le nord du Canada; et 2. Le dépôt de déchets nucléaires (géothermiquement actifs) selon les exigences de NWMO. La gamme de température pour cette étude comprenait de -20°C à $+45^{\circ}\text{C}$ et le période de durcissement de 3 jours à 90 jours. Les spécimens ont été assemblés avec le barre d'armature 20M avec la longueur d'ancrage de 1.3 m et deux types de coulis de ciment disponible dans le commerce. Ce projet a utilisé la technique de fibres optiques distribuées en tirant parti de la Réflectométrie Optique de Rayleigh en Domaine de Fréquence développée par le groupe de recherche au Collège militaire royal du Canada avec une résolution spatiale de 0,65 mm. Les modifications de la méthodologie ont permis la capture du profil de déformation et le changement de température interne pendant les tests. Les résultats fournissent les tendances des performances du système composite et les considérations pour leur chargement et le développement des capacités en les environnements de durcissement. Comprendre les changements de comportement à cause des environnements extrêmes sera vital pour des conceptions sûres et optimisées du soutènement au sol.

Co-Authorship Statement

This thesis was written in the article-based format as described in the Royal Military College of Canada Thesis Preparation Guidelines. The author of this thesis, Captain Chuyue (Chelsey) Guo, was the main author for the articles contained in this document as Chapter 4 and Chapter 5, while co-authors provided guidance, assistance, and feedback. The author intends to submit the articles for publication in a peer-reviewed journals, which will include both academic supervisors as co-authors.

Table of Contents

Acknowledgements	ii
Abstract.....	iii
Résumé	iv
Co-Authorship Statement	v
List of Figures	xi
List of Tables	xxii
List of Abbreviations and Acronyms	xxiv
List of Symbols	xxvi
1 Introduction	1
1.1 Purpose of Study.....	1
1.2 Thesis Objectives	4
1.3 Investigation Methodology.....	5
1.4 Thesis Organization.....	6
1.5 Relevance to Research.....	7
2 Background	8
2.1 Rock Support.....	8
2.2 Rock Bolts.....	10
2.2.1 Mechanically Anchored Rock Bolts.....	13
2.2.2 Fully Grouted Rock Bolts.....	13
2.2.3 Frictionally Anchored Rock Bolts	15
2.2.4 Load Transfer Mechanisms	16
2.2.4.1 Continuously Mechanically Coupled Rock Bolt.....	19
2.2.5 Effect of Grout Type.....	20
2.2.6 Effect of Embedment Length	21
2.2.7 Effect of Radial Confinement Pressure	22
2.2.8 Failure Mechanism of Fully Grouted Rock Bolts	24
2.2.9 Design of Rock Bolt Systems	26

2.3	Distributed Fiber Optic Sensors	29
2.4	Cold Regions.....	35
2.5	Hot Regions	36
2.6	Historical Research.....	38
2.6.1	Temperature Effects	46
2.6.2	Cement Grouts in Cold Temperatures	46
2.6.3	Temperature Effects on Fully Grouted Rock Bolts.....	49
2.7	Historical Research Gaps.....	54
2.8	Summary of Past Research Group Testing and Findings	55
2.9	Relevance to Research.....	58
3	Material Testing	59
3.1	Introduction	59
3.2	Test Specimens Materials Requirements	59
3.3	Grout Baseline Study	61
3.3.1	Compressive Strength.....	63
3.3.2	Tensile Strength	66
3.3.3	Baseline Comparison Discussion.....	67
3.3.4	Lessons Learned.....	70
3.4	Polyimide Coated Fiber Optic	71
3.5	Monitoring Instrumentation Operating Temperature	73
3.6	Prototype	74
3.6.1	Prototype Overview	74
3.6.2	Temperature Sensor Calibration.....	77
3.6.3	Temperature DOS Verification.....	78
3.6.4	Strain DOS Verification and Rebar Bolt Properties.....	80
3.7	Confinement Material.....	84
3.8	Cement Grouts.....	85
3.8.1	Compressive Strength, Modulus of Elasticity, and Poisson’s Ratio	91

3.8.2	Tensile Strength	99
3.9	Chapter Summary	103
4	Utilizing Distributed Fiber Optic Sensors to Investigate the Effects of Permafrost Temperature Conditions on the Axial Response of Fully Grouted Rock Bolts	104
4.1	Introduction	105
4.2	Background	106
4.3	Methodology.....	110
4.3.1	Rebar Bolt Preparation	111
4.3.2	DOS Installation.....	112
4.3.3	Confinement Pipe Preparation	113
4.3.4	Specimen Assembly and Grouting	114
4.4	Laboratory Testing Program	119
4.4.1	Monitoring Program	119
4.4.2	Testing Scheme	122
4.4.3	Grout Strength Testing.....	122
4.5	Results.....	123
4.5.1	Pull-Out Test Results.....	123
4.5.2	Strain Profiles	128
4.5.3	Grout Strength Development	133
4.6	Discussion	133
4.6.1	Strain Profile Comparisons.....	135
4.6.2	Capacity Development.....	137
4.6.3	Axial Stiffness	141
4.6.4	DOS Performance in Cold Temperatures.....	145
4.7	Conclusions	147
5	Investigating the Effects of Geothermally Active Temperature Conditions on Fully Grouted Rock Bolts with Distributed Fiber Optic Sensors	149
5.1	Introduction	151

5.2	Background	151
5.3	Methodology.....	154
5.3.1	Rebar Bolt Preparation	155
5.3.2	DOS Installation.....	156
5.3.3	Specimen Assembly and Grouting	157
5.4	Laboratory Testing Program	161
5.4.1	Monitoring Program	162
5.4.2	Testing Scheme	165
5.4.3	Grout Strength Testing.....	165
5.5	Results.....	166
5.5.1	Pull-Out Test Results	166
5.5.2	Strain Profiles	171
5.5.3	Grout Strength Development	175
5.6	Discussion	176
5.6.1	Strain Profile Comparisons.....	178
5.6.2	Capacity Development.....	180
5.6.3	Axial Stiffness	183
5.6.4	DOS Performance in High Temperatures.....	187
5.7	Conclusions	188
6	Summary of Main Findings	190
6.1	Introduction	190
6.2	Permafrost Temperature Effects	190
6.3	Geothermally Active Temperature Effects	193
6.4	Whole Temperature Spectrum	195
6.5	Major Contributions.....	196
6.6	Summary of Research Group Objectives and Findings	198
7	Conclusions and Recommendations.....	202
7.1	Conclusions	202

7.2	Future Recommendations	202
8	References	204
	Appendix A Specimen Results.....	A-1
	Appendix B Comparisons & Miscellaneous	B-1

List of Figures

Figure 1-1. Example of support and reinforcement elements used in underground excavations (tunnel in this case) (modified after Forbes et al, 2018)	2
Figure 1-2. Typical research group pull out test setup (Cruz, 2017).....	3
Figure 1-3. Thesis investigation program workflow	5
Figure 1-4. Thesis chapter layout and structure	7
Figure 2-1. Example of support and reinforcement elements used in underground excavations (modified after Oke et al, 2014).....	9
Figure 2-2. Typical rock bolt and dowel application in different rock masses during tunnelling (Hoek, 2007)	11
Figure 2-3. Systems of classification of rock bolts (Frenelus et al, 2022)	12
Figure 2-4. Mechanically anchored rock bolt (Hoek, 2007).....	13
Figure 2-5. Left: Fully grouted rock bolt; Right: Resin grouted rock bolt (modified after Hoek, 2007)	14
Figure 2-6. Left: Split Set stabiliser; Right: Swellex bolt (modified after Hoek et al, 2000)	15
Figure 2-7. Components of rock reinforcement system (Thompson & Villaescusa, 2014)	16
Figure 2-8. Reinforcement mechanisms (Pinazzi et al, 2020).....	17
Figure 2-9. Reinforcement element load transfer (Thompson & Villaescusa, 2014)	18
Figure 2-10. Left: CMC and CFC load transfer; Right: DMFC load transfer (modified after Bobet & Einstein, 2011)	18
Figure 2-11. Load distribution along a rock bolt (Stille, 1992).....	20
Figure 2-12. Effects of grout water/cement ratio on bolt capacity: A. w/c 0.30; B. w/c 0.40; C. w/c 0.50 (modified after Hyett et al, 1992)	21
Figure 2-13. Peak bolt capacity vs Embedment length (Hyett et al, 1992)	22
Figure 2-14. Effects of confining pressure on bond capacity (Moosavi et al, 2003)	23
Figure 2-15. Comparison of radial stiffness to load capacity (Hyett et al, 1992) ...	24
Figure 2-16. Left: Tension due to bed dilation or bed separation; Right: Tension and bending due to bed slipping (Mart et al, 2002)	24
Figure 2-17. Failure modes of fully grouted rock bolts: A. Grout failure; B. Bolt failure; C. Inadequate embedment length (grout column failure) (Serbousek & Signer, 1987)	26
Figure 2-18. Bolt-grout interface failure mechanism (Vlachopoulos et al, 2018) ..	26

Figure 2-19. Longitudinal Displacement Profile (Vlachopoulos & Diederichs, 2009)	28
Figure 2-20. ASTM D4435-13e1 Rock bolt pull test schematic (ASTM, 2013)	29
Figure 2-21. . Schematics of previous laboratory testing setups: A and B. Modified test setups based on split-pipe test (modified after Hyett et al, 1992); C. Pull-out strength test (Li et al, 2017b); D. Pull-out test setup (Benmokrane et al, 1995)	30
Figure 2-22. Continuous vs Discrete strain profile (Vlachopoulos, 2017)	32
Figure 2-23. Basic OFDR optical network (Luna Inc., 2015)	32
Figure 2-24. Fiber optic sensing configuration (Vlachopoulos et al, 2018)	33
Figure 2-25. DOS debonding testing and strain profile with transition sections (modified after Moore, 2021)	34
Figure 2-26. Map of permafrost in Canada (Natural Resources Canada, 2016)	36
Figure 2-27. Temperature change with distance from repository centre: a. Local; b. Global (modified after Xue et al, 2021)	38
Figure 2-28. Stress situation in a grouted bolt (Farmer, 1975)	39
Figure 2-29. Theoretical stress distribution along a fully grouted rock bolt (Farmer, 1975)	40
Figure 2-30. Bond strength model (Yazici & Kaiser, 1992)	41
Figure 2-31. Trilinear bond-slip model (Benmokrane et al, 1995)	42
Figure 2-32. Shear stress distribution along fully grouted rock bolt under axial load (Li & Stillborg, 1999)	43
Figure 2-33. Evolution of interfacial shear stress distribution and propagation of debonding (Ren et al, 2010)	44
Figure 2-34. Analytical model of fully grouted rock bolt in pull-out test (Ma et al, 2013)	45
Figure 2-35. Compressive and shear bond strength tests results (Morris, 1970)	47
Figure 2-36. Laboratory grout compressive strength results (Reny et al, 2017)	48
Figure 2-37. Unconfined compressive strength test results for CSA and ordinary PC (Huang, 2021)	49
Figure 2-38. Test specimen schematic and strain gauge layout (modified after Li et al, 2017b)	50
Figure 2-39. Effects of temperature on axial force and shear stress distribution under same tensile force: (a) 10 kN; (b) 30 kN; (c) 70 kN; (d) 90 kN (modified after Li et al, 2017b)	51
Figure 2-40. Effect of temperature on ultimate tensile force: (a) 7 days curing; (b) 28 days curing (modified after Li et al, 2017a)	52
Figure 2-41. Curve fitting (Li et al, 2017a)	53

Figure 3-1. Portion of FGRB focused by pull-out test (modified after Stille, 1992)	60
Figure 3-2. Cut open FGRB test specimen	60
Figure 3-3. Preparation and curing of baseline grout test cylinders	62
Figure 3-4. Preparation of UCS cylinders using grinding machine	63
Figure 3-5. RIEHLE testing machine	64
Figure 3-6. Pre-test grout cylinder measurement process	64
Figure 3-7. Typical fracture patterns (ASTM, 2021)	65
Figure 3-8. Failure pattern of compressive test specimen	66
Figure 3-9. Preparation measurements and STS testing setup	66
Figure 3-10. Tensile testing of grout cylinders	67
Figure 3-11. Visual comparison of PC and Nordic grouts	68
Figure 3-12. Manufacturer published compressive strengths (left: modified after Ciment Québec (n.d); right: modified after King A Sika Company (n.d.))	68
Figure 3-13. DOS de-bonding testing and strain pickup transition (modified after Moore, 2021)	72
Figure 3-14. Transition section of strain pickup for polyimide coated fiber	73
Figure 3-15. Full-length prototype	75
Figure 3-16. Instrumentation conceptual design for reduced-length prototype (Guo et al, 2023)	76
Figure 3-17. TCal sensor used for temperature calibration testing	77
Figure 3-18. Temperature sensor calibration setup – Glycol bath	77
Figure 3-19. Relationship of strain and temperature (Guo et al, 2023)	78
Figure 3-20. Testing and monitoring setup for prototype testing (Guo et al, 2023)	79
Figure 3-21. Strain profile of T DOS at different stages of prototype loading (Guo et al, 2023)	79
Figure 3-22. T DOS response to applied heat source	80
Figure 3-23. Strain profile of ϵ DOS at different loads along entire fiber length (Guo et al, 2023)	81
Figure 3-24. Stress vs strain – ϵ DOS	82
Figure 3-25. Strain profile ϵ DOS and SG (Guo et al, 2023)	82
Figure 3-26. Load vs strain in elastic zone – SG	83
Figure 3-27. Test confinement rig	85
Figure 3-28. Water-cement mixing and cleaned/oiled moulds	87
Figure 3-29. Grout cylinders in each curing condition	88
Figure 3-30. Split cylinders of PC at 0.4 w/c ratio and Nordic at 0.29 w/c ratio	88
Figure 3-31. Test age tolerances for compressive tests (ASTM, 2021)	89

Figure 3-32. P20-28 UCS observations: A. Typical P20 cylinder test; B. P20-28 C2 and C3 during testing; C. P20-28 cylinders post-test.....	92
Figure 3-33. Grout compressive strength development over 90 days for each curing condition: (a) Points only; (b) Points and connecting lines	96
Figure 3-34. UCS testing setup including conditioned steel plate	97
Figure 3-35. Setup for grout Modulus of Elasticity and Poisson’s Ratio testing.....	97
Figure 3-36. Grout tensile strength development over 90 days for each curing condition: (a) Points only; (b) Points and connecting lines	102
Figure 4-1. Map of continuous and discontinuous permafrost regions in Canada (Natural Resources Canada, 2016)	107
Figure 4-2. Components of rock reinforcement system (Thompson & Villaescusa, 2014)	108
Figure 4-3. Location of machined grooves: (a) Three groove orientation; (b) Diametrically opposing grooves along transverse ribs; (c) Diametrically opposing grooves along longitudinal ribs (modified after Moore, 2021)	111
Figure 4-4. Rebar cleaned of rust.....	112
Figure 4-5. DOS configuration in diametrically opposing grooves	113
Figure 4-6. DOS instrumented rebar bolts.....	113
Figure 4-7. Instrumented confinement pipe and rock bolt installed prior to grouting	114
Figure 4-8. Schematic of assembly of FGRB specimen	115
Figure 4-9. Grouting rack and specimen assemble.....	116
Figure 4-10. Grouted specimens and test cylinders in freezer room; grouting tools	117
Figure 4-11. Grouted FGRB specimens: (a) P5 specimens; (b) P20 specimens – grout expanded out of the confinement pipes after grouting completed.....	118
Figure 4-12. Prepared FGRB specimen with thermal insulation wrap and grout cap removed.....	118
Figure 4-13. Laboratory pull-out test assembly and monitoring setup	119
Figure 4-14. Test setup instrumentation details.....	121
Figure 4-15. Load-Displacement curve from P5-3: (a) Whole system response; (b) Axial displacement corrected for test rig movement and elongation.....	125
Figure 4-16. Load-Displacement curve from P20-3: (a) Whole system response; (b) Axial displacement corrected for test rig movement and elongation.....	125
Figure 4-17. P5-3 specimen axial displacement profile	126
Figure 4-18. Load-Displacement curve – DOS: (a) P5-3 specimen; (b) P20-3 specimen	127

Figure 4-19. Pipe dilation monitoring at 50 mm: (a) P5-3 specimen; (b) P20-3 specimen.....	127
Figure 4-20. P5-28 specimen cut open for post-test evaluations.....	128
Figure 4-21. P5-3 specimen strain profile along rebar bolt during pull-out testing	129
Figure 4-22. P5-3 specimen temperature strain profile along rebar bolt during pull-out testing.....	130
Figure 4-23. Strain profiles over entire loading sequence: (a) P5-7 partial length; (b) P20-28 partial length	130
Figure 4-24. P5-28 specimen temperature change during pull-out testing	131
Figure 4-25. T DOS: (a) Only reacting to temperature change; (b) Reacting to rebar loading; (c) Post-test observation of T DOS stainless steel tube lifted out of groove	132
Figure 4-26. Strength development curves: (a) Grout UCS; (b) Grout STS.....	133
Figure 4-27. Bolt-grout interface failure mechanisms (Vlachopoulos, 2018).....	135
Figure 4-28. P5 Condition comparison of strain profiles and mobilized embedment length: (a) at 20 kN; (b) at 100 kN.....	136
Figure 4-29. P20 Condition comparison of strain profiles and mobilized embedment length: (a) at 20 kN; (b) at 100 kN.....	136
Figure 4-30. Critical embedment length at 120 kN: (a) P5; (b) P20.....	137
Figure 4-31. Comparison of strain profiles between P5 and P20 at 28-day and 35-day cure: (a) at 20 kN; (b) at 100 kN	137
Figure 4-32. Maximum load vs curing temperature	138
Figure 4-33. Maximum load vs curing duration.....	139
Figure 4-34. P5-90 specimen rebar tensile failure inside of embedment length, green tape marks location of borehole collar	141
Figure 4-35. Axial stiffness comparisons: (a) Grout UCS; (b) Confidence interval (α 0.05); (c) Mean bond strength; (d) critical embedment length.....	143
Figure 4-36. Axial stiffness plotted against temperature: (a) DOS – rebar; (b) Conventional instruments – Whole system.....	145
Figure 4-37. DOS temperature spatial resolution verification.....	147
Figure 5-1. Schematic of deep geological repository plan by NWMO (Nuclear Waste Management Organization, 2023).....	152
Figure 5-2. Load transfer mechanism of rock bolts (modified after Vlachopoulos, 2017)	153

Figure 5-3. Location of machined grooves: (a) Three groove orientation; (b) Diametrically opposing grooves along transverse ribs; (c) Diametrically opposing grooves along longitudinal ribs (modified after Moore, 2021)	156
Figure 5-4. DOS configuration in diametrically opposing grooves	157
Figure 5-5. Schematic of FGRB specimen	158
Figure 5-6. Confinement pipe preparations	159
Figure 5-7. FGRB Specimen installation in grouting rack with grout pump.....	160
Figure 5-8. Evaporation protection of FGRB specimen ends and grout cylinders	161
Figure 5-9. Laboratory pull-out test assembly and monitoring setup	162
Figure 5-10. Test setup instrumentation details.....	164
Figure 5-11. Load-Displacement curve from C20-7: (a) Whole system response; (b) Axial displacement corrected for test rig movement and elongation.....	168
Figure 5-12. Load-Displacement curve from G45-3: (a) Whole system response; (b) Axial displacement corrected for test rig movement and elongation.....	168
Figure 5-13. C20-7 specimen axial displacement profile	169
Figure 5-14. Pipe dilation monitoring at 50 mm: (a) C20-7 specimen; (b) G45-3 specimen.....	170
Figure 5-15. G45-3 specimen cut open for post-test evaluations	171
Figure 5-16. G45-3 specimen strain profile along rebar bolt during pull-out testing	172
Figure 5-17. Strain profiles over entire loading sequence: (a) C20-7; (b) G45-35	173
Figure 5-18. G45-28 specimen temperature change during pull-out testing.....	174
Figure 5-19. Reaction of T DOS: (a) Only reacting to temperature change; (b) Reacting to rebar loading; (c) Post-test observation of T DOS stainless steel tube lifted out of groove	174
Figure 5-20. Grout strength development curves: (a) UCS; (b) STS.....	176
Figure 5-21. Bolt-grout interface failure mechanisms (Vlachopoulos et al, 2018)	177
Figure 5-22. Grout mobilization observed in C20-35 specimen	177
Figure 5-23. C20 Condition comparison of strain profiles and mobilized embedment length: (a) at 20 kN; (b) at 100 kN.....	178
Figure 5-24. G45 Condition comparison of strain profiles and mobilized embedment length: (a) at 20 kN; (b) at 100 kN.....	179
Figure 5-25. Critical embedment length at 120 kN: (a) C20; (b) G45	179
Figure 5-26. Comparison of strain profiles between C20 and G45 at 28-day and 35-day cure: (a) at 20 kN; (b) at 100 kN	180
Figure 5-27. Maximum load vs curing temperature	181

Figure 5-28. Maximum load vs curing duration.....	182
Figure 5-29. Axial stiffness comparisons: (a) Grout UCS; (b) Confidence interval (alpha 0.05); (c) Mean bond strength; (d) critical embedment length.....	185
Figure 5-30. Axial stiffness plotted against temperature: (a) DOS – rebar; (b) Conventional instruments – Whole system.....	186
Figure 5-31. DOS temperature spatial resolution assessment	188
Figure 6-1. Summary of laboratory testing program	190
Figure A-1. Load-Displacement curve from P20-3: (a) Whole system response; (b) Axial displacement corrected for test rig movement and elongation.....	A-1
Figure A-2. P20-3 specimen strain profile along rebar bolt during pull-out testing.....	A-1
Figure A-3. P20-3 specimen axial displacement profile.....	A-2
Figure A-4. P20-3 specimen pipe dilation monitoring at 50 mm.....	A-2
Figure A-5. P20-3 specimen temperature change during pull-out testing	A-3
Figure A-6. Load-Displacement curve from P20-7 [DAQ malfunction resulted in inaccurate load recording]: (a) Whole system response; (b) Axial displacement corrected for test rig movement and elongation	A-3
Figure A-7. P20-7 specimen pipe dilation monitoring at 50 mm [[DAQ malfunction resulted in inaccurate load recording]: SG 1 failure during testing.....	A-4
Figure A-8. P20-7 specimen temperature change during pull-out testing	A-4
Figure A-9. Load-Displacement curve from P20-28: (a) Whole system response; (b) Axial displacement corrected for test rig movement and elongation.....	A-5
Figure A-10. P20-28 specimen strain profile along rebar bolt during pull-out testing [partial length]	A-5
Figure A-11. P20-28 specimen axial displacement profile [partial length].....	A-6
Figure A-12. P20-28 specimen pipe dilation monitoring at 50 mm.....	A-6
Figure A-13. P20-28 specimen temperature change during pull-out testing	A-7
Figure A-14. Load-Displacement curve from P20-35: (a) Whole system response; (b) Axial displacement corrected [LVDT malfunction]	A-7
Figure A-15. P20-35 specimen strain profile along rebar bolt during pull-out testing	A-8
Figure A-16. P20-35 specimen axial displacement profile.....	A-8
Figure A-17. P20-35 specimen pipe dilation monitoring at 50 mm.....	A-9
Figure A-18. P20-35 specimen temperature change during pull-out testing	A-9
Figure A-19. Load-Displacement curve from P20-60 [DAQ malfunction resulted in inaccurate load recording]: (a) Whole system response; (b) Axial displacement corrected for test rig movement and elongation	A-10

Figure A-20. P20-60 specimen axial displacement profile [partial length].....	A-10
Figure A-21. P20-60 specimen axial displacement profile [partial length].....	A-11
Figure A-22. P20-60 specimen pipe dilation monitoring at 50 mm [DAQ issues] ..	A-11
Figure A-23. P20-60 specimen temperature change during pull-out testing [T DOS malfunction].....	A-12
Figure A-24. Load-Displacement curve from P20-90: (a) Whole system response; (b) Axial displacement corrected for test rig movement and elongation.....	A-12
Figure A-25. P20-90 specimen strain profile along rebar bolt during pull-out testing [partial length]	A-13
Figure A-26. P20-90 specimen axial displacement profile [partial length].....	A-13
Figure A-27. P20-90 specimen pipe dilation monitoring at 50 mm: SG 1 failure	A-14
Figure A-28. P20-90 specimen temperature change during pull-out testing.....	A-14
Figure A-29. Load-Displacement curve from P5-3: (a) Whole system response; (b) Axial displacement corrected for test rig movement and elongation.....	A-15
Figure A-30. P5-3 specimen strain profile along rebar bolt during pull-out testing	A-15
Figure A-31. P5-3 specimen axial displacement profile.....	A-16
Figure A-32. P5-3 specimen pipe dilation monitoring at 50 mm.....	A-16
Figure A-33. P5-3 specimen temperature change during pull-out testing	A-17
Figure A-34. Load-Displacement curve from P5-7 [DAQ collection overload]: (a) Whole system response; (b) Axial displacement corrected [DAQ malfunction]	A-17
Figure A-35. P5-7 specimen strain profile along rebar bolt during pull-out testing [partial length]	A-18
Figure A-36. P5-7 specimen axial displacement profile [partial length].....	A-18
Figure A-37. P5-7 specimen temperature change during pull-out testing	A-19
Figure A-38. Load-Displacement curve from P5-28: (a) Whole system response; (b) Axial displacement corrected for test rig movement and elongation.....	A-19
Figure A-39. P5-28 specimen strain profile along rebar bolt during pull-out testing	A-20
Figure A-40. P5-28 specimen axial displacement profile.....	A-20
Figure A-41. P5-28 specimen pipe dilation monitoring at 50 mm.....	A-21
Figure A-42. P5-28 specimen temperature change during pull-out testing	A-21
Figure A-43. Load-Displacement curve from P5-35: (a) Whole system response; (b) Axial displacement corrected for test rig movement and elongation.....	A-22
Figure A-44. P5-35 specimen strain profile along rebar bolt during pull-out testing	A-22

Figure A-45. P5-35 specimen axial displacement profile.....	A-23
Figure A-46. P5-35 specimen pipe dilation monitoring at 50 mm.....	A-23
Figure A-47. Load-Displacement curve from P5-60: (a) Whole system response; (b) Axial displacement corrected for test rig movement and elongation.....	A-24
Figure A-48. P5-60 specimen strain profile along rebar bolt during pull-out testing	A-24
Figure A-49. P5-60 specimen axial displacement profile.....	A-25
Figure A-50. P5-60 specimen pipe dilation monitoring at 50 mm.....	A-25
Figure A-51. Load-Displacement curve from P5-90: (a) Whole system response; (b) Axial displacement corrected for test rig movement and elongation [LVDT malfunction].....	A-26
Figure A-52. P5-90 specimen pipe dilation monitoring at 50 mm.....	A-26
Figure A-53. P5-90 specimen temperature change during pull-out testing	A-27
Figure A-54. Load-Displacement curve from C20-3: (a) Whole system response; (b) Axial displacement corrected for test rig movement and elongation.....	A-27
Figure A-55. C20-3 specimen strain profile along rebar bolt during pull-out testing	A-28
Figure A-56. C20-3 specimen axial displacement profile.....	A-28
Figure A-57. C20-3 specimen pipe dilation monitoring at 50 mm.....	A-29
Figure A-58. Load-Displacement curve from C20-7: (a) Whole system response; (b) Axial displacement corrected for test rig movement and elongation.....	A-29
Figure A-59. C20-7 specimen strain profile along rebar bolt during pull-out testing	A-30
Figure A-60. C20-7 specimen axial displacement profile.....	A-30
Figure A-61. C20-7 specimen pipe dilation monitoring at 50 mm.....	A-31
Figure A-62. Load-Displacement curve from C20-28: (a) Whole system response; (b) Axial displacement corrected for test rig movement and elongation.....	A-31
Figure A-63. C20-28 specimen strain profile along rebar bolt during pull-out testing	A-32
Figure A-64. C20-28 specimen axial displacement profile.....	A-32
Figure A-65. C20-28 specimen pipe dilation monitoring at 50 mm.....	A-33
Figure A-66. Load-Displacement curve from C20-35: (a) Whole system response; (b) Axial displacement corrected for test rig movement and elongation.....	A-33
Figure A-67. C20-35 specimen strain profile along rebar bolt during pull-out testing	A-34
Figure A-68. C20-35 specimen axial displacement profile.....	A-34
Figure A-69. C20-35 specimen pipe dilation monitoring at 50 mm.....	A-35

Figure A-70. Load-Displacement curve from C20-60: (a) Whole system response; (b) Axial displacement corrected for test rig movement and elongation	A-35
Figure A-71. C20-60 specimen strain profile along rebar bolt during pull-out testing	A-36
Figure A-72. C20-60 specimen axial displacement profile.....	A-36
Figure A-73. C20-60 specimen pipe dilation monitoring at 50 mm.....	A-37
Figure A-74. Load-Displacement curve from C20-90: (a) Whole system response; (b) Axial displacement corrected for test rig movement and elongation.....	A-37
Figure A-75. C20-90 specimen strain profile along rebar bolt during pull-out testing	A-38
Figure A-76. C20-90 specimen axial displacement profile.....	A-38
Figure A-77. C20-90 specimen pipe dilation monitoring at 50 mm.....	A-39
Figure A-78. Load-Displacement curve from G45-3: (a) Whole system response; (b) Axial displacement corrected for test rig movement and elongation.....	A-39
Figure A-79. G45-3 specimen strain profile along rebar bolt during pull-out testing	A-40
Figure A-80. G45-3 specimen axial displacement profile	A-40
Figure A-81. G45-3 specimen pipe dilation monitoring at 50 mm	A-41
Figure A-82. G45-3 specimen temperature change during pull-out testing.....	A-41
Figure A-83. Load-Displacement curve from G45-7 [MTS grip slipped during loading]: (a) Whole system response; (b) Axial displacement corrected for test rig movement and elongation	A-42
Figure A-84. G45-7 specimen strain profile along rebar bolt during pull-out testing	A-42
Figure A-85. G45-7 specimen axial displacement profile	A-43
Figure A-86. G45-7 specimen pipe dilation monitoring at 50 mm	A-43
Figure A-87. G45-7 specimen temperature change during pull-out testing.....	A-44
Figure A-88. Load-Displacement curve from G45-28 [Power supply tripped]: (a) Whole system response; (b) Axial displacement corrected for test rig movement and elongation	A-44
Figure A-89. G45-28 specimen strain profile along rebar bolt during pull-out testing	A-45
Figure A-90. G45-28 specimen axial displacement profile	A-45
Figure A-91. G45-28 specimen pipe dilation monitoring at 50 mm	A-46
Figure A-92. G45-28 specimen temperature change during pull-out testing	A-46
Figure A-93. Load-Displacement curve from G45-35: (a) Whole system response; (b) Axial displacement corrected for test rig movement and elongation.....	A-47

Figure A-94. G45-35 specimen strain profile along rebar bolt during pull-out testing	A-47
Figure A-95. G45-35 specimen axial displacement profile	A-48
Figure A-96. G45-35 specimen pipe dilation monitoring at 50 mm	A-48
Figure A-97. G45-35 specimen temperature change during pull-out testing	A-49
Figure A-98. Load-Displacement curve from G45-60: (a) Whole system response; (b) Axial displacement corrected for test rig movement and elongation.....	A-49
Figure A-99. G45-60 specimen strain profile along rebar bolt during pull-out testing	A-50
Figure A-100. G45-60 specimen axial displacement profile	A-50
Figure A-101. G45-60 specimen pipe dilation monitoring at 50 mm	A-51
Figure A-102. Load-Displacement curve from G45-90: (a) Whole system response; (b) Axial displacement corrected for test rig movement and elongation	A-51
Figure A-103. G45-90 specimen pipe dilation monitoring at 50 mm	A-52
Figure B-1. P20 condition specimens strain profile comparisons at different loads: (a) 20 kN; (b) 50 kN; (c) 80 kN; (d) 100 kN; (e) 120 kN	B-1
Figure B-2. P5 condition specimens strain profile comparisons at different loads: (a) 20 kN; (b) 50 kN; (c) 80 kN; (d) 100 kN; (e) 120 kN; (f) 140 kN	B-2
Figure B-3. C20 condition specimens strain profile comparisons at different loads: (a) 20 kN; (b) 50 kN; (c) 80 kN; (d) 100 kN; (e) 120 kN; (f) 140 kN.....	B-3
Figure B-4. G45 condition specimens strain profile comparisons at different loads: (a) 20 kN; (b) 50 kN; (c) 80 kN; (d) 100 kN; (e) 120 kN; (f) 140 kN.....	B-4
Figure B-5. Critical embedment length comparisons: (a) P20; (b) P5; (c) C20; (d) G45	B-5
Figure B-6. P20-3 specimen post-test forensics	B-5
Figure B-7. P20-28 specimen post-test forensics	B-6
Figure B-8. P20-60 specimen post-test forensics	B-6
Figure B-9. P5-3 specimen post-test forensics.....	B-7
Figure B-10. P5-7 specimen post-test forensics	B-7
Figure B-11. P5-28 specimen post-test forensics	B-8
Figure B-12. C20-3 specimen post-test forensics	B-8
Figure B-13. C20-35 specimen post-test forensics	B-9
Figure B-14. G45-3 specimen post-test forensics	B-9
Figure B-15. G45-28 specimen post-test forensics.....	B-10
Figure B-16. G45-60 specimen post-test forensics.....	B-10

List of Tables

Table 2-1. Typical laboratory confining material radial stiffness and rock type (O’Connor, 2020)	23
Table 2-2. Summary of operational features/capabilities of fiber optic sensing techniques (modified after Forbes et al, 2018)	35
Table 2-3. Summary of past research group Master’s Degree Thesis objectives...56	
Table 2-4. Summary of past research groups investigations.....	57
Table 2-5. Summary of past research groups thesis conclusions	57
Table 3-1. Summary of materials testing regime.....	59
Table 3-2. Grout type utilized for each simulated condition and temperature	62
Table 3-3. Grout baseline UCS test results	65
Table 3-4. Grout baseline STS test results	67
Table 3-5. Average UCS and STS comparison of PC and Nordic	68
Table 3-6. Relationship STS and compressive strength (Arioglu et al, 2006)	69
Table 3-7. Estimated STS for baseline test compressive strength results	70
Table 3-8. Summary of operating temperature ranges for monitoring instrumentation	74
Table 3-9. Reduced-length prototype material summary	76
Table 3-10. Comparison of strain measurements between ϵ DOS and SG (Guo et al, 2023)	83
Table 3-11. Modulus of Elasticity results (modified after Guo et al, 2023)	83
Table 3-12. Summary of grouting times	86
Table 3-13. Summary of total grout test cylinders	86
Table 3-14. Summary of test ages – P20.....	89
Table 3-15. Summary of test ages – P5.....	90
Table 3-16. Summary of test ages – C20	90
Table 3-17. Summary of test ages – G45	90
Table 3-18. Summary of UCS Results – P20	93
Table 3-19. Summary of UCS Results – P5	93
Table 3-20. Summary of UCS Results – C20	94
Table 3-21. Summary of UCS Results – G45.....	95
Table 3-22. Summary of Modulus of Elasticity and Poisson’s Ratio of Grout Cylinders	98
Table 3-23. Summary of STS results – P20.....	99
Table 3-24. Summary of STS results – P5.....	100
Table 3-25. Summary of STS results – C20.....	100
Table 3-26. Summary of STS results – G45	101

Table 4-1. Material properties of the rebar.....	112
Table 4-2. Specimens preparation schedule (24 total specimens).....	115
Table 4-3. Sensor details and locations	120
Table 4-4. Sensor settings and uncertainties.....	121
Table 4-5. Summary of Nordic grout UCS and STS test results in P20 condition..	123
Table 4-6. Summary of Nordic grout UCS and STS test results in P5 condition....	123
Table 4-7. Pull-Out testing results for P20 and P5 specimens	124
Table 4-8. Specimen temperature change results.....	132
Table 4-9. MLR coefficients of curing time and grout UCS on max load	140
Table 4-10. Axial stiffness	142
Table 4-11. MLR coefficients of grout UCS and mean bond strength on axial stiffness - DOS	144
Table 4-12. MLR coefficients of grout UCS and mean bond strength on axial stiffness – whole system	144
Table 4-13. Summary of monitoring instrumentation operating temperature ranges	146
Table 5-1. Summary of materials testing results of the rebar	156
Table 5-2. Specimens preparation schedule (24 total specimens).....	158
Table 5-3. Sensor details and locations	163
Table 5-4. Sensor settings and uncertainties.....	164
Table 5-5. Summary of PC grout UCS and STS test results in C20 condition	166
Table 5-6. Summary of PC grout UCS and STS test results in G45 condition.....	166
Table 5-7. Pull-Out testing results for C20 and G45 specimens	167
Table 5-8. G45 specimen temperature change results.....	175
Table 5-9. MLR coefficients of curing time and grout UCS on max load	183
Table 5-10. Axial stiffness	184
Table 5-11. MLR coefficients of grout UCS and mean bond strength on axial stiffness - DOS	185
Table 5-12. MLR coefficients of grout UCS and mean bond strength on axial stiffness – whole system	186
Table 5-13. Summary of monitoring instrumentation operating temperature ranges	187
Table 6-1. Updated summary of research group Master’s Degree Thesis objectives	198
Table 6-2. Updated summary of research groups investigations	199
Table 6-3. Updated summary of research groups thesis conclusions	200

List of Abbreviations and Acronyms

APM	Adaptive Phased Management
ASTM	American Society for Testing and Materials
Approx.	Approximately
Avg.	Average
CAF	Canadian Armed Forces
CFC	Continuously Frictionally Coupled
CMC	Continuously Mechanically Coupled
CSA	Calcium Sulfoaluminate
DAQ	Data Acquisition System
DMFC	Discretely Mechanically or Frictionally Coupled
DOS	Distributed Optical Sensing
e.g.	Exempli Gratia
etc.	Et Cetera
FGRB	Fully Grouted Rock Bolt
FOS	Fiber Optic Sensor
HLRW	High-Level Radioactive Waste
i.e.	Id Est
LC	Lucent Connector
LDP	Longitudinal Displacement Profiles
LVDT	Linear Variable Displacement Transducer
MLR	Multiple Linear Regression
MTS	Material Testing System
NGI	Norwegian Geotechnical Institute
ODISI-B	Optical Distributed Sensor Interrogator
PC	Portland Cement

PVC	Polyvinyl Chloride
RMC	Royal Military College of Canada
RMR	Rock Mass Rating
RQD	Rock Quality Designation
ROFDR	Rayleigh Optical Frequency Domain Reflectometry
SG	Strain Gauge
STS	Splitting Tensile Strength
T DOS	Temperature DOS
TDS	Technical Data Sheet
UCS	Uniaxial Compressive Strength
w/c	Water to Cement Ratio
ϵ DOS	Strain DOS

List of Symbols

d_b	Bolt diameter
E	Young's Modulus
F_y	Yield Strength
F_u	Ultimate Strength
L	Length
L_e	Embedment Length
P_{max}	Maximum Load
r_b	Bolt radius
s	Mean Bond Strength
T	Temperature
U_x	Axial Displacement
x	Distance along rebar
$^{\circ}C$	Degrees Celsius
Δ	Delta
\varnothing	Diameter
ν	Poisson's Ratio
ε	Strain
Σ	Summation

1 Introduction

1.1 Purpose of Study

Over the course of human history, underground excavations and tunnelling have been essential in cultural and infrastructure advancement. Ancient civilizations developed tunnelling techniques in order to support diverse activities: Ancient Egyptians utilized them in burial and religious construction works (El Salam, 2002), Ancient Greeks used them for water distribution (Vlachopoulos, 2022), and Ancient Romans employed tunnels for military operations, and transportation (Castellani & Dragoni, 1997). In the modern era, they have vital infrastructure roles such as transportation, nuclear waste management, underground research facilities, communications, mining operations, utilities distribution, hydroelectric power generation, and flood control, among others. Underground construction and mining are major engineering endeavours as the removal of rock during excavation causes a disturbance in the stress equilibrium resulting in rock displacement (i.e. radial convergence).

Rock instability during underground excavations is a global phenomenon that, if not properly mitigated, risks the loss of equipment, assets, and even human life. As projects are becoming larger and more complex, venturing deeper below the surface, the demands and risks also escalate. The design and employment of ground support systems are a non-trivial pursuit. One of the most widely used support systems in underground excavations are rock bolts. Typically, a combination of the different support and reinforcement types will be employed as seen in Figure 1-1. The types chosen are dependent on the extent of fractured or loosened material around the excavation and the ground type/conditions (Hoek & Wood 1987). The purpose of support is to maintain confinement in the rock mass so that it remains self-supported (Vlachopoulos et al, 2013).

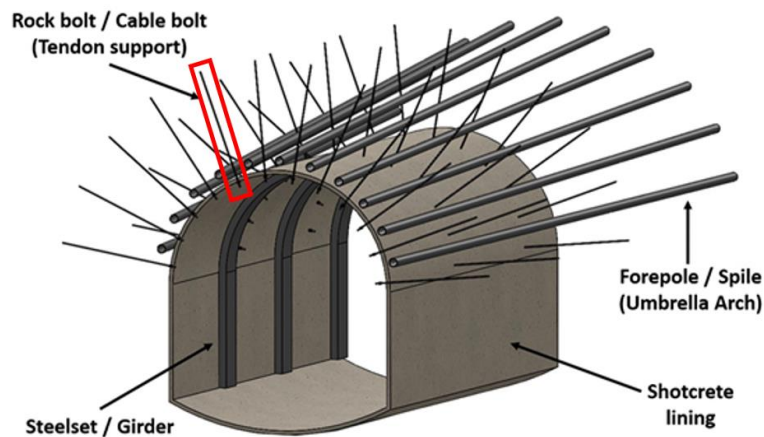


Figure 1-1. Example of support and reinforcement elements used in underground excavations (tunnel in this case) (modified after Forbes et al, 2018)

In the 1970s, the fully grouted rock bolt (FGRB) surged in popularity and is now one of the most widely used systems in rock support (Bobet & Einstein, 2011). They have been proven to be more versatile and adaptable to wider range of ground conditions than traditional mechanically anchored rock bolts (Hoek & Wood, 1987). In order to effectively design support systems, in situ geological conditions and support element behaviours need to be well understood. In addition, how the systems and rock mass interact are essential to planning and support design. Although rock bolts have been employed for over a century, the full-range of mechanical behaviour and interactions in situ are still not completely understood. A multitude of global research programs including field monitoring, laboratory and in situ testing, analytical methods, and numerical modelling have been undertaken to better understand and model their behaviour, however, gaps continue to persist in current knowledge and theories. There is a requirement to continue improving the understanding of relevant geo-mechanisms in this regard, in order to remove assumptions and guess work in design so that systems are not under-designed or unnecessarily rigorous.

FGRBs are employed in a wide spectrum of operational environments and must adapt to in order to maintain safe operations. As underground operations expand to all areas of the world and increase in depth, environmental conditions will become more challenging. Temperatures at the extremes can potentially affect the bonding and performance of FGRBs and it is vital to understand these effects in order to create safe and optimized support designs. Two operational temperature extreme scenarios in Canada were considered during the conceptualization of the

investigation undertaken and summarized herein: 1. Canadian strategic interests in the North, and 2. Nuclear waste repositories. Generally, these unique scenarios will be referred to as the permafrost (cold) condition and geothermally active (hot) condition.

Numerous pull-out tests on rock bolts have been conducted over the years to study various components and their effects, however, there has been limited studies investigating the effects of surrounding rock mass temperatures on FGRBs and the majority of these focus on higher temperatures (Li et al, 2017b; Wang et al, 2018; Zhang et al, 2021). Conventional monitoring instrumentation is the most common technique utilized in past and present studies. These techniques certainly have their limitations. This research project aims to bridge selected gaps in knowledge through the use of state-of-the-art fiber optic technology that provides an unprecedented spatial resolution of 0.65 mm in laboratory testing of FGRBs in pull-out tests. This study is the latest in the series of research to better understand the mechanics of FGRB utilizing distributed optical sensing (DOS) (Forbes, 2015; Cruz, 2017; O'Connor, 2020; Moore, 2021) and part of the global effort of the Canadian Military Geoworks Laboratory at the Royal Military College of Canada (RMC) to better understand individual and combined effects/behaviours of ground support elements. Typical pull-out test setup using the Material Testing System (MTS) and DOS within the Structures laboratory of RMC is seen in Figure 1-2.

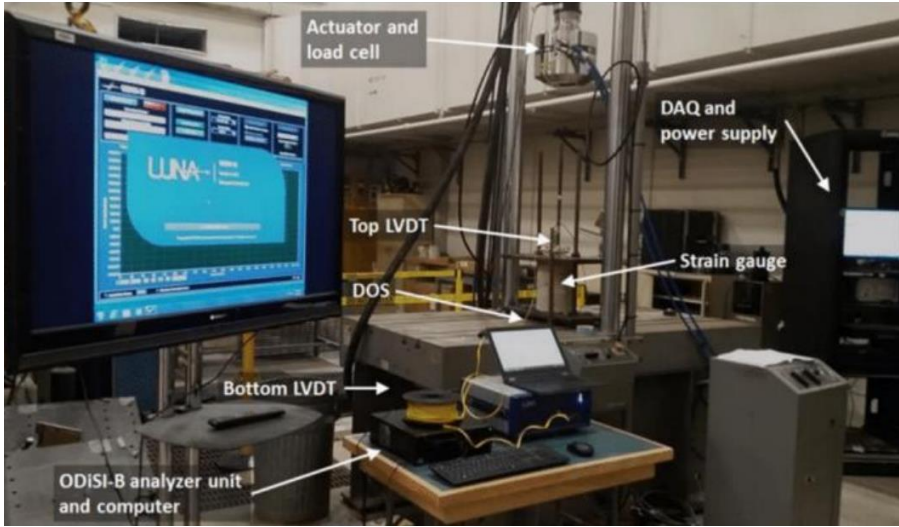


Figure 1-2. Typical research group pull out test setup (Cruz, 2017)

1.2 Thesis Objectives

The main objectives of this thesis were the following:

1. Improve upon current DOS technique and methodology for strain monitoring;
2. Develop and plan calibration and installation technique for fiber optic to monitor specimen temperature;
3. Investigate previous group member's recommendation into use of new sensing fiber for monitoring;
4. Develop specimens curing plan and schedule for multiple temperatures;
5. Investigate cement type(s) required for grouting in diverse temperature ranges and refine the grouting process as required;
6. Investigate the effects of a range of temperatures and short-long term curing durations on embedment length, the stress distribution, and other geo-mechanical behaviours of FGRBs subjected to axial loading;
7. Modify pull out test setup and procedures for longer specimens and dual temperature and strain monitoring; and,
8. Compare the results of experimental tests with existing literature and applicable analytical models.

The objectives of this research projects were completed through sequential phases from preliminary materials investigation and prototyping to specimen preparation and testing to data processing and analysis. A robust laboratory investigation including 24 FGRB specimens that were subjected to axial pull-out tests were tested as part of this research venture. These tests were conducted over a range of curing temperatures (-20°C to +45°C) as well as curing times (3 to 90 days). Prototype testing for a new polyimide coated fiber optic was also conducted in order to investigate the differences from research group's traditionally used acrylate coated fiber optic. Additionally, material testing was completed for: a.

cement grouts (total 138 cylinders), and b. steel rebar, in order to make comparisons to similar materials published in literature.

1.3 Investigation Methodology

This thesis investigation was conducted in sequential phases as seen in Figure 1-3. The process commenced with a review of past group member’s research projects with a view to understand the history of the research programme and to understand the research group’s best practices. A literature review of relevant historical and current research into the subject of rock support and any relevant, existing temperature studies was also conducted. An exploration into suitable materials for the range of temperatures chosen for the project was accomplished and baseline/prototype testing was completed. These activities were followed by planning and monitoring program development, test specimen production, and laboratory testing. As testing progressed, a feedback loop for improving the setup from issues encountered and lessons learned during each pull out test was developed. Finally the data from the laboratory testing program was collected and analyzed and conclusions were drawn and compared with existing literature.

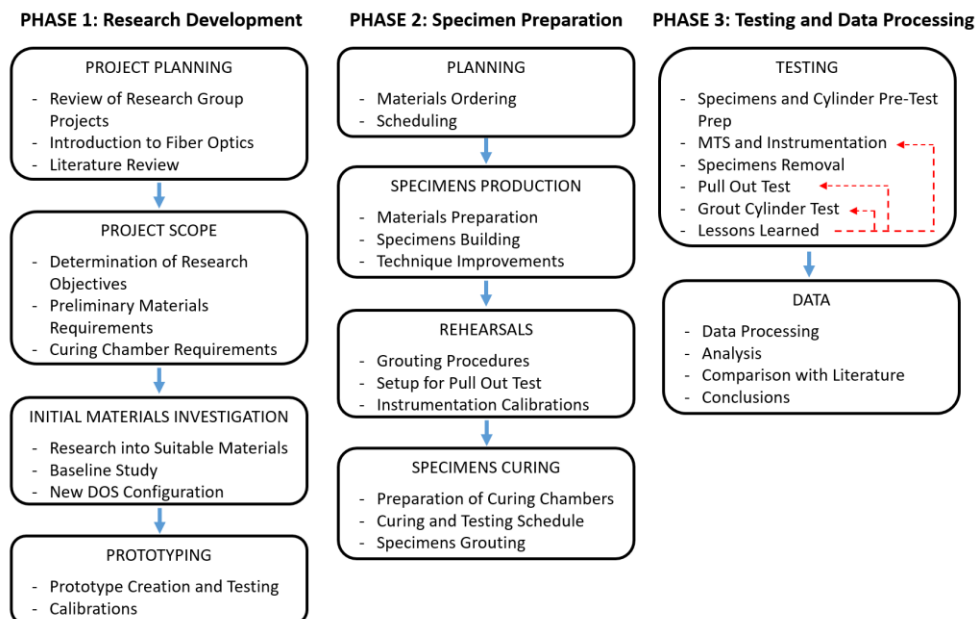


Figure 1-3. Thesis investigation program workflow

1.4 Thesis Organization

This thesis has been completed in the article-based format and in accordance to the Royal Military College of Canada's *Thesis Preparation Guidelines (2015)*. The organization and chapter contents are seen in Figure 1-4 and are as follows:

Chapter 1 – Introduction. This chapter introduces the themes, objectives, and structure of this thesis.

Chapter 2 – Background. This chapter explores the fundamental concepts of rock support with emphasis on fully grouted rock bolts. It also introduces the fiber optic sensing technique and background temperature regime for testing. Additionally this chapter presents the historical research into the behaviours and understanding of rock bolts and identifies scientific gaps that exist in the current literature.

Chapter 3 – Material Testing. This chapter provides an overview of the materials used and associated test results with respect to the laboratory research activities. This chapter covers the prototyping, initial testing and calibrations, and the preparation of the test specimens.

Chapter 4 – Journal Article #1 - Utilizing Distributed Fiber Optic Sensors to Investigate the Effects of Permafrost Temperature Conditions on the Axial Response of Fully Grouted Rock Bolts. This chapter presents the results and discussions of the test specimens that cured in the simulated permafrost conditions.

Chapter 5 – Journal Article #2 - Investigating the Effects of Geothermally Active Temperature Conditions on Fully Grouted Rock Bolts with Distributed Fiber Optic Sensors. This chapter presents the results and discussions of the test specimens that cured in the simulated geothermally active conditions and control condition.

Chapter 6 – Summary of Main Findings. This chapter amalgamates the main findings provided in the two journal articles and results from the testing program and data analysis.

Chapter 7 – Conclusions and Recommendations. This chapter summarizes the major conclusions, contributions to industry, and future recommendations.

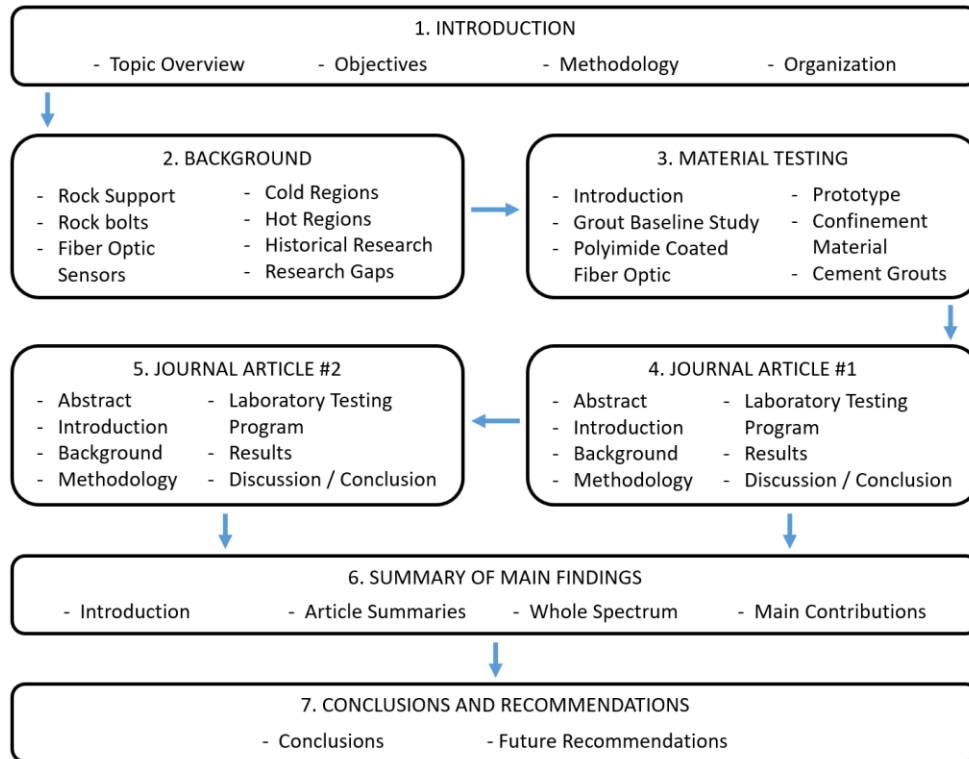


Figure 1-4. Thesis chapter layout and structure

An extensive list of each test specimen’s results, such as graphs and images, are located in the Appendices. The chapters will only present an example figure.

1.5 Relevance to Research

This chapter introduced the objectives and main themes of the research project and also presented the workflow structure and organization of this thesis.

2 Background

2.1 Rock Support

One of the challenges for underground excavation projects is the stability of the rock mass surrounding the excavation openings. Removal of rock during excavation causes a disturbance in the stress equilibrium resulting in potential rock displacement (i.e. radial convergence). The severity of the responses depends on a plethora of factors: type of rock, depth of excavation, magnitude and orientation of stress fields, degree of anisotropy, and excavation geometry and orientation (Forbes, 2015). The in-situ rock stresses increase with depth and rock conditions generally become more severe. In hard rocks, rock bursts may occur whereas in soft and weak rocks, large deformations from squeezing may arise (Li, 2010). Rock bursts in mining operations have been reported in all mining countries and in civil engineering projects such as deep tunnels in various countries. The frequency and severity of events have increased as projects are advancing deeper below the surface (Wang et al, 2022). It is generally agreed that depth is a parameter that negatively impacts stability and the significant effects are usually seen below 1000 m, but have been observed in some cases at 600 m (Li, 2010; Bednarek & Majcherczyk, 2020). Rock instability during excavation is a global problem, decades of testing, analysis, and modelling have been completed to improve upon support designs. The term rock support is widely used to denote the following:

“[T]he procedures and materials used to improve the stability and maintain the load bearing capacity of the rock near to the boundaries of an underground excavation... The primary objective of a support system is to mobilize and conserve the inherent strength of the rock mass so that it becomes self-supporting.” (Hoek & Wood, 1987)

There is a distinction between rock reinforcement (active) and rock support (passive). The former involves installing structural members internal to the rock mass to conserve or improve the overall properties such as rock bolts, cable bolts, and anchors. The latter is external to the rock mass utilizing reactive forces to act as surface restraints in response to inward rock movement. Such support measures include shotcrete, mesh, and steel sets (Hoek & Wood, 1987; Brady & Brown, 2004;

Bobet & Einstein, 2011). In general, the term ground support refers to both the rock reinforcement and support (He et al, 2014).

The traditional manner to describe rock support was temporary or permanent. Temporary support referred to support or reinforcement used during excavation to protect workers while permanent support was installed if the excavation was to remain open for extended time. The temporary supports were partially or wholly removed for the installation of permanent supports. It is more contemporary to use the terms primary and secondary. Primary support is installed before, during, or immediately following excavation to retain the rock mass integrity and any additional support or reinforcement installed at later stages are termed secondary (Brady & Brown, 2004). In a given project, a combination of the different support and reinforcement types will be utilized (Figure 2-1). The type of support chosen is dependent on the extent of fractured or loosened material around the excavation (Hoek & Wood, 1987). The combination, arrangement and sequencing of support members is described in depth by Vlachopoulos et al. (2013).

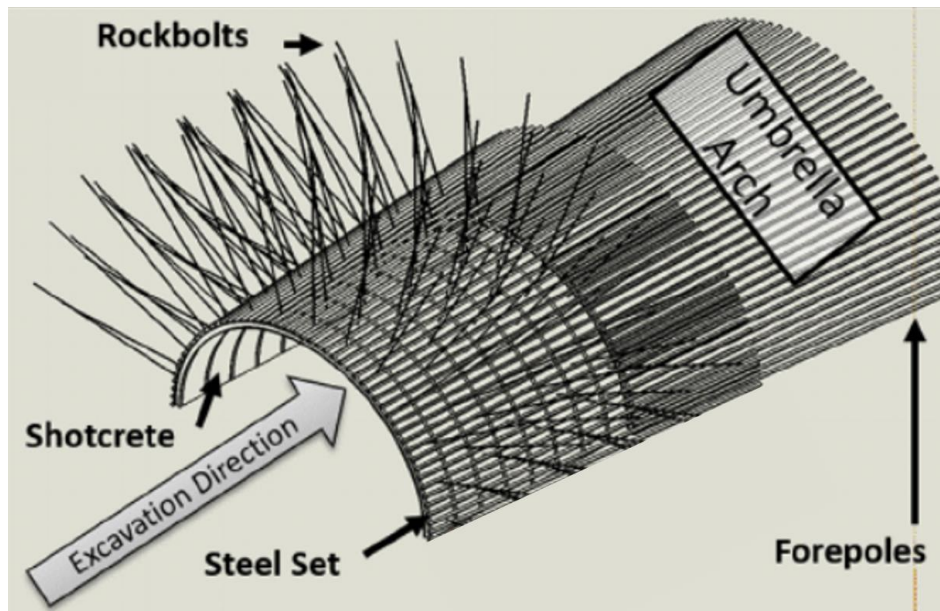


Figure 2-1. Example of support and reinforcement elements used in underground excavations (modified after Oke et al, 2014)

Under confined conditions, individual rock pieces interlock to form a stable rock mass. Ultimately, the purpose of support is to maintain confinement in the rock mass so that it remains self-supported (Vlachopoulos et al, 2013). Each type of

support or reinforcement member has their application and different behaviours under loading. Thus, understanding how they interact with other members and the rock mass is critical to designing (and optimizing) the overall support system.

For reinforcement systems, the dimensional and spatial arrangement/configurations of primary and secondary systems are known as a reinforcement scheme. Three ranges of reinforcement – near surface (1.5-3 m), medium depth (3-15 m), and deep seated (>15 m) – have been identified (Windsor & Thompson, 1993).

2.2 Rock Bolts

The first use of rock bolts in tunnel support date back as early as 1913 gaining significant widespread use in the 1970's (Bobet & Einstein, 2011). Rock bolting is now one of the most common forms of support in underground engineering and mining operations (Li et al, 2011; He et al, 2014). Rock bolts have advanced significantly in the past 40 years with increased understanding of load transfer mechanisms and innovations in the technology. They have been employed as temporary and permanent support systems (Cao et al, 2012). The basic assembly of a rock bolt consists of a plain steel rod that is mechanically or chemically anchored into the rock mass on one end and a faceplate and nut on the other (Vlachopoulos et al, 2018). The fundamental concept is to create a zone of reinforcement in the rock mass thereby improving confinement and utilizing its inherent mass strength to be self-supportive. The reinforcement system enables the transfer of load from the unstable regions near the boundary of the excavation to the stable rock mass at depth (Thompson & Villaescusa, 2014). In order for a rock bolt to effectively transfer load, it must be anchored into the rock mass. The most common anchoring methods are mechanical apparatus, grouting (cement or resin), and friction (Ren et al, 2010). Typical applications to control failure in different types of rock masses are seen in Figure 2-2. In non-pre-tensioned bolts, the movement of rock mass towards the excavation face elongates the bolt creating tension in the element, the tension is transferred as compression to the rock mass thus increasing confinement. In pre-tensioned bolts, the confinement is increased between the two ends of the element as the element is put into tension (Bobet & Einstein, 2011; Cao et al, 2012; He et al, 2014).

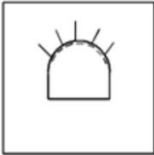
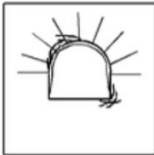

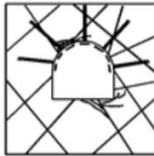
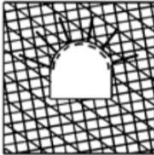
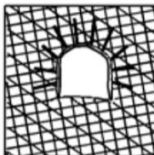
	Low stress levels	High stress levels
Massive rock	 <p>Massive rock subjected to low in situ stress levels. No permanent support. Light support may be required for construction safety.</p>	 <p>Massive rock subjected to high in situ stress levels. Pattern rockbolts or dowels with mesh or shotcrete to inhibit fracturing and to keep broken rock in place.</p>
Jointed rock	 <p>Massive rock with relatively few discontinuities subjected to low in situ stress conditions. 'Spot' bolts located to prevent failure of individual blocks and wedges. Bolts must be tensioned.</p>	 <p>Massive rock with relatively few discontinuities subjected to high in situ stress conditions. Heavy bolts or dowels, inclined to cross rock structure, with mesh or steel fibre reinforced shotcrete on roof and sidewalls.</p>
Heavily jointed rock	 <p>Heavily jointed rock subjected to low in situ stress conditions. Light pattern bolts with mesh and/or shotcrete will control ravelling of near surface rock pieces.</p>	 <p>Heavily jointed rock subjected to high in situ stress conditions. Heavy rockbolt or dowel pattern with steel fibre reinforced shotcrete. In extreme cases, steel sets with sliding joints may be required. Invert struts or concrete floor slabs may be required to control floor heave.</p>

Figure 2-2. Typical rock bolt and dowel application in different rock masses during tunnelling (Hoek, 2007)

Rock bolts are generally categorized as rock reinforcement and one of the main advantages in tunnel reinforcement is the flexibility and adaptability to changing rock conditions. By systematically modifying the number and length of rock bolts, excessive convergence can be effectively controlled (Bobet & Einstein, 2011). The versatility has contributed to its popularity in use for underground

excavations. In the 1990s, annual global rock bolt installation estimates were around 500 million in civil engineering and mining works, however, a large portion was suspected to not be performing per design due in part to difficulties of installation and misconceptions of suitability (Windsor & Thompson, 1993). A study by Potvin and Nedin on rock fall in mines between 1998 and 2003 found that the areas further from the work face were at lower risk for injury, however, most fatalities actually occurred under the reinforced and supported ground. This was attributed to corrosion, inadequate bolt length, broken bolts, incorrect installation, and bolts spaced too wide (Potvin & Nedin, 2003). In 2016, 29% of fatalities underground in the International Council on Mining and Metals report were caused by falling ground (Pinazzi et al, 2020). There is clearly a requirement to continue improvement on rock bolt system design methodologies and expand current understanding of the fundamentals of the technology.

Although rock bolts have been in use for over a century, there is still no universal definition or classification system (Frenelus et al, 2022). Classifications have been carried out under different criteria, the most popular being anchoring mechanism, load transfer mechanism, performance, anchoring state, and reinforcement mode (Figure 2-3).

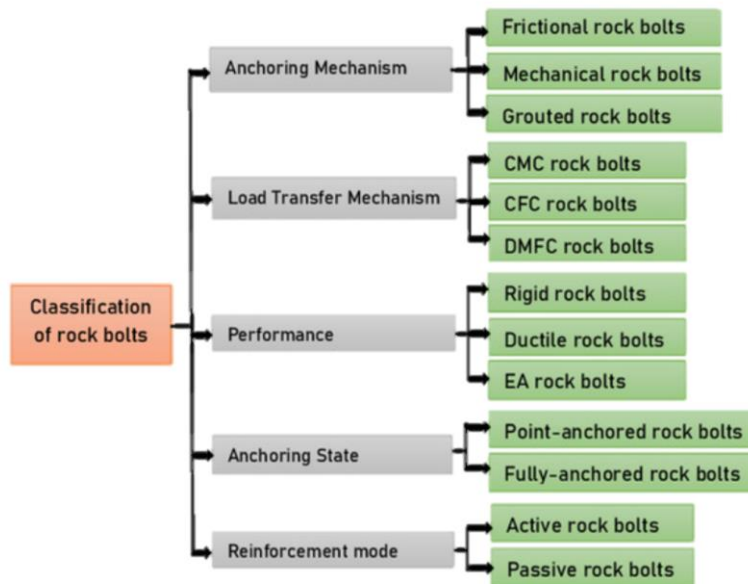


Figure 2-3. Systems of classification of rock bolts (Frenelus et al, 2022)

2.2.1 Mechanically Anchored Rock Bolts

Mechanically anchored rock bolts are the oldest form of rock bolts and were widely popular in mining. It is an end-anchored system that functions through tensioning of the rod to apply a positive force to the rock. The assembly is comprised of an expansion shell anchor (variety of styles – typically a tapered cone with two wedges) screwed onto the threaded end of the bolt (toe end) and a faceplate with nut at other end (Figure 2-4) (Hoek, 2007). The rock bolt is inserted into the pre-drilled borehole and given a tight pull to seat the anchor. They are normally tensioned up to 70% of the bolt capacity. Grout can be applied as well, this is primarily done for corrosion prevention and to lock the mechanical anchor in place thus the strength of the grout is not as important (Hoek, 2007).

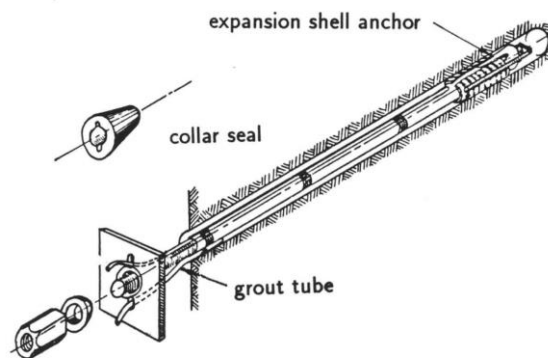


Figure 2-4. Mechanically anchored rock bolt (Hoek, 2007)

Mechanically anchored rock bolts are most effective at retaining loose blocks of rock caused by intersecting joints and bedding planes. They perform well in hard rocks but are less effective in soft rocks and closely jointed rocks. Typically failure from overloading will result at the threads on either end of the bolt rather than by anchor slip, however overtime, the anchors will likely progressively slip due to blast vibrations (Hoek & Wood, 1987).

2.2.2 Fully Grouted Rock Bolts

One of the main disadvantages with mechanically anchored rock bolts was the complete loss of capacity if the bolt broke or the anchor slipped. An improvement

was made to the rock bolt system by creating a bond between the rock mass and reinforcing element along its entire length. A fully grouted rock bolt (FGRB) minimized the previous concerns since the remaining anchored length maintained capacity (Hoek & Wood, 1987). FGRBs cannot typically be tensioned and the grout has a cure time so they must be installed prior to significant rock movement. The reinforcing action is activated by movement in the rock mass so FGRBs are generally considered passive support. FGRBs can be installed very close to the advancing face which minimizes movement in the rock mass by maximizing the retention of inherent rock interlock (Hoek & Wood, 1987).

There are two common types of grout used in industry: cement grout and resin grout (Figure 2-5). For cement grout, a grouting tube is inserted to the end of the pre-drilled borehole. As the grout is pumped in, the tube is withdrawn and the bolt rod is inserted. A faceplate is added after the grout has set to restrain rock close to the borehole collar from pulling away. But in cases of light support, a faceplate may not be required. For resin, typically two cartridges are inserted into the borehole and as the bolt rod is spun into the cartridges, it breaks the plastic sheath and mixes the resin and catalyst. Resin typically sets within a few minutes to create a very strong anchor. Thus they can be used in many rock conditions, including weak shales and mudstones (Hoek, 2007). The versatility and advantages of FGRBs have bolstered them to become one of the most widely used form of rock bolts.

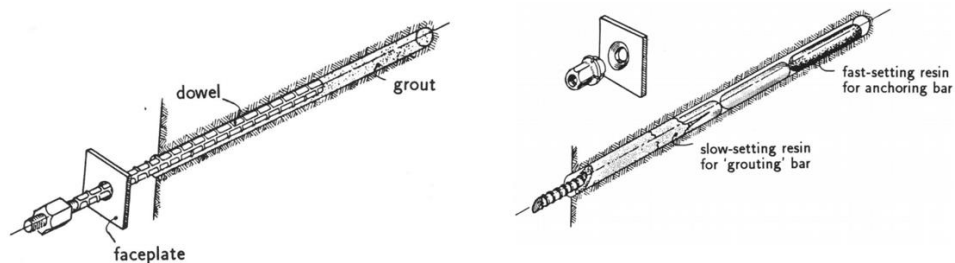


Figure 2-5. Left: Fully grouted rock bolt; Right: Resin grouted rock bolt (modified after Hoek, 2007)

Resin grouted rock bolts can be tensioned when using slow-setting and fast-setting resin cartridges. The fast-setting resin cures thus allowing tensioning in the initial 2-3 minutes of installation, and the slow-setting resin holds the tension and a fully grouted tensioned rock bolt is created (Hoek, 2007). The benefit of the speed of installation of resin grouted rock bolts can balance the more expensive unit cost of resin cartridges. However, there are limitations with resin systems as they

typically have a limited shelf life and effectively breaking and mixing the cartridges poses another practical problem (Hoek, 2007).

2.2.3 Frictionally Anchored Rock Bolts

Frictionally anchored rock bolts also provide a bond between the entire element length and the rock mass. There are two main types: Split Set stabilisers and Swellex bolt (Figure 2-6). Split Set stabilisers are frictionally anchored when the slotted high strength steel tube is pushed through a slightly undersized borehole generating a radial spring force (Hoek, 2007). Swellex bolt consists of a folded dowel that inflates via high pressure water (approx. 30 MPa) injection (Hoek, 2007). The anchoring mechanism for Swellex bolts differ depending on the rock type. In hard rocks, mechanical interlock by the rock asperities is the main contributor whereas in soft rocks, it is friction from the primary contact stress due to expansion of the bolt (Li & Håkassan, 1999).

The main advantages of friction rock bolts include speed of installation and relative low cost compared to other rock bolt systems. They are ideal for use with automated rock bolting machines. The ease of installation for Split Set stabilisers have made them popular for mining operations. And they are particularly beneficial in mild rock burst environments as they slip rather than rupture allowing the retention of broken rocks when used with mesh (Hoek, 2007).

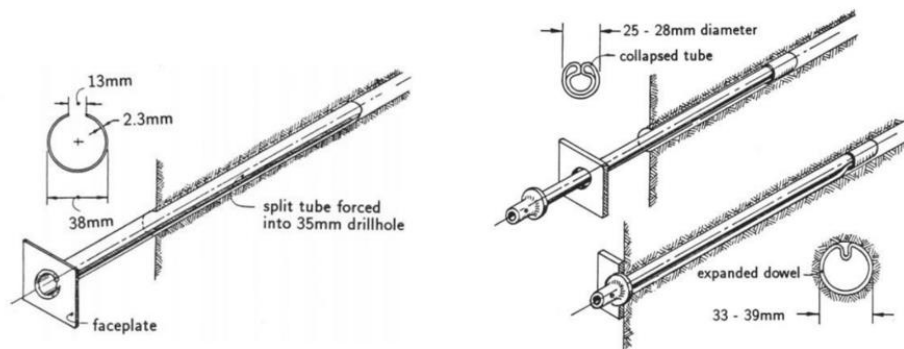


Figure 2-6. Left: Split Set stabiliser; Right: Swellex bolt (modified after Hoek et al, 2000)

Frictionally anchored rock bolts have the disadvantage of lacking corrosion resistance since protection of the outer surface is not feasible. Galvanization can reduce corrosion but is not fully dependable as a preventative measure.

2.2.4 Load Transfer Mechanisms

Reinforcement systems are comprised of four components and their interactions (Figure 2-7) – the rock, the element, internal fixture, and external fixture – originally proposed by Windsor & Thompson (1993). Although the rock was not always thought to be a component of the reinforcement system, the significant influence on the systems behaviour required its consideration. The element refers to the bolt itself. The external fixture being the faceplate and nut. The internal fixture provides the coupling interaction, being the cement or resin grout for fully grouted rock bolts or the mechanical action of friction for frictionally anchored bolts (Cao et al, 2012).

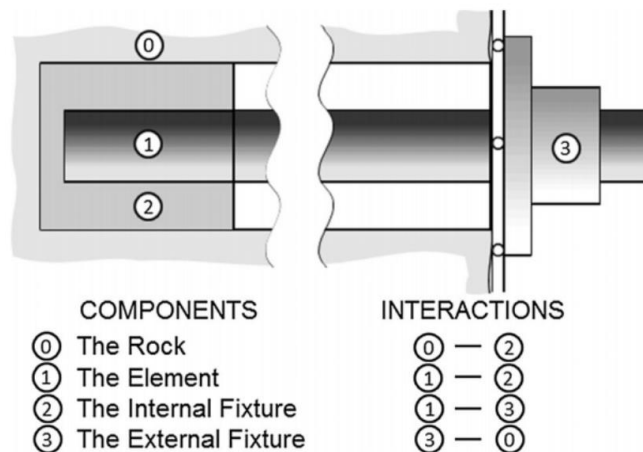


Figure 2-7. Components of rock reinforcement system (Thompson & Villaescusa, 2014)

The in situ loading conditions will vary from one project to another requiring different reinforcement mechanisms. The support requirements are dependent on a multitude of factors including stress regime, stress changes over the lifetime, shape and size of excavation, and geological conditions. The common reinforcement mechanisms are depicted in Figure 2-8, each to address a different loading mechanism (Pinazzi et al, 2020):

1. In Key block mechanism, the rock bolts hold the dead weight of the block and the load acting on the bolt changes depending on the location (i.e. roof or wall) and distribution/orientation of discontinuities;
2. For beam building mechanism when the roof of the excavation has bedded, the rock bolt joins the beams to form one laminated beam. Typically the centre bolt only experiences axial load whereas the other bolts can experience a combination of axial, shear, and bending; and,
3. For suspension mechanism the weak rock beds are suspended from a thicker and stronger layer, the rock bolts function similar to beam building.

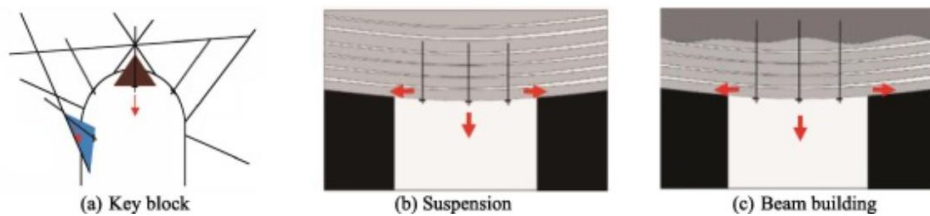


Figure 2-8. Reinforcement mechanisms (Pinazzi et al, 2020)

This research project has focused on the tensile axial loading on rock bolts. The fundamental behaviour of rock bolt reinforcement was detailed by Windsor & Thompson (1993) as the load transfer concept. The concept comprised of three basic mechanisms:

1. Rock movement with load transfer from unstable rock to reinforcement element;
2. Reinforcement element transfers the load from unstable regions to stable regions at depth; and,
3. Load transferred from reinforcement element to stable rock mass.

Summarized as the transfer of load from unstable regions close to the excavation to more stable regions beyond the depth of instability, visualized in Figure 2-9.

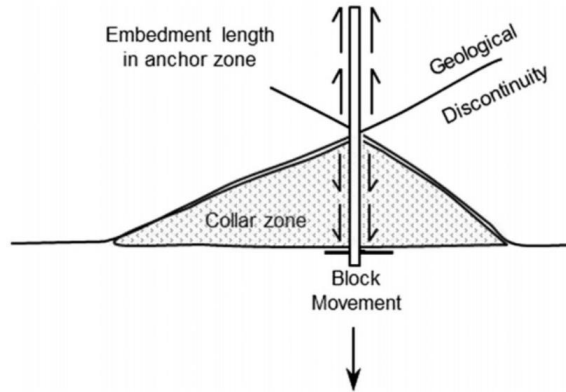


Figure 2-9. Reinforcement element load transfer (Thompson & Villaescusa, 2014)

Based on the load transfer mechanism from the element to the rock mass, three categories were developed to classify rock bolts (Windsor & Thompson, 1993):

1. Continuously Mechanically Coupled (CMC);
2. Continuously Frictionally Coupled (CFC); and,
3. Discretely Mechanically or Frictionally Coupled (DMFC).

In CMC and CFC, the load is continuously transferred along the entire length of the element. In DMFC, the load is transferred over a short length at the toe end of the element via bonding by grout or by friction (Bobet & Einstein, 2011). Depicted in Figure 2-10.

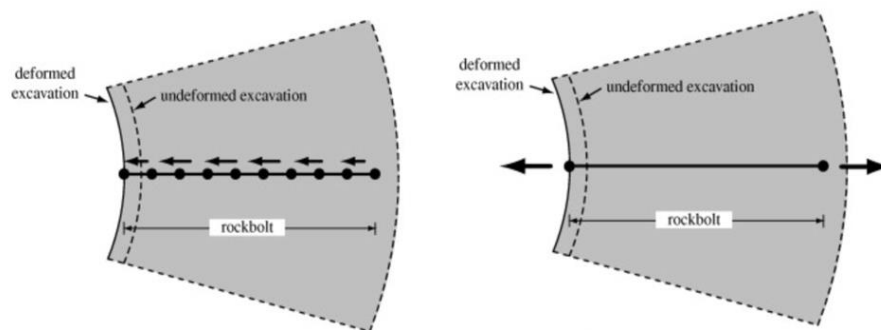


Figure 2-10. Left: CMC and CFC load transfer; Right: DMFC load transfer (modified after Bobet & Einstein, 2011)

2.2.4.1 Continuously Mechanically Coupled Rock Bolt

FGRBs are classified as CMC, providing an extended shear surface for load transfer and development of higher anchorage capacities than mechanically anchored rock bolts (Signer, 1990). The efficiency of load transfer depends on the properties of the grout, bolt, borehole diameter, anchorage length, rock type, confinement pressure, spinning, and installation procedures (Hyett et al, 1992; Bobet & Einstein, 2011; Forbes, 2015). The grout is an essential component as it provides the mechanism for transfer of load between the rock and the bolt. Redistribution of forces along the bolt is the result of strata movement which activates the reinforcement action (grout shear resistance). The movement can be vertical (strata separation) or horizontal (strata slippage). The dowelling effect helps reduce strata slippage as the grout and bolt fully fill the hole whereas the bolt's axial strength resists strata separation (Signer, 1990).

There are three components affecting shear strength at the bolt interface: 1. adhesion, 2. mechanical interlock, and 3. friction. Adhesion is the bond between rock, grout, and bolt. Mechanical interlock is the embedding effect resulting when grout fills the irregularities between the bolt and rock (Cao et al, 2012). The components are lost in sequence (i.e. adhesion, then mechanical interlock, and then friction) as load is applied and compatibility of deformation is lost. The result is a decoupling front that reduces with distance from the applied load. As each strength component is mobilized, shear strength of the interface decreases and the remainder regarded as the residual shear strength (Li & Stillborg, 1999). Previous research in laboratory and field tests have demonstrated that the effects of adhesion are negligible in FGRBs and that mechanical interlock is the predominant component for load transfer (Signer, 1990; Yazici & Kaiser, 1992; Serbousek & Signer, 1987; Aziz et al, 2006). Once the ultimate shear strength is reached, the weakest material will fail and friction will take over (Serbousek & Signer, 1987).

Mechanical interlock transfers load through contact surfaces – boreholes have irregularities due to drilling process and rock lithology, steel bolts are rolled with ribs, and the grout fills the irregularities and voids – as load is applied, stress concentrations build between the irregularities. The localized stress can exceed the strength of the rock and/or grout resulting in crushing allowing additional deflection of the bolt. In 1978, T.J. Freeman completed pioneering work studying axial loading in FGRBs in the Kiedler Experimental Tunnels coining the terms neutral point, pick up length, and anchor length (seen in Figure 2-11) (Freeman, 1978). At the neutral point (location of discontinuity), the shear stress at the bolt-grout

interface is zero while the axial load has a peak value (He et al, 2014). Later Björnfot and Stephansson testing a series of instrumented FGRBs in the Kiirunavaara Mine determined that there may not exist only one but several neutral points on the same bolt (Björnfot & Stephansson, 1984). The pickup length is the length between the borehole collar and the neutral point. And the anchor length is from the neutral point to the toe end of the bolt seated in more stable rock (Li & Stillborg, 1999). Thus the anchorage length (also referred to as the embedment length) is the length required for mechanical interlock to transfer all the developed load in the bolt to the stable rock, which is dependent on the material properties, quality of installation, smoothness of borehole, among other factors (Signer, 1990). The rate at which load is transferred from bolt to rock is dependent on the systems' material properties and interfaces. The load-transfer rate is the change in bolt load with respect to change in distance along the bolt (Serbousek & Signer, 1987). Many analytical studies have demonstrated that the axial stresses in the bolt and bolt-grout interface resemble exponential decay curve from loading end to embedded end (Serbousek & Signer, 1987; Ren et al, 2010).

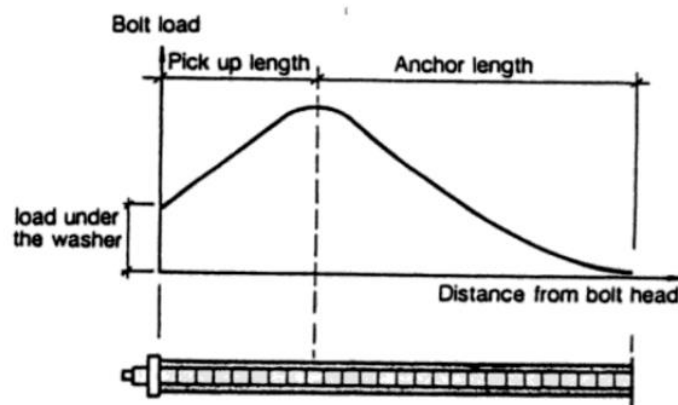


Figure 2-11. Load distribution along a rock bolt (Stille, 1992)

2.2.5 Effect of Grout Type

The grout is an essential component as it provides the mechanism for load transfer and the reinforcement action through shear resistance. The most common types of grout being resin or cement based. Past studies from this research group have found that resin grouts generally have higher bond strength than cement grouts

and attained higher load bearing capacities (Cruz, 2017; O'Connor, 2020). This study uses cement-based grouts. In cement grouts, the water to cement (w/c) ratio is the primary influence on the properties of the grout. The grout strength resides with the solid portion of the material so void spaces negatively impact the properties. Cement gains strength during the curing process after water is mixed. Kilic et al. (2002) recommended that the w/c ratio should be no greater than 0.40, optimum ranging from 0.34-0.40. The volume of voids depends on the amount of water mixed at the start of hydration and the degree of hydration achieved. During hydration, a portion of the water is consumed by the process and the remainder evaporates resulting in voids in the structure. The voids cause the grout's internal structure to be inhomogeneous leading to reduction in long-term strength (Kilic et al, 2002). Generally, as grout w/c ratio increases, the bolt capacity decreases (Figure 2-12). In field pull tests by Hyett et al. (1992), in both granite and limestone rock masses the ultimate bolt capacity increased by 50-70% as w/c ratio decreased from 0.50-0.30. Whereas in shale, the increase in strength was considerably less (Hyett et al, 1992). Although lower w/c ratio results in increased strength, the pumpability and utility in industry is affected.

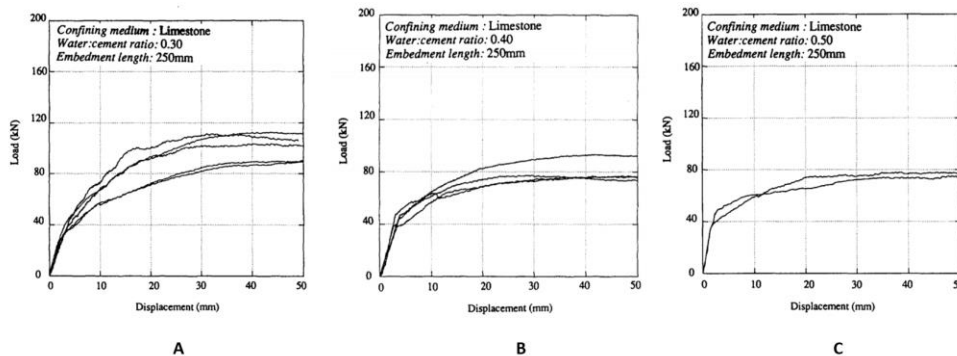


Figure 2-12. Effects of grout water/cement ratio on bolt capacity: A. w/c 0.30; B. w/c 0.40; C. w/c 0.50 (modified after Hyett et al, 1992)

2.2.6 Effect of Embedment Length

For FGRBs, the effects of adhesion are negligible and the main component affecting shear strength is mechanical interlock (Signer, 1990; Yazici & Kaiser, 1992; Serbousek & Signer, 1987; Aziz et al, 2006), which transfers load via contact surfaces over the bolt's embedment length. Generally, as the embedment length increases, the capacity increases (Figure 2-13). The critical embedment length is the

minimum length that expends all bolt tensile capacity and is a key component to determining the design length of rock bolts. The critical embedment length can be systematically evaluated through monitoring the bolt's complete strain profile to determine where the stress distribution attenuates to zero (Cruz, 2017). The embedment length also governs the mode of failure as shorter embedment lengths results in bond failure at the bolt-grout interface and longer embedment lengths result the bolt failure (Li et al, 2016; Cruz, 2017).

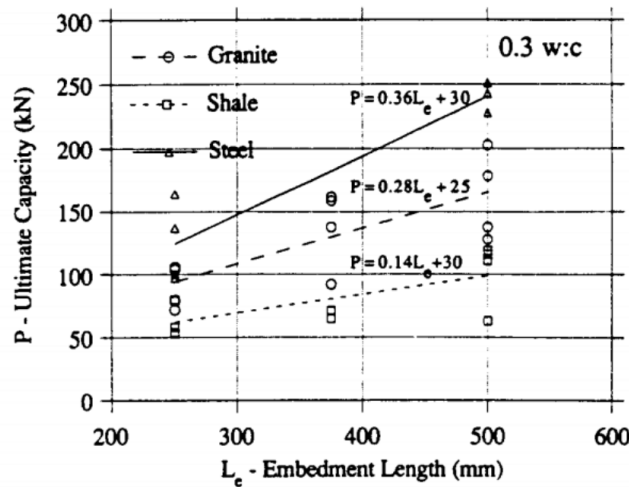


Figure 2-13. Peak bolt capacity vs Embedment length (Hyett et al, 1992)

2.2.7 Effect of Radial Confinement Pressure

Radial confinement is provided by the surrounding rock mass of the borehole. In field tests, the radial confinement of in situ rock mass is found by determining the radial stiffness of drilled boreholes using dilatometers (Hyett et al, 1992). In laboratory tests the rock confinement effects are replicated through the use of steel, aluminum, and concrete pipes. The pipe size and properties are used to calculate the radial stiffness and correlate to an equivalent rock type (Table 2-1). Reinforcement with roughness on the surface when installed in rock mass will generate some radial dilation with any axial slip. The lateral movement from dilation is restricted by the surround rock mass stiffness. At lower radial stiffness, less confining pressures is able to be generated while higher stiffness generates higher confining pressures.

Table 2-1. Typical laboratory confining material radial stiffness and rock type (O'Connor, 2020)

Confining Material	Radial Stiffness (MPa/mm)	Rock Type
Steel – Schedule 160	2942	Granite
Steel – Schedule 40	1623	Limestone – Granite
Concrete	639	Sandstone
Aluminum –Schedule 40	584	Shale
PVC	21	-

The confinement pressure results in more bond capacity in the reinforcement, the higher the pressure the higher the bond capacity as seen in Figure 2-14 (Moosavi et al, 2003). Laboratory and field tests have found that load capacities of bolts increased with confining radial stiffness see in Figure 2-15 (Hyett et al, 1992).

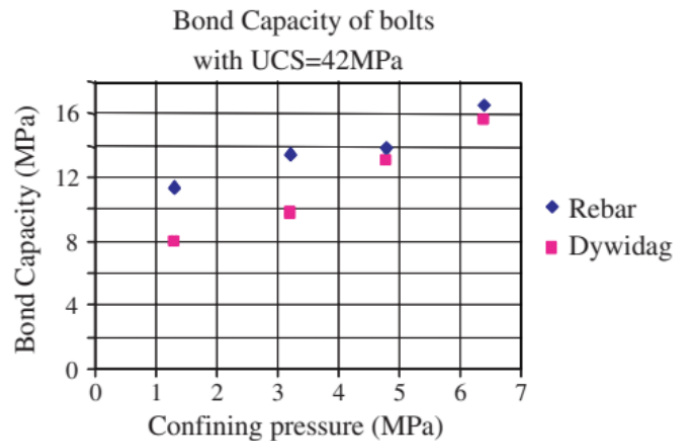


Figure 2-14. Effects of confining pressure on bond capacity (Moosavi et al, 2003)

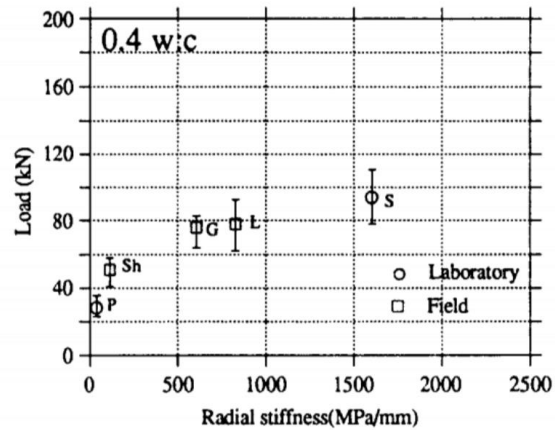


Figure 2-15. Comparison of radial stiffness to load capacity (Hyett et al, 1992)

2.2.8 Failure Mechanism of Fully Grouted Rock Bolts

Since a typical FGRB is a passive reinforcement system, it provides reinforcement when there is movement in the rock. When the movement is aligned coaxially to the bolt then the bolt experiences axial loading, if not then it will experience shear loading. The movement can be a combination of causes including vertical sagging, shearing along a bedding plane, or dilation of a roof layer buckled (Figure 2-16). In rock bolts the predominant load is tension, however, it is normally combined with some bending stresses (Mark et al, 2002).

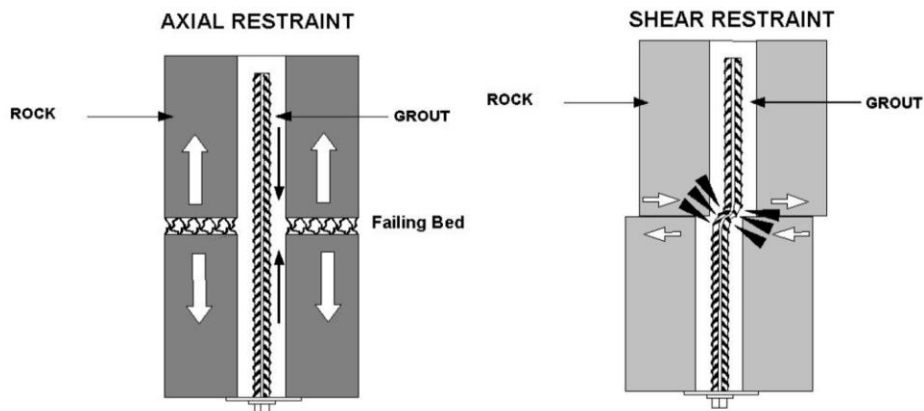


Figure 2-16. Left: Tension due to bed dilation or bed separation; Right: Tension and bending due to bed slipping (Mart et al, 2002)

As the load in the bolt increases with additional movement, the rate of that movement is reduced as the developed load is transferred to the more stable rock at depth. During slab separation, the stresses in the bolt are primarily axial whereas in the rock and grout are shear (Serbousek & Signer, 1987). The locations of failure are the following:

1. The bolt;
2. The grout;
3. The rock;
4. The bolt-grout interface; or,
5. The grout-rock interface.

The location of failure in the system is dependent on the following:

1. Material properties of individual components;
2. Characteristics of the bolt installation (grout quality, installation procedures, surrounding rock type, etc.); and,
3. Location of discontinuities.

The shear stress at the bolt-grout interface is greater than that at the grout-rock interface due to reduced effective area. If embedment length is inadequate and the rock and grout have similar strengths, then the failure will most likely occur at the bolt-grout interface (Serbousek & Signer, 1987). If the rock is weaker then failure is more likely at the grout-rock interface. If the embedment length is adequate to develop the full capacity of the steel then the bolt will likely rupture if applied loads reach ultimate tensile capacity (Figure 2-17) (Serbousek & Signer, 1987).

Extensive past research conducting numerous pull-out tests have found that FGRBs are most likely to fail by decoupling at the bolt-grout interface or grout-rock interface (Serbousek & Signer, 1987, Ren et al, 2010, He et al, 2014). The two types of failure mechanisms at the bolt-grout interface are seen in Figure 2-18. When confinement pressure is high, dilation is resisted, and grout shearing occurs. However, at lower confinement the lateral movement results in volumetric increase at the bolt-grout interface induces bolt movement over the grout ridges referred to as dilation slip (Vlachopoulos et al, 2018).

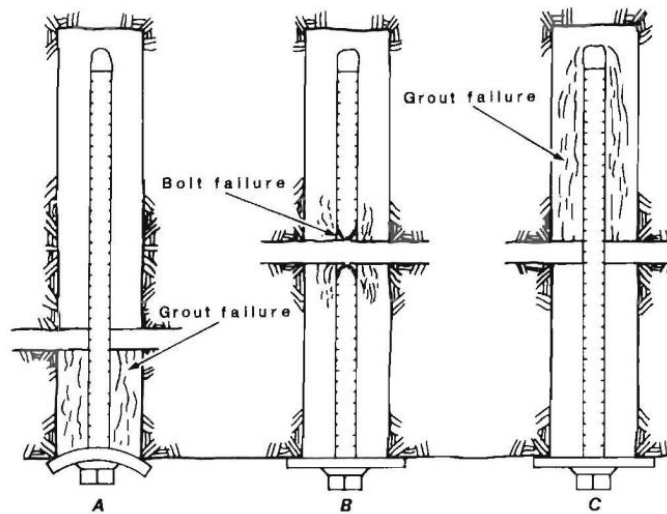


Figure 2-17. Failure modes of fully grouted rock bolts: A. Grout failure; B. Bolt failure; C. Inadequate embedment length (grout column failure) (Serbousek & Signer, 1987)

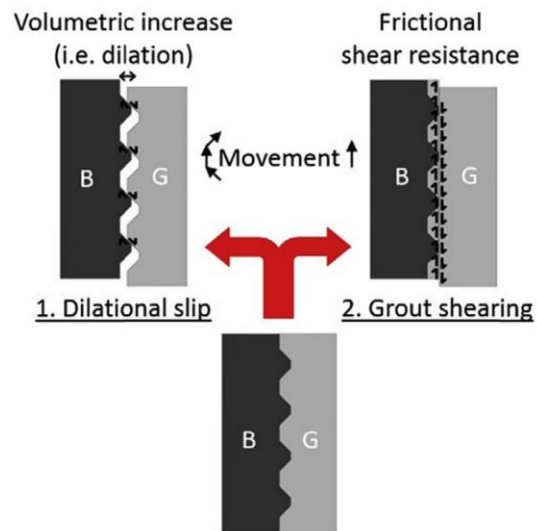


Figure 2-18. Bolt-grout interface failure mechanism (Vlachopoulos et al, 2018)

2.2.9 Design of Rock Bolt Systems

The requirement for improvements in design of rock bolt support systems continues to be at the forefront of underground excavation design. Rock bolts,

especially, grouted rock bolts that are one of the most popular forms of ground support with hundreds of millions of bolts being installed around the world each year. The complexities of and demands on the systems are increasing as underground projects push the limits of size and depth. Existing design methodologies depend on a combination of engineering experience and analogy, empirical methods, closed-form solutions (i.e. analytical approach), and numerical models. Numerical modelling is an efficient method in analyzing and comparing rock bolt performance, however, field monitoring is a more direct approach. A full understanding of rock bolt performance and interactions between bolt and rock mass is required to improve upon designs (Zhang et al, 2014).

The initial steps involve site and ground investigations to understand the geological conditions and the properties of the in-situ rock and stress conditions. The observational method is a low cost and time efficient method with its main steps involving exploration of properties and general nature of deposits, assessment of probable conditions and most unfavourable deviation, establish anticipated behaviour, calculations to quantify observations during implementation, establish potential modifications, observe and measure, and implement modifications. The inherent shortcoming of the system is the time delay during implementation (Peck, 1969). Another method is rock mass classification which is based on empirical design and a quantitative approach. The methods are discussed in depth by Singh & Goel (1999). Current practices utilize the “design as you go” approach or the use of an observational method commencing with feasibility studies to estimate rock parameters, then tests during design phase to quantify the actual parameters, collection of field data during initial implementation, and completing cycles of forward and back analysis during implementation. Since rock mass classification accounts for homogenous units, this does not work for underground excavations (i.e. tunnels) that can cross many zones. Methods have been developed to assess rock masses affected by shear zones (Singh & Goel, 1999). The Q-system, developed at the Norwegian Geotechnical Institute (NGI) assigns Q-values to different weak zones and a mean Q-value is determined, accounting for the width of the zone. The Rock Quality Designation (RQD) was introduced by D.U. Deere as an index to assess rock quality quantitatively. The Rock Mass Rating (RMR) system, initially developed by Bieniawski and has since undergone various modifications, divides a site into various geological structural units and then determines six parameters for each unit (Singh & Goel, 1999).

Various tools and techniques are used to analyze the potential ground response to excavations so that an appropriate support plan is created. In tunnels, Convergence-Confinement Method is widely used for preliminary assessment of radial convergence and support requirements. In this approach, rock bolts add an equivalent internal pressure to the tunnel wall, which originates from the axial force of the rock bolt (Cai et al, 2004). It is also important to establish the Longitudinal Displacement Profiles (LDP) to determine the timing and optimize support installations. The tunnel will experience a portion of the maximum radial displacement as the excavation face advances to a certain point, once past, displacement will continue inward as seen in Figure 2-19 (Vlachopoulos & Diederichs, 2009). Each site has its own unique geological, stress, and response conditions, understanding them and how support elements will interact is essential.

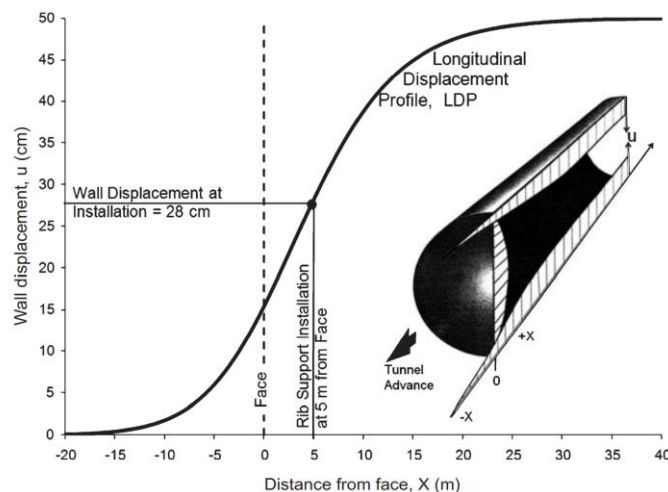


Figure 2-19. Longitudinal Displacement Profile (Vlachopoulos & Diederichs, 2009)

For rock bolt support systems, one of the most important aspects of successful employment is the bolt pattern. A systematic pattern produces the most consistent results with the key elements being bolt length and spacing. Bolt lengths are chosen depending on rock mechanical characteristics and excavation opening dimensions, such that the bolt is anchored in the most competent strata. The lengths should be varied such that the longest bolts are generally in the centre so that anchorage is not concentrated on one horizon. Standards for bolt spacing is based on empirical rules (Peng & Tang, 1984).

2.3 Distributed Fiber Optic Sensors

Pull-out tests are the most common test method conducted to quantify the performance of a rock bolt anchor system by determining working and ultimate capacities. These tests can be carried out both in situ and in a laboratory environment. ASTM D4435-13e1 Standard Test Method for Rock Bolt Anchor Pull Test (ASTM, 2013) outlined the procedure for measurement of load and displacement to determine the rock bolt capacities. The method could be applied to mechanically, cement or resin grout, and other similar anchors and the objective was to measure the performance of the anchor and not the rock bolt itself. A tensile load is applied to the rock bolt specimen until failure, which is defined when the system or rock is incapable of taking on additional load without rapidly increasing deformation. Typical test setup seen in Figure 2-20. It is noted that ASTM D4435-13e1 (ASTM, 2013) was withdrawn on 14 January 2022 and has yet to be replaced. Since this standard was widely used in the past decade, it remains an applicable reference for this study.

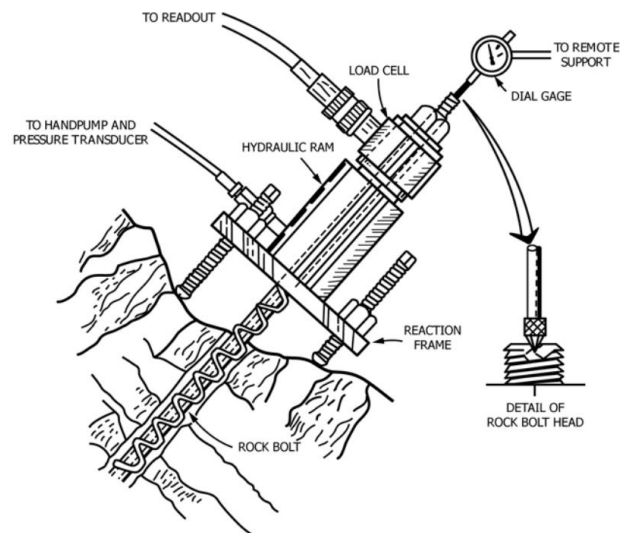


Figure 2-20. ASTM D4435-13e1 Rock bolt pull test schematic (ASTM, 2013)

In situ testing looks at overall efficiencies of the support system whereas laboratory testing focuses on general tendencies resulting from variation of specific component of the system (Cruz, 2017). The in situ testing setup has been adopted for laboratory testing in numerous studies using a variety of testing rigs and

instrumentation. Various renditions have been utilized through the past decades, examples shown in Figure 2-21, in numerous research programs (Farmer, 1975; Hyett et al, 1992; Benmokrane et al, 1995; Kilic et al, 2002; Li et al, 2017b; Wang et al, 2018; Vlachopoulos et al, 2018). Each setup is unique with slight differences but generally feature a fixed base/free end, a pull/loaded end, an embedded section, and monitoring for displacement and load.

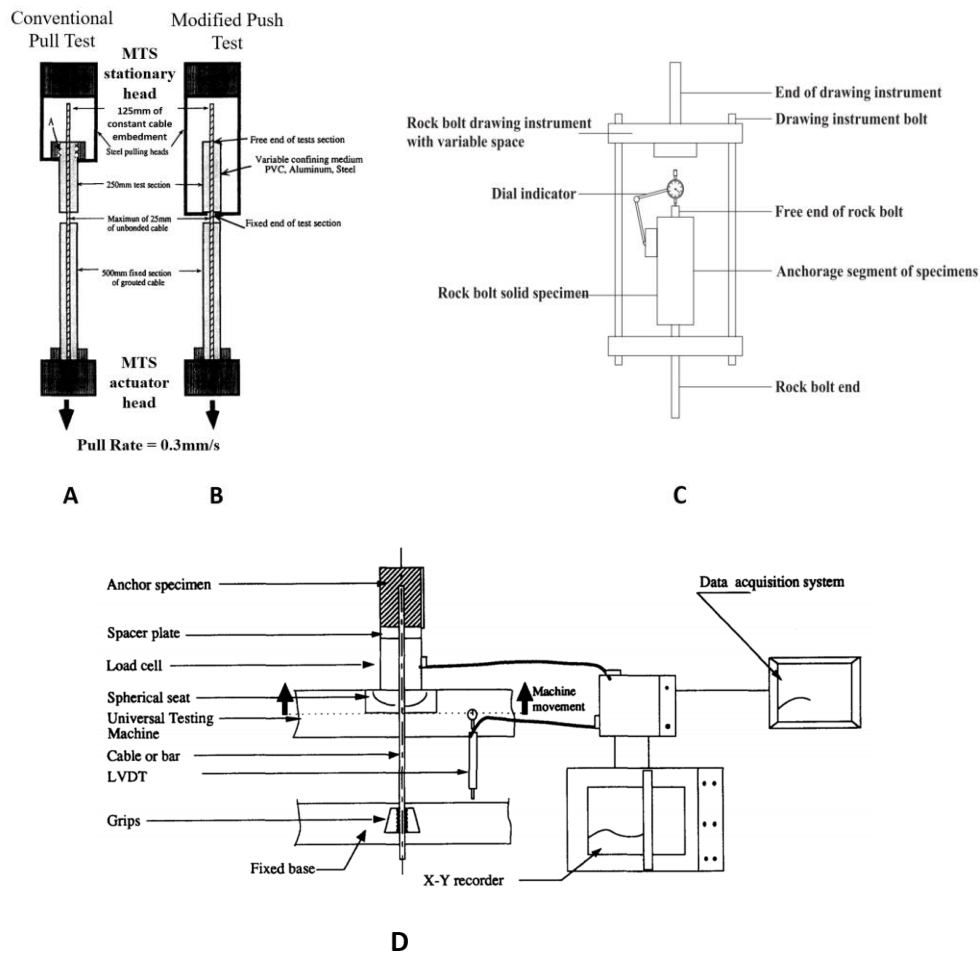


Figure 2-21. . Schematics of previous laboratory testing setups: A and B. Modified test setups based on split-pipe test (modified after Hyett et al, 1992); C. Pull-out strength test (Li et al, 2017b); D. Pull-out test setup (Benmokrane et al, 1995)

The monitoring spatial resolution varies significantly between studies depending on selected instrumentation and methodology. The accuracy of

measurements also differed depending on provisions for redundancy, for example if the testing rig was measured to isolate bolt movement from rig movement or monitoring of the free end to differentiate between displacement due to slip or bolt elongation.

The majority of past research has utilized conventional instrumentation to monitor pull-out test setups. The common approach was to measure applied load and displacement at the borehole collar, however, this technique provided little insight into the stress distribution along the entire length of the bolt. Load cells are the most common instruments for monitoring the applied load during the test. Dial gauges or linear variable displacement transducers (LVDT) are commonly used to monitor deflection at the free end. Improvements to monitoring techniques to better understand fundamental behaviour of rock bolts was the application of discrete monitoring technique (typically foil strain gauges) to the bolt (Farmer, 1975; Serbousek & Signer, 1987; Signer, 1990), which remains one of the most common techniques today (Li et al, 2017b; Zhang et al, 2021). Since strain gauges are installed on the surface of the bolt, they may interfere with bolt-grout interaction. Also due to the discrete nature of strain gauges, strain distributions between the measuring points have to be interpolated so localized phenomena will be missed where a gauge is not present. The typical spatial resolution was greater than 50mm thus the resultant profile may not accurately represent the behaviour (Cruz et al, 2016).

In order to improve upon the spatial resolution and achieve a continuous strain profile along the entire length of the bolt (Figure 2-22) in-situ under axial loads, new and innovative methods were explored by researchers. Fiber optic sensing (FOS) became a potential solution as a single optical fiber could be used as the lead and transducer for various measurements. An optical fiber consists of three main components: a glass core, a cladding layer, and an outer buffer coating (Cruz, 2017). Multiplexed Fiber Bragg Gratings (FBG) was explored but it was limited to the number of Bragg gratings that could be inscribed on an optical sensor thus had the same spatial resolution limitations. Distributed fiber optic sensors (DOS) were found to be capable of continuous strain monitoring.

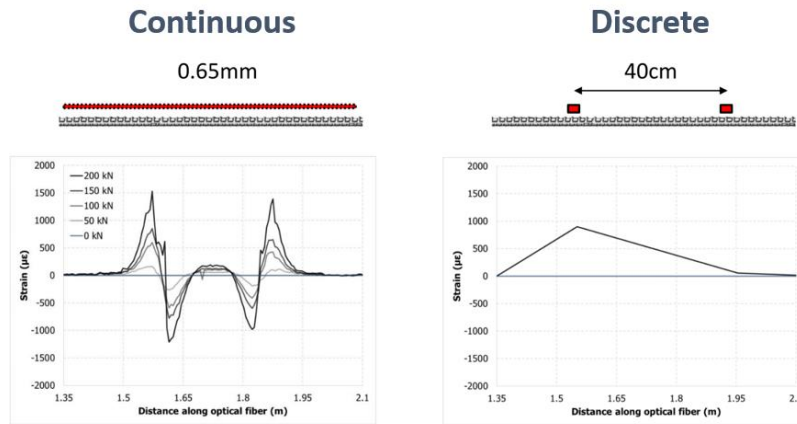


Figure 2-22. Continuous vs Discrete strain profile (Vlachopoulos, 2017)

One of the new methodologies utilizing DOS was developed by the research program led by Dr. Vlachopoulos within the RMC Green Team Military Geoworks Laboratory at the Royal Military College of Canada (Vlachopoulos et al, 2014; Vlachopoulos et al, 2018) in combination with an industrial partner and utilized in this research series (Forbes, 2015; Cruz, 2017; O’Connor, 2020; Moore, 2021). The method leverages the Rayleigh Optical Frequency Domain Reflectometry (ROFDR) to measure strain. When light is sent through an optical fiber, an index profile is created. Rayleigh backscattering results from random variations in the profile with the scatter amplitude being a function of the distance along the fiber. External factors, such as strain and temperature, cause a spectral shift that can then be calibrated for use as a distributed sensor (Gifford et al, 2005). Basic network schematic seen in Figure 2-23. This technique has resulted in an unprecedented spatial resolution of 0.65mm for this research group.

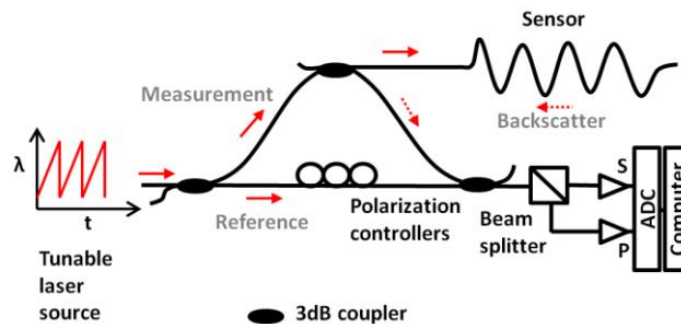


Figure 2-23. Basic OFDR optical network (Luna Inc., 2015)

For temperature monitoring, a spatial resolution of 0.1°C was found in Gifford et al. (2005). The technique provided an unprecedented spatial resolution of up to 0.65 mm thus able to capture behaviour at the micro-scale. The fiber is embedded into the rock bolt in diametrically opposing grooves to not affect the bolt-grout interface, Figure 2-24.

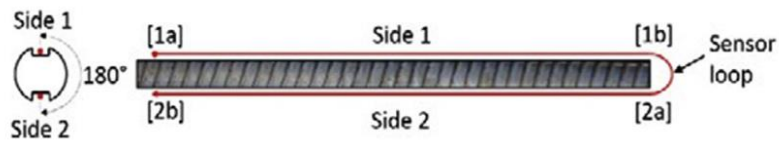


Figure 2-24. Fiber optic sensing configuration (Vlachopoulos et al, 2018)

There is a transition section of DOS from unloaded to loaded has effects on the strain profile, tested and described in detail by Moore (2021). Results demonstrated that there is a section where the strains are more gradually picked up prior to being accurately captured, the distance was found to be 50 mm (Figure 2-25). This was a result of the slippage between layers of the DOS.

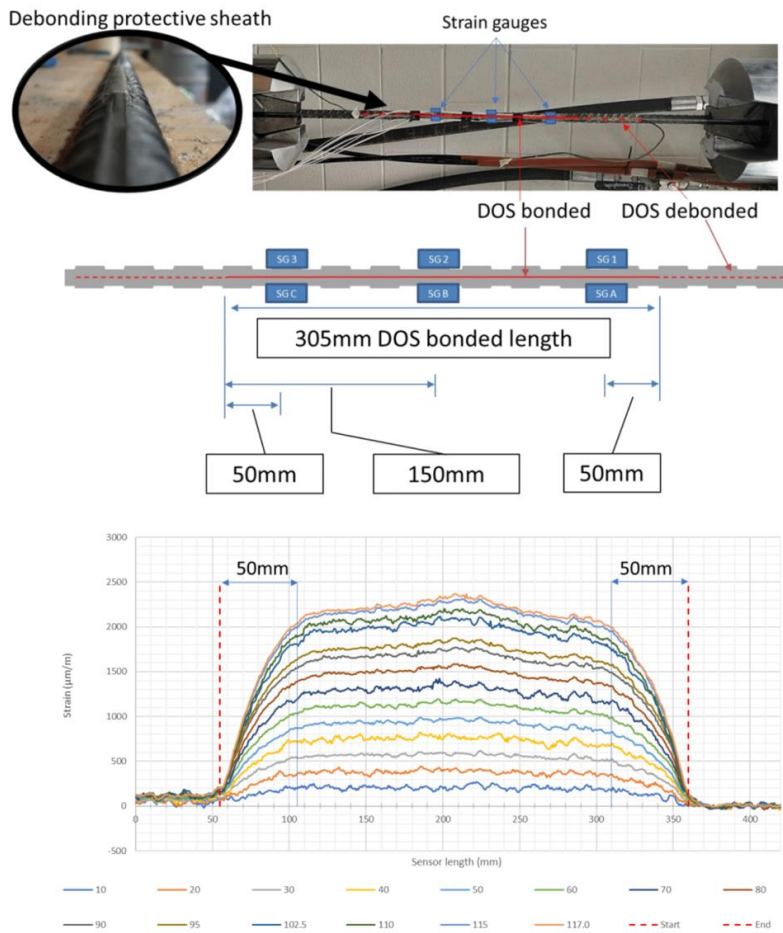


Figure 2-25. DOS debonding testing and strain profile with transition sections (modified after Moore, 2021)

The selected fiber technique's strain measurement features and capabilities are highlighted in the red box in Table 2-2. In addition, the temperature measurement performance range is from -40°C to $+220^{\circ}\text{C}$, found on the Luna ODiSI-B data sheet published on a third-party site (AdvancedPhotonix, n.d.).

Table 2-2. Summary of operational features/capabilities of fiber optic sensing techniques (modified after Forbes et al, 2018)

Technique	FBG (Micron Optics Inc. 2012; FBGS 2013)	DFBG (Lama Innovation Inc. 2017; Sensuron 2017)	BOTDR/BOTDA (Omnisens 2014)	ROFDR (Lama Innovation Inc. 2017)
Maximum sensing length	>1000 m	<52 m	>1000 m	<40 m
Measurement repeatability ^a	±0.1–10 µε	±1 µε	±1 µε	±5 µε
Spacing of measurements (i.e., spatial resolution)	0.10 m (practically)	6.35 mm	0.10–1 m	0.65 mm
Maximum number of measurement points	10–20 (practically)	>1000	>1000	>1000
Sensing range	±17 500 µε	±30 000 µε	±30 000 µε	±30 000 µε
Acquisition time	<1000 Hz	<250 Hz	<1 Hz	<60 Hz
Unit price (approximate USD)	\$15 000–\$125 000	>\$70 000–\$125 000	\$100 000–\$250 000	\$60 000–\$150 000
Sensor price (approximate USD)	~\$300–\$1000 per sensor	~\$300–\$5000 per sensor	\$0.10 per meter of fiber	\$0.10 per meter of fiber
Maximum number of connected sensors ^b	>10	8	2	1

^aRepeatability will ultimately be related to the level of strain experienced by the optical sensor. At higher strain levels (>10 000 µε) repeatability will decrease.

^bMaximum number of connected sensors without the purchase of an additional switch unit.

2.4 Cold Regions

This section contains excerpts from the author’s conference paper submitted to and presented at the annual Canadian Geotechnical Society’s conference, GeoSaskatoon 2023, Saskatoon, Canada (Guo et al, 2023).

The first scenario considered in the development on this research project which focusses on the FGRB system performance over a range of temperatures, was underground projects in permafrost. Canada’s northern region is abundant in natural resources including minerals, oil and gas, and fisheries. There are several open-pit and underground mines throughout the northern territories extracting rare earths, diamonds, gold, iron, etc. As of 2022, in the Northwest Territories and Nunavut there are eight active mines. The region is one of the least tapped mining zones in the world (NWT & Nunavut Chamber of Mines, 2016) due in part to limited access and short working season of the Arctic. However, global interests in the region have increased as demands for limited natural resources continue to grow. Climate change and increasing temperatures in the Arctic has improved accessibility to the resources and extended the working season of the region.

The Canadian Armed Forces (CAF) has a key role in demonstrating Canada’s sovereignty in the North through permanent presence and patrol activities. The CAF has several sites across the North including Yellowknife NWT, Iqaluit NU, and Whitehorse YT. These sites support training, exercises, and operations; the infrastructure is located on permafrost (Government of Canada, 2022).

Almost half of Canada's landmass and areas of the western Arctic seabed is underlain with permafrost. Permafrost is any soil, or even bedrock, irrespective of its texture, degree of induration, water content, or geological character, in which the temperature has been continuously below freezing over a period of years (Jenness, 1949). The minimum frozen period is generally considered two consecutive winters. The coloured regions in Figure 2-26 represent discontinuous and continuous permafrost areas. Deep profiles of mean ground temperatures at various monitoring stations have sub-zero temperatures up to 400-650 m below ground. The most northern CAF site is CFS Alert located on Ellesmere Island NV where the mean ground temperature up to 15 m below surface is -15°C .

As activities in the North increase, understanding frozen ground behaviour and monitoring the interactions of support systems in these remote regions will be essential for infrastructure support and future regional developments, especially within the context of climate change.

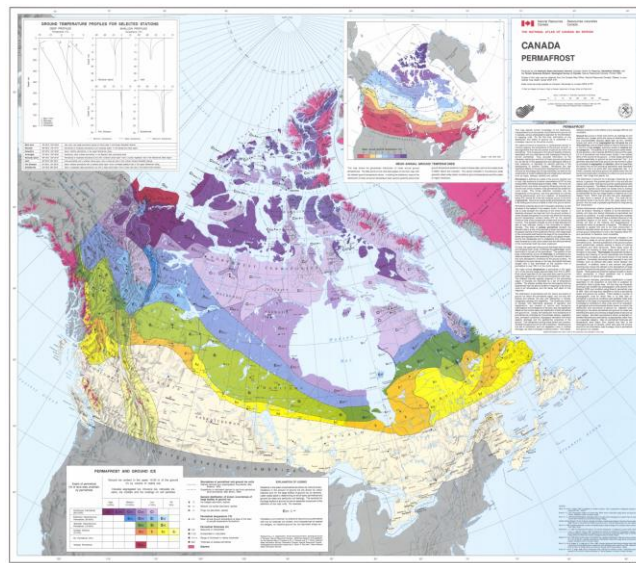


Figure 2-26. Map of permafrost in Canada (Natural Resources Canada, 2016)

2.5 Hot Regions

This section also contains excerpts from the author's conference paper submitted to and presented at GeoSaskatoon 2023 (Guo et al, 2023).

The second scenario considered in the development of this research project was geothermally active tunnels. Increasing global concerns on climate change and the effects of greenhouse gases is pushing industries to more sustainable practices. Nuclear energy is generally considered a reliable and clean electrical power generation source as it is low-carbon emitting (World Nuclear Association, 2023).

Approximately 15% of electrical power in Canada is a result of nuclear power generation, with the majority of plants located in Ontario (World Nuclear Association, 2023). Canada has generated electrical power for over half a century using the CANDU nuclear reactors and a by-product of the process is spent nuclear fuel. CANDU fuel, which is the main nuclear fuel in Canada, is a solid that consists of uranium dioxide. Existing used nuclear fuel is temporarily stored at or near power generation sites. The Adaptive Phased Management (APM) is Canada's plan for the long-term management of used nuclear fuel, which will be contained and isolated in a deep geological repository between 500-1000 m below ground. This approach is in-line with best practices of the international community for high-level radioactive waste (HLRW) (Nuclear Waste Management Organization, 2023).

Deep geological repositories are generally agreed to be one of the more efficient and safe long-term storage solutions for HLRW, which will require isolation periods between 10^5 to 10^6 years. They provide a significant geological barrier for the waste and decrease the risks of future condition changes as the effects of changes decrease with depth (Gibb, 1999). Many countries including Canada, China, Finland, France, Germany, India, Italy, and Japan have decided to use this method. The total used nuclear fuel bundles at the end of operations of existing reactors are estimated at 5.5 million. The estimates will change depending on if reactor operations are terminated early or extended longer. When the used nuclear fuel bundle is removed from the reactors, they are placed in water pools to decrease temperature and radioactivity for seven to ten years before being placed in dry storage (Nuclear Waste Management Organization, 2023).

The general design of deep geological repositories include a series of shafts and tunnels with the containment of the HLRW canisters inside a buffer material (commonly bentonite) and surrounded by the natural geological barrier (i.e. surrounding rock) (King et al, 2017; Xue et al, 2021). The typical thermal criterion for peak temperature at the surface of the canister or interior of the buffer material is 100°C in order to control thermal stress and maintain mechanical stability of the repository. Xue et al. (2021) presented mathematical models as solutions for temperature development and distribution during the exothermic process of nuclear waste. As seen in Figure 2-27, the temperature decays exponentially with

distance from the canister centre in the local solution and slowly decreases at the global scale. The average temperature first increases with disposal time and then decreases.

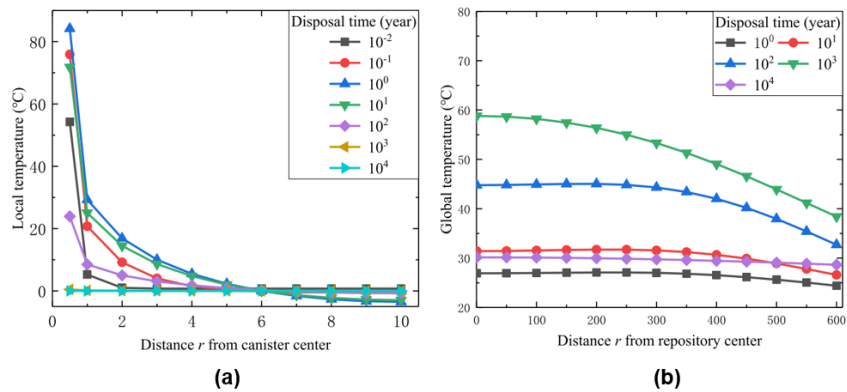


Figure 2-27. Temperature change with distance from repository centre: a. Local; b. Global (modified after Xue et al, 2021)

2.6 Historical Research

As discussed previously, the improvement of rock bolting design has been and continues to be a major aspect in the design and application of rock support systems. A multitude of research endeavours have been undertaken in order to better understand the mechanical behaviour of rock bolts through field monitoring and testing, laboratory testing, analytical methods, and numerical modeling. This study will be focused on axial loading of FGRBs thus research discussed in this section will be relevant to the topic. The expansion in studies related to FGRBs began in the 1970s, corresponding to their rise in popularity in mining and underground civil engineering operations.

In 1978, pioneering field monitoring work by Freeman using instrumented FGRBs in the Kielder Experimental Tunnel established the behavioural descriptors of rock bolts in terms of neutral point, pick up length, and anchor length. He observed a range of behaviours in similar bolts in the same rock and the effects of anchor length (Freeman, 1978). Björnfort & Stephansson (1984) testing a series of instrumented FGRBs in the Kiirunavaara Mine determined that there may not exist only one but several neutral points on the same bolt (Björnfort & Stephansson, 1984).

In 1975, Farmer developed the first analytical model and compared it to experimental test results. His analysis regarded a resin grouted steel bolt as an elastic anchor surrounded by a shearable grout (Figure 2-28). Axial tensile force in the bolt is transferred as shear stress to the grout at the bolt-grout interface resulting in differential bolt extension and grout shear, represented in Equation 1.

$$\pi a^2 \delta \sigma_x = -2\pi a \tau_x \delta x \quad (1)$$

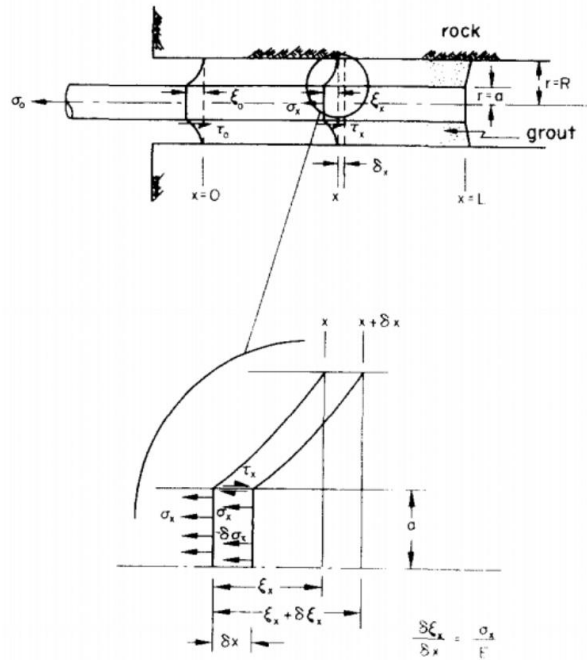


Figure 2-28. Stress situation in a grouted bolt (Farmer, 1975)

His model took into account the effects of thin and thick grout annuli on shear stress. For thin grout annulus, shear stress at the bolt-grout interface is representative of the shear stress in the annulus itself. In thick grout annulus, shear stress at the interface is affected by radial changes in shear stress. By accounting for annulus effects, elastic deformation, and solving for boundary conditions, the transfer length (i.e. critical embedment length) could be calculated, Equation 2. Farmer defined it as the length where bolt strain and stress are reduced to 1% of their magnitude at the borehole collar. This was determined to be an exponential decay (Figure 2-29) as the load dissipates across the length of the bolt.

$$LT = \frac{4.6}{\alpha} \quad (2)$$

Farmer tested a series of 20mm diameter bolts grouted into different materials, each bolt instrumented with six or seven strain gauges. The test results found a non-linear load-displacement curve. The model could only accurately predict for low axial loads but at higher loads the experimental results and predicted values diverged significantly since decoupling mechanism was not taken into account (Farmer, 1975).

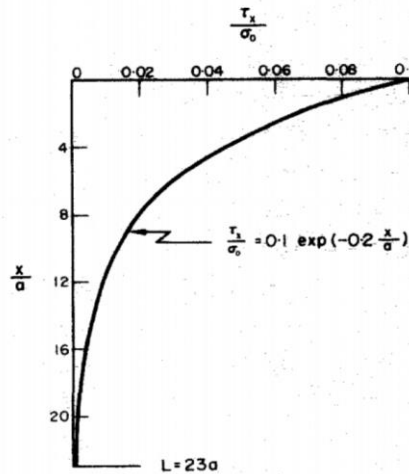


Figure 2-29. Theoretical stress distribution along a fully grouted rock bolt (Farmer, 1975)

In 1992, Yazici and Kaiser developed a bond strength model (Figure 2-30) that considered axial and lateral displacement, stress at bolt-grout interface, and bond strength. It explained the development of strength at the bolt-grout interface and represented the ultimate strength as a function of the mechanical properties of the rock and grout, as well as the geometry of the borehole and bolt (Yazici & Kaiser, 1992).

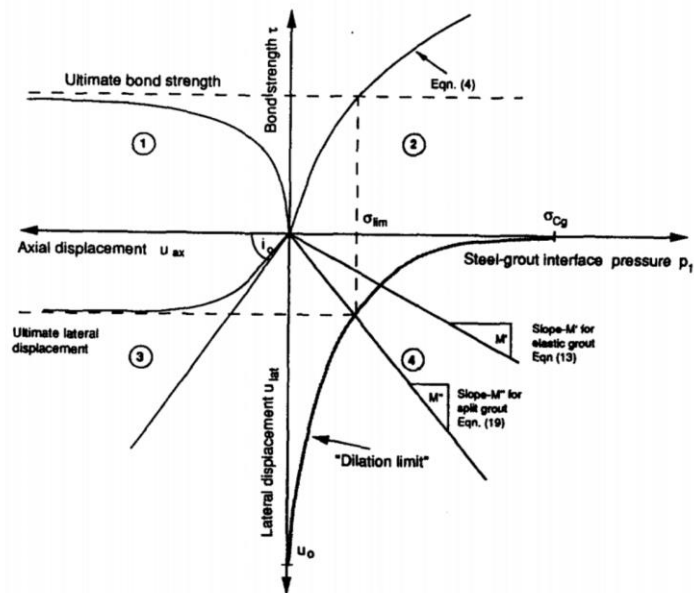


Figure 2-30. Bond strength model (Yazici & Kaiser, 1992)

Hyett, Bawden, and Reichert (1992) investigated major factors influencing bond capacity of grouted cable bolt – cement properties, embedment length, and radial confinement – through laboratory and field programs. They found bolt loads approached yield strength of steel cables only under specific conditions (i.e. combination of long embedment lengths and high radial confinement) differing from the traditional design assumptions that full capacity will be mobilized. And demonstrated that radial stiffness of the surround media greatly influenced the bolts' capacity (Hyett et al, 1992).

In 1995, Benmokrane, Chennouf, and Mitri proposed a different analytical model, a trilinear slip-bond model (Figure 2-31). Unlike Farmer's study that focused on shear stress distribution at the bolt-grout interface, Benmokrane et al. (1995) focused on bond-slip relationship. They tested a series of seven-strand cable bolts and Dywidag threadbar bars with different cement grouts. Short anchorage lengths were used so that a uniform distribution of bond stress along the bolt-grout interface near failure could be assumed. The shear bond stress at the bolt-grout interface was proposed as Equation 3.

$$\tau = ms + n \quad (3)$$

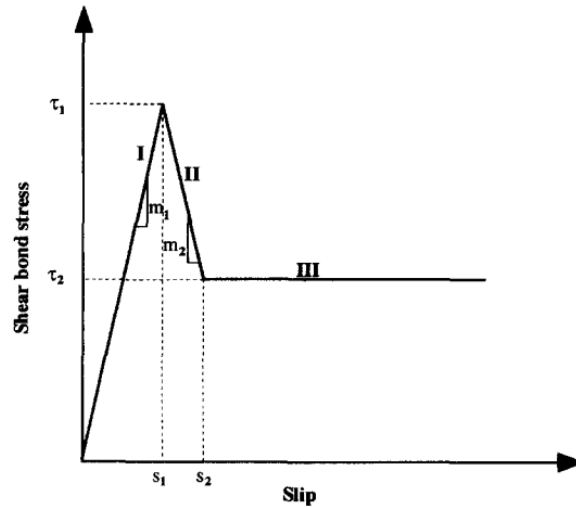


Figure 2-31. Trilinear bond-slip model (Benmokrane et al, 1995)

The model is comprised of three linear stages: Stage I. Elastic behaviour (linear relation between shear stress and slip); Stage II. Process of decoupling; Stage III. Residual resistance. The peak value between I and II corresponds to interface shear strength. They also found that maximum bolt capacity increased with embedment length (Benmokrane et al, 1995). These results are in agreement with other studies (Signer, 1990; Hyett et al 1992; Kilic et al, 2002).

In 1999, Li and Stillborg developed two analytical models for fully coupled rock bolts, one in uniformly deformed rock mass and one in jointed rock mass. They introduced the concept of a decoupling front that attenuates as distance increases from the borehole collar. The models feature the exponential decay previously theorized by Farmer (1975) and accounts for the decoupling behaviour (Li & Stillborg, 1999). Simplified model seen in Figure 2-32.

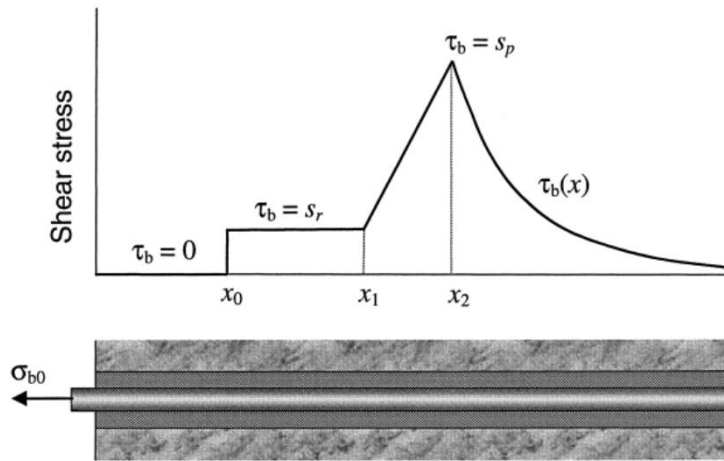


Figure 2-32. Shear stress distribution along fully grouted rock bolt under axial load (Li & Stillborg, 1999)

In 2004, Cai, Esaki, and Jiang proposed an analytical model to predict axial forces of FGRBs analyzing coupling and decoupling behaviours. The resultant axial force was dependent on the released deformation of the rock mass. They applied the model to back analysis with measurements from the Kielder Experimental Tunnel, predicted results were in agreement with measured data and had improved from previous models such as Oreste & Peila (1996) (Cai et al, 2004).

In 2010, Ren, Yang, Chen, and Chen presented a full-range analytical model to describe behaviour of FGRBs under tension based on a realistic tri-linear bond-slip model. The model covered all stages of performance: elastic, elastic-softening, elastic-softening-debonding, softening-debonding and debonding (Figure 2-33) (Ren et al, 2010).

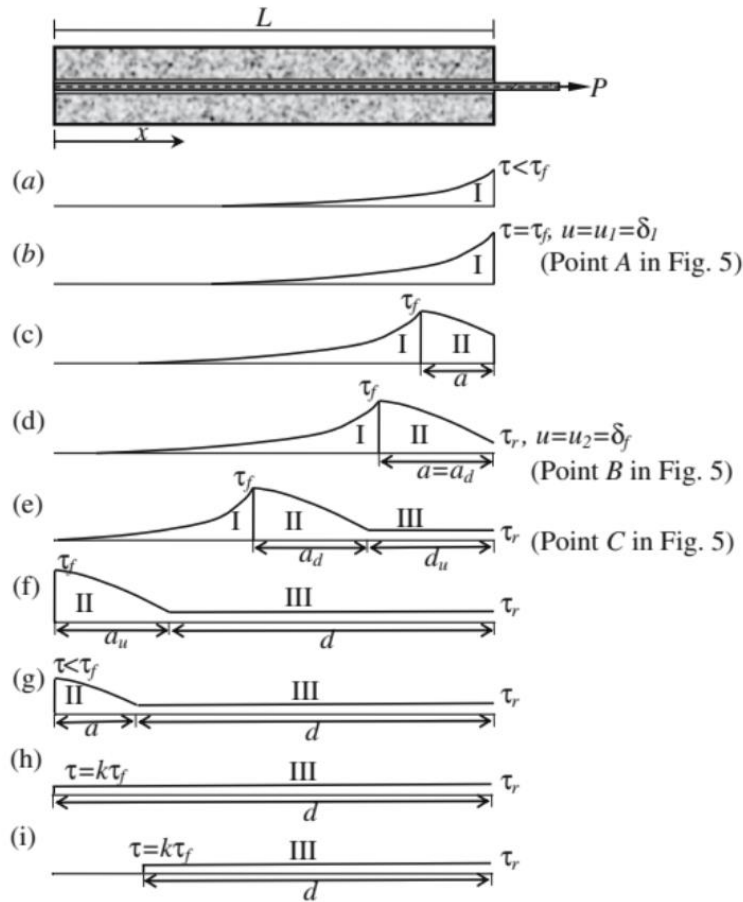


Figure 2-33. Evolution of interfacial shear stress distribution and propagation of debonding (Ren et al, 2010)

The control parameters of the model can be directly calibrated from pull-out tests. Ren et al performed two pull-out tests and found the model was in high agreement with the experimental results for load-displacement, interfacial shear stress distribution, and axial stress distribution in the bolt. It provided a rigorous theoretical basis for understanding the full-range mechanical behaviour of grouted rock bolts and could be used in detailed numerical modelling (Ren et al, 2010).

Soon after in 2011, Blanco Martín, Tijani, and Hadj-Hassen expanded on the tri-linear model to present a complete solution for the mechanical behaviour of FGRBs under tensile load. Their model is unique in that the boundary conditions do not concern the loading point, only the free end of the bolt. Thus the displacement at the free end is the key parameter in predicting behaviour. Their predictions were

compared to two in-situ tests and were found to be in agreement (Blanco Martín et al, 2011).

The same year, Bobet and Einstein proposed analytical solutions for stresses and displacement of tunnels supported by DMFC, CMC, and CFC rock bolts. They used nine assumptions and derived a complete set of formulas for DMFC and CMC systems. Their analytical results were compared to those obtained from the Finite Element Method and there was a reasonable degree of agreement. Their model had several limitations based on the assumptions made and would not be applicable in many cases such as non-circular tunnels, when rock bolts are not uniformly distributed around the tunnel, or three-dimensional analysis (Bobet & Einstein, 2011).

In 2013, Ma, Nemcik, and Aziz worked to improve on limitations of previous works and presented a new analytical model based on bond-slip (Figure 2-34). They introduced decoupling behaviour into the model and considered the complete decoupling behaviour with zero shear stress. They completed pull-out tests and used in-situ test data from previous studies to evaluate their model, results were in agreement (Ma et al, 2013).

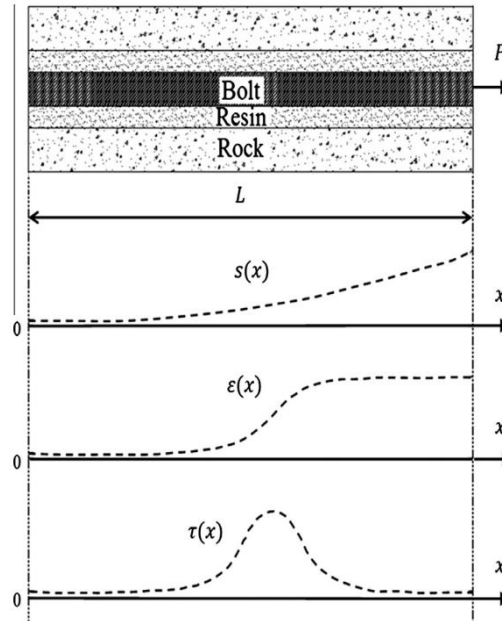


Figure 2-34. Analytical model of fully grouted rock bolt in pull-out test (Ma et al, 2013)

2.6.1 Temperature Effects

As mentioned previously, FGRBs are one of the most widely used systems in rock support and are employed in a wide spectrum of operational environments and must adapt to in order to maintain safe operations. As underground operations expand to all areas of the world and increase in depth, environmental conditions will become more challenging. Future mining operations will likely encounter virgin coal temperatures above 50°C (Belle & Biffi, 2018) and gas temperatures from mine/tunnel fires can be up to 1350°C (Li & Ingason, 2014). Permafrost is found on different continents and remains frozen year-round (i.e. 0°C and lower), the temperature can be as low as -20°C depending on depth and region (Reny et al, 2019; Wang et al, 2020). The temperatures at the extremes can potentially affect the bonding and performance of the rock bolts. In industry, both resin and cement grouts are utilized at various temperatures underground. In this study, cement grout will be used.

2.6.2 Cement Grouts in Cold Temperatures

As mining and construction activities expand into permafrost regions, the use of cement-based materials will increase in below freezing temperatures. Cold temperatures slow strength development of cement-based mixtures and early-age frost damage may occur if cement mixtures are unable to gain sufficient strength (3.5 MPa) prior to freezing. The on-set of early-age frost damage results in uncertainty if the mixture will gain adequate strength. Regular Portland Cement (PC) will not properly hydrate in sub-zero conditions thus will not likely gain sufficient strength (Reny et al, 2019; Huang, 2021). Modifications to the cement mixture is required in order to be effectively cured in cold regions. Admixtures (i.e. accelerators or anti-freeze) have varying results and consequences (e.g. Corrosion potential). Different cement types have also been tested, the cement needs to have high early strength and high hydration rate (Huang, 2021).

In 1970, Morris evaluated five cement systems for permafrost: Neat Cement Fondu; 50:50 Cement Fondu: Flyash; 50:50 Portland:Gypsum (20% of mix water replaced with alcohol); 50:50 Portland:Gypsum (15% Sodium Chloride by weight of water); and high early strength Portland plus 2% Calcium Chloride (Figure 2-35). It was concluded that Neat Cement Fondu or 50:50 Cement Fondu: Flyash will set to

adequate compressive strength and obtain adequate bond strength in 15°F (-9.4°C) environment (Morris, 1970).

COMPRESSIVE STRENGTH TESTS				SHEAR BOND STRENGTHS		
Cement System	Curing Temp. °F	psi at		Cement System	Bond Strength in Psi	
		16 Hrs.	24 Hrs.		Cement to Pipe	Cement to Ice
Neat Cement Fondu	40	2594	3505	Neat Cement Fondu	988	538
50:50 Fondu:Flyash	35	1937		50:50 Fondu:Flyash	374	438
50:50 Gypsum:Portland Cement (Mix water 20% by Volume Alcohol)	15	N.D.*	885	50:50 Gypsum: Portland Cement (Mix water 20% by Volume Alcohol)	67	43
50:50 Gypsum:Portland Cement (18% Sodium Chloride by Weight of Water)	15	N.D.*	574	50:50 Gypsum:Portland Cement (18% Sodium Chloride by Weight of Water)	56	151
*N.D.- NOT DETERMINED						

Figure 2-35. Compressive and shear bond strength tests results (Morris, 1970)

In 2017, Reny, Cruz, and Clements completed a study on cement grouts for mining operations in cold climates, specifically adapting the mixtures for use with automatic bolters. In the laboratory, two types of grouts were tested: Neat permafrost grout and Neat thick consistency (TC) permafrost grout. Both types of cement met the benchmark cable bolting strength for most mines of 20 MPa at 24 hours, laboratory results seen in Figure 2-36. Compressive strength of Neat permafrost grout was found to be slightly higher than TC permafrost grout, the difference was attributed to higher viscosity of the grout. In situ testing used fresh water and brine water to batch TC permafrost grout. Results found the compressive strength of TC batched with fresh water to be higher than that batched with brine water (Reny et al, 2017).

Consistency	Age of break (days)	Compressive strength (MPa)	Compressive strength average (MPa)
Fluid (neat permafrost grout)	1	50.7	46.4
	1	42.0	
	7	50.8	49.1
	7	47.3	
	28	51	49.5
	28	48	
Thick consistency (TC permafrost grout)	1	36.8	36.5
	1	36.1	
	7	38.7	39.6
	7	40.4	
	28	40.6	41.3
	28	41.9	

Figure 2-36. Laboratory grout compressive strength results (Reny et al, 2017)

In 2021, Huang presented a study on the performance of calcium sulfoaluminate (CSA) cement-based mixture for use in permafrost regions. The results showed that CSA cement had a higher hydration rate and strength development rate than PC in cold temperatures (defined for the study as $< -5^{\circ}\text{C}$). CSA also displayed high resistance to early-age frost damage due to its fast strength development. The main components of CSA cement include 30-70% weight of ye'elimite ($\text{C}_4\text{A}_3\text{S}$), 10-25% calcium sulfate (C_2S including anhydrite, gypsum or hemihydrate), and other constituents such as calcium aluminate (CA) and belite (C_2S). Typically, when studying effects of cold temperature samples are cured in cold air, however, the thermal conductivity of air (about $0.025 \text{ W/m}\cdot\text{K}$) is significantly lower than permafrost (typically about $1.2\text{-}3.6 \text{ W/m}\cdot\text{K}$). The research adopted a novel curing method, surrounding the sample with frozen saturated sand. CSA cement and ordinary PC were tested at different temperatures and times of curing. Results found that CSA cement can gain strength when cured in cold temperatures whereas ordinary PC did not gain strength in cold temperatures until 28 days cure, which the values were minimal (Figure 2-37) (Huang, 2021).

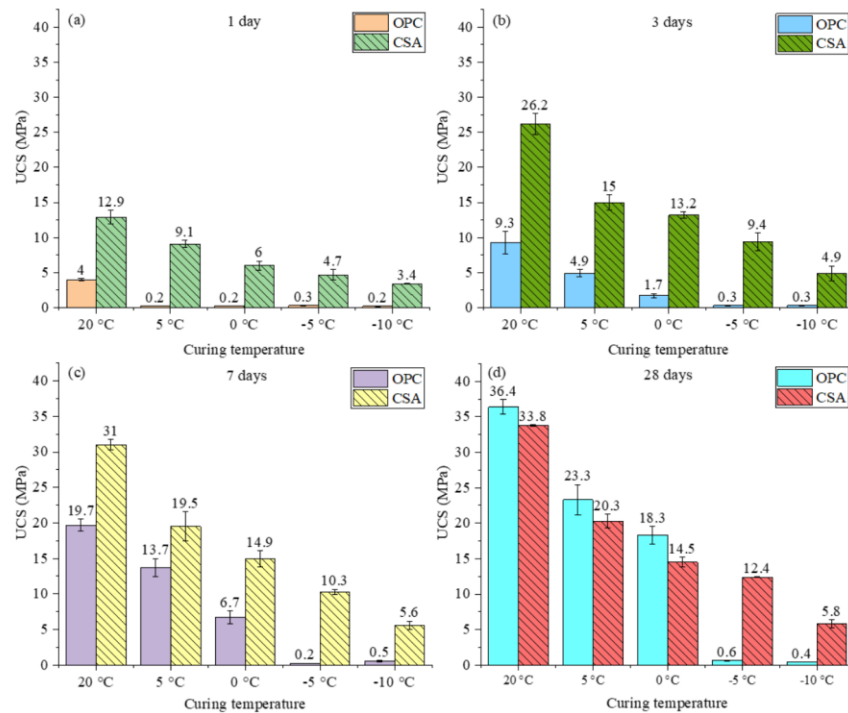


Figure 2-37. Unconfined compressive strength test results for CSA and ordinary PC (Huang, 2021)

2.6.3 Temperature Effects on Fully Grouted Rock Bolts

In 2017, Lahouar, Caron, Pinoteau, Forêt, and Benzarti presented a study on resin anchors at high temperatures and outlined the non-conservative design issues with existing codes. Although this study was not rock bolt specific, its results can provide insight into chemical reactions of grouted members to temperature. Two series of pull-out tests were conducted: stabilized temperature and constant load. The objective of the stabilized temperature was to determine the relationship between bond resistance and anchor temperature. The results found that the epoxy resin had a constant mechanical performance between 20°C and 50°C. Above 50°C the resin lost about 30% of its bond strength and at 130°C lost about 96% of its initial bond resistance. The aim of the constant load test was to associate a failure bond temperature to different applied of shear stress. Results found that for epoxy resin, bond failure occurred at 27°C for a quantity of 27 MPa bond stress. Failure temperature increased as applied bond stress decreased. It was concluded that at high temperatures, the mechanical properties of the anchor rapidly decreased. The two different tests produced similar results at normal operating temperatures (<

50°C) but diverged at higher temperatures, difference was attributed to creep, water migration, and post cure phenomena (Lahouar et al, 2017).

The same year, Li, Quan, Jia, Wang, Zhang, and Chen completed an experimental study looking at the effects of high temperatures on the interfacial properties of FGRBs. When rock bolts are installed in geothermally active tunnels, physical and chemical reactions may occur resulting in bond behaviour degradation and structural damage. Since anchorage capacity of FGRBs are mainly dependent on interfacial bond strength and strength of the rod, a series of tensile tests under different environmental temperatures were conducted. Three specimens were tested, comprised of hollow threaded rock bolts cemented with 0.45 w/c ratio and 1.00 cement/sand ratio PC grout, instrumented with strain gauges (Figure 2-38). The embedment length tested was 100 cm. The samples were maintained in temperature boxes of 20°C, 35°C, and 50°C and indoor tensile tests were performed after 28 days (Li et al, 2017b).

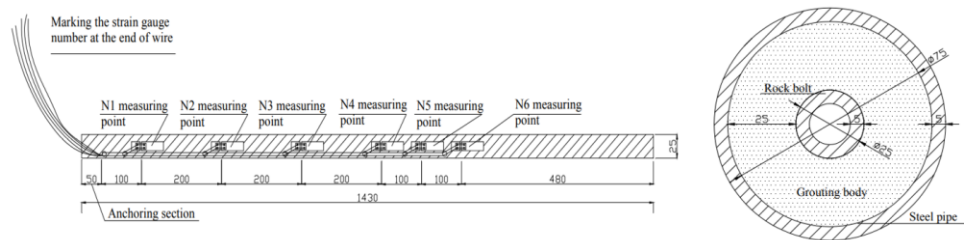


Figure 2-38. Test specimen schematic and strain gauge layout (modified after Li et al, 2017b)

The test results, seen in Figure 2-39, found that as temperature increased, under the same tensile force, the axial force along the embedment length decreased slower and at the same locations were larger. The rate of exponential decay of axial force and shear stress decreases along the embedment length as temperature increases, with the slowest being at 50°C. However, with an increase in temperature, the maximum shear stress on the bolt-grout interface decreased and its distribution along the embedment length became more uniform thus, concluding that FGRB are not greatly impacted by geothermal activity. Although the authors concluded that high temperatures had little affect on FGRB tunnel support performance in geothermally active tunnels, this experiment did kick start a series of research for this team. They also noted that extra care needed to be taken to ensure water did not evaporate during grout curing (Li et al, 2017b).

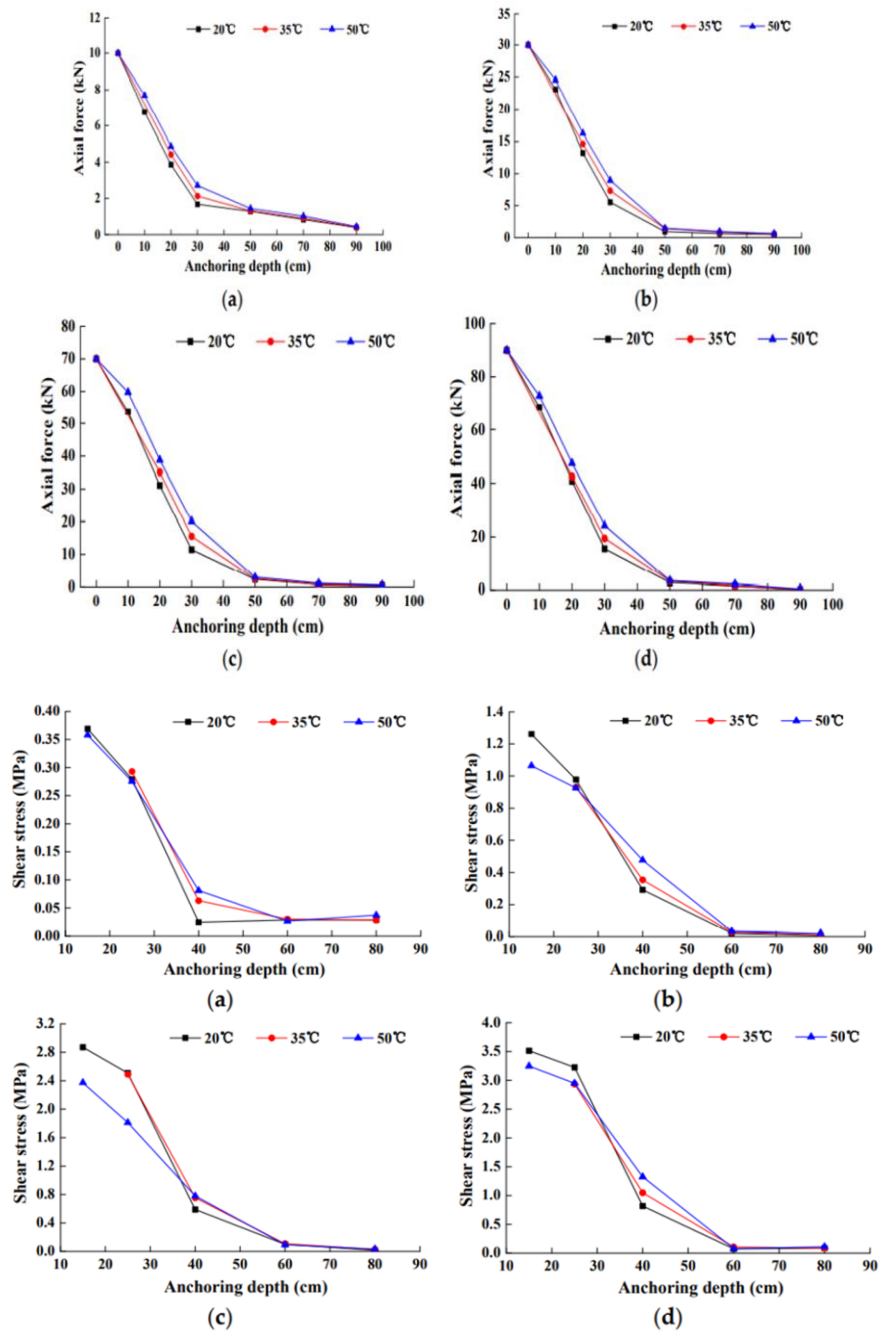


Figure 2-39. Effects of temperature on axial force and shear stress distribution under same tensile force: (a) 10 kN; (b) 30 kN; (c) 70 kN; (d) 90 kN (modified after Li et al, 2017b)

Later that year, Li, Jin, Hu, Wang, and Jia expanded on their previous research and published results looking at the effects of surrounding rock mass temperature and roughness on pull-out capacity of FGRBs. Numerous previous studies have conducted a multitude of pull-out tests researching the mechanical performance of rock bolts but very rarely had any looked at temperature and roughness. The authors noted that the temperature of the bolt can affect its performance and that the bolt temperature is significantly dependent on the surrounding rock mass. Three different bolt types were tested – non-threaded, single threaded, and double threaded – at embedment lengths of 100 mm. Cement grout (same as Li et al, 2017b) was used and specimens were cured at 20°C, 35°C, 50°C, and 70°C, tested after 7 days and 28 days. They looked at failure at the bolt-grout interface and grout-pipe interface and concluded that at different temperatures, there are different degrees of shear failure, and some can occur at the middle of the fracture failure due to lack of strength in the grout. For ultimate pull-out strength (results seen in Figure 2-40), it was concluded that temperature range had an effect. Strength increased between 20°C and 35°C but decreased from 50°C to 70°C. The authors recommended the use of thermal insulators during installation of rock bolts (Li et al, 2017a).

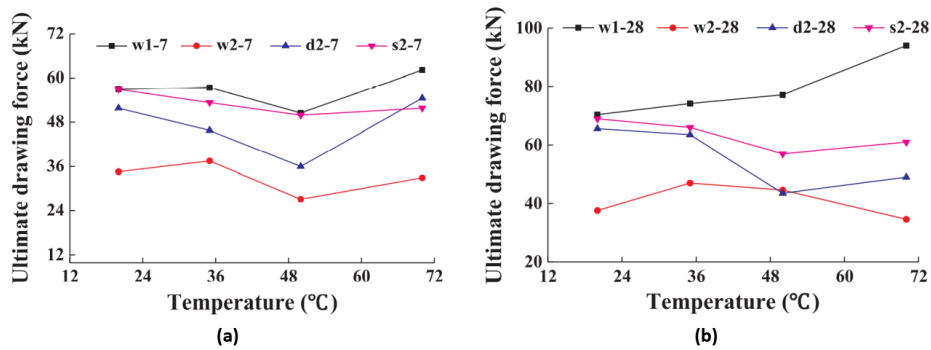


Figure 2-40. Effect of temperature on ultimate tensile force: (a) 7 days curing; (b) 28 days curing (modified after Li et al, 2017a)

Regression analysis was performed to better define the relationship between temperature and ultimate tensile force. It was calculated through curve fitting using logarithmic function, exponential, function, power function and polynomial. They found that the relationship corresponded to the cubic polynomial function (Figure 2-41), expressed in Equation 4 (7 days) and Equation 5 (28 days) (Li et al, 2017a).

$$P = 0.00079t^3 - 0.09519t^2 + 3.2449t + 14.65556 \quad (4)$$

$$P = 0.00091t^3 - 0.12229t^2 + 4.69203t + 5.15556 \quad (5)$$

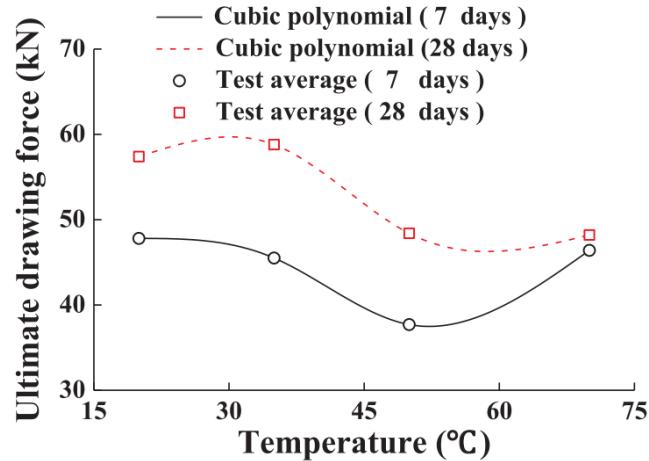


Figure 2-41. Curve fitting (Li et al, 2017a)

In 2018, Wang, Guo, Li, Hu, and Jia further expanded on the previous studies on high temperature effects on FGRBs looking to form a theoretical basis for rock bolts in complex engineering environments. Pull-out tests were conducted on specimens, one set looking at temperature and another set looking at roughness. The embedment lengths were 100 mm and a waterproof gasket was added, curing temperatures were 20°C, 35°C, 50°C, and 70°C. Three working loads of 10 kN, 35 kN, and 60 kN were tested. The results of the study was in agreement with Li et al. (2017a) that temperature had a certain effect on ultimate pull-out strength: increasing first and then decreasing as temperature increased. In addition, under a curing environment, the variation of range in ultimate pull-out force was smaller with higher preloadings than compared to that under ambient temperature (Wang et al, 2018).

In 2020, McTyer presented a study on the effects of elevated temperatures on resin-anchored rock bolts. They are the minimum level of ground support required in Australian underground coal mines, which typically operate around 10°C to 30°C. The concern was with extremely high temperatures in the mine caused by underground fires, limited research was present looking at the potential effects on resin-grouted rock bolts. The protruding tail end of the bolts were exposed to a high temperature furnace at 950°C for 28 hours to simulate heat application during a mine fire. The bolts were tested using the push-testing method. Results concluded

that heat conduction along the length displayed exponential decay away from the source. Temperatures after 600 mm dropped to less than 100°C. Load transfer in the first 150 mm of the length reduced by 83%, from 150-600 mm reduced by 33%, and after 600 mm there was no difference between heated and non-heated bolts. The results also correlate with those found in Lahouar et al. (2017). Tensile tests found heated bolts lost approx. 20% of their peak load capacity (McTyer, 2020).

In 2021, Zhang, Wang, Song, and Tan completed an experimental study looking at the effects of the freeze-thaw cycle and sulfate attacks on FGRBs. Sulfate ions are heavily present in underground water due to industrial wastewater discharge. Their presence affects the durability of rock bolts due to corrosion-induced degradation. The durability of rock bolts is also significantly impacted by freeze-thaw cycling but the effects had not been substantially investigated. The study tested cement grouted rock bolts, exposed to 25, 50, 75, 100, and 125 freeze-thaw cycles (from -30°C to +60°C) in pure water and sulfate solution. Pull-out tests were conducted on short specimens, embedment length of 50 mm. The compressive strength and shear strength of the cement grout was found to decrease with increasing freeze-thaw cycles as pores in the grout were enlarged by ice stress during the freezing process. The authors concluded that both the freeze-thaw cycling and sulfate attack reduced the load bearing capacity and increased the deformation of the rock bolt causing stress relaxation in the bolt. The effects of the freeze-thaw damage was faster than that of sulfate attack and has the dominant role during short-term testing. But in the long-term sulfate attacks would cause greater damage (Zhang et al, 2021).

2.7 Historical Research Gaps

There are a myriad of factors that affect the performance of fully grouted rock bolts, temperature is an important factor and as underground excavations go deeper and expand into different regions the environments the design and assessment of rock bolts for these conditions will only become more complex. Existing research into temperature effects on FGRBs has been limited, with most of the literature concentrated in higher temperature realm. The studies mainly looked at experimental results and correlations through regression analysis. The research gaps are found below:

1. Effects of temperature on mechanical performance of FGRBs has not been extensively investigated;
2. Limited studies in higher temperature realm exist and fewer were found looking at cold regions;
3. Research into effect of cement grout on the system at extreme temperatures is limited;
4. The majority of research used short embedment lengths; and,
5. Instrumentation and monitoring techniques used in existing studies do not account for micro mechanisms as they lack spatial resolution.

2.8 Summary of Past Research Group Testing and Findings

This research project is the latest in a series of projects into behaviours of ground support elements utilizing the DOS technique of the author's research group. The current methodology and testing setup is the cumulative result of several iterations and improvements through each member. The technology has been employed in laboratory and in-situ testing conditions. The focus of this paper is on FGRB, which previous research group members at RMC have conducted robust studies into confining medium, embedment length, grouting materials, rib spacing, and grout annulus. A summary of past research group members' Masters Thesis are found in Table 2-3, Table 2-4, and Table 2-5.

Table 2-3. Summary of past research group Master's Degree Thesis objectives

Masters Thesis	Research Objectives
Forbes (2015)	<ul style="list-style-type: none"> • Determine most appropriate commercially available optical strain sensing technology for monitoring support elements • Develop technique to apply chosen system for rock bolts and forepoles • Verify the capability of the optical technique
Cruz (2017)	<ul style="list-style-type: none"> • Develop lab testing scheme to monitor fully grouted rock bolts (FGRB) under axial load • Critical embedment length • Loading mechanisms • Failure mechanisms
O'Connor (2020)	<ul style="list-style-type: none"> • DOS as internal (rebar) and external (confining pipe) sensor • Effects of grout type • Effects of embedment length • Effects of radial stiffness of confining material
Moore (2021)	<ul style="list-style-type: none"> • Further refine and understand limitations of DOS technique • Effects of rib spacing • Effects of grout annulus

Table 2-4. Summary of past research groups investigations

Masters Thesis	Investigation
Forbes (2015)	<ul style="list-style-type: none"> • Fiber Bragg grating • Brillouin distributed sensing • Rayleigh Optical Frequency Domain Reflectometry (ROFDR) • Technique development • Rock bolt and forepole testing
Cruz (2017)	<ul style="list-style-type: none"> • Confining material: Concrete • Borehole diameters: 31 and 41 mm • Grout: Cement and resin • Changes in embedment length, borehole diameter, and grout type
O'Connor (2020)	<ul style="list-style-type: none"> • Confining material: Various materials (steel, aluminum, PVC, concrete cylinder) • Grout: Cement and resin
Moore (2021)	<ul style="list-style-type: none"> • Confining material: Steel pipe (various sizes) • Grout: Cement • Rib spacing: 14, 28, 41, 54, and 68 mm • Grout annulus: 7.7, 9.9, 14, 22.8 mm

Table 2-5. Summary of past research groups thesis conclusions

Masters Thesis	Conclusion
Forbes (2015)	<ul style="list-style-type: none"> • ROFDR was chosen • Continuous sensing at low cost • Reliability and accuracy verified in situ at an operational coal mine • DOS was a feasible sensing solution for ground support elements and should be used in-situ

Masters Thesis	Conclusion
Cruz (2017)	<ul style="list-style-type: none"> • Larger borehole diameter improved system capacity • Embedment length was most significant factor, capacity increased with length • Resin grout generally had higher capacity
O'Connor (2020)	<ul style="list-style-type: none"> • Grout type was major factor for critical embedment length and bond strength • Increase in embedment length increased both, increase was not proportional • Confinement materials did not have correlations to either
Moore (2021)	<ul style="list-style-type: none"> • Rib spacing had significant effect on rock bolt behaviour (stiffness, load to fully mobilize embedment length, bond performance, load transfer, peak and residual strength, etc.) • Grout annulus effects were not consistent

2.9 Relevance to Research

This chapter presented the background and real-world basis of this research project. The fundamental concepts associated with ground support focusing on FGRB were discussed to provide an understanding on rock bolting and mechanical behaviours. In addition, past technological limitations of conventional monitoring instrumentation and how the introduction to the DOS technique were covered. A summary of historical research gaps was also provided.

3 Material Testing

3.1 Introduction

A series of laboratory tests and studies were conducted in order to understand the materials utilized in this project and confirm material properties. A review of past research group projects and existing literature of temperature effects on materials was completed in order to select suitable materials for the test specimens. Mainly, options of readily available commercial materials were explored with consideration of availability and applications to civil engineering and mining industries. This chapter presents an overview of the materials selection, prototyping, use in specimen production, and results of materials properties testing and comparison with literature or manufacturer published values. All tests were conducted at the RMC Structures Laboratory and a summary of the testing regime follows in Table 3-1.

Table 3-1. Summary of materials testing regime

Type of Test	Material	No. of Specimen	Notes
Uniaxial Compressive Strength	PC grout cylinder Nordic grout cylinder	72	6 used in grout baseline study
Splitting Tensile Strength	PC grout cylinder Nordic grout cylinder	66	6 used in grout baseline study
Modulus of Elasticity / Poisson's Ratio	PC grout cylinder Nordic grout cylinder	8	Conducted prior to UCS test
Tensile Strength	20M 400W rebar	1	

3.2 Test Specimens Materials Requirements

Rock bolt reinforcement systems are comprised of four components – the rock, the element, internal fixture, and external fixture (Windsor & Thompson, 1993). For this research endeavour, the focus was on three of these components as the

laboratory pull-out test setup utilized by this research group concentrates on the embedment (anchorage) length as seen in the highlighted portion of Figure 3-1.

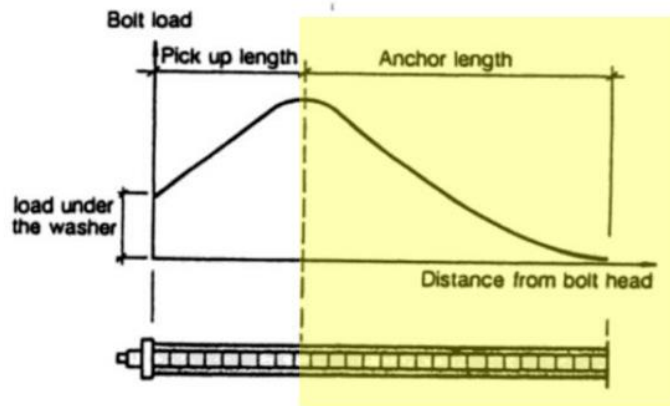


Figure 3-1. Portion of FGRB focused by pull-out test (modified after Stille, 1992)

The FGRB test specimens are required to replicate the rock, the element, and the internal fixture as seen in Figure 3-2. As discussed in the previous chapter, the effects of rock confinement are often replicated by various materials in laboratory tests. This research group has utilized several types and steel pipes were confirmed to be suitable. Previous members (Cruz, 2017; O'Connor, 2020) utilized No. 6 Grade 60 (20M 420W) rebar for the rock bolt, however, due to local availability the bar was changed to 20M 400W. Both cementitious and resin grouts have been tested before but this project only used cement grouts.

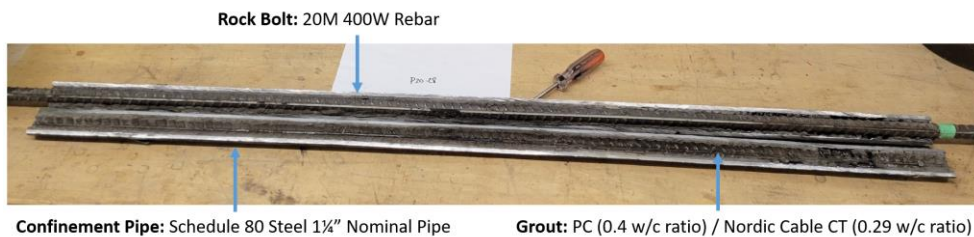


Figure 3-2. Cut open FGRB test specimen

3.3 Grout Baseline Study

Cement is a binding material that undergoes hydration and hardens with the addition of water, the w/c ratio is an important factor for strength and material properties (Kilic et al, 2002). Due to the wide range of temperatures in this study, -20°C to +45°C, two different types of cement grouts were required (Table 3-2). Regular PC has been typically used by this research group as the grout (Cruz, 2017; Moore 2021) with specimen curing and testing conducted at ambient laboratory temperature (approx. 20°C). Ciment Québec Type 1 GU was locally available and selected for the project. However, PC cannot adequately hydrate and gain sufficient strength in below freezing temperatures (Reny et al, 2019; Huang, 2021). Samples of Nordic Cable CT were provided by Sika Canada and used for the permafrost condition grouting being specifically formulated for *“cold weather applications such as the anchoring of cables, tendons or bolts of various dimensions, in permafrost and other substrates subject to frost”* (King A Sika Company, n.d.). This product is commercially available therefore, would be applicable and easily accessible to industry, in contrast to formulating a novel mixture particularly for this project.

Since the grout is the load transfer medium from rock bolt to surrounding confinement material and two types of cement grouts were to be employed, a grout strength baseline study was completed to compare the materials when cured at the same temperature and assess the potential effects on the test specimens. Each cement type had a set of six grout test cylinders produced in accordance with ASTM C470 (ASTM, 2015) and ASTM C192 (ASTM, 2019) casted in 100mm Ø x 200mm L moulds. The grout mixtures for both types of cement were prepared in the same manner using a handheld mixer, poured in two layers, and consolidated on a shaker table. One mixed batch was sufficient to make all six cylinders. The cylinders were placed in a refrigerator set at 5°C and cured for 28 days (Figure 3-3). Both grouts were mixed at a 0.4 w/c ratio as recommended in literature to balance grout strength and pumpability (Kilic et al, 2002; Hyett et al, 1992) and typically used by the research group. The mixture recommendation according to the Nordic Cable CT, which will be referred to as Nordic, Technical Data Sheet (TDS) was 0.29 w/c. However, the same w/c ratio was chosen for both types of cements in order to limit the number of variabilities that could potentially affect the specimens other than curing temperature.

Table 3-2. Grout type utilized for each simulated condition and temperature

Simulated Condition	Curing Temperature (°C)	Grout Type
Permafrost	-20	Nordic
Permafrost	-5	Nordic
Control	20	PC
Geothermally Active	45	PC

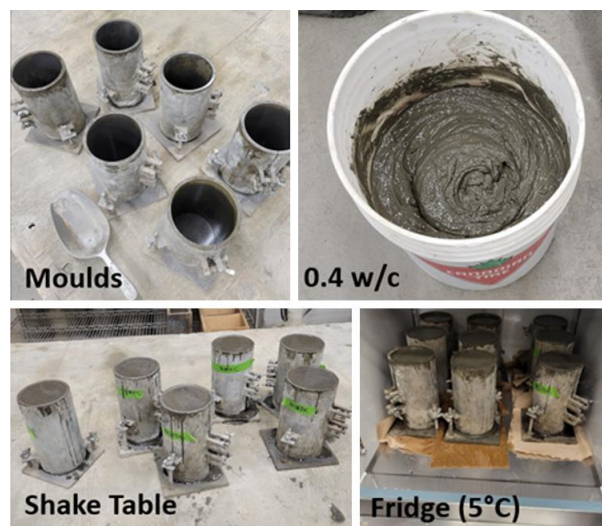


Figure 3-3. Preparation and curing of baseline grout test cylinders

The common temperature of 5°C was chosen for the baseline study as it was at the lower temperature extreme for PC since masonry works commonly add heating around 4.5°C and at the upper limit for Nordic according to its TDS. The curing condition was maintained by a VWR Temp-Tech 3000 refrigerator at a range of $\pm 1.5^\circ\text{C}$ due to factory settings for the compressor and generally observed on the temperature display over time. The grout cylinders remained in their moulds for the curing duration with the intention of better resembling in situ conditions of the grout inside boreholes. The cylinders were removed from their moulds one day prior to testing in order to prepare them. Two series of strength tests were conducted: Uniaxial Compressive Strength (UCS) test and Splitting Tensile Strength (STS) test. It is common practice to cap the cylinder ends for UCS tests, however, for this project all UCS cylinders were grinded smooth using a Marui Concrete Specimen End Grinding Machine Triple Hi-Kenma as seen in Figure 3-4.



Figure 3-4. Preparation of UCS cylinders using grinding machine

Due to the temperature range, notably for the permafrost conditions, the concern was with the hot cap bonding material either not completely adhering or affecting the properties of the material with sudden high temperature change thus end grinding was determined as the more optimal choice. The cylinders were placed in an insulated cooler during transport and temporary storage at the preparation station to minimize ambient temperature changes. Any residual water from the grinding process was wiped off so not to introduce excess water to the samples. The cylinders were then placed back in the refrigerator until testing.

3.3.1 Compressive Strength

A 300,000 lbs RIEHLE Testing Machine was utilized to perform the compressive strength tests as shown in Figure 3-5. The UCS tests were conducted following the guidelines of ASTM C39 (ASTM, 2021). Prior to testing, each cylinder's diameter, length, and mass measurements were taken (Figure 3-6). Three cylinders were tested for each grout type loaded at a controlled rate of 0.28 MPa/s as outlined by the testing machine's operating instructions, which was within the ASTM's specified loading rate of $0.25 \text{ MPa/s} \pm 0.05 \text{ MPa/s}$.

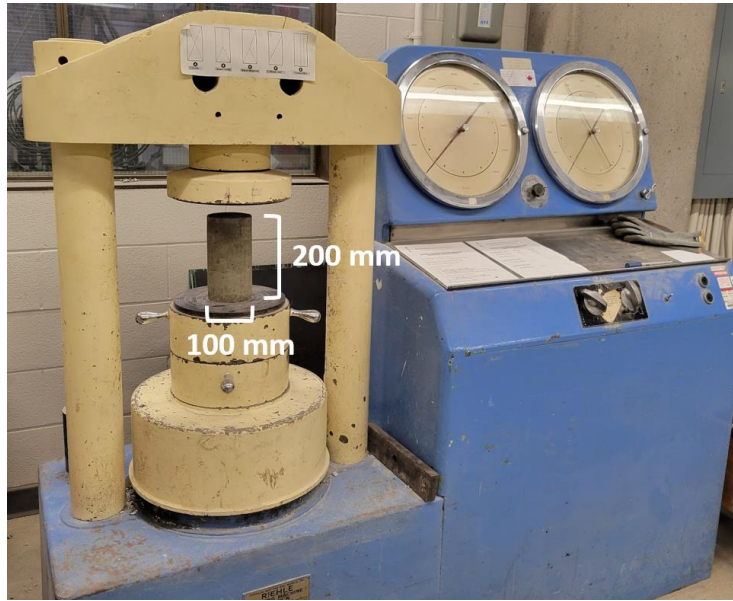


Figure 3-5. RIEHLE testing machine



Figure 3-6. Pre-test grout cylinder measurement process

The grout specimen naming convention included letters and numbers. The first section of letters was 'PC' for PC grout or 'NOR' for Nordic grout. The second letter was 'C' for compressive strength test or 'S' for splitting tensile strength test, followed by the test number of specimen. Each grout specimen experienced brittle failure and observed patterns were recorded according to Figure 3-7 and seen in Figure 3-8. The failure loads were read from the machine's dial gauges. The results of each test are summarized in Table 3-3 and each reading was within the acceptable range of individual cylinder strength for ASTM C39 (ASTM, 2021). The test of Specimen PC-C1 was omitted due to inconsistencies in loading as it was the first time the author operated the testing machine and during cylinder failure the

loading rate was accidentally excessively increased pushing the dial further. Post-test inspections of each specimen did not find any excessive voids in the grout.

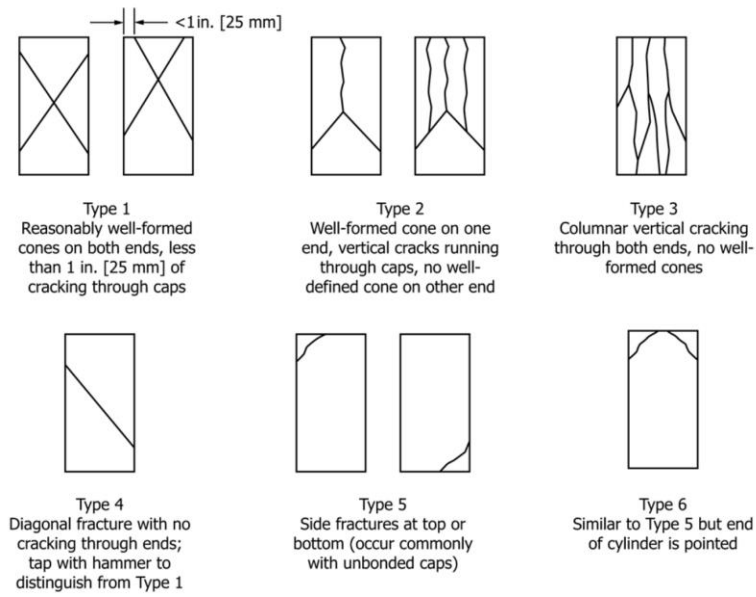


Figure 3-7. Typical fracture patterns (ASTM, 2021)

Table 3-3. Grout baseline UCS test results

Specimen	Density (kg/m ³)	Compressive Strength (MPa)	Failure Mode / Comments
PC-C1 ¹	2022.36	50.5	Type 1
PC-C2	2019.02	41.5	Type 3
PC-C3	2012.37	46.6	Type 1
NOR-C1	1962.24	20.4	Type 2
NOR-C2	1976.62	18.8	Type 3
NOR-C3	1982.35	17.5	Type 3

¹ Test omitted due to inconsistencies during loading caused by inexperience operating machine

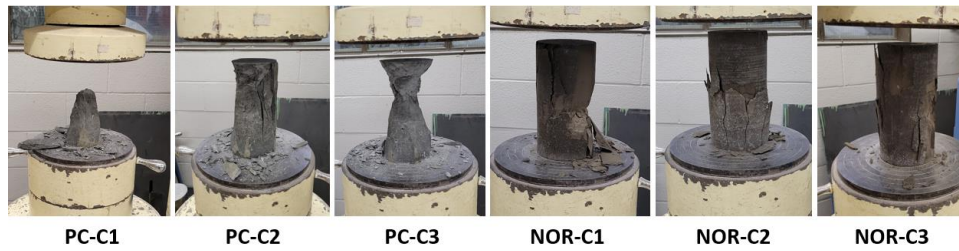


Figure 3-8. Failure pattern of compressive test specimen

3.3.2 Tensile Strength

STS testing was the selected method for quantifying the grout tensile strength as it has been proven to be an effective means by past group members (Cruz, 2017; O'Connor, 2020; Moore 2021). The testing was carried out on a 300,000 lbs RIEHLE Testing Machine following the guidelines of ASTM C496 (ASTM, 2017). Prior to testing, each cylinder's diameter and length measurements were taken and positioning lines drawn (Figure 3-9). Three cylinders were tested for each grout type loaded at a controlled rate of 1.3 MPa/min as outlined by the testing machine's operating instructions, which was within the ASTM's specified loading rate of 0.7 to 1.4 MPa/min. The cylinder was placed between plywood strips and steel plates to provide properly distributed loading across the length of the cylinder. One deviation noted was that the plywood bearing strips were reused during testing.



Figure 3-9. Preparation measurements and STS testing setup

Each grout specimen was placed in the STS test setup and the resulting failure split seen in Figure 3-10. The failure loads were read from the machine’s dial gauges. The results of each test are summarized in Table 3-4. The reading for Specimen PC-S2 was omitted as it was uncharacteristically low and was outside of the acceptable range for ASTM C496 (ASTM, 2017). It is noted that the ASTM range is based on average STS around 2.8 MPa, which the results from this test are not. However, the precision range was still used to omit tests along with judgment of actual results as too uncharacteristic compared to others. Post-test inspections of each specimen did not find any excessive voids in the grout.

Table 3-4. Grout baseline STS test results

Specimen	Diameter (mm)	Length (mm)	Split Tensile Strength (MPa)
PC-S1	100.75	198	4.6
PC-S2	100.58	194	3.3 ¹
PC-S3	100.33	197	4.8
NOR-S1	99.83	201	2.2
NOR-S2	99.75	202	1.8
NOR-S3	99.92	201	1.8

¹ Result omitted due to being uncharacteristically low



Figure 3-10. Tensile testing of grout cylinders

3.3.3 Baseline Comparison Discussion

Preliminary visual and subjective comparisons were made between PC and Nordic during grout mixing and testing preparations, examples as seen in Figure 3-11. The most evident difference was in colour and mix texture. At the same w/c ratio, the Nordic mixture was more fluid and thinner in consistency than the PC mixture,

which likely corresponded to Nordic being developed to be pumpable in cold weather.

The average results of the UCS and STS tests for PC and Nordic grout cured at 5°C for 28 days are presented in Table 3-5. The percentage difference between the grout types for UCS was 79.8% and for STS was 84.7%, which are significant strength differences. The manufacturers' compressive strength results for PC and Nordic are found in Figure 3-12. For PC, the testing complied with CSA A3000-13 requirement section A3001-13, Type GU and for Nordic, the standard followed was ASTM C39 (ASTM, 2021).



Figure 3-11. Visual comparison of PC and Nordic grouts

Table 3-5. Average UCS and STS comparison of PC and Nordic

Grout Type	Average UCS (MPa)	Average STS (MPa)
PC	44.0	4.7
Nordic	18.9	1.9

Compressive strength (MPa)
 3 days..... 26.4
 7 days..... 30.9
 28 days..... 37.8

Ciment Québec Type 1 GU

COMPRESSIVE STRENGTH**		
ASTM C 39		
75 MM (3") DIAMETER x 150 MM (6") HIGH CYLINDER		
GROUT TEMPERATURE OF 5 °C (40 °F)		
	-10 °C (14 °F)	-5 °C (23 °F)
6 Hours	30 MPa (4350 psi)	45 MPa (6525 psi)
1 Day	35 MPa (5075 psi)	50 MPa (7250 psi)
7 Days	40 MPa (5800 psi)	55 MPa (7975 psi)
28 Days	45 MPa (6525 psi)	60 MPa (8700 psi)

Nordic Cable CT

Figure 3-12. Manufacturer published compressive strengths (left: modified after Ciment Québec (n.d.); right: modified after King A Sika Company (n.d.))

The compressive strength result for PC was comparable to the manufacturer’s published strength at 28 days cure with a 15.3% difference, however, the w/c ratio for the manufacturer’s tests are unknown. The results are also within the range of Moore (2021) with compressive strength for PC grout at 0.4 w/c ratio ranging between 35.3 – 44.6 MPa cured for a minimum of 28 days and at ambient laboratory temperature. The STS test results were also comparable to the range of PC in Moore (2021) between 1.6 – 3.9 MPa. In addition for further STS results confirmation, a summary of relationships between STS and compressive strength was provided by Arioglu et al. (2006) seen in Table 3-6. Some of these relationships were selected to calculate the STS based on the UCS test result for PC, found in Table 3-7. The results of the ACI relationships were noted to underestimate STS when the compressive strength is greater than 40 MPa. The estimates and the test results are similar. These comparisons provide confidence in the results of the PC testing and that the lower operational limit temperature does not significantly affect the strength.

Table 3-6. Relationship STS and compressive strength (Arioglu et al, 2006)

Source	Relationship	IAE, %							Range, ° MPa	Remarks
		Compressive strength, MPa (psi)								
		0 to 20 (0 to 2900)	20 to 40 (2900 to 5800)	40 to 60 (5800 to 8700)	60 to 80 (8700 to 11,600)	80 to 100 (11,600 to 14,500)	100 to 120 (14,500 to 17,400)	All ranges		
ACI 363R-92 ²⁶	$f_{isp} = 0.59f_c^{0.5}$	14.4	5.8	9.7	12.4	18.9	12.4	8.1	$21 \leq f_c \leq 83$	—
ACI 318-99 ²⁷	$f_{isp} = 0.56f_c^{0.5}$	10.9	8.6	14.0	16.8	23.0	16.7	—	—	—
CEB-FIB ¹⁰	$f_{isp} = 0.3f_c^{2/3}$	8.9	6.0	5.6	2.5	7.9	8.2	5.9	$f_c < 83$	—
Mokhtarzadeh and French ²⁸	$f_{isp} = 0.56f_c^{0.5}$ $f_{isp} = 0.32f_c^{0.63}$	10.8	8.6	14.0	16.8	23.0	16.7	18.4	$48 \leq f_c \leq 103$	For all data, moist and heat-cured
Carino and Lew ²⁹	$f_{isp} = 0.272f_c^{0.71}$	12.4	8.3	7.1	3.0	7.8	8.9	—	—	—
Raphael ³⁰	$f_{isp} = 0.313f_c^{0.667}$	10.7	8.9	9.1	6.5	9.9	6.2	9.1	$f_c \leq 40$	Normal concrete
Ahmad and Shah ³¹	$f_{isp} = 0.462f_c^{0.55}$	9.3	10.0	14.0	15.4	20.4	13.2	13.8	$15 \leq f_c \leq 84$	—
Gardner et al. ¹²	$f_{isp} = 0.47f_c^{0.59}$	13.8	7.3	4.4	3.0	7.7	7.8	7.0	$3 \leq f_c \leq 46$	Type I cement concretes ($r = 0.865$)
	$f_{isp} = 0.46f_c^{0.60}$	14.1	8.1	5.1	4.2	7.6	9.7	6.8	$13 \leq f_c \leq 72$	Type III cement concretes ($r = 0.989$)
Gardner ¹¹	$f_{isp} = 0.34f_c^{0.66}$	8.8	5.8	5.4	2.4	7.9	8.1	9.7	$4 \leq f_c \leq 57$	Best-fit relationship for Type I, III cement and fly ash concrete ($r = 0.98$, IAE = 5.8%)
	$f_{isp} = 0.33f_c^{2/3}$	8.9	6.0	5.6	2.5	7.9	8.2	6.0		Proposed relationship for Type I, III cement and cement/fly ash concrete (IAE = 6%)
Oluokun et al. ⁸	$f_{isp} = 0.294f_c^{0.69}$	10.9	7.7	7.1	3.3	8.1	7.8	7.5	$3.5 \leq f_c \leq 63$	Normalweight concrete (IAE = 7.43%)
Arioglu ³²	$f_{isp} = 0.321f_c^{0.661}$	10.0	8.5	8.8	6.3	10.0	6.1	8.5	$15 \leq f_c \leq 120$	Cement and cement/silica fume concretes ($r = 0.950$)
Current study	$f_{sp} = 0.387f_c^{-0.37}$	9.0	5.6	4.8	2.3	8.0	7.4	5.9	$4 \leq f_c \leq 120$	Proposed for (0 to 30 °C) curing temperatures, Type I, III, cement/ fly ash, cement/bottom ash, cement/silica fume concretes

¹Including control data used.
Note: 1 MPa = 145.038 psi.

Table 3-7. Estimated STS for baseline test compressive strength results

Source ¹	Relationship	STS for f_c	
		44.0 MPa	18.9 MPa
ACI 363R-92 ²	$0.59 \cdot f_c^{0.5}$	3.9	2.6
ACI 318-99	$0.56 \cdot f_c^{0.5}$	3.7	2.4
Gardner et al	$0.47 \cdot f_c^{0.59}$	4.4	2.7
CEB-FIB	$0.3 \cdot f_c^{2/3}$	3.7	2.1

¹ Sourced from Arioglu et al. (2006)

² ACI models underestimate STS for $f_c > 40$ MPa

The compressive strength test results for Nordic are not reasonably comparable to the manufacturer’s published strengths due to the testing temperature and w/c ratio. The baseline test used a curing temperature of 5°C and 0.4 w/c ratio, whereas the manufacturer tested at -5°C and -10°C (seen in Figure 3-12) and recommended 0.29 w/c ratio. The compressive strength of Nordic is significantly affected by the curing temperature as seen in the manufacturer’s results, there is a substantial change in strength from -5°C to -10°C; as exemplified for 28 days the strength difference was 28.6%. The difference between the baseline UCS result and manufacturer’s at -5°C at 28 days was 104.2%, part of this difference also being attributed to the difference in w/c ratio. As there are no STS values on the TDS, literature relationship models were used to verify the test results. The estimated values (Table 3-7) are a little higher than the average test result but are comparable. Based on the investigation, it can be concluded that the strength of Nordic are significantly affected by curing temperature and w/c ratio.

3.3.4 Lessons Learned

One of the limitations identified with the baseline test preparation procedures was the initial temperatures of the mixing equipment and moulds. They were at ambient laboratory temperatures and were placed into the curing temperature after the grout mixtures were cast. An improvement would be to incorporate materials conditioning so that the process better replicates grouting in situ and the “rock” would already be at proper temperature. For the FGRB test specimens production, all mixing tools, buckets, confinement pipes, rock bolts, and moulds were conditioned inside the curing chambers prior to grouting.

The common 0.4 w/c ratio had initially been chosen to reduce the number of variables that could potentially affect the FGRB capacity results besides temperature. However, with the reduction in strength compared with PC results and manufacturer values (although not directly comparable) and that industry would likely mix according to manufacturer recommendation, the additional variable of w/c ratio would produce more relevant results than using a ratio that would unlikely be employed in the real world for this product. For Nordic, the 0.29 w/c ratio was used for the future test specimens.

According to the Nordic TDS, the max working time should not exceed 20 minutes. It was found that the Nordic grout began to set quickly, especially in comparison to PC grout. Considerations for batching were needed to be made in order to ensure the FGRB specimens and test cylinders are all grouted in time prior to the mixture hardening.

3.4 Polyimide Coated Fiber Optic

In order to capture a continuous strain profile of FGRBs experiencing axial loading during pull-out tests, this research group has employed DOS technology. The fiber optics are embedded in and bonded to the rock bolt through a methodology that will be detailed in the next chapter. The basic composition of the DOS includes a single-mode sensing fiber spliced to an LC connector on the lead end and a coreless fiber on the termination end. Past group members have utilized an acrylate coated fiber as the sensing fiber, however, limitations were identified. Notably a 50 mm transition zone for strain pickup, likely due to slippage between the fiber optic layers. Testing of the transition section are described in Moore (2021) and results demonstrated that the strains are more gradually picked up prior to being accurately captured (Figure 3-13).

A new single mode polyimide coated fiber was proposed for this project. The fiber was tested in the prototype and the results found the transition section for strain pickup in the polyimide fiber as 10 mm, as seen in Figure 3-14. Results from Weisbrich et al. (2020) concluded that polyimide and ORMOCER® had immediate strain pickup and did not require consideration of a transition section, only the acrylate coating needed a 40 mm consideration. This is likely due to the stronger bond between the layers as the polyimide coating cannot be mechanically separated. However, the polyimide coated fiber had a disadvantage of increased brittleness and required a larger minimum operational bend radius than the

acrylate coated fiber. The use of a flame to remove the coating also increased the brittleness, if not controlled precisely, and required more practice for flame exposure and fiber cleaning in contrast to mechanical coating stripping.

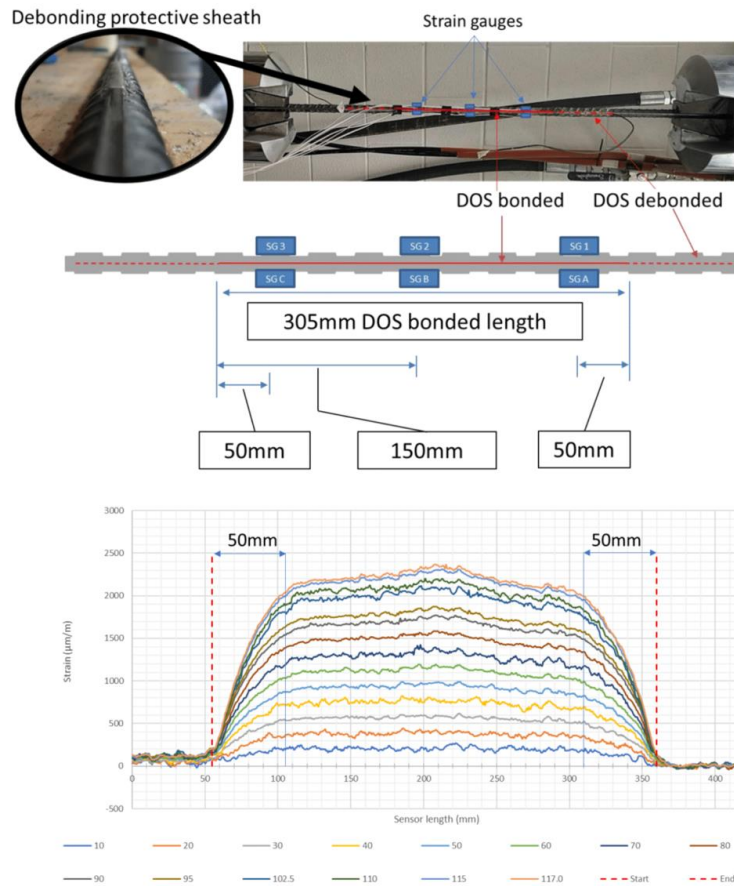


Figure 3-13. DOS de-bonding testing and strain pickup transition (modified after Moore, 2021)

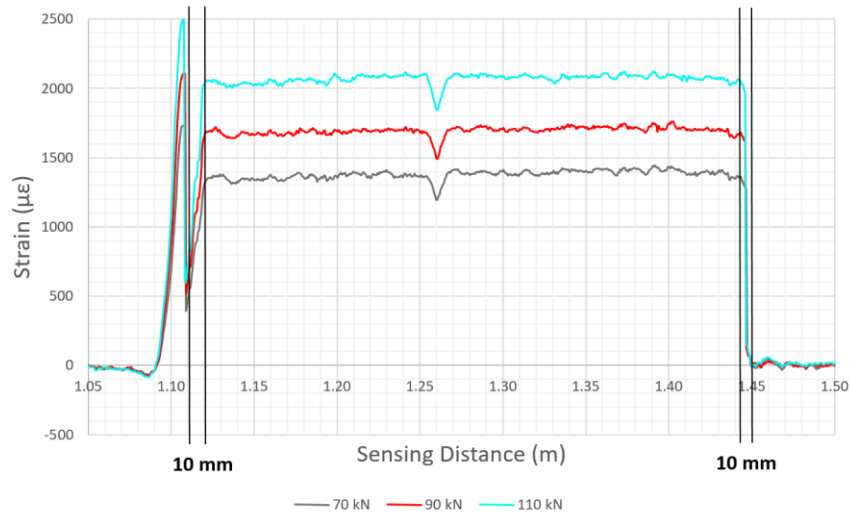


Figure 3-14. Transition section of strain pickup for polyimide coated fiber

3.5 Monitoring Instrumentation Operating Temperature

The production and mounting/embedment of monitoring instrumentation onto the FGRB specimen along with the initial operational confirmation were completed at laboratory ambient temperature and then placed into the curing chambers. The instrumentation planned to be used are the same as previous group members as they have been tested and proven, other than the introduction of a new polyimide coated fiber. A verification was completed for the operating temperature range of each main component to ensure this study's test range would be included. A summary of the operating temperatures is presented in Table 3-8. All instruments were confirmed to be operational at required temperatures.

Table 3-8. Summary of operating temperature ranges for monitoring instrumentation

Instrument	Details	Operating Temperature (°C)
Strain Gauge ¹	N11-FA-5-120-11	-30 to +80 ²
Sensing Fiber	Corning® SMF-28e+	-60 to +85 ³
	SM1550P Fiber Polyimide	-190 to +350 ⁴
Termination Fiber	FG125LA Coreless	-40 to +85 ⁵
LC Connection	Patch Cable	-20 to +70 ⁶

¹ Mounting adhesive (M-Bond 200) operating temperature range works (Micro Measurements, 2014)

² SHOWA Measuring Instruments (2022)

³ Corning (2021)

⁴ ThorLabs (2024b)

⁵ ThorLabs (2024a)

⁶ Fiber Instrument Sales (n.d.)

3.6 Prototype

For this research project, a series of pull-out tests were conducted to study the effects of temperature on FGRB. In order to observe the specimens' behaviour under axial loading, fiber optic sensors were utilized to monitor and provide a continuous strain profile of the rock bolt during testing. Since the specimens would be removed from their curing chambers for testing under ambient laboratory temperatures, DOS was also applied to monitor temperature changes in the specimen during testing to identify any impacts. As this was the first time this research group used the DOS technique to monitor temperature so thoroughly and along the entire length of the rock bolts, prototyping was completed with a view to verify the new DOS configuration. The prototype was also used to verify the material properties of the rebar.

3.6.1 Prototype Overview

A conceptual design with a strain DOS (ϵ DOS) loop and a temperature DOS (T DOS) line was developed. Two prototype rock bolts were instrumented using the new

polyimide coated fiber, the first being a full-length bolt as the actual test specimen (1600 mm) and the second was a reduced length bolt (600 mm). The ϵ DOS was applied following the typical methodology of this research group while the T DOS was fully de-bonded from the bolt, other than a single anchorage point. This provided freedom of movement for the fiber so to isolate strains measured as a result of temperature change instead of bolt loading. The proof-of-concept testing was conducted on the reduced length prototype due to the size limitations of the 810 MTS. Through the development of the full-length prototype, the bending radius limitation of the polyimide fiber was identified, and a larger external loop was implemented (Figure 3-15). The final concept and reduced length prototype are detailed in Table 3-9 and Figure 3-16.

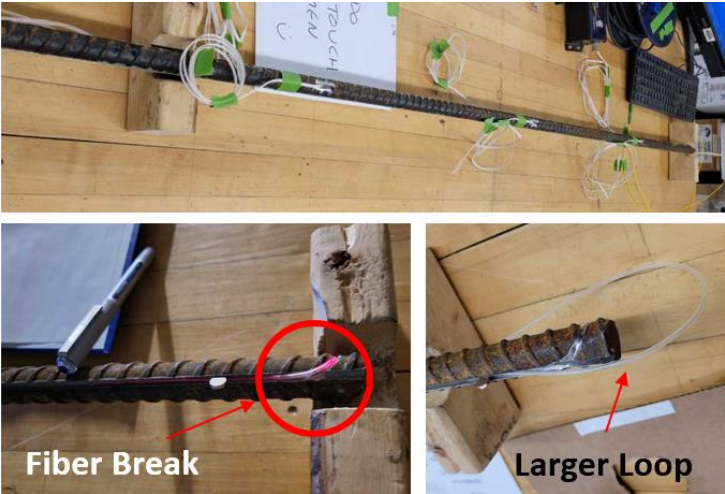


Figure 3-15. Full-length prototype

Table 3-9. Reduced-length prototype material summary

Item	Description	Supplier
Rebar	20M 400W	
<ul style="list-style-type: none"> • Overall Length • Sensing Length • Avg. Diameter 	600 mm 300 mm 19.05 mm	Kimco Steel
DOS	SM1550P Fiber Polyimide FG125LA Coreless Termination Fiber	ThorLabs
Bonding	FUSOR 108B Medium Metal Bonding Adhesive	LEVAC
SG	N11-FA-5-120-11	SHOWA

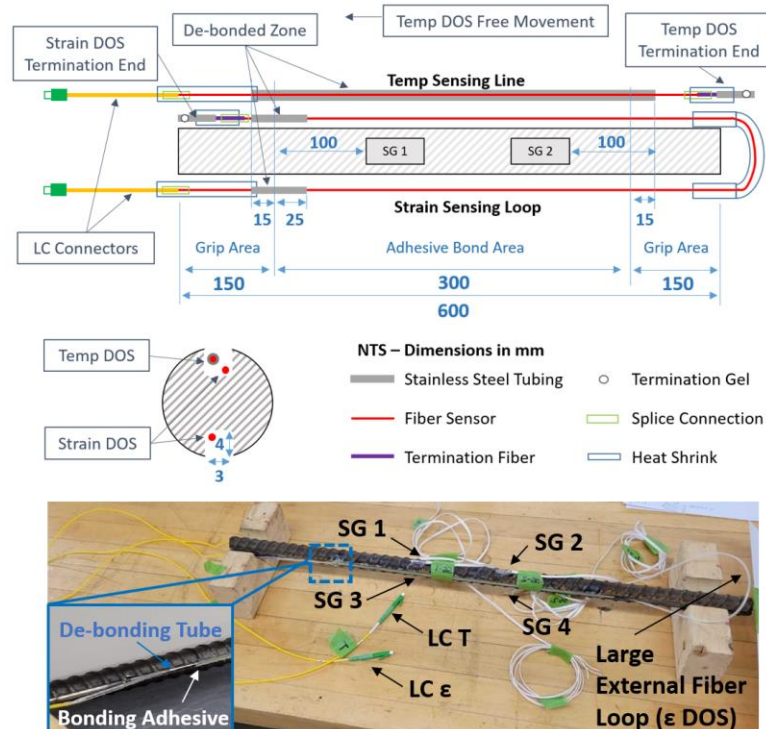


Figure 3-16. Instrumentation conceptual design for reduced-length prototype (Guo et al, 2023)

Various locations for de-bonding of the fiber optic from the rebar were identified, this was achieved through stainless steel tubing. Four strain gauges (SG) – two per side – were mounted to the rebar (surfaces grinded smooth) as the verification method for strain measurements during prototype testing.

3.6.2 Temperature Sensor Calibration

A temperature calibration test was carried out on the polyimide coated fiber, referred to as TCal sensor, configured in the same manner as the T DOS in order to determine the relationship between measured strain and change in temperature (Figure 3-17).

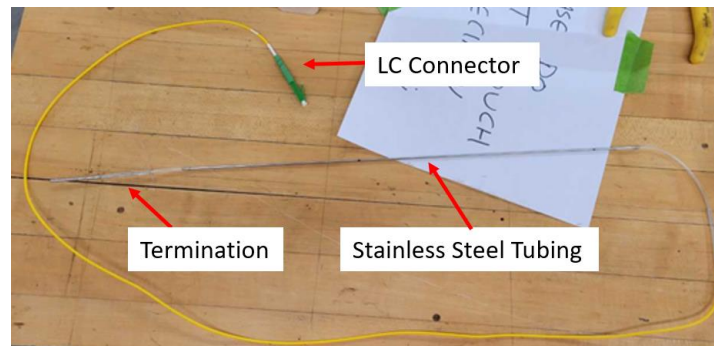


Figure 3-17. TCal sensor used for temperature calibration testing

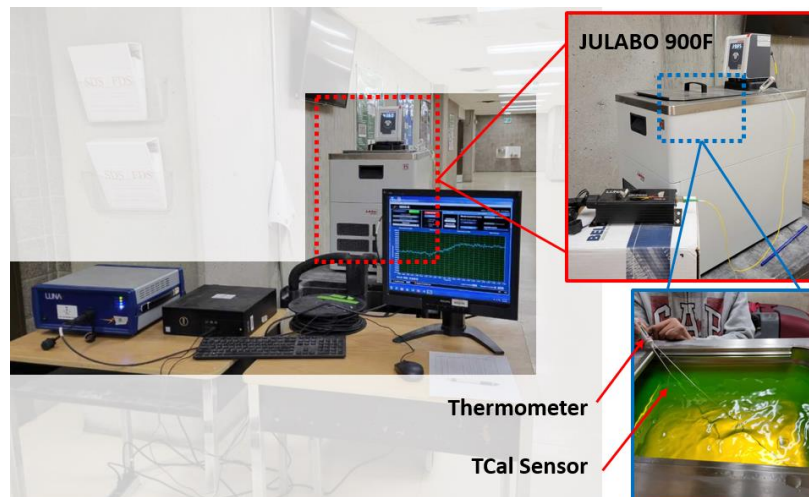


Figure 3-18. Temperature sensor calibration setup – Glycol bath

A JULABO 900F machine was used for the calibration with the TCal sensor and an independent thermometer placed in the glycol bath, as seen in Figure 3-18. A Traceable® Extra-Long-Stem thermometer was used to monitor the temperature of the glycol bath as it had been noted by other students that the machine's temperature display was not always accurate. The temperature of the glycol bath was first set to -20°C and increased at 5°C increments until 50°C, the strain measurements were recorded for each stage. The calibration range covered the experimental temperature range for this project. The calibration result had an average slope of 8.49 $\mu\epsilon/^\circ\text{C}$ (Figure 3-19).

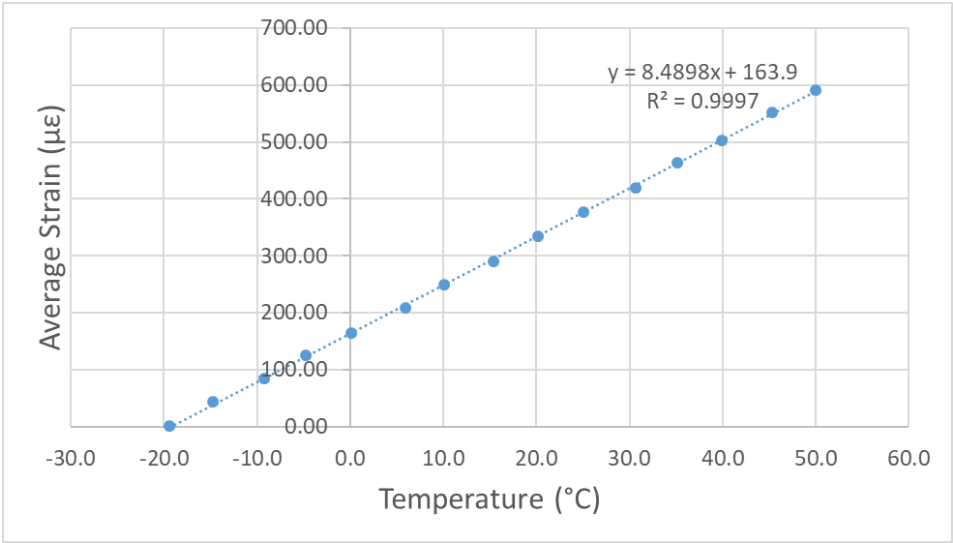


Figure 3-19. Relationship of strain and temperature (Guo et al, 2023)

3.6.3 Temperature DOS Verification

A tensile test of the prototype was setup according to Figure 3-20 in order to verify the new DOS configurations and material properties of the rebar bolt. The DOS are connected to a Luna ODiSi-B Analyzer; one analyzer (single channel) was available at the time so the T DOS and ϵ DOS were tested separately. The T DOS was verified first with the data collection rate at 2 Hz and the MTS loading rate at 1 mm/min.

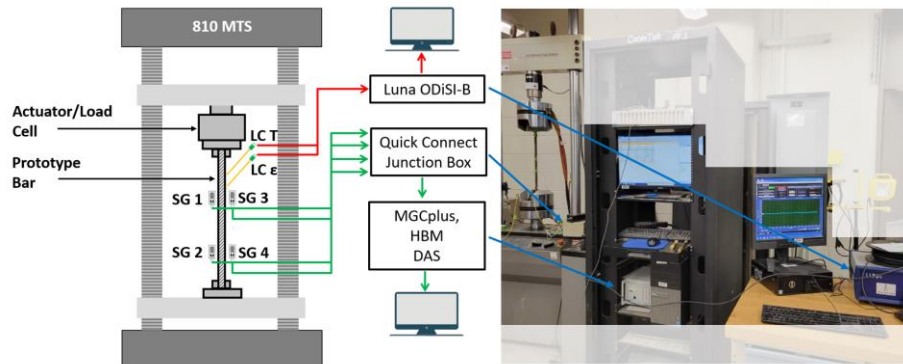


Figure 3-20. Testing and monitoring setup for prototype testing (Guo et al, 2023)

The prototype was loaded to $0.45F_y$ (54.5 kN) in order to remain within the elastic zone. Figure 3-21 shows that the strain profiles of the T DOS at different stages of rock bolt loading are similar – the average strain at start test was $0.0\mu\epsilon$, at mid test $1.2\mu\epsilon$, and at end test $1.7\mu\epsilon$ – well within the $\pm 25\mu\epsilon$ uncertainty of the data collector. The test confirmed that the T DOS configuration and embedment method using stainless steel tubing to de-bond the fiber was successful as the sensor did not respond to loading. At the end of test and the loading was stopped, a heat gun was applied to the prototype and observations were made in real-time of the localized strain profile changes due to the applied heat (Figure 3-22). The testing confirmed that the T DOS configuration isolated strain sensing to temperature change. The prototype was unloaded after testing ended.

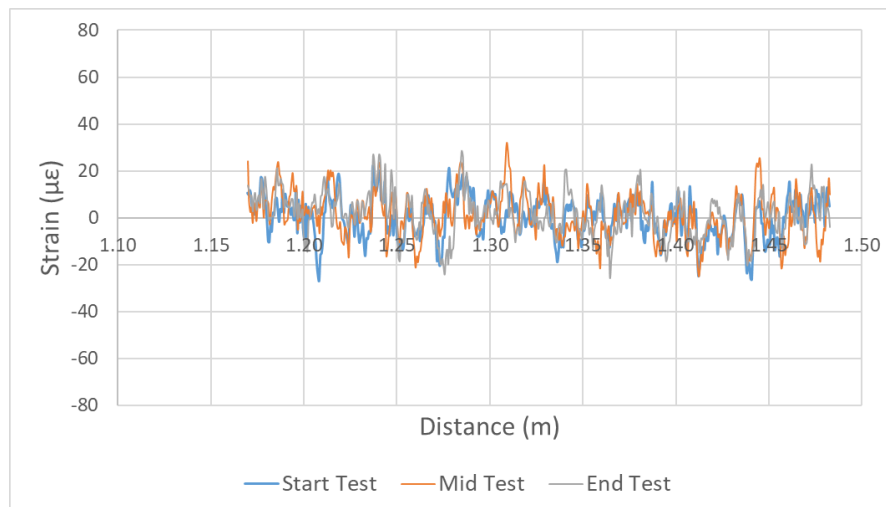


Figure 3-21. Strain profile of T DOS at different stages of prototype loading (Guo et al, 2023)

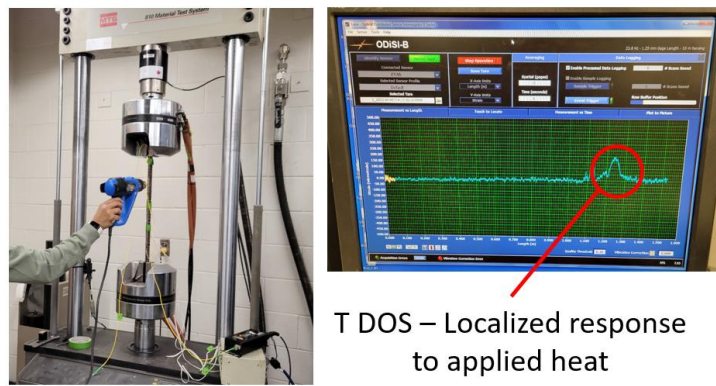
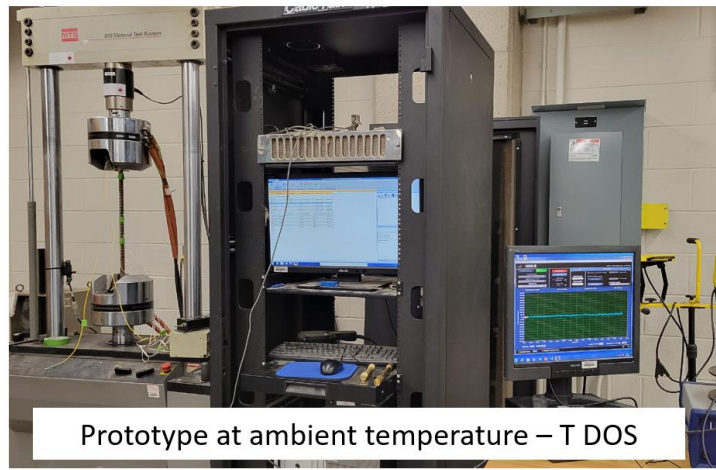


Figure 3-22. T DOS response to applied heat source

3.6.4 Strain DOS Verification and Rebar Bolt Properties

The ϵ DOS verification was the same setup with the data collection rate at 2 Hz and the MTS loading rate at 1 mm/min and later increased to 2 mm/min. The initial plan was to confirm the yield strength and ultimate strength of the rebar thus loading the prototype to rebar fracture. However, the maximum machine stroke was reached at 162.4 kN so the test was ended prior to rebar failure. Figure 3-23 includes snapshots of the strain profiles along the entire fiber (i.e. both sides of the rebar) at various loads. The strains were quite symmetrical about the loop indicating that axial loading during testing did not result in any significant bending.

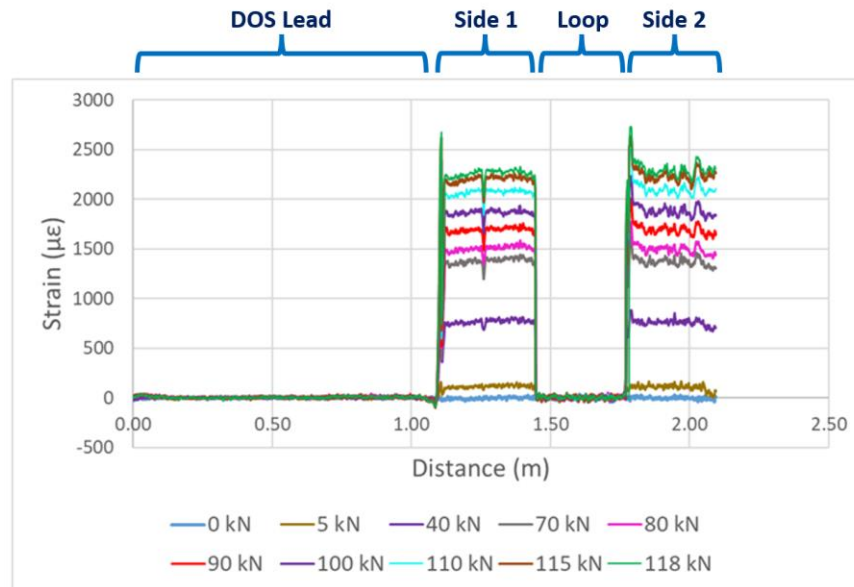


Figure 3-23. Strain profile of ϵ DOS at different loads along entire fiber length (Guo et al, 2023)

The ϵ DOS failed as the rebar bolt yielded at 120 kN and the yield strength was found to be 460 MPa. The result was within literature range for 400W rebar and comparative to results of 470-480 MPa from Moore (2021). Although the maximum machine stroke stopped the testing, later during FGRB specimen pull-out testing the rebar fractured at an average load of 172 kN with an ultimate strength of 658 MPa. The Modulus of Elasticity (E) was found to be 200.00 GPa using results of the ϵ DOS (Figure 3-24), which is comparable to literature values for mild steel. The strain measurements of the polyimide fiber were verified using four SG mounted to the rebar. Comparisons were made of the DOS measured strains at the location of the SGs seen in Figure 3-25 and Table 3-10. The percent difference of DOS strains were small when compared to SG 1 and SG 4, with larger differences with SG 2 and SG 3. This was likely a result of SG misalignment when mounted to the rebar. The Modulus of Elasticity was calculated from the results of each SG (Figure 3-26) and found in Table 3-11. The comparison of the Modulus of Elasticity found that SG 2 and SG 3 results were less accurate compared to SG 1 and 4, thus, they likely had some misalignment.

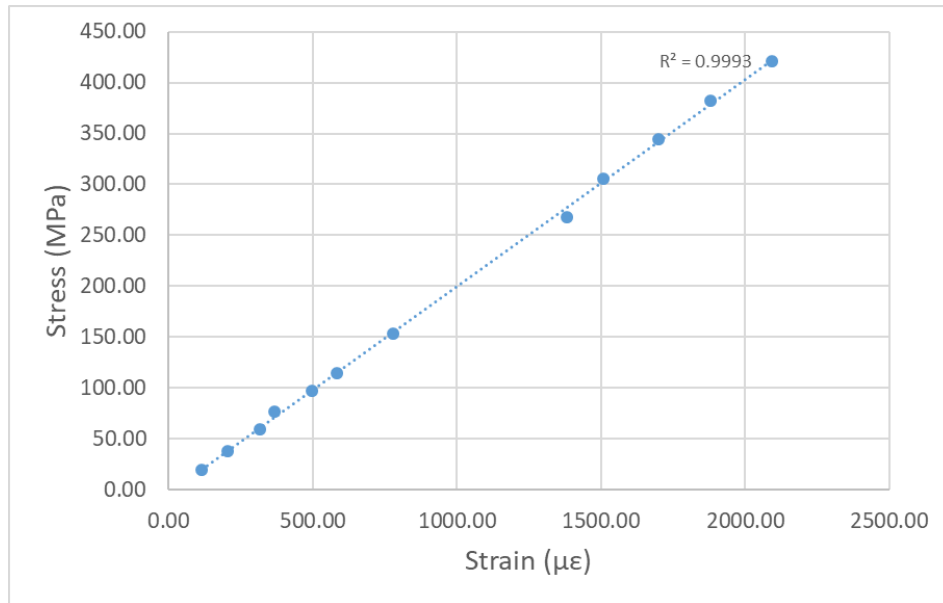


Figure 3-24. Stress vs strain – ϵ DOS

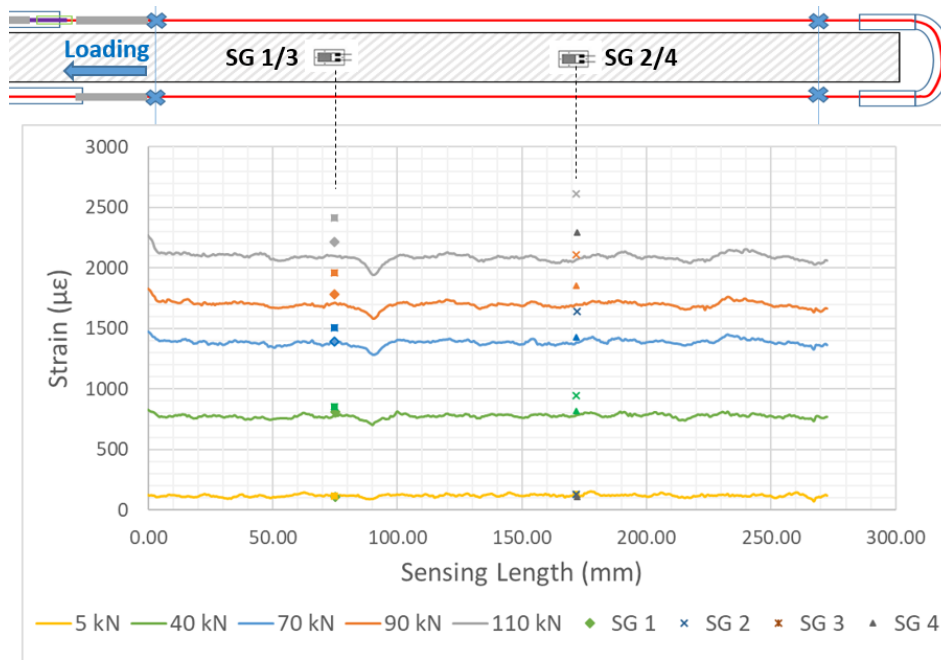


Figure 3-25. Strain profile ϵ DOS and SG (Guo et al, 2023)

Table 3-10. Comparison of strain measurements between ϵ DOS and SG (Guo et al, 2023)

Load (kN)	% Difference from ϵ DOS			
	SG 1	SG 2	SG 3	SG 4
5	10.20%	2.46%	6.85%	13.90%
40	2.74%	16.49%	7.50%	1.32%
70	0.64%	15.57%	8.45%	1.41%
90	3.99%	20.14%	13.46%	7.21%
110	4.23%	21.70%	13.05%	8.85%

Figure 3-26. Load vs strain in elastic zone – SG

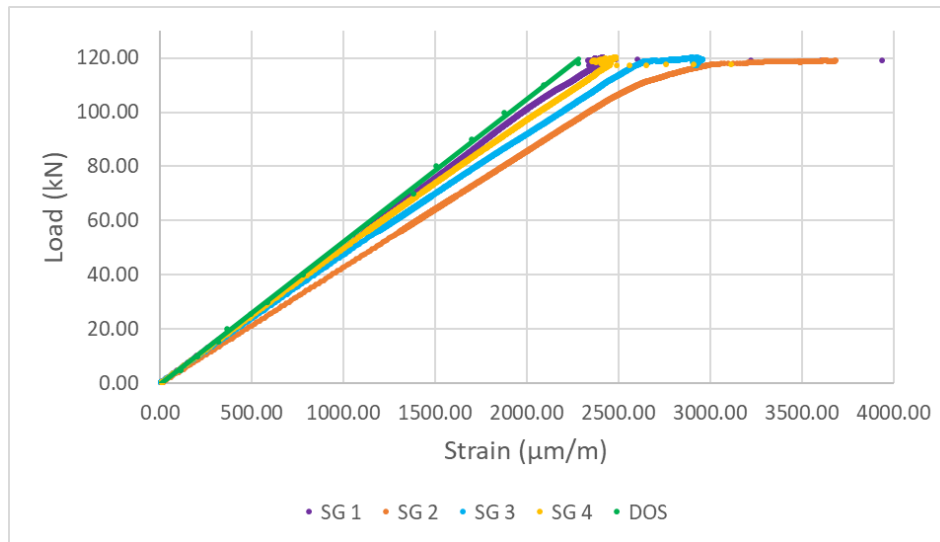


Table 3-11. Modulus of Elasticity results (modified after Guo et al, 2023)

SG 1	SG 2	SG 3	SG 4	DOS
E (GPa)	E (GPa)	E (GPa)	E (GPa)	E (GPa)
200.00	160.00	170.83	200.00	200.00

Avg. (SG 1/3) E = 185.42
 Avg. (SG 2/4) E = 180.00

¹ Averages of strain gauges at same distance on opposite sides of rebar

Although the polyimide fiber had a significantly improved transition section for strain pickup (as detailed previously) and accurate strain measurements, the brittleness and large external loop resulted in reconsideration for the use of the polyimide fiber for strain sensing. The loop would be a weak point during handling and setup. Thus for the test specimens, the previous group member's acrylate fiber was continued to be used for the ϵ DOS and the polyimide fiber was introduced for the T DOS since it was a single line.

3.7 Confinement Material

As discussed in the previous chapter, the capacity of FGRB generally has a positive correlation with the radial confinement pressure of the surrounding rock. Materials such as steel, aluminum, concrete, and PVC are commonly used to replicate the rock by providing a similar confinement pressure. In this investigation, a granitic rock was chosen as the surrounding rock type for the FGRB specimen. According to Hyett et al. (1992), thick wall cylinder theory (Equation 6) can be used to find the radial stiffness (K_r) of pipes. A series of calculations were made for commercially available steel pipes by schedule and size in order to select a suitable pipe to provide granite-like confinement pressure of around 3000 MPa/mm.

$$K_r = \frac{2E}{(1+\nu)} \left\{ \frac{d_o^2 - d_i^2}{d_i[(1-2\nu)d_i^2 + d_o^2]} \right\} \quad (6)$$

Past group members have found that selected pipes failed by crushing near the top bearing plate during testing (confinement setup schematic seen in Figure 3-27). A 1/2" grouting hole was drilled into each pipe near the top of the pipe (methodology discussed in next chapter) reduced the strength of the pipes at the grouting location. The top portion of the pipe experienced the most stress as the pull-out test rig had the load applied from the top and was vital for the transfer of load in the FGRB specimens to the confinement material given the exponential decay of the stress profiles. Initially, the selected confining medium was a schedule 40 steel 1" nominal pipe. An optimal location of the grouting holes was assessed to confirm that the pipe would not fail at higher loads due to the reduced pipe area and balance grouting requirements. The strain profile from the most similar sized pipe used by Moore (2021) was taken to find the probable stresses at different distances along the pipe. However, during test mock-up rehearsals it was

discovered that the pipe diameter could partially fit through the base plate holes. Options were discussed including welding an additional section of pipe or washer onto the top/bottom portions of the confinement pipe. Ultimately, it was decided to increase the confinement pipe to schedule 80 steel 1½" nominal pipe, which has a similar K_r and a larger outside diameter. The location of the grouting hole was set at 80 mm from top of pipe.

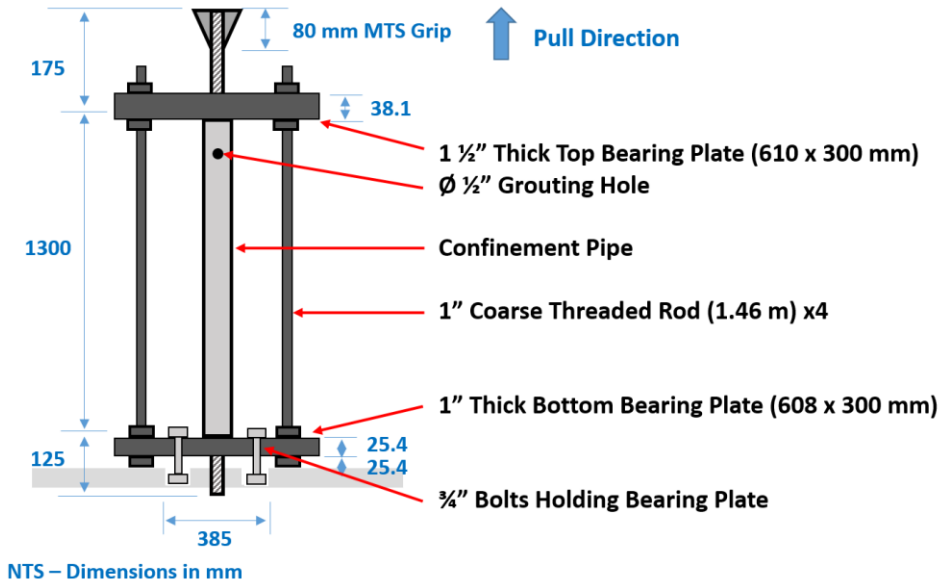


Figure 3-27. Test confinement rig

3.8 Cement Grouts

As discussed in Section 3.3, two types of cement grouts were utilized for the FGRB specimen preparation – PC at 0.4 w/c ratio and Nordic at 0.29 w/c ratio – to span the wide spectrum of test temperatures. Grout strength testing was conducted for all specimen in order to quantify the grout properties for each FGRB over time and under each curing condition. The cylinders were cast at the same time as the grouting of the FGRB specimens. Due to the setting rate and limited working time of Nordic, the grout was batched per FGRB specimen and their corresponding grout cylinders. The same preparation was made for Nordic and PC grouts in order to maintain consistency. Time was recorded (Table 3-12) from start of mixing to end

of grouting per specimen in order to confirm working time was within the allowable limit of Nordic TDS (max 20 minutes) and general consistency between batches.

The number of cylinders per specimen are found in Table 3-13. Due to the total supply of Nordic grout available, cylinder numbers were adjusted with fewer in the longer-term curing durations as strength was expected to become more stable with time. Naming convention for each condition with 'P' for permafrost, 'C' for control, and 'G' for geothermally active followed by the temperature. i.e. P20 denotes permafrost (cold) condition at -20°C.

Table 3-12. Summary of grouting times

Simulated Condition (Naming Convention)	Temperature (°C)	Grout Type	Grouting Time (mins)
Permafrost (P20)	-20	Nordic	8-12
Permafrost (P5)	-5	Nordic	7-8
Control (C20)	20	PC	13-18
Geothermal (G45)	45	PC	12-15

Table 3-13. Summary of total grout test cylinders

Simulated Condition	Curing Duration (days)	No. of UCS Cylinders	No. of STS Cylinders
P20	3	3	2
	7	3 ¹	2
	28	3	2
	35	3	2
	60	2	2
	90	2	2
P5	3	3	2
	7	3	2
	28	3	2
	35	2	2
	60	2	2
	90	2	2

Simulated Condition	Curing Duration (days)	No. of UCS Cylinders	No. of STS Cylinders
C20	3	3	3
	7	3	3
	28	3	3
	35	3	3
	60	3	3
	90	3	3
G45	3	3	3
	7	3	3
	28	3	3
	35	3	3
	60	3	3
	90	3	3

¹ Reduced to 2 during testing as one cylinder could not be removed from mould

Following the experiences and lessons learned from the grout baseline study, the mixing buckets, tools, and moulds were conditioned to temperature in the curing chambers at least 48 hours prior to grouting. The mixing of the grout was conducted outside of the chamber using a hand mixer and grouting was completed inside the chambers. Figure 3-28 shows the grouting materials and tools. The cylinders were produced in accordance with ASTM C470 (ASTM, 2015) and ASTM C192 (ASTM, 2019) casted in 100mm \varnothing x 200mm L moulds in two layers, consolidated using vibration from a Sawzall with the blade removed (same method as FGRB specimen grouting).



Figure 3-28. Water-cement mixing and cleaned/oiled moulds

The casted cylinders, seen in Figure 3-29, remained in the moulds for the curing duration, except for P20 cylinders as the moulds were required for re-use to cast P5 cylinders. The cylinders were removed from the moulds and prepared 24 hours prior to testing for short duration curing times and 2-4 days prior to testing for long duration curing times. As recommended in Li et al (2017b), extra care was made to prevent excess evaporation during grout curing in the G45 chamber using vapour barrier sheets. The grinding method detailed in Section 3.3 was employed. The cylinders were inspected post-test and no significant voids were discovered (example seen in Figure 3-30).

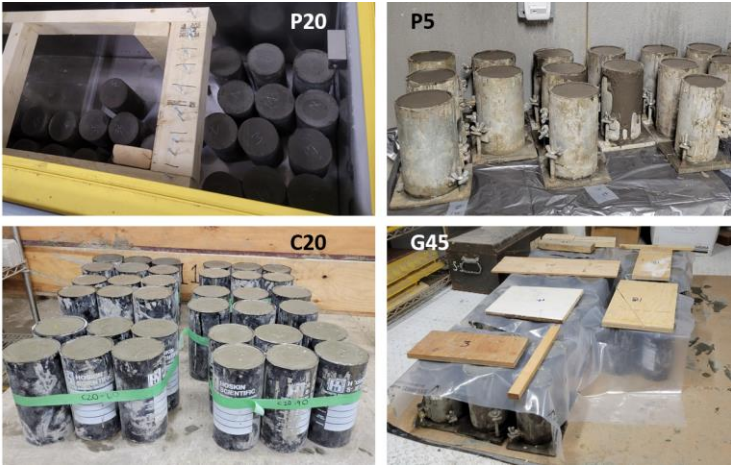


Figure 3-29. Grout cylinders in each curing condition



Figure 3-30. Split cylinders of PC at 0.4 w/c ratio and Nordic at 0.29 w/c ratio

The testing age tolerances from ASTM C39 (ASTM, 2021), as seen in Figure 3-31, were followed for FGRB pull-out testing and corresponding UCS and STS testing. The times for end of grouting and start of each test’s series were recorded. Some deviations from the tolerances were noted due to qualified personnel availability to operate testing machines and coordination for efficient use of machines once configured for each test. A summary of the timings and any deviations outside of age tolerances for curing conditions P20, P5, C20, and G45 are listed in Table 3-14, Table 3-15, Table 3-16, and Table 3-17, respectively.

Test Age ^A	Permissible Tolerance
24 h	±0.5 h
3 days	±2 h
7 days	±6 h
28 days	±20 h
90 days	±2 days

^AFor test ages not listed, the test age tolerance is ±2.0% of the specified age.

Figure 3-31. Test age tolerances for compressive tests (ASTM, 2021)

Table 3-14. Summary of test ages – P20

P20 – Curing Time (days)	Grout Time (HH:MM)	UCS Test Time (HH:MM)	STS Test Time (HH:MM)
3 ¹	10:58	14:51	15:29
7	10:30	14:20	15:05
28	10:00	16:05	16:58
35	12:26	11:22	13:26
60	11:40	13:33	15:25
90	11:12	11:07	9:25

¹ UCS and STS test time were outside of ±2 hour ASTM C39 (ASTM, 2021) tolerance

Table 3-15. Summary of test ages – P5

P5 – Curing Time (days)	Grout Time (HH:MM)	UCS Test Time (HH:MM)	STS Test Time (HH:MM)
3 ¹	9:29	13:42	13:25
7	9:44	11:17	10:51
28	9:59	10:04	9:44
35	10:13	10:07	9:52
60	10:28	12:33	12:22
90	10:42	10:30	10:04

¹ UCS and STS test time were outside of ±2 hour ASTM C39 (ASTM, 2021) tolerance

Table 3-16. Summary of test ages – C20

C20 – Curing Time (days)	Grout Time (HH:MM)	UCS Test Time (HH:MM)	STS Test Time (HH:MM)
3 ¹	14:35	11:42	15:13
7	15:08	14:46	15:21
28	15:47	15:07	16:33
35	16:16	10:33	13:01
60	16:49	13:06	15:08
90	17:20	11:23	9:08

¹ UCS test time outside of ±2 hour ASTM C39 (ASTM, 2021) tolerance

Table 3-17. Summary of test ages – G45

G45 – Curing Time (d)	Grout Time (HH:MM)	UCS Test Time (HH:MM)	STS Test Time (HH:MM)
3 ¹	9:40	11:28	14:50
7	10:11	12:59	11:03
28	10:40	9:58	11:09
35	11:03	10:12	11:02
60	11:30	10:24	11:00
90	12:00	10:08	9:52

¹ STS test time outside of ±2 hour ASTM C39 (ASTM, 2021) tolerance

3.8.1 Compressive Strength, Modulus of Elasticity, and Poisson's Ratio

The UCS testing detailed in Section 3.3.1 for the baseline study was conducted for each FGRB specimen grout cylinders to determine the compressive strength of the grout. The testing was carried out on a 300,000 lbs RIEHLE Testing Machine following the guidelines of ASTM C39 (ASTM, 2021). The measured compressive strength results for each series of cylinders were not all within the precision ranges as outlined in the standard. It was noted that the ASTM range corresponds to UCS between 17-35 MPa; generally the compressive strength results were higher. Thus judgements were made in excluding any significant outliers or including based on trend and a slightly bigger acceptance range. Results of the UCS tests for each grout cylinder and temperature condition are found in Table 3-18 through Table 3-21. The densities between cylinders in the same curing conditions were comparable thus there is confidence of consistency between batching and consolidation processes. Care was taken to reduce specimen temperature changes during testing. The cylinders were kept inside their curing chambers (P20, C20, and G45 chambers were adjacent to the testing location) and removed one at a time for measurements followed by immediate testing. For the P5 cylinders, the freezer was further away thus the cylinders were transported and temporarily stored inside a thermally insulated container with ice from the curing chamber. The container was also conditioned inside the chamber prior to movement.

The average UCS results in each curing condition were plotted against time in Figure 3-33 to obtain the compressive strength development curve. The lines connecting the points in the (b) plot is not for the purpose of interpolation but to be indicative of general trends between the conditions and make observations easier. In P5 and C20 conditions, the strength development increased consistently with time as can be expected since these temperatures are in the optimal range for Nordic and PC. At the cold extreme, strength significantly decreased from P5 to P20 in all curing time durations. This was expected as Nordic grout was designed for conditions up to -10°C and the UCS results on the TDS show that strength decreased from -5°C to -10°C. There was an extreme dip in strength at 28-day cure for P20, concluded as an anomaly and attributed to the batching process. P20-28 was the first mixture made for this project and the grout began to set as the cylinders were being grouted. Improvements were made for subsequent Nordic batches by continuing to slowly mix the grout during entire work time (which was advised in the TDS). Observations of pre-mature cracking and oozing mixture at the bases

were made for all three cylinders (Figure 3-32) that were not seen in any other tests. On the hot extreme, the initial strength gain for G45 was higher than that of C20. Overtime, the strength development was not stable under the high heat conditions. The trend of both extremes (P20 and G45) had strength decrease at the longest curing duration.

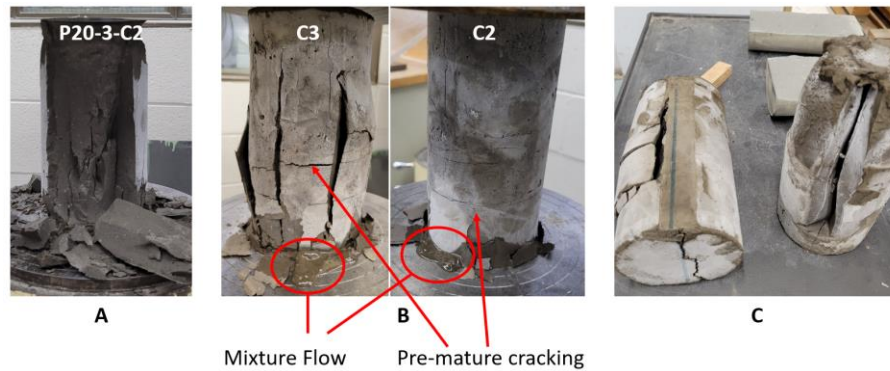


Figure 3-32. P20-28 UCS observations: A. Typical P20 cylinder test; B. P20-28 C2 and C3 during testing; C. P20-28 cylinders post-test

Improvements were made to the procedures as testing progressed. The cylinder bases were observed to begin thawing during UCS tests as they sat directly over the motor and tests could take upwards of 15-20 minutes to reach failure. In order to reduce the temperature changes to the grout cylinders, an additional base steel plate was added that had been conditioned in the freezers prior to testing (Figure 3-34). It was also later discovered that a DAQ could be connected to the RIEHLE Testing Machine thus load readings for subsequent tests were made using the DAQ rather than the dial gauges, seen in Figure 3-35.

Table 3-18. Summary of UCS Results – P20

Specimen	Density (kg/m ³)	Compressive Strength (MPa)	Failure Mode	Notes
P20-3-C1	2149.3	38.6	Type 3	
P20-3-C2	2138.7	41.2	Type 3	
P20-3-C3	2140.6	44.7	Type 3	
P20-7-C1	2157.9	40.4	Type 3	
P20-7-C2	2149.0	31.8	Type 3	
P20-7-C3	-	-	-	Unable to unmould
P20-28-C1	2111.6	18.0	Type 3	Mixture oozed out
P20-28-C2	2121.9	15.4	Type 3	Mixture oozed out
P20-28-C3	2115.4	11.2	Type 3	Mixture oozed out
P20-35-C1	2121.8	39.7	Type 3	Omit / Uncharacteristically high
P20-35-C2	2118.9	28.3	Type 3	
P20-35-C3	2131.5	28.3	Type 3	
P20-60-C1	2170.0	50.2	Type 3	
P20-60-C2	2141.5	42.1	Type 3	
P20-90-C1	2151.8	22.5	Type 3	
P20-90-C2	2133.9	55.5	Type 3	

Table 3-19. Summary of UCS Results – P5

Specimen	Density (kg/m ³)	Compressive Strength (MPa)	Failure Mode	Notes
P5-3-C1	2154.7	42.8	Type 3	
P5-3-C2	2155.3	40.1	Type 3	
P5-3-C3	2167.2	47.1	Type 3	
P5-7-C1	2153.8	50.8	Type 3	
P5-7-C2	2151.3	58.1	Type 3	
P5-7-C3	2140.3	55.7	Type 3	
P5-28-C1	2193.1	65.6	Type 1	

Specimen	Density (kg/m³)	Compressive Strength (MPa)	Failure Mode	Notes
P5-28-C2	2175.7	50.9	Type 3	
P5-28-C3	2182.2	43.4	Type 3	
P5-35-C1	2199.2	68.4	Type 3	
P5-35-C2	2171.7	48.3	Type 3	
P5-60-C1	2188.0	60.0	Type 1	
P5-60-C2	2195.3	55.6	Type 3	
P5-90-C1	2199.8	61.0	Type 3	
P5-90-C2	2221.0	66.2	Type 3	

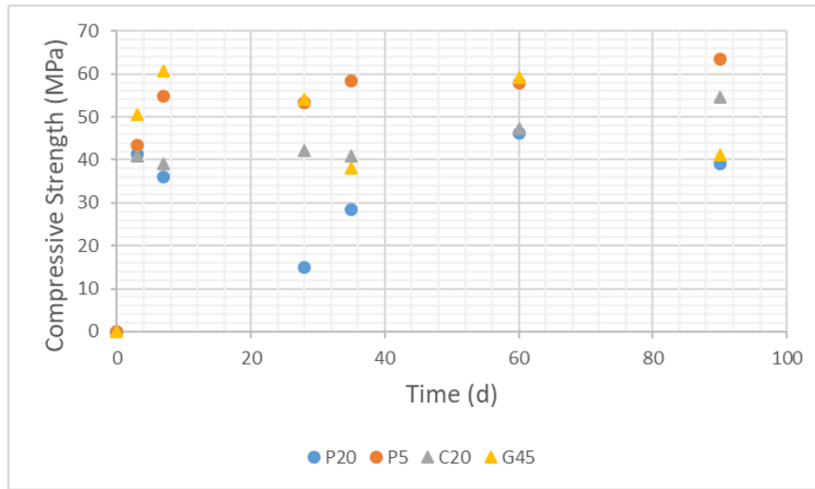
Table 3-20. Summary of UCS Results – C20

Specimen	Density (kg/m³)	Compressive Strength (MPa)	Failure Mode	Notes
C20-3-C1	1977.8	36.4	Type 3	
C20-3-C2	1982.8	43.6	Type 3	
C20-3-C3	1978.5	42.7	Type 3	
C20-7-C1	1993.7	49.7	Type 3	
C20-7-C2	1984.2	36.3	Type 3	
C20-7-C3	1983.2	41.9	Type 3	
C20-28-C1	2038.3	37.2	Type 3	
C20-28-C2	2029.3	47.8	Type 3	
C20-28-C3	2085.4	41.7	Type 3	
C20-35-C1	1991.6	45.6	Type 3	
C20-35-C2	1991.7	39.5	Type 3	
C20-35-C3	1997.9	37.3	Type 3	
C20-60-C1	1988.6	46.1	Type 3	
C20-60-C2	1995.7	41.0	Type 3	
C20-60-C3	1971.0	54.3	Type 3	
C20-90-C1	2003.6	51.1	Type 3	
C20-90-C2	2029.6	55.1	Type 3	

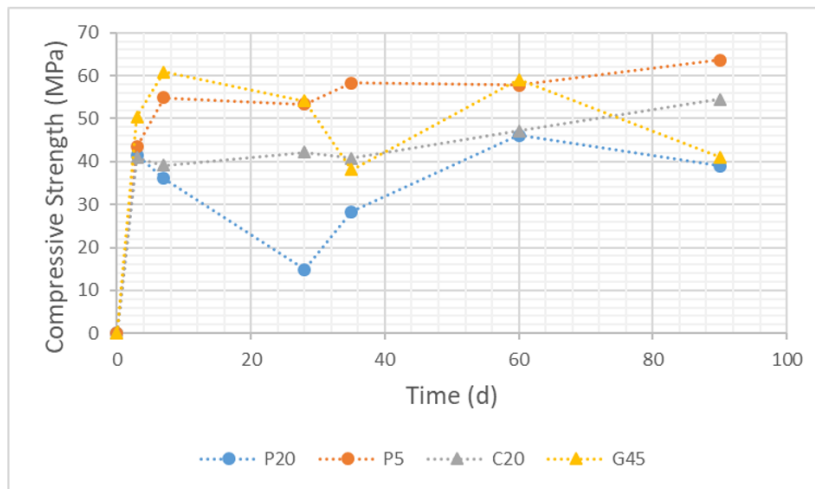
C20-90-C3	2023.0	57.4	Type 3
-----------	--------	------	--------

Table 3-21. Summary of UCS Results – G45

Specimen	Density (kg/m ³)	Compressive Strength (MPa)	Failure Mode	Notes
G45-3-C1	1975.2	47.8	Type 3	
G45-3-C2	1982.2	51.4	Type 1	
G45-3-C3	1980.9	52.0	Type 3	
G45-7-C1	2005.5	63.3	Type 3	
G45-7-C2	1985.6	58.3	Type 3	
G45-7-C3	2001.7	60.7	Type 3	
G45-28-C1	1943.0	53.2	Type 3	
G45-28-C2	1943.0	54.1	Type 3	
G45-28-C3	1970.6	55.0	Type 3	
G45-35-C1	1943.3	36.4	Type 3	
G45-35-C2	1939.8	38.1	Type 3	
G45-35-C3	1949.9	40.0	Type 3	
G45-60-C1	1922.0	66.6	Type 3	
G45-60-C2	1931.1	60.7	Type 3	
G45-60-C3	1929.8	49.9	Type 3	
G45-90-C1	1951.3	54.7	Type 3	Omit / Uncharacteristically high
G45-90-C2	1945.6	43.3	Type 3	
G45-90-C3	1965.7	38.7	Type 3	



(a)



(b)

Figure 3-33. Grout compressive strength development over 90 days for each curing condition: (a) Points only; (b) Points and connecting lines

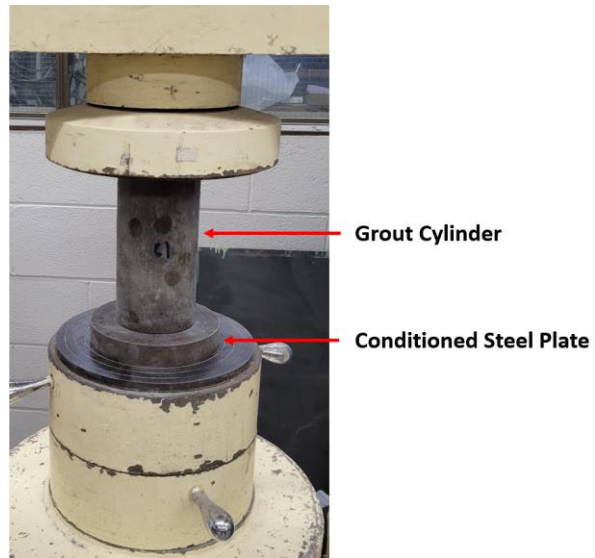


Figure 3-34. UCS testing setup including conditioned steel plate

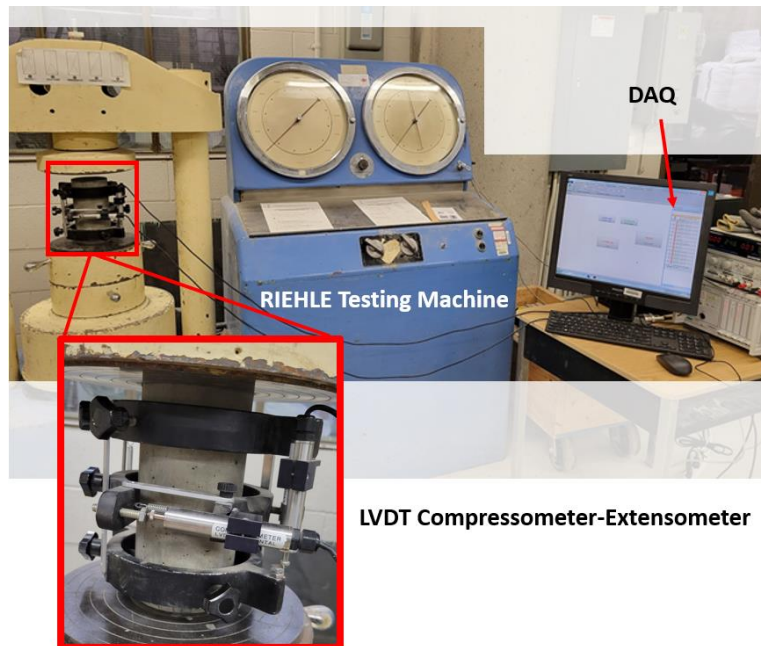


Figure 3-35. Setup for grout Modulus of Elasticity and Poisson's Ratio testing

The Young's Modulus and Poisson's Ratio were obtained for each temperature condition at 28-day and 35-day cure durations following ASTM C469 (ASTM, 2022) at the same loading rate as the UCS tests, results seen in Table 3-22. The setup, found in Figure 3-35, had a LVDT compressometer-extensometer mounted to the grout test cylinder to monitor vertical and horizontal displacements during three load-unload cycles to 40% of ultimate strength. The load for the first tests were recorded by hand at set time increments until it was found that the DAQ could also be connected to the testing machine. P20-28 was not tested due to the premature cracking and failure of the grout cylinders under compression, which made it unfeasible to use the testing rig. The results of Young's Modulus are comparable for PC grout at 0.4 w/c ratio cured for 28 days in Moore (2021), although G45-35 was uncharacteristically high. The results of Poisson's Ratio are significantly higher than typical values for cement, with some specimens being higher than the possible ν range. Thus, the values obtained for Poisson's ratio are not considered accurate. Some problems were encountered with the horizontal LVDT when calibrating and zeroing; it was found that the LVDT had lower sensitivity to change and would not completely zero. When tested, the LVDT seemed to be functioning and reacting properly. But post-processing revealed the problems with the horizontal LVDT.

Table 3-22. Summary of Modulus of Elasticity and Poisson's Ratio of Grout Cylinders

Specimen	Average Young's Modulus, E (GPa)	Average Poisson's Ratio, ν	Notes
P20-28	-	-	Unable to test
P20-35	18.6	0.58	ν outside of possible range
P5-28	14.5	1.89	ν outside of possible range
P5-35	16.7	0.42	ν uncharacteristically high for cement
C20-28	11.2	0.36	ν uncharacteristically high for cement
C20-35	10.0	0.40	ν uncharacteristically high for cement
G45-28	11.6	0.47	ν uncharacteristically high for cement
G45-35	15.7	1.04	ν outside of possible range

3.8.2 Tensile Strength

The STS testing detailed in Section 3.3.2 for the baseline study was conducted for each FGRB specimen grout cylinders to determine the tensile strength of the grout. The testing was carried out on a 300,000 lbs RIEHLE Testing Machine following the guidelines of ASTM C496 (ASTM, 2017). The plywood strips were changed throughout testing. Care was taken to reduce specimen temperature changes. Cylinder thawing during STS testing was not as much a concern as the tests were generally between 2-5 minutes. Results of the STS tests for each grout cylinder and temperature condition are found in Table 3-23 through Table 3-26. Judgements were made to include or exclude results based on precision tolerances slightly larger than ASTM standard and trend of data. The average STS results in each curing condition were plotted against time in Figure 3-36 to obtain the tensile strength development curve. The lines connecting the points in the (b) plot is not for the purpose of interpolation but to be indicative of general trends between the conditions and make observations easier. The development was not consistent throughout for all conditions, however, generally Nordic (P20 and P5) performed better than PC under tension (C20 and G45).

Table 3-23. Summary of STS results – P20

Specimen	Density (kg/m³)	Tensile Strength (MPa)	Notes
P20-3-S1	2154.5	6.9	
P20-3-S2	2157.5	4.6	
P20-7-S1	2129.4	4.8	
P20-7-S2	2149.0	4.9	
P20-28-S1	2108.7	3.8	
P20-28-S2	2125.1	3.6	
P20-35-S1	2109.6	6.9	
P20-35-S2	2124.3	5.2	
P20-60-S1	2155.1	4.1	
P20-60-S2	2121.8	3.3	
P20-90-S1	2158.1	4.3	
P20-90-S2	2164.6	3.5	

Table 3-24. Summary of STS results – P5

Specimen	Density (kg/m ³)	Tensile Strength (MPa)	Notes
P5-3-S1	2168.4	4.0	
P5-3-S2	2152.8	3.6	
P5-7-S1	2177.1	4.7	
P5-7-S2	2136.8	3.8	
P5-28-S1	2171.0	5.7	
P5-28-S2	2152.5	5.3	
P5-35-S1	2176.6	4.8	
P5-35-S2	2187.9	3.5	
P5-60-S1	2191.9	5.2	
P5-60-S2	2190.7	6.3	
P5-90-S1	2184.7	4.4	
P5-90-S2	2190.9	6.4	

Table 3-25. Summary of STS results – C20

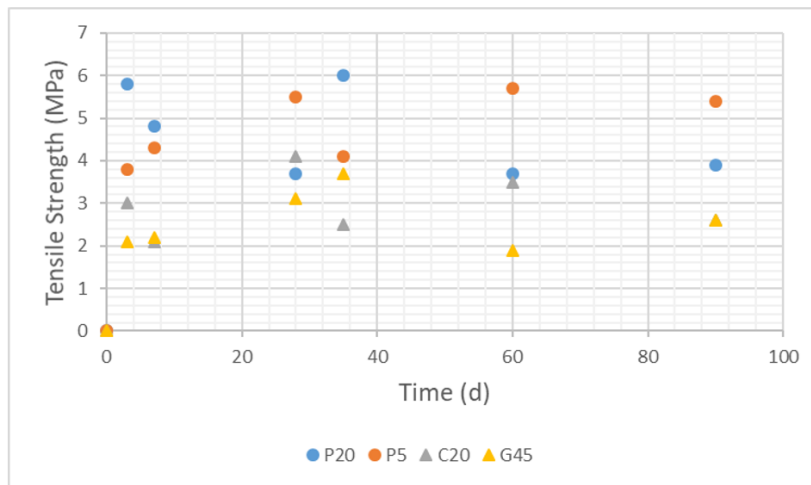
Specimen	Density (kg/m ³)	Tensile Strength (MPa)	Notes
C20-3-S1	1982.4	4.0	Omit / Uncharacteristically high
C20-3-S2	1981.7	2.8	
C20-3-S3	1977.4	3.2	
C20-7-S1	1974.7	4.8	Omit / Uncharacteristically high
C20-7-S2	1963.6	2.1	
C20-7-S3	1965.2	2.2	
C20-28-S1	2033.7	4.4	
C20-28-S2	2071.6	2.6	
C20-28-S3	2063.6	5.4	
C20-35-S1	1992.9	2.2	

Specimen	Density (kg/m³)	Tensile Strength (MPa)	Notes
C20-35-S2	1975.1	2.2	
C20-35-S3	1993.4	3.0	
C20-60-S1	1976.9	1.8	Omit / Uncharacteristically low
C20-60-S2	1988.7	3.0	
C20-60-S3	1991.6	4.0	
C20-90-S1	2015.8	2.2	
C20-90-S2	2026.2	2.9	
C20-90-S3	2006.3	2.8	

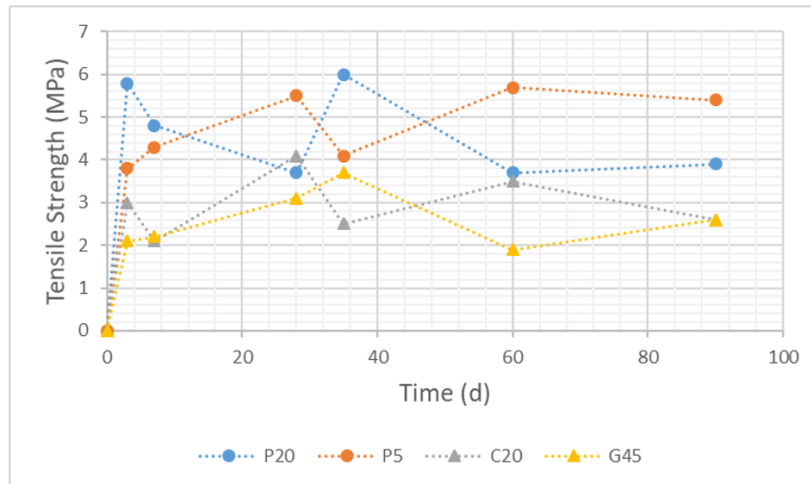
Table 3-26. Summary of STS results – G45

Specimen	Density (kg/m³)	Tensile Strength (MPa)	Notes
G45-3-S1	1974.7	1.2	
G45-3-S2	1982.2	2.3	
G45-3-S3	1908.1	2.7	
G45-7-S1	1993.7	4.6	Omit / Uncharacteristically high
G45-7-S2	1980.1	2.0	
G45-7-S3	1973.0	2.4	
G45-28-S1	1958.2	1.3	Omit / Clumpy mixture / Uncharacteristically low
G45-28-S2	1950.7	3.0	
G45-28-S3	1944.3	3.2	
G45-35-S1	1907.8	4.4	
G45-35-S2	1962.7	1.9	Omit / Uncharacteristically low
G45-35-S3	1924.6	3.0	
G45-60-S1	1907.0	3.1	
G45-60-S2	1912.0	0.9	

Specimen	Density (kg/m ³)	Tensile Strength (MPa)	Notes
G45-60-S3	1936.4	1.7	
G45-90-S1	1945.3	2.4	
G45-90-S2	1946.6	3.0	
G45-90-S3	1956.9	2.3	



(a)



(b)

Figure 3-36. Grout tensile strength development over 90 days for each curing condition: (a) Points only; (b) Points and connecting lines

3.9 Chapter Summary

This chapter presented the materials used in this investigation, the selection process, and tests performed to confirm and quantify material properties, including 72 grout UCS tests, 66 grout STS tests, 8 grout E/v, one rebar tensile test, and 3 DOS validation tests. Monitoring instrumentation was confirmed to be operational at the study temperature range. The lessons learned from prototyping and baseline studies were beneficial to improved specimen production procedures. The results from each test (UCS, STS, tensile, and DOS verification) were compared to manufacturer, literature, and/or previous group members' values and were found to be largely similar; results that differed significantly were reasoned and used to improve later testing. Any discrepancies from standard procedures were noted.

4 Utilizing Distributed Fiber Optic Sensors to Investigate the Effects of Permafrost Temperature Conditions on the Axial Response of Fully Grouted Rock Bolts

This chapter consists of the journal article that is planned to be submitted to a peer-reviewed journal. This article describes the methodology and testing scheme, along with presenting selected results of the laboratory testing related to cold temperature curing conditions.

Article

Utilizing Distributed Fiber Optic Sensors to Investigate the Effects of Permafrost Temperature Conditions on the Axial Response of Fully Grouted Rock Bolts

Chuyue (Chelsey) Guo ¹, Kieran Moore ¹ and Nicholas Vlachopoulos ¹

¹ Department of Civil Engineering, Royal Military College of Canada, Kingston, Ontario, K7K7B4, Canada

Abstract: Fully grouted rock bolts are one of the most employed ground support systems in underground mining and civil engineering projects. Industrial demands have pushed under-ground projects deeper and into more extreme environments, such as in Canada's Northern regions, increasing their complexity and potential hazards. Permafrost temperature conditions can potentially affect the performance of the FGRB systems, however, the existing research into these effects are limited. A series of laboratory pull-out tests were conducted on specimens with an 1.3 m overall embedment length in order to observe behaviour changes and study the capacity development of FGRBs in two curing conditions (-20°C and -5°C) utilizing distributed fiber optic technology leveraging Rayleigh Optical Frequency Domain Reflectometry. The cold temperatures proved to be a challenge to grouting FGRBs and affected the grout strength development. The support systems' capacity development stabilized at 35-day in both conditions, however at -20°C, the ultimate capacity remained 10% lower than the specimens cured at -5°C at 90 days.

Keywords: Fully grouted rock bolt; Fiber optic technology; Permafrost; Cold temperature effects; Stress distribution; Pull-out test

4.1 Introduction

Over the course of human history, underground excavations and tunnelling have been essential in cultural and infrastructure advancement. Demands for resources and space, in conjunction with innovations and improvements in ground support techniques, have resulted in more complex projects and expansion into more extreme and demanding conditions. The first use of rock bolts in tunnelling date

back to 1913, with fully grouted rock bolts (FGRBs) becoming one of the most popular forms for rock bolting (Bobet & Einstein, 2011). Rock bolts stabilize the boundaries of the excavation by transferring loads to more stable ground, typically, dealing with axial loads (Pinazzi et al, 2020). The design and employment of ground support systems are a non-trivial pursuit as potential risks include loss of equipment, assets, and human life. An in-depth understanding of these support and reinforcement systems are vital. Although FGRBs have been studied for decades, a full-range of geo-mechanical behaviour and interactions in situ are still not completely understood. This was due in part to spatial resolution limitations of past research monitoring schemes. The state-of-the-art strain monitoring technique utilized herein consists of fiber optic sensors, which has enabled continuous strain profiling and capturing of behaviour at the micro-scale. FGRBs are employed in diverse ground temperature conditions and research into how these conditions affect their performance and behaviour are yet to be extensively studied. This paper presents the methodology, results, and analysis of a full-scale laboratory investigation into the geo-mechanical response of FGRBs in sub-zero conditions.

4.2 Background

Underground civil engineering and mining operations have increased in complexity and have expanded to all areas of the globe in the pursuit of natural resources (minerals, oil/gas, etc.), research (ex. Permafrost Tunnel Research Facility), and human development. More than half of Canada's landmass is covered by continuous and/or discontinuous permafrost, which is any soil or rock that remains frozen for at least two consecutive winter seasons (Jenness, 1949). The coloured regions in Figure 4-1 represent discontinuous and continuous permafrost areas.

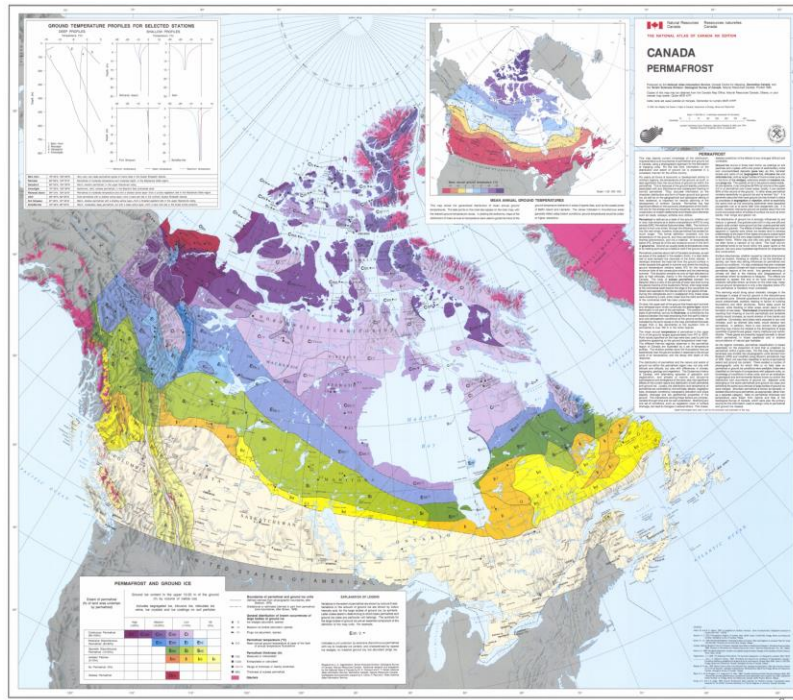


Figure 4-1. Map of continuous and discontinuous permafrost regions in Canada (Natural Resources Canada, 2016)

The Arctic is one of the last fully untapped locations with an abundance of natural resources (NWT & Nunavut Chamber of Mines, 2016), mainly due to limited access and working season. However, with climate change, the North has become more accessible and desirable to various industries and the global community. It would be expected that future activities, especially mining, in these northern areas will increase significantly. Various monitoring stations across the North have recorded deep profiles with sub-zero temperatures up to 400-650 m below ground (Natural Resources Canada, 2016). Thus understanding how the behaviours of underground support elements are affected by cold temperatures will be vital for safe ground support design and underground operations.

Since the 1970's, rock bolting has become one of the most popular types of support in underground engineering and mining operations (Bobet & Einstein, 2011; Li et al, 2011; He et al, 2014). A rock bolt in the most basic form consists of a plain steel rod that is mechanically or chemically anchored into the rock mass on one end and a faceplate and nut on the other (Vlachopoulos et al, 2018). Windsor & Thompson (1993) proposed that the reinforcement systems are comprised of four components and their interactions (Figure 4-2) – the rock, the element,

internal fixture, and external fixture. The element refers to the bolt itself. The external fixture being the faceplate and nut. The internal fixture provides the coupling interaction (Windsor & Thompson, 1993). The grout is typically cement or resin based. The load from the unstable rock near the excavation boundary is transferred to the more stable rock mass at depth (Windsor & Thompson, 1993). FGRBs create a bond between the rock mass and reinforcement element along the entire length of the bolt, providing increased capacity and eliminating the single point of failure on the anchorage side in comparison to mechanically anchored rock bolts.

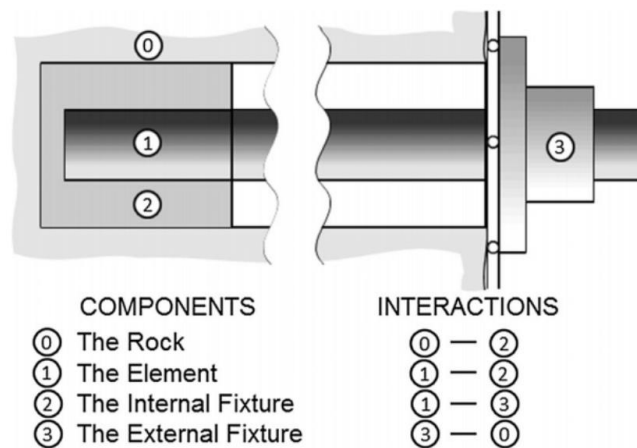


Figure 4-2. Components of rock reinforcement system (Thompson & Villaescusa, 2014)

FGRBs are classified as continuously mechanically coupled and there are three components affecting shear strength at the bolt interface: adhesion, mechanical interlock, and friction. Historical research has found that the effects of adhesion are negligible, and that mechanical interlock is the predominant component for load transfer in FGRBs (Yazici & Kaiser, 1992; Aziz et al, 2006), which transfers load via contact surfaces over its embedment length. The distribution of axial stresses in the bolt and bolt-grout interface resemble an exponential decay curve for full length specimens, while shorter length specimens can resemble linear decay (Serbousek & Signer, 1987). Past studies have found the importance of grout, embedment length, confinement pressure, among other factors on the capacity of FGRBs (Hyett et al, 1992; Kilic et al, 2002; Moosavi et al, 2003; Cruz, 2017; Moore, 2021; Li et al, 2016). Various analytical models have been developed and proposed to improve the understanding and describe the behaviours of FGRBs (Yazici & Kaiser, 1992;

Farmer, 1975; Benmokrane et al, 1995; Li & Stillborg, 1999; Cai et al, 2004; Ren et al, 2010; Ma et al, 2013). However, a full range understanding of the geo-mechanical response of FGRBs still does not exist due in part to past technological limitations of monitoring instrumentation and mainly a lack of spatial resolution. Initial studies measured the load and displacement at the borehole collar (i.e. a singular point) using a load cell and dial gauge/LVDT. The rocks where FGRBs are installed can be anisotropic and/or heterogeneous thus, in order to have a comprehensive understanding the load transfer mechanism requires the full strain distribution along the entire element. Conventional instrumentation, commonly strain gauges (SGs), are mounted to the surface of the rock bolt have been and still are the most prevalent form of monitoring the strain during pull-out tests (Farmer, 1975; Li et al, 2017b, Zhang et al, 2021). Owing to the discrete nature of these instruments, strain profiles have to be interpreted between points and therefore, localized phenomenon may be missed where a SG was not placed as spatial resolutions are typically greater than 50 mm (Cruz et al, 2016).

New and innovative methods using fiber optic technology have been explored in order to improve the spatial resolution and achieve a continuous strain profile. One of the new methodologies utilizing DOS was developed by the research program led by Dr. Vlachopoulos (Vlachopoulos et al, 2018; Vlachopoulos et al, 2014) in combination with an industrial partner. The technique leverages Rayleigh Optical Frequency Domain Reflectometry (ROFDR) to measure strain and has achieved an unprecedented spatial resolution of 0.65 mm by this research group. When light is sent through an optical fiber, an index profile is created. Rayleigh backscattering results from random variations in the profile with the scatter amplitude being a function of the distance along the fiber. External factors, such as strain and temperature, cause a spectral shift that can then be calibrated for use as a distributed sensor (Gifford et al, 2005). The use of DOS captures geo-mechanisms associated with axial loading, as well as, improves conformance as compared to SGs since the fiber is embedded into the rock bolt and does not cause issues at the bolt-grout interface. The methodology has been improved by an iterative manner by each past and present member of the authors' research group and has been implemented in laboratory and in-situ testing spanning investigations concerning confining medium, embedment length, grouting materials, rib spacing, grout annulus, and now, temperature (Cruz et al, 2016; Forbes et al, 2018; O'Connor, 2020; Moore & Vlachopoulos, 2021; Guo et al, 2023).

Cold temperatures can potentially affect the bonding and performance of FGRBs. For cement grouts, the main concerns in cold environments are slow

strength development and early-age frost damage. Regular Portland cement (PC) will not properly hydrate in sub-zero conditions and thus, will not likely gain sufficient strength (Huang, 2021). Research into cement mixtures for permafrost have found different mixtures and additives that improve performance with the key characteristics being high early strength and high rate of hydration (Huang, 2021; Morris, 1970; Reny et al, 2019). There have been limited studies investigating the effects of surrounding rock mass temperatures on FGRBs, especially in cold conditions. Johnston & Ladanyi (1972) conducted field studies of grouted pile anchors for power/communications transmission guyed towers in permafrost to investigate the time-dependent behaviour of anchors. The grout used was a mixture of Ciment Fondu and a clean medium-to-coarse sand with grout lengths varying between 2.5 – 3 m. Results showed that after a certain amount of displacement by creep, the anchors failed by slip at the soil-pile interface. Zhang et al. (2021) studied the effects of freeze-thaw cycles and sulfate attacks on cement grouted short embedment length FGRB. The compressive strength and shear strength of the cement grout was found to decrease with increasing freeze-thaw cycles as the pores in the grout were enlarged by ice stress during freezing.

4.3 Methodology

A series of laboratory pull-out tests and materials tests were conducted in order to study the effects of cold temperatures on FGRBs. Two temperatures were tested as the curing conditions: -20°C (referred to as the P20 condition) and -5°C (referred to as the P5 condition). DOS instrumented FGRB specimens were assembled and cured in temperature-controlled chambers for different durations of time in order to better understand the capacity development in these conditions. The most recent preparation and testing procedure is a summation of the iterative development process from the RMC research group, with lessons learned and recommendations being explored during the conceptual design and proof-of-concept testing of the investigation herein. Novel to this project, DOS was utilized to continuously monitor temperature. The presented methodology was used to monitor specimen strain and temperature changes of the FGRB specimens simultaneously during axial load testing. The background associated with the DOS technique that has been developed by this research group can be seen in Forbes (2015).

4.3.1 Rebar Bolt Preparation

20M 400W (ϕ 19.05 mm) rebar at 1600 mm lengths were procured from Kimco Steel Sales Ltd. The bars were sent to a local machine shop to be machine grooved with 3 mm x 4 mm diametrically opposing grooves along the entire length of the bar. Traditionally, the grooves (2.5 mm x 2.5 mm) were placed along the transverse ribs (Forbes, 2015; Cruz, 2017; O'Connor, 2020), however, Moore (2021) moved the grooves (3 mm x 3 mm) along the longitudinal ribs as shown in Figure 4-3. The new groove location enhanced conformance conditions by decreasing impacts on mechanical interlock and as such was adopted by this investigation.

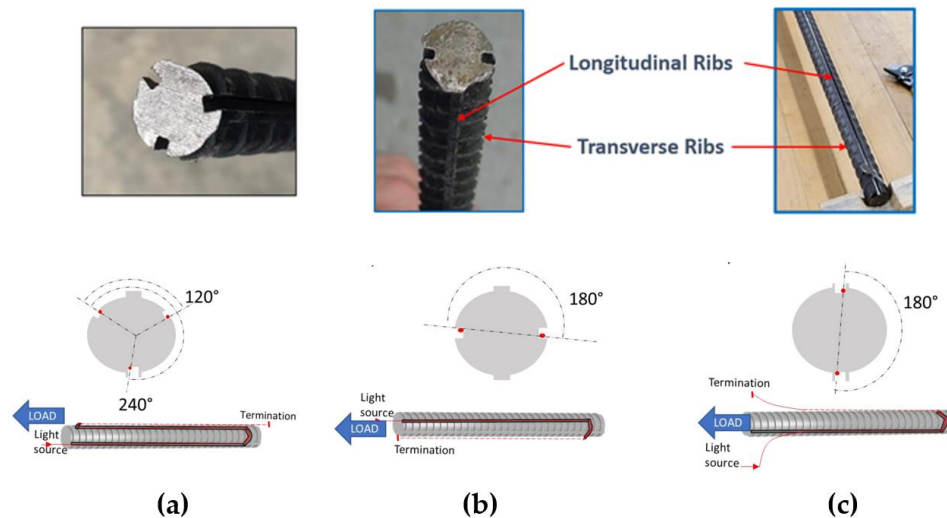


Figure 4-3. Location of machined grooves: (a) Three groove orientation; (b) Diametrically opposing grooves along transverse ribs; (c) Diametrically opposing grooves along longitudinal ribs (modified after Moore, 2021)

The dimensions of the grooves were increased in order to accommodate the extra DOS and de-bonding stainless steel tubing. The bars and grooves were cleaned prior to DOS installation using a drill with a wire cup brush attachment, steel brush, acetone, and compressed air for rust and debris removal (Figure 4-4). The grooved rebar was tested to confirm material properties (results found in Table 4-1), and results were comparable to literature values for mild steel and to results of past group members (Cruz, 2017; Moore, 2021).



Figure 4-4. Rebar cleaned of rust

Table 4-1. Material properties of the rebar

Material Property	Test Result (MPa)	Test Result (kN)
Yield Strength	460	120
Ultimate Strength	658	172
Modulus of Elasticity	200,000	-

4.3.2 DOS Installation

The DOS configuration is shown in Figure 4-5 and the installation was conducted in two phases: 1. ϵ DOS (the distributed sensing associated with determining the strain every 0.65 mm along the length of the rock bolt); and, 2. T DOS (the distributed sensing associated with determining the temperature at every 0.65 mm along the entire length of the rock bolt). The T DOS underwent temperature calibration testing for the sensing fiber in order to determine the relationship between strain and temperature change, the process and results are presented in Guo et al. (2023), and the resulting conversion factor was $8.49 \mu\epsilon/^\circ\text{C}$. One of the limitations of previous set ups was the premature failure of the DOS; the fiber was bonded to the bolt along the rebar length, therefore, the sensor failed when the rebar yielded. During the pull-out test, the portion of the rebar outside of the embedment length failed earlier than the rest of the system, thus, the DOS was unable to capture the strain profile over the entire loading sequence. Moore (2021) introduced a 25 mm de-bonded zone for the DOS into the embedment length on the loaded end in order to address the premature failure and unsupported loading as the grout often sheared during failure. The concept of the de-bonded zone was further expanded upon in this investigation and improved using stainless steel tubing. The ϵ DOS was placed inside the grooves, slightly tensioned, and temporarily bonded to the rebar with an epoxy resin. A 50 mm stainless steel tube was placed along the fiber on both sides at the start of the embedment length to provide 25 mm of de-bonded zone and 25 mm of extra protection for the fiber

outside of the embedment length in the higher stress location(s). The ϵ DOS was then coupled to the rebar using a proprietary metal bonding adhesive. One layer of the adhesive was initially applied to “Side 2” to fully bond the ϵ DOS to the bolt and avoid air voids, and any damage when installing the T DOS. The T DOS had the entire fiber line placed inside of a stainless-steel tube along the full length of the embedment length of the rock bolt on a single side. It was placed into the groove and anchored to the rebar at a single point, doing so ensured the fiber location remained consistent during the testing, but was independent from the axial deformation of the bolt during loading. The T DOS was gently pushed into the adhesive and an additional layer of adhesive was added to fully cover the groove. Figure 4-6 depicts examples of the rebar bolts instrumented with DOS that was used for this study. Positioning markers were recorded at four locations on the ϵ DOS and one on the T DOS.

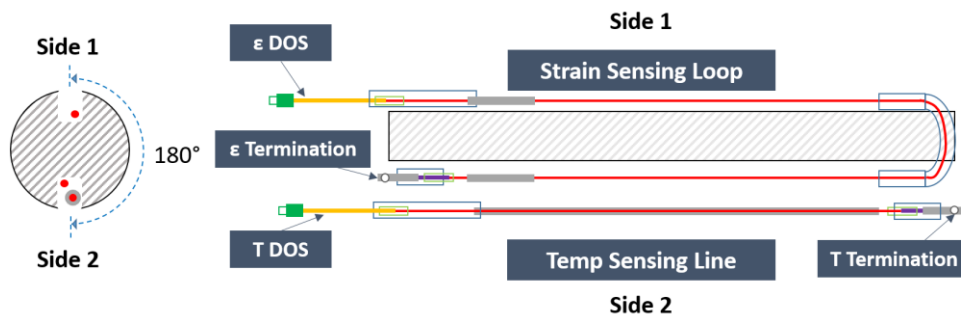


Figure 4-5. DOS configuration in diametrically opposing grooves

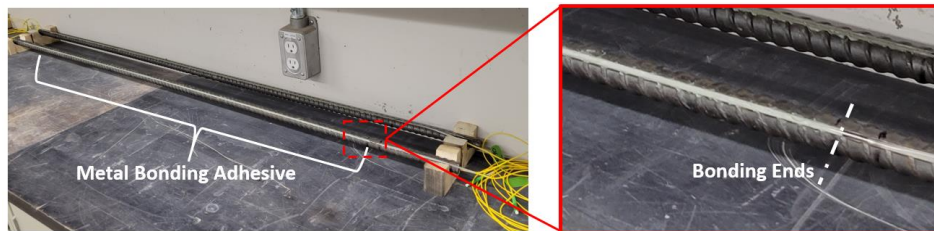


Figure 4-6. DOS instrumented rebar bolts

4.3.3 Confinement Pipe Preparation

Schedule 80 1¼” diameter nominal pipes were selected as the confinement material to replicate a granitic rock radial confinement pressure of approx. 3000 MPa/mm; calculated using thick wall cylinder theory (Hyett et al, 1992).

Additionally, the size of the pipe provides a thin grout annulus and according to Farmer (1975), the shear stress at the bolt-grout interface represents that which is within the annulus. The pipe length was 1300 mm as is equivalent to the same embedment length.

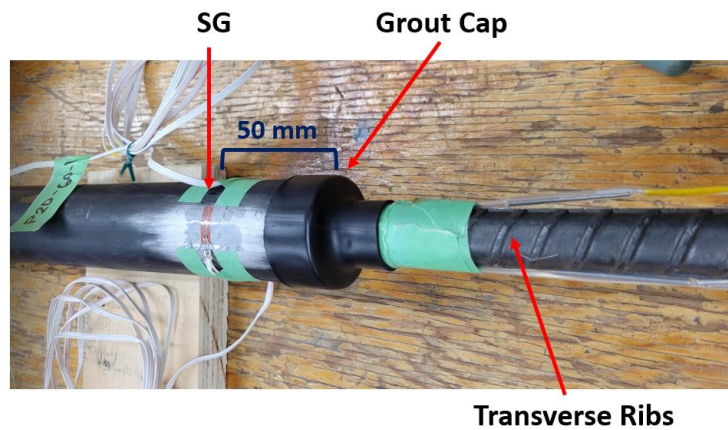
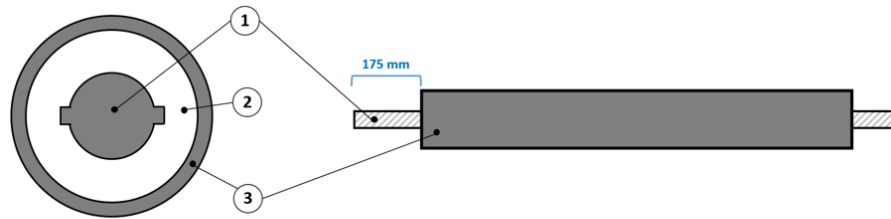


Figure 4-7. Instrumented confinement pipe and rock bolt installed prior to grouting

Each pipe was instrumented with two N11-FA-10-120-11 SGs in order to monitor pipe dilation during pull-out, axial load testing. The surface coating of the pipe was sanded off and the SG were mounted perpendicular to axial loading on diametrically opposing sides at 50 mm from top of pipe. They were positioned over the transverse ribs of the rebar bolt, which are critical to load transfer in FGRBs (Moore, 2021), as the location was predicted to experience higher amounts of dilation. The rebar bolt was inserted into the pipe and a grouting cap was added as shown in Figure 4-7. A new capping method was used for this project through adhesive-lined heavy duty heat shrink tubing.

4.3.4 Specimen Assembly and Grouting

A total of 24 FGRB specimens were assembled according to the schematic seen in Figure 4-8 and the schedule in Table 4-2 in the laboratory. The FGRB specimen naming convention included a letter and numbers. The first letter was 'P' for permafrost (or cold) condition, followed by the numbers representing the curing temperature followed by the curing duration. The 12 FGRB specimens utilized in this cold temperature study were the ones labelled with prefix 'P'. Prior to installation, the ϵ DOS and T DOS fiber optics for each of the rebar bolts were verified to be operational.



NTS

1: 20M 400W Rebar (\varnothing 19.05 mm, L 1600 mm)

2: PC 0.4 w/c ratio; Nordic 0.29 w/c ratio

3: 1¼" Sch 80 Steel Pipe (\varnothing_{out} 42.2 mm ; \varnothing_{in} 32.5 mm, L 1300 mm)

Figure 4-8. Schematic of assembly of FGRB specimen

Table 4-2. Specimens preparation schedule (24 total specimens)

Cure Time (days)	Number of Specimens ¹	Type of Grout	Name of Specimens
3	4	Nordic (cold) / PC (hot)	P20-3, P5-3, C20-3, G45-3
7	4	Nordic (cold) / PC (hot)	P20-7, P5-7, C20-7, G45-7
28	4	Nordic (cold) / PC (hot)	P20-28, P5-28, C20-28, G45-28
35	4	Nordic (cold) / PC (hot)	P20-35, P5-35, C20-35, G45-35
60	4	Nordic (cold) / PC (hot)	P20-60, P5-60, C20-60, G45-60
90	4	Nordic (cold) / PC (hot)	P20-90, P5-90, C20-90, G45-90

¹ Each specimen includes grout strength cylinders for UCS and STS testing

As seen in Figure 4-9, the specimens were installed vertically and levelled with a torpedo level, the top of the rebar (pull end) was placed at the bottom of the rack. This orientation was utilized to ensure the grout would be flush with the top of the confinement pipe. The monitoring instrumentation wires were secured with hooks to protect them during transport and grouting. The specimens rack, grout test cylinder moulds, grouting tools and buckets were transported to the freezer curing

room for temperature conditioning at least 24 hours prior to grouting. Due to the availability of freezers, the P20 specimens (freezer set to -20°C) and the P5 specimens (freezer set to -5°C) were grouted on separate dates. P20 specimens and cylinders were transported to a horizontal freezer after 3 days of curing so that the freezer room could be used for P5 grouting and curing. The temperatures of the curing chambers were verified over the duration of the testing with a Traceable® Extra-Long-Stem thermometer and the P5 and P20 freezers had a variation of $\pm 2^{\circ}\text{C}$ and $\pm 3^{\circ}\text{C}$, respectively. There were two power outages (2-4 hours) and a campus maintenance power shutdown of 8 hours during the testing period, which lasted a total of 90 days per curing condition.

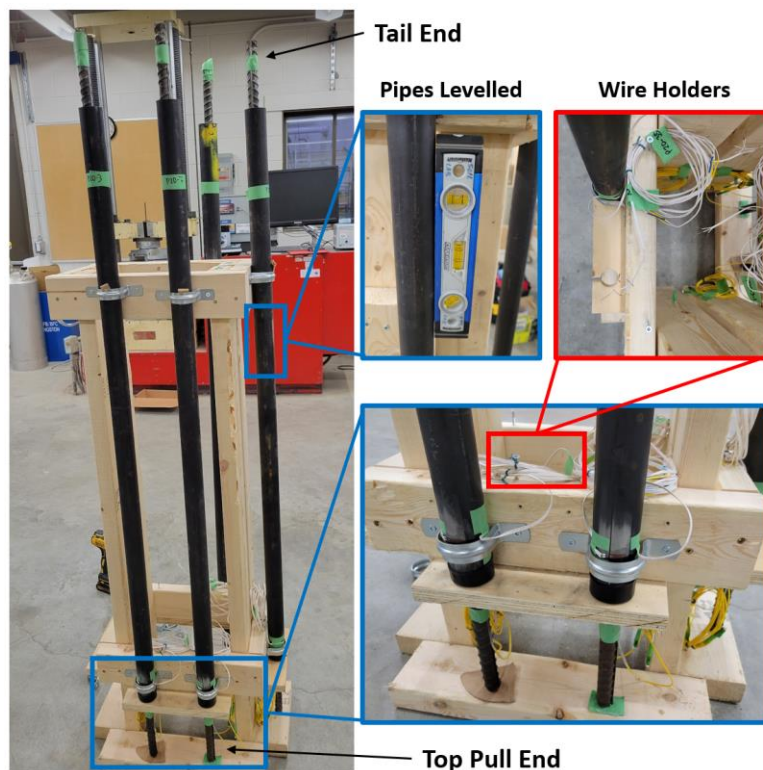


Figure 4-9. Grouting rack and specimen assemble

The cement grout used for all specimens was Nordic Cable CT provided by Sika Canada, which was specifically formulated to cure in frozen ground conditions (manufacture tested up to -10°C) for anchoring of cables and bolts. The grout was mixed to 0.29 w/c ratio with a handheld drill and paddle attachment in accordance

with manufacturer Technical Data Sheet (TDS) (King A Sika Company, n.d.). Batching was completed due to the limited working time of Nordic, each batch of grout was sufficient for the FGRB specimen and respective strength test cylinders. Initial grout mixing was conducted outside of the freezer room and grouting was accomplished inside the room. Due to the more liquid consistency of the Nordic grout, a cup with spout was used to pour the grout down the confinement pipe(s) of the test specimens. All specimens were externally vibrated along the entire specimen length to eliminate any potential air voids. The mixture was continuously slow mixed during the grouting process to increase grout working time, as recommended within the Nordic TDS (King A Sika Company, n.d.). Examples of the grouted specimens and cylinders and tools in Figure 4-10.

The grout was poured and vibrated until within 1-2 mm of the top of the pipe and a piece of cardboard was placed inside to centre the rebar as the grout set. After all grouting was completed, it was observed that a small portion of the grout in the P20 specimens had expanded out over top of the confinement pipes (Figure 4-11), which did not occur for the grout cylinders or during the P5 specimen(s) grouting. The expanded portions were already hardened.



Figure 4-10. Grouted specimens and test cylinders in freezer room; grouting tools

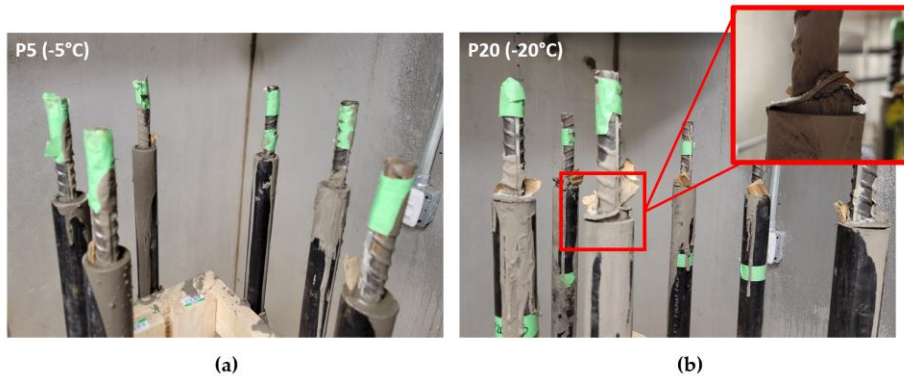


Figure 4-11. Grouted FGRB specimens: (a) P5 specimens; (b) P20 specimens – grout expanded out of the confinement pipes after grouting completed

At least 24 hours prior to the pull-out testing, the grout cap was removed and the specimen was wrapped with thermal insulation tubing (pre-conditioned in the freezer) and any expanded grout was chipped off of the P20 specimens. The new heat shrink tubing cap method had provided a seal for the end of the pipe and around the rebar, and resulted in flat and flush grout surface, which was an improved finish from past capping methods. A prepared sample is shown in Figure 4-12. A FLUKE multimeter was used to verify the functionality of the SG's.

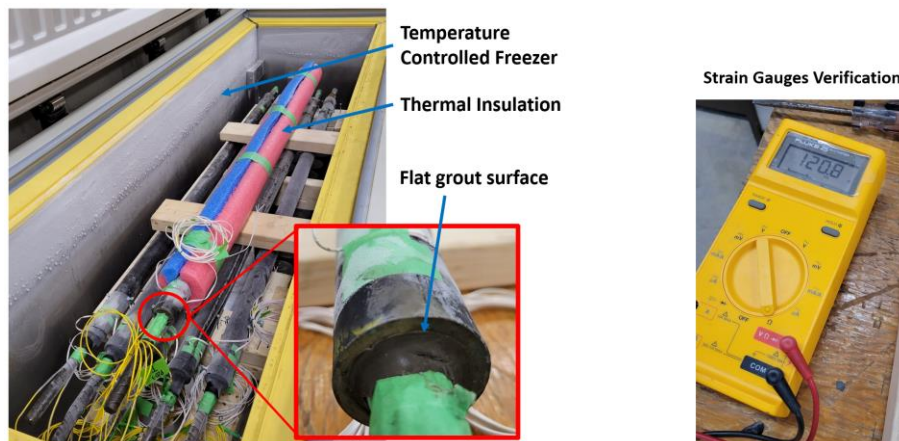


Figure 4-12. Prepared FGRB specimen with thermal insulation wrap and grout cap removed

4.4 Laboratory Testing Program

A series of pull-out tests were conducted at the RMC structures laboratory on the 12 instrumented FGRB specimens. The tests were performed using a 322.41 MTS with a capacity of 500 kN outfitted with the testing rig setup seen in Figure 4-13. This test rig is the same as has been used by previous investigations conducted by the author's research group and is representative of full-scale anchorage length axial loading (Cruz, 2017; O'Connor, 2020; Moore, 2021). In addition, a series of material testing were conducted to quantify the material properties of the grout and confirm the properties of the rebar. The rebar testing was completed during prototype testing, the investigation and results are presented in Guo et al. (2023). Each FGRB specimen had grout strength test cylinders casted and cured for their corresponding durations and tested for uniaxial compressive strength (UCS) testing and splitting tensile strength (STS) testing. A total of 33 UCS tests and 24 STS tests were completed using a 300,000 lbs RIEHLE Testing Machine.

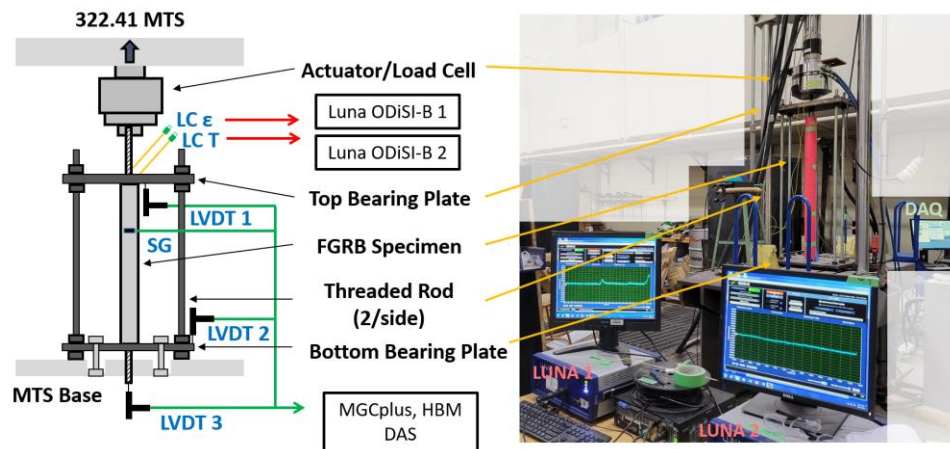


Figure 4-13. Laboratory pull-out test assembly and monitoring setup

4.4.1 Monitoring Program

The FGRB specimen was placed between two steel bearing plates – 1.5” top plate and 1” bottom plate – affixed by four 1” coarse threaded rods and nuts. The bottom bearing plate was mounted to the MTS base using four ¾” bolts. The top bearing plate was lifted and lowered using a lifting plate placed over the MTS actuator with lifting rods. Two LVDTs were mounted on independent retort stands to monitor any

movement in the bearing plates during testing. A third LVDT with a washer attached to its tip was placed under the MTS on an independent retort stand to monitor the free tail-end of the rock bolt in order to monitor any potential slip of the rebar. The two SGs mounted to the confinement pipe were connected to a quick connect junction box. The ϵ DOS and T DOS were connected via to two extension boxes. The conventional instrumentation was connected to the DAQ (MGCplus, HBM Catman) and the 2x DOS (i.e. ϵ DOS and T DOS) were connected to 2x independent, 1 channel Luna ODiSI-B analyzers. The monitoring instrumentation settings, locations, and measurement uncertainties are detailed in Table 4-3, Table 4-4, and Figure 4-14. The testing machines were professionally calibrated by VACS Calibrations between 14-15 August 2023. For pull-out testing, the DAQ and two (2) Luna analyzers were synchronized by simultaneously starting data collection at the commencement of testing. Specimen loading started at 1 mm/min and increased to 2 mm/min at approximately 130-140 kN.

Table 4-3. Sensor details and locations

Instrumentation	Range	Location	Measured Parameter
Load Cell	500 kN	MTS	Applied Load
Actuator	250 mm	MTS	Stroke
LVDT 1	150 mm	Top Bearing Plate	Displacement
LVDT 2	200 mm	Bottom Bearing Plate	Displacement
LVDT 3	250 mm	Under MTS / Rebar Tail	Displacement
SG 1	10 mm	Confinement Pipe	Radial Dilation
SG 2	10 mm	Confinement Pipe	Radial Dilation
ϵ DOS	-	Rock Bolt	Rebar Strain
T DOS	-	Rock Bolt	Rebar Temperature
MGCplus	-	Analyzer	Time
Luna ODiSI-B	-	Analyzer	Time

Table 4-4. Sensor settings and uncertainties

Instrumentation	Analyzer	Uncertainty ¹	Connection / Sampling Rate
Load Cell	DAQ MGCplus	0.244%	Ch 1-1
Actuator	DAQ MGCplus	2.5%	Ch 1-2
LVDT 1	DAQ MGCplus	0.65%	Ch 1-4
LVDT 2	DAQ MGCplus	0.65%	Ch 1-3
LVDT 3	DAQ MGCplus	0.65%	Ch 1-5
SG 1	DAQ MGCplus	2.2%	Ch 2-1
SG 2	DAQ MGCplus	2.2%	Ch 2-2
ε DOS	Luna ODiSI-B	25 με	Luna 1
T DOS	Luna ODiSI-B	25 με	Luna 2
GW Instek DC power Supply	-	0.5%	-
MGCplus	-	0.000001 s	1 Hz
Luna ODiSI-B	-	0.37 s	1 Hz

¹ Listed uncertainties are provided specifications (modified after O'Connor, 2020; Moore, 2021)

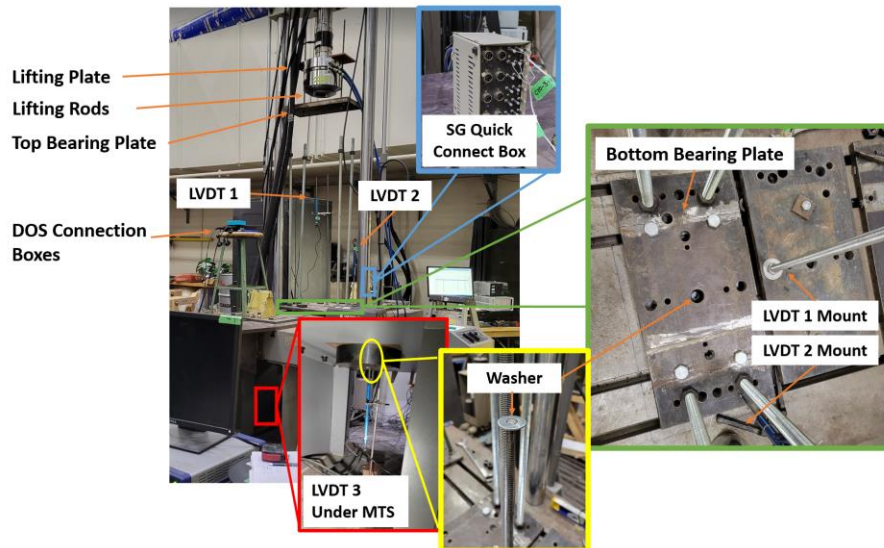


Figure 4-14. Test setup instrumentation details

4.4.2 Testing Scheme

The pull-out testing was conducted in order to investigate the effects of curing temperature in permafrost conditions and capacity development over time on FGRBs. Two temperatures were explored (-5°C and -20°C) at curing durations including short- and long- term. The testing schedule included the cold specimens indicated in Table 4-2. Rehearsals were completed before the testing began in order to optimize setup procedures and time the process. Since temperature was the main factor being studied, the aim was to minimize changes to the test specimen's temperature. The times improved from 20-25 minutes to 10-15 minutes from the time the specimen was removed from the freezer to the time that the test specimen was connected to all of the sensors after several practices. In order to minimize setup times and specimen temperature changes, a test DOS was created to ensure the Luna analyzers were operational and recognizing sensors, as selected issues had been experienced during prototype testing and specimen preparation.

4.4.3 Grout Strength Testing

Grout strength testing was conducted for all specimens in order to quantify the grout properties for each FGRB over time and under each curing condition. The cylinders were cast at the same time as the grouting of the FGRB specimens. The cylinders corresponded with the grout utilized in each FGRB specimen. Time was recorded from the start of mixing to the end of the grouting per specimen in order to confirm that the working time was within the allowable limit of the Nordic TDS (maximum 20 minutes) and general consistency between batches. The cylinders were produced in accordance with ASTM C470 (ASTM, 2015) and ASTM C192 (ASTM, 2019) casted in 100mm Ø x 200mm L moulds in two layers. The grout was tested for UCS following the guidelines of ASTM C39 (ASTM, 2021) and STS following the guidelines of ASTM C496 (ASTM, 2017). The average results of the UCS and STS tests for the P20 and P5 conditions are found in Table 4-5 and Table 4-6, respectively. The measured compressive strength results for each series of cylinders were not all within the precision ranges as outlined in the standard. It was noted that the ASTM range corresponds to UCS between 17-35 MPa; generally the compressive strength results were higher. Thus judgements were made in excluding any significant outliers or including based on trend and a slightly bigger acceptance range.

Table 4-5. Summary of Nordic grout UCS and STS test results in P20 condition

Curing Duration (days)	Average UCS (MPa)	Average STS (MPa)
3	41.5	5.8
7	36.1	4.8
28	14.9	3.7
35	28.3	6.0
60	46.1	3.7
90	39.0	3.9

Table 4-6. Summary of Nordic grout UCS and STS test results in P5 condition

Curing Duration (days)	Average UCS (MPa)	Average STS (MPa)
3	43.4	3.8
7	54.9	4.3
28	53.3	5.5
35	58.3	4.1
60	57.8	5.7
90	63.6	5.4

4.5 Results

4.5.1 Pull-Out Test Results

The results of the pull-out tests are seen in Table 4-7. The testing age tolerances adhered to ASTM C39 (ASTM, 2021) guidelines with deviations noted for the 3-day cure specimens outside of the ± 2 hour tolerance: P20-3 pull-out test was 0.5 hours and grout strength tests were 2-3 hours, and P5-3 grout strength tests were 2 hours outside of the tolerance range. The failure mechanism and load results at end of each pull-out test were observed and recorded in Table 4-7. Two specimens (P20-3 and P5-60) had reached the ultimate strength of the rebar at the point of the test termination, however, they are not assessed as premature stoppage prior to rebar tensile failure. P20-3 was observed to have significant rebar pull-out when ultimate strength of the rebar was surpassed, thus, the testing was terminated. The ϵ DOS

results of P5-60 showed that almost the full embedment length had been mobilized prior to DOS failure at 129 kN.

Table 4-7. Pull-Out testing results for P20 and P5 specimens

Specimen	Max Load (kN)	Test End ¹	Notes
P20-3	155.0 ²	Rebar Pull-Out	Test end load was 173.5 kN
P20-7 *	140.0 ³	Rebar Pull-Out	Max load estimated (DAQ recorded 34.7 kN)
P20-28 **	127.9	Rebar Pull-Out	
P20-35	148.7	Rebar Pull-Out	
P20-60 **	150.0 ³	Rebar Pull-Out	Max load estimated (DAQ recorded 59.0 kN)
P20-90 **	152.5	Rebar Pull-Out	
P5-3	119.6	Rebar Pull-Out	
P5-7 **	155.4	Rebar Pull-Out	DAQ overloaded (reset to 50 Hz collection rate after test started), captured data after 130 kN
P5-28	146.7	Rebar Pull-Out	
P5-35	166.7	Rebar Pull-Out	
P5-60	172.9	Rebar Pull-Out	
P5-90 *	172.9	Rebar Break	

* Entire ϵ DOS not functioning

** Partial ϵ DOS was functioning

¹ Observed failure mechanism resulting in ending of testing

² Load at point of pull-out deemed by slip measurements

³ Significant discrepancy between MTS output load vs load collected by DAQ, max load estimated based on observations and manual records of MTS loading at milestones during testing

The load-displacement curves from the conventional instruments were plotted for each test specimen in order to try and determine the behaviour of the whole system. The top bearing plate was observed to be yielding during tests that ended at higher loads. The axial displacement of the system from the MTS actuator stroke was corrected using the displacement captured by the LVDT monitoring the

top bearing plate and the elongation of the rebar portion outside of the embedment length, such that the displacement at the beginning of the embedment length could be presented and compared. For P20-7, P20-60, and P5-7 tests, load time stamps were estimated based on trends of other tests as loading rate was the same in the elastic region in order to process DOS data. Across all specimens, two general axial displacement behaviours were observed. One being rock bolt pull-out with residual capacity observed. An example from P5 condition is seen in Figure 4-15: the loading in the elastic region is linear and load peaked with failure of the bolt-grout interface, a residual capacity area is observed prior to test termination. However, the majority of P5 and P20 curves displayed a plateau of maximum loading with increasing displacement. An example from P20 condition is found in Figure 4-16, the pull-out point was determined with the rebar tail slip LVDT monitoring as significant axial displacement occurred with small increase of load until testing ended. Significant grout mobilization was also observed post-test. The majority of P5 and P20 curves resemble that of Figure 4-16.

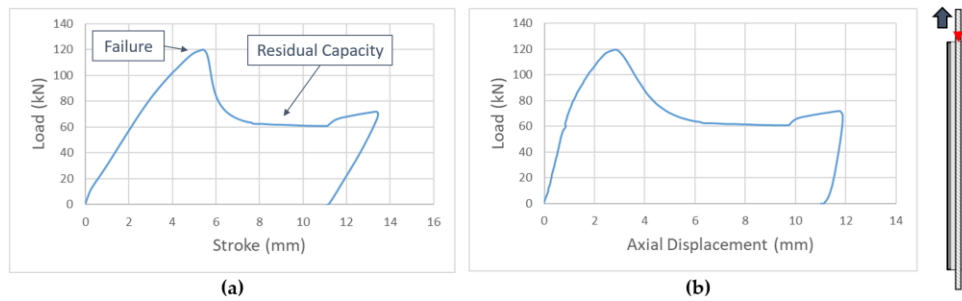


Figure 4-15. Load-Displacement curve from P5-3: (a) Whole system response; (b) Axial displacement corrected for test rig movement and elongation

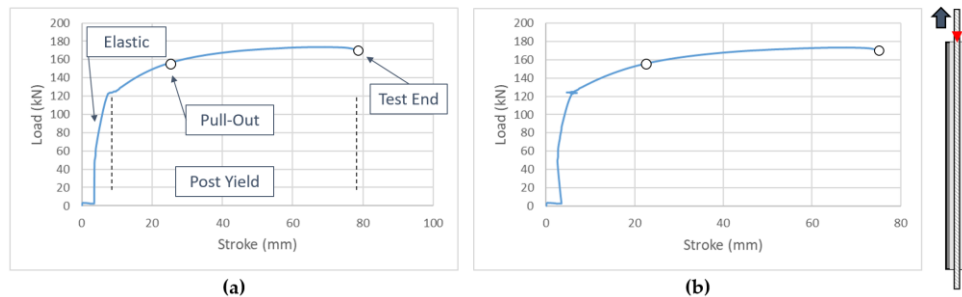


Figure 4-16. Load-Displacement curve from P20-3: (a) Whole system response; (b) Axial displacement corrected for test rig movement and elongation

The ϵ DOS monitored the axial response of the rebar bolt itself. The bolt displacement was calculated utilizing the strain data collected by the DOS and Equation 7 (Cruz, 2017; Moore, 2021). The DOS data began at 75 mm from the borehole collar due to the 50 mm strain pickup transition section (Moore, 2021) and 25 mm de-bonding zones thus the displacement curves were extrapolated in order to find the displacements at the borehole collar (Figure 4-17).

$$U_x = \sum \left(\frac{\epsilon_{i+1} + \epsilon_i}{2} \right) \cdot (x_{i+1} - x_i) \quad (7)$$

where, U_x , is bolt displacement at distance x , ϵ_i , is bolt strain at position i , and x_i , is distance along bolt at position i .

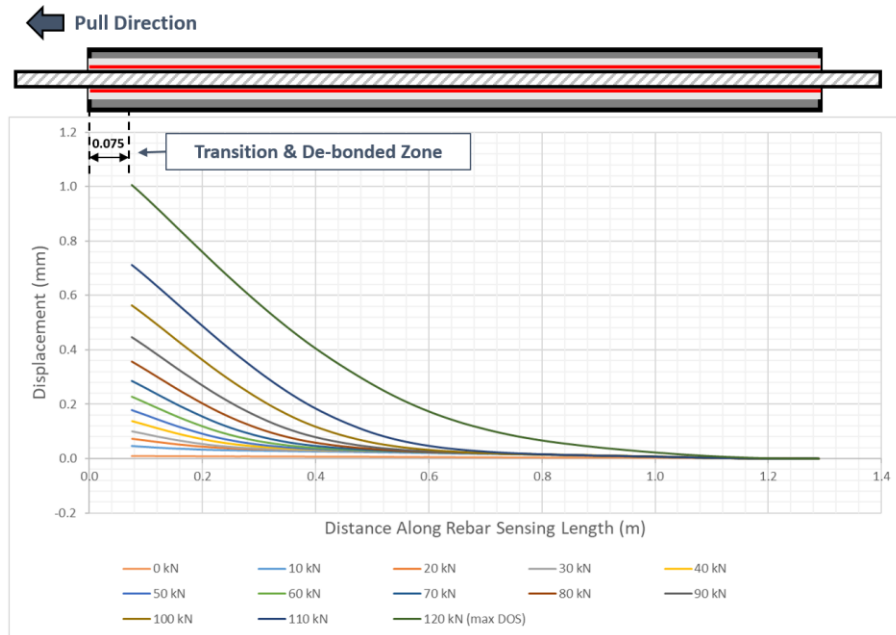


Figure 4-17. P5-3 specimen axial displacement profile

The amount of displacement data was limited to the operational life of the DOS as most of the sensors captured most of the loading sequence. Examples of the resulting load-displacement curves for the bolts are found in Figure 4-18. This displacement represents that only in the rebar itself and not additional responses of the whole system (e.g. slip of the rebar), which are captured and accounted for by the conventional instruments.

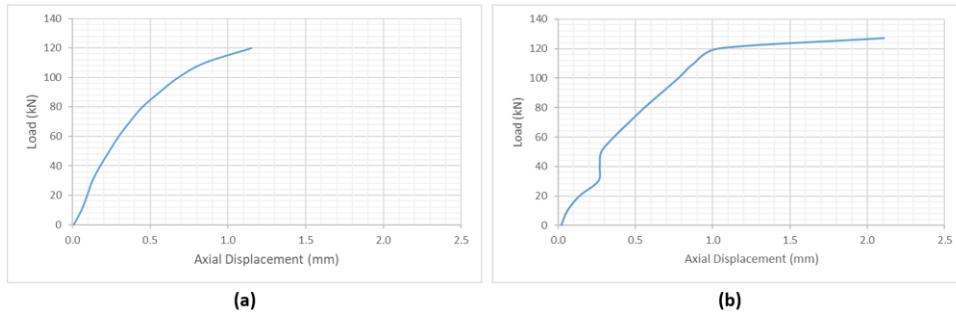


Figure 4-18. Load-Displacement curve – DOS: (a) P5-3 specimen; (b) P20-3 specimen

The pipe dilation at 50 mm from top of pipe was monitored by two SGs (mounted on diametrically opposing sides) aligned over the transverse ribs. Figure 4-19 is an example of the pipe strains as loading increased. Across all 12 specimens (P20 and P5), the highest pipe strain recorded was 680 $\mu\epsilon$. Thus, concluding that the confinement pipes did not experience significant dilation during testing and pipe failure was not a potential factor, which is in-line with predictions due to the wall thicknesses of the Schedule 80 pipes. Some differences between SG1 and SG2 are attributed to alignment and positioning over the rebar ribs.

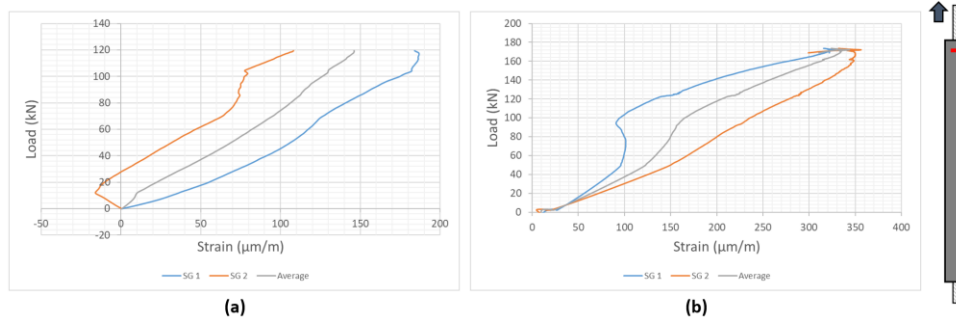


Figure 4-19. Pipe dilation monitoring at 50 mm: (a) P5-3 specimen; (b) P20-3 specimen

After testing concluded, post-test forensics were conducted and specimens were cut open along the longitudinal axis in order to assess and to make evaluations and observations to provide additional insights and complement the DOS results. The main observations were of grout mobilization, grout shearing, bolt slip, debonding, and grout voids (not often observed). An example of a cut open (pipe) specimen is presented in Figure 4-20, observations were made that some rusting occurred over the curing duration as all rebar were cleaned prior to specimen assembly. The lack of voids across the specimens confirmed that the grouting

method was effective and in agreement with Moore (2021) and was a significant improvement from past procedures.

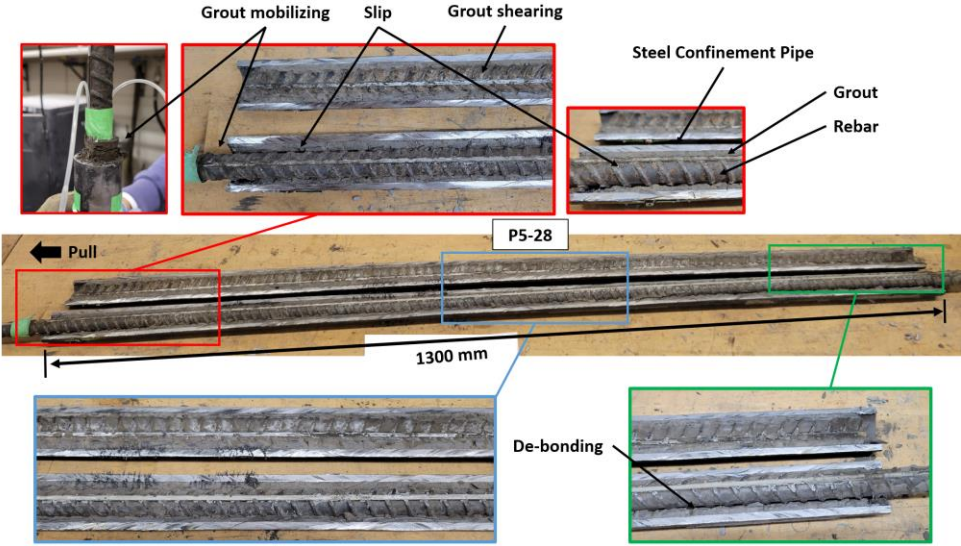


Figure 4-20. P5-28 specimen cut open for post-test evaluations

4.5.2 Strain Profiles

The strain measurements captured by the ϵ DOS for each specimen were plotted as continuous strain profiles along the length of the sensing span, analyzed and presented at 10 kN loading increments (an example can be seen in Figure 4-21). The strains captured on the two sides of the rebar were averaged following Equation 8 in order to remove any bending that may have been experienced by the bolt during pull-out testing. The strains displayed at the start of the 75 mm transition and de-bonded zones are the calculated theoretical strains based on the effective cross-sectional rebar area and confirmed Young’s Modulus (200 GPa) of the rebar during materials testing.

$$\epsilon_y = \frac{\epsilon_y^{side\ 1} + \epsilon_y^{side\ 2}}{2} \tag{8}$$

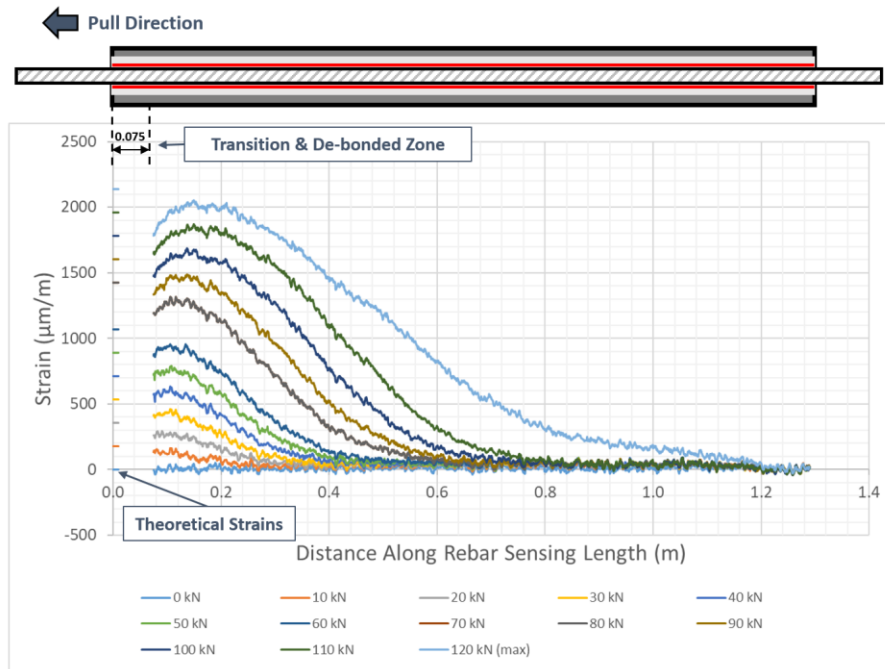


Figure 4-21. P5-3 specimen strain profile along rebar bolt during pull-out testing

In addition, the strain profiles were corrected for any excess noise as required and all profiles were adjusted for temperature changes experienced by the ϵ DOS. Most sensors failed after the yield point and prior to the end of testing thus full loading profiles were not captured. The premature failure was attributed to the location of the DOS termination being in the actuator grip and therefore, experiencing significantly higher strains than the embedded portions. The strains due to specimen temperature change were captured by the T DOS, as seen in Figure 4-22. The average strain at the loading increment was calculated and subtracted from each ϵ DOS strain measurement along the rebar to account for the increase in bolt temperature.

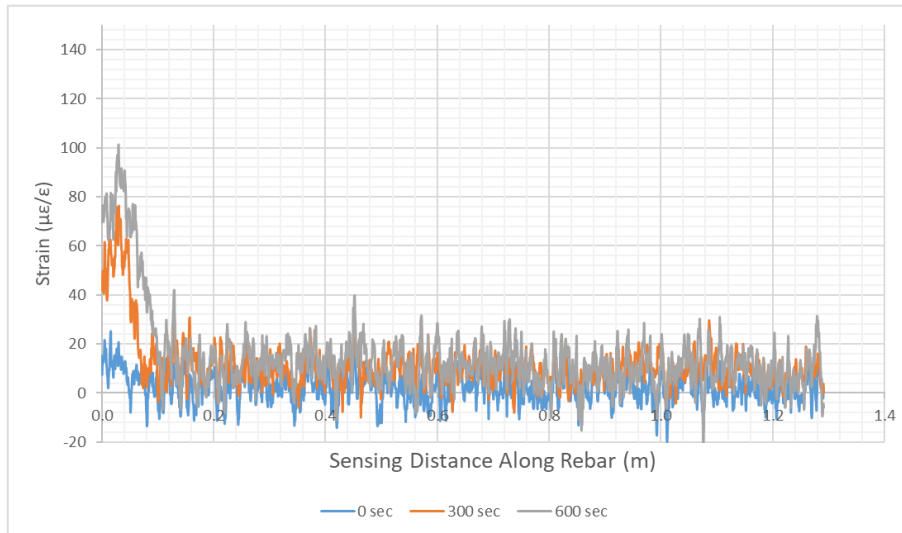


Figure 4-22. P5-3 specimen temperature strain profile along rebar bolt during pull-out testing

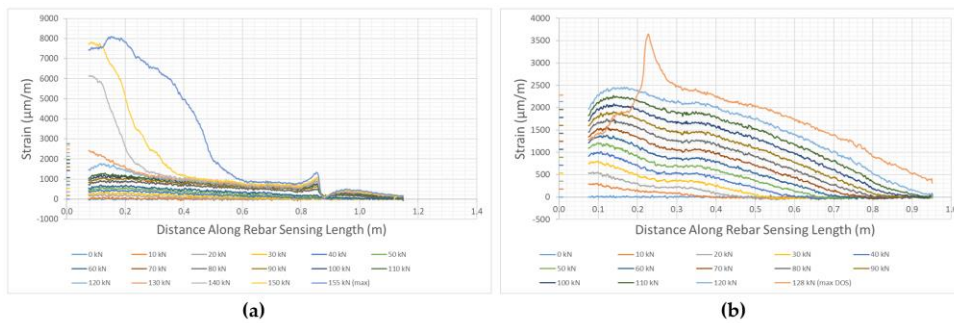


Figure 4-23. Strain profiles over entire loading sequence: (a) P5-7 partial length; (b) P20-28 partial length

Figure 4-23 shows the continuous strain profiles along partial lengths of the embedment length due to the partial strain capture by the ϵ DOS. In Cao et al. (2012), the different failure modes and analytical models are described, the results of the DOS strain profiles capture and demonstrate the behaviours from the elastic stage to the plastic. The elastic stage, the profiles had relatively linear decay. The plateaus observed in the front portion may be due to presence of voids that were observed in post-test forensics. As the loads increased, plastic slip can be seen prior to DOS failure. The P5-7 specimen had a sudden drop in profile at 850-900 mm distance along the bolt, post-test forensics did not find any grouting issues or any other notable observations at that area. The issue may be due to an improper bonding of the DOS to the rebar itself during the sensor embedment process. For

P20-28 specimen, the initial plateau has been attributed to presence of grout voids in the first 100 mm as observed during post-test forensics.

The temperature change was calculated from the measured strain using the conversion factor in Equation 9, resulting from temperature calibration of the T DOS sensing fiber.

$$\Delta T = 8.49 \cdot \varepsilon_{y,t} \tag{9}$$

where, ΔT , is absolute temperature change and $\varepsilon_{y,t}$, is strain due to temperature change. The temperature change during the pull-out test was calculated at 30 second intervals and plotted in Figure 4-24. Several T DOS began to react to bolt loading at a singular point as seen in Figure 4-25, likely due to pinching or lifting at the entry of the de-bonding stainless steel tubing. Results of the T DOS that were affected by rebar loading were removed and extrapolation was used to account for any gaps in the data. Table 4-8 presents the temperature change results between the removal of specimen from the curing chamber until the maximum load occurred during testing. The rates of temperature change (i.e. slope) were calculated from the change in temperature graphs for each specimen, which collected data once pull-out testing began. The transport and set-up times were recorded and pre-test temperature change was estimated using the same slope, this was considered a conservative approach as the MTS would have exposed the specimens to warmer ambient temperatures with the hydraulics.

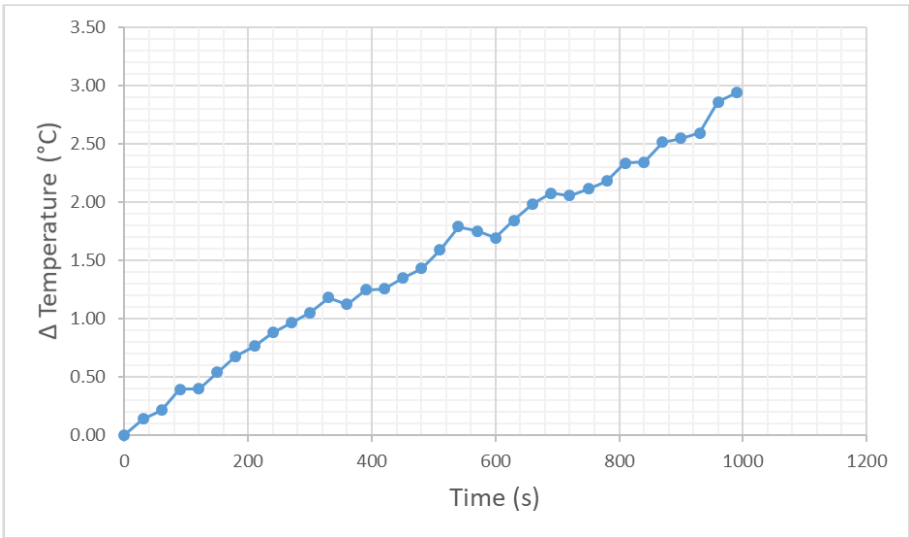


Figure 4-24. P5-28 specimen temperature change during pull-out testing

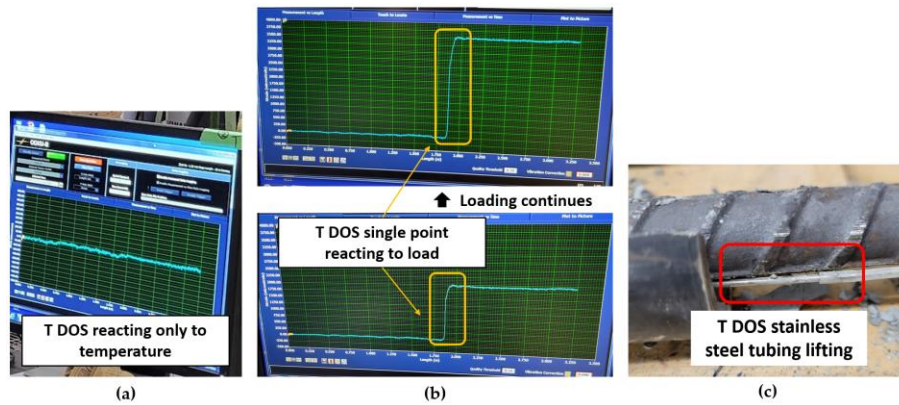


Figure 4-25. T DOS: (a) Only reacting to temperature change; (b) Reacting to rebar loading; (c) Post-test observation of T DOS stainless steel tube lifted out of groove

Table 4-8. Specimen temperature change results

Specimen	Slope (°C/s)	Time to Max Load (s)	ΔT Test (°C)	Pre-Test Time (s)	ΔT Pre-Test (°C)	ΔT Total (°C)
P20-3	0.0065	1588	10.3	900	5.9	16.2
P20-7 *	0.0065	1011	6.6	840	5.5	12.0
P20-28	0.0057	673	3.8	1380	7.9	11.7
P20-35	0.0065	790	5.1	660	4.3	9.4
P20-60 **	0.0065	741	4.8	1260	8.2	13.0
P20-90	0.0056	904	5.1	900	5.0	10.1
P5-3	0.0024	337	0.8	960	2.3	3.1
P5-7	0.0022	890	2.0	900	2.0	3.9
P5-28	0.0027	1093	3.0	1200	3.2	6.2
P5-35 ***	0.0027	893	2.4	900	2.4	4.8
P5-60 ***	0.0027	1085	2.9	900	2.4	5.4
P5-90	0.0027	1271	3.4	780	2.1	5.5

* T DOS reacted to loading from start of test (used P20-3 data)

** T DOS functionality (used P20-3 data)

*** T DOS reacted to loading from start of test (used P5-23 data)

4.5.3 Grout Strength Development

Each test specimen had grout test cylinders for UCS and STS, the strength development curves are presented in Figure 4-26, the dotted lines connecting points are to be indicative of trend observations and not for the purpose of interpolation. The compressive strength significantly decreased from P5 to P20 in all curing time durations. This was expected as the Nordic grout was designed for conditions up to -10°C and the UCS results on the TDS show that strength decreased from -5°C to -10°C . The extreme dip in strength at the 28-day cure for P20 was inconsistent with expected cement strength development behaviour, this test included 3 grout cylinders which met ASTM standards. It was concluded that this was an anomaly attributed to the batching process. P20-28 was the first mixture made for these series of tests research endeavour and the grout began to set as the cylinders were being grouted. Improvements were made for subsequent Nordic batches by continuing to slowly mix the grout during entire work time (which was advised in the TDS). Observations of pre-mature cracking and oozing mixture at the bases were made for all three P20-28 UCS cylinders that were not seen in any other tests. The tensile strength development generally increased with time for P5 but was not as consistent for P20.

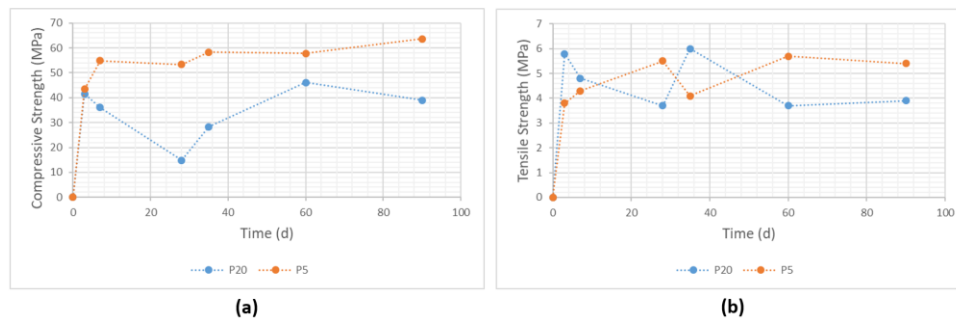


Figure 4-26. Strength development curves: (a) Grout UCS; (b) Grout STS

4.6 Discussion

The FGRB specimen behaviours during pull-out testing were observed at the micro-strain scale owing to the 0.65 mm spatial resolution of DOS technology. The specimens generally experienced the failure mechanisms of: (1) bolt-grout interface failure and (2) grout-pipe (rock) interface failure resulting in rebar bolt

pull-out. The first mechanism is considered to be more likely in FGRBs as the shear stress at the bolt-grout interface is greater than that at the grout-rock interface due to reduced effective area. If embedment length is inadequate and the rock and grout have similar strengths, then the failure will most likely occur at the bolt-grout interface (Serbousek & Signer, 1987). In this study, the confinement pipe experienced minimal dilation as witnessed during testing from the low radial strains. For the failure at the bolt-grout interface, there are two types of failure mechanisms – dilation slip and grout shearing – as visualized in Figure 4-27. At high confinement pressure, dilation is resisted and grout shearing occurs. However, at lower confinement the lateral movement results in volumetric increase at the bolt-grout interface induces bolt movement over the grout ridges referred to as dilation slip (Vlachopoulos et al, 2018).

From the post-test forensics, mainly grout shearing was observed as expected from the high confinement pressure of the pipe, however, some slip was observed notably in the first 100 mm. This was likely a result of decreasing confinement and grout integrity due to grout mobilization from the second failure mechanism. Grout-pipe interface failure is a result of an improper bonding surface between the grout and confinement pipe. As seen in Figure 4-20, the grout had mobilized outside of the borehole, which was observed to some extent across all specimens. The interior of the pipes had been cleaned prior to specimen assembly of any debris and lubricant oil from the cutting process. However, the smooth steel pipe interior may not have had adequate surface texture to provide proper mechanical interlock, especially, at the top portions of the system that was subjected to the most stress. As the shear stress increased with loading at the top of the pipe, the shear strength of the interface was exceeded and mechanical interlock failed, incrementally friction was activated until the grout was fully mobilized.

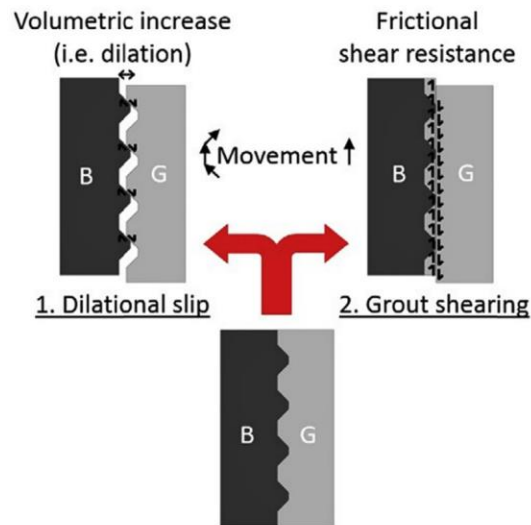


Figure 4-27. Bolt-grout interface failure mechanisms (Vlachopoulos, 2018)

4.6.1 Strain Profile Comparisons

The strain profiles and mobilized embedment length of each specimen were compared within their own curing conditions in order to observe trends as curing duration increased. Some specimens either had fully or partially non-functioning ϵ DOS (i.e. no strain data or only from one side or partial length). Examples at low (20 kN) and high (100 kN) loads for P5 and P20 are seen Figure 4-28 and Figure 4-29, respectively. For both conditions, the strain profiles observed had exponential decay along the embedment length, which is in-line with the expected behaviour of FGRBs. The mobilized embedment lengths increased with loading. In general for P5 condition, the shorter curing durations (i.e. 3 and 7 day) experienced higher strains at the same distance along the rebar compared to the longer curing duration specimens, thus, the support system required time to stabilize and achieve higher capacity. For the P20 condition, the strain trends were not consistent due in part to the greater variations in the grout UCS between specimens, which is discussed in the following section.

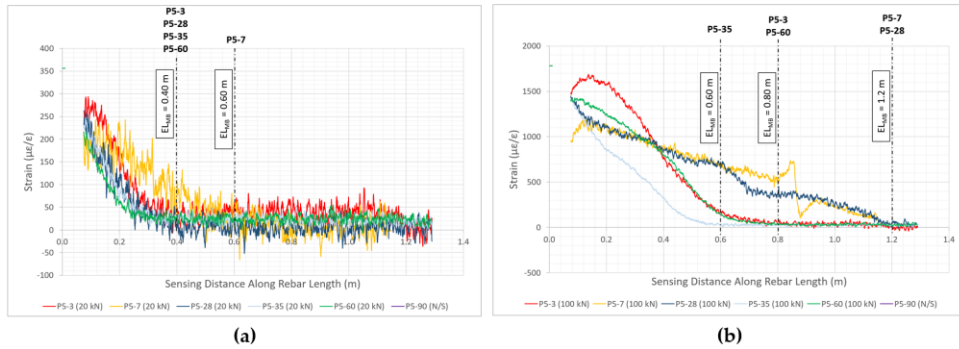


Figure 4-28. P5 Condition comparison of strain profiles and mobilized embedment length: (a) at 20 kN; (b) at 100 kN

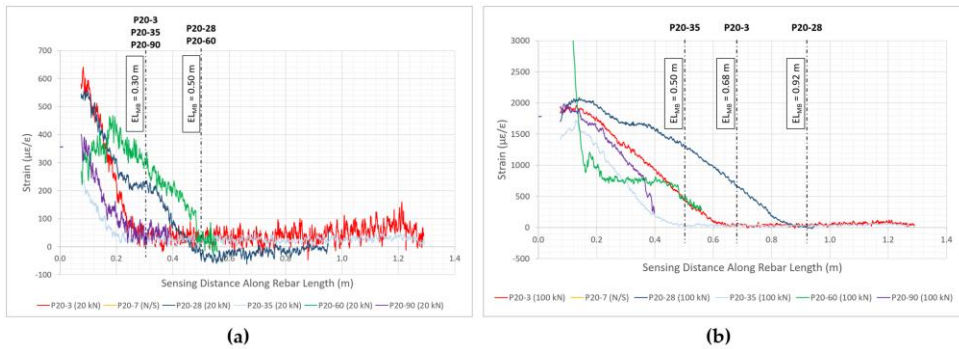


Figure 4-29. P20 Condition comparison of strain profiles and mobilized embedment length: (a) at 20 kN; (b) at 100 kN

The critical embedment length is the minimum length that expends all bolt tensile capacity and is a key component to determining the design length of rock bolts. The critical embedment length can be systematically evaluated through monitoring the bolt's complete strain profile to determine where the stress distribution attenuates to zero (Cruz, 2017). The yield critical embedment lengths for the P5 and P20 conditions were determined as a whole of all their respective specimens at 120 kN (Rebar F_y) since the design and application of FGRBs would not exceed the bolt's yield strength. Figure 4-30 shows the critical embedment length for P5 condition was 1.2 m and P20 condition was 1.0 m. It was noted that P20 specimens did experience more ϵ DOS failures thus results are based on fewer samples.

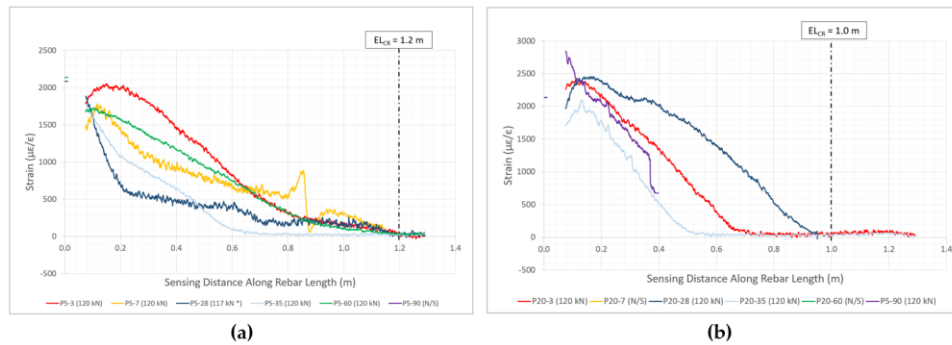


Figure 4-30. Critical embedment length at 120 kN: (a) P5; (b) P20

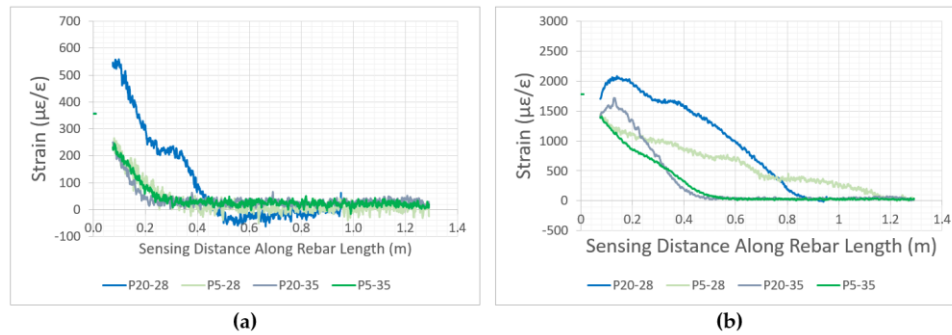


Figure 4-31. Comparison of strain profiles between P5 and P20 at 28-day and 35-day cure: (a) at 20 kN; (b) at 100 kN

The strain profiles were also compared between the two conditions, example in Figure 4-31 shows results at 28- and 35- day curing. In general across all specimens, P20 specimens experienced higher strains at the same distance along the rebar when compared to P5 specimens at the same curing duration. Therefore, as the temperatures decreased, the FGRB specimens experienced higher internal stresses at the same applied load. Strain attenuation patterns (i.e. mobilized embedment lengths) did not observe a consistent trend in the comparisons.

4.6.2 Capacity Development

The maximum loads of the specimens were compared with curing temperature as well as curing duration in order to assess the capacity development in P5 and P20 conditions. The plot in Figure 4-32 shows the development over curing temperatures and also includes temperatures from the geothermally active condition that was investigated concurrently with this study (detailed in a separate

article). The extended temperature range was presented in order to provide a more complete picture of temperature effects. All variables, except for curing temperature and type of grout, were the same in both investigations were the same. In general there is positive correlation between maximum load and curing temperatures for the permafrost conditions. However impacts of grout UCS must also be considered as the P20 specimens had a greater variation since the Nordic grout was designed up to -10°C. For an overall assessment, the 3-day capacity curve has the most variation across the curing durations, which may be due to the short time for curing and support system stabilizing. As duration increases to 90 days, the systems across all conditions generally achieve similar ultimate capacities

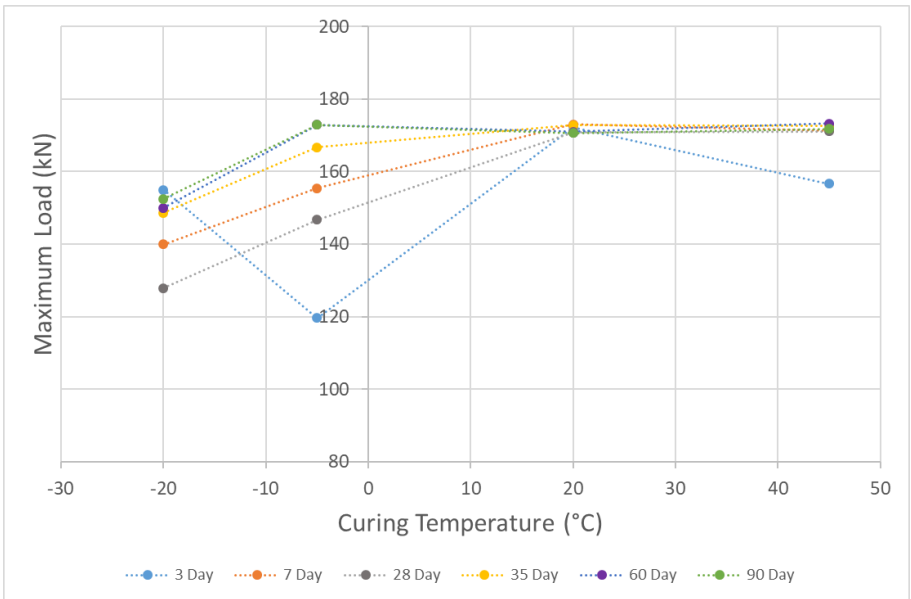


Figure 4-32. Maximum load vs curing temperature

The capacity development over time is seen in Figure 4-33. The P5 condition had a more of a positive correlation ($R^2 = 0.59$, $p = 0.08$) of increasing capacity with curing duration compared to that of the P20 condition ($R^2 = 0.08$, $p = 0.59$), which did not have a significant correlation between duration and maximum load. The capacity at 3-day cure at P5 condition was significantly lower than all other curing durations, thus, consideration should be made when to load the system. As compared to the P20 condition that had higher 3-day capacity but generally overtime the capacity did not significantly increase. However, there was the UCS

anomaly at 28-day for P20 that likely impacted the capacity. The trend of the load vs duration closely resembles that of the grout UCS development curve.

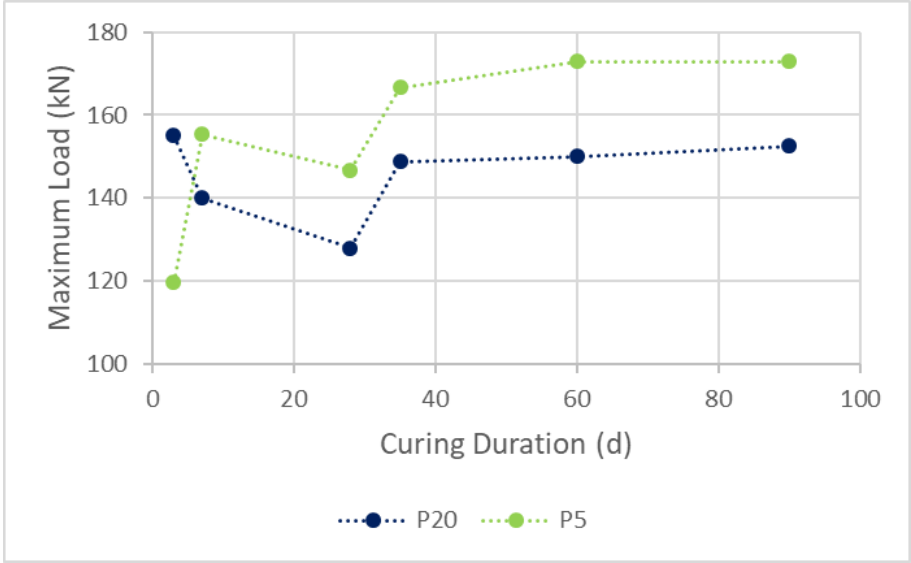


Figure 4-33. Maximum load vs curing duration

Multiple Linear Regression (MLR) analysis was completed using an open-source analysis software JASP version 0.18.3.0 (JASP Team, 2024) to statistically determine the significance of impact of curing time and grout UCS on maximum load. The R^2 indicates the amount of variance that can be predicted by the independent variable of the model (Gross-Sampson, 2024), the p-value indicates statistical significance (typically 0.05) (Alexopoulos, 2010). The coefficients specify whether there is a positive or negative correlation between the variables and how the dependent variables change when the independent variable changes, unstandardized coefficients are associated with one unit change whereas standardized coefficients are associated with one standard deviation change. The results of the analysis are found in Table 4-9. There was a positive correlation of grout UCS on maximum load, while cure time was a weak predictor. The removal of the outlier at P20-28 did not improve curing time as a predictor, thus, grout UCS had a more significant impact on results than time. In addition, regression analysis was completed to determine the significance of the effect of the specimen temperature changes on the results comparing total temperature change to maximum load. The analysis concluded that the temperature change during setup

and testing did not significantly impact results with $R^2 = 0.03$ ($B = -0.61$, $SE = 1.21$, $p = 0.62$).

Table 4-9. MLR coefficients of curing time and grout UCS on max load

Model H ₁	R ²	Unstandardized	Standard Error	Standardized	t	p
(Intercept)	0.63	112.36	11.08		10.15	<.001
Cure Time		0.20	0.11	0.28	1.80	0.11
Grout UCS		0.70	0.25	0.60	2.82	0.02

Although a long embedment length (for laboratory testing conditions) and competent confinement material (i.e. rock) were employed in this study, all but one (P5-90) of the specimens in both permafrost conditions failed by pull-out. The entire ϵ DOS on P5-90 did not function thus, strain profile comparisons were not able to be used for forensic purposes. The location of rebar tensile failure, as seen in Figure 4-34, was different from other rebar breaks observed in geothermally (i.e. hot) active conditions as it was inside of the embedment length rather than midway between the MTS grip and borehole collar. Generally in existing literature, shorter embedment lengths result in bond failure at the bolt-grout interface and longer embedment lengths result in bolt failure (Li et al, 2016; Cruz, 2017). The failure of the grout-pipe interface may have considerably impacted the testing and resulted in pull-out observations (i.e. bolt-grout interface was not sole governing factor). When compared to the specimens in the geothermally active conditions that utilized Portland cement grout at the same embedment lengths, majority of the specimens resulted in rebar tensile failure. Selected specimens also had minimal grout mobilization at the end of testing. Thus, the mechanical interlock or friction between PC grout and the pipe could have been greater than the case with Nordic grout and the pipe, allowing the bolt-grout interface to govern in the geothermal conditions. A qualitative difference was observed between the grouts' texture. Further testing should be conducted with confinement pipes that have roughness added in order to verify the ultimate failure mechanism of the permafrost conditions.



Figure 4-34. P5-90 specimen rebar tensile failure inside of embedment length, green tape marks location of borehole collar

4.6.3 Axial Stiffness

Further analysis was conducted to determine the factors affecting the system. Axial stiffness was determined for each specimen as a whole system, as well as, the rebar bolt using the quasi linear portion of the load-displacement curves from the conventional instruments and the ϵ DOS. The results are found in Table 4-10, with axial stiffness derived from the conventional system accounting for the whole support system and axial stiffness from the DOS just that of the rebar, hence the order of magnitude difference, which was also seen in the axial stiffness results of Cruz (2017). The whole system corrected accounts for adjusting the axial displacement (i.e. actuator stroke) with the LVDT monitoring the top plate as well as elongation for the portion of the rebar outside of the embedment length. For comparisons, axial stiffness of the whole system was used. Initial comparisons of the axial stiffness, the range of results for the P5 condition were higher than that of the P20 condition for both the rebar and when considering the whole system.

Table 4-10. Axial stiffness

Specimen	Axial Stiffness (kN/mm) – DOS ¹	Axial Stiffness (kN/mm) - Whole System ²	Axial Stiffness (kN/mm) - Whole System Corrected ²
P20-3	129.8	14.8	18.8
P20-7	-	-	-
P20-28	89.9	15.0	15.4
P20-35	233.1	23.2	-
P20-60	193.4	-	-
P20-90	170.3	28.4	34.9
P5-3	192.5	25.3	53.4
P5-7	133.0	-	-
P5-28	276.6	24.0	52.3
P5-35	282.7	27.1	99.5
P5-60	295.0	24.8	28.4
P5-90	-	28.0	-

¹ Blank entries due to ϵ DOS not functioning

² Blank entries due to missing data from DAQ or LVDT malfunctions

The axial stiffness was compared against grout UCS, mean bond strength, and yield critical embedment length (taking the average of the specimens) as seen in Figure 4-35. The data sets are comprised of singular measurements at each curing duration, therefore, the confidence interval (alpha 0.05) displayed in the (b) plot is based on the mean values of axial stiffness and grout UCS per curing condition (i.e. P20, P5, C20, and G45); the purpose is to present the data variation within the curing condition. The comparison of critical embedment length includes geothermal conditions in order to have more data points for effective analysis as the critical lengths were determined per condition. The mean bond strength was calculated using Equation 10.

$$s = \frac{P_{max}}{\pi d_b L_e} \quad (10)$$

where, s , is the mean bond strength, P_{max} is the load at pull-out, d_b , is the bolt diameter, and L_e , is the embedment length. MLR analysis of grout UCS and mean bond strength were completed for axial stiffness – DOS (Table 4-11) and for axial

stiffness – whole system (Table 4-12). The correlation of the grout UCS and the mean bond strength with axial stiffness – DOS determined that the former was a more significant predictor ($p = 0.06$, which is close to 0.05 for statistical significance) than the latter. The correlation with axial stiffness – whole system was weaker with less variation and lower statistical significance. Regression analysis of axial stiffness – DOS and yield critical embedment length for the whole spectrum of temperature conditions found a negative correlation ($R^2 = 0.74$, $p = 0.14$) between the factors but may not be a significant factor. However when considering the whole system, there was not a significant correlation and had low statistical significance ($R^2 = 0.28$, $p = 0.47$).

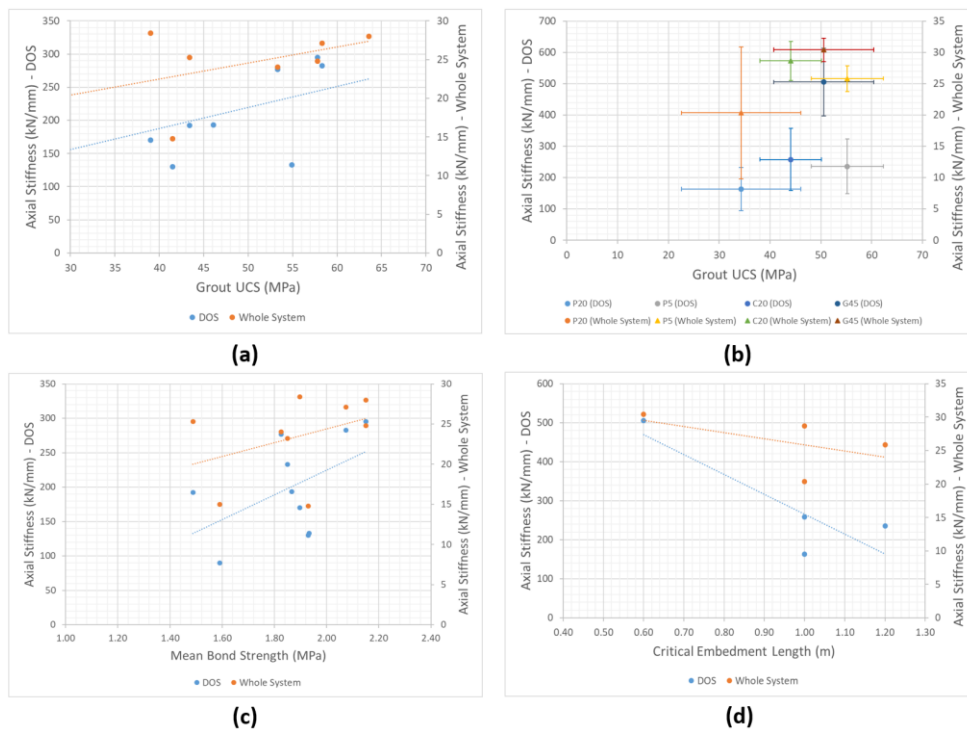


Figure 4-35. Axial stiffness comparisons: (a) Grout UCS; (b) Confidence interval (alpha 0.05); (c) Mean bond strength; (d) critical embedment length

Table 4-11. MLR coefficients of grout UCS and mean bond strength on axial stiffness - DOS

Model H ₁	R ²	Unstandardized	Standard Error	Standardized	t	p
(Intercept)	0.50	37.86	69.14		0.55	0.60
Grout UCS		3.14	1.42	0.61	2.21	0.06
Mean Bond Strength		0.70	0.70	0.28	1.00	0.35

Table 4-12. MLR coefficients of grout UCS and mean bond strength on axial stiffness – whole system

Model H ₁	R ²	Unstandardized	Standard Error	Standardized	t	p
(Intercept)	0.60	13.41	3.99		3.36	0.02
Grout UCS		0.16	0.09	0.48	1.75	0.13
Mean Bond Strength		0.07	0.04	0.46	1.69	0.14

The effects of temperature and curing duration compared against axial stiffness are seen in Figure 4-36, the full temperature spectrum is included. Linear regression found positive correlation of axial stiffness (both) with temperature as the R² values for each curing duration was between 0.70-0.96 and p values between 0.03-0.14. The curing durations that observed the highest correlation and significance for axial stiffness – DOS were 7-day and 60-day. The curing durations that observed the highest correlation and significance for axial stiffness – whole system were 35-day and 60-day. The 7-day specimen for the whole system was removed from the analysis due to a lack of data. Therefore, as the curing temperature decreases, generally, so does the axial stiffness of the support system, which in turn affects the displacements that would be observed at the boundaries of underground excavations.

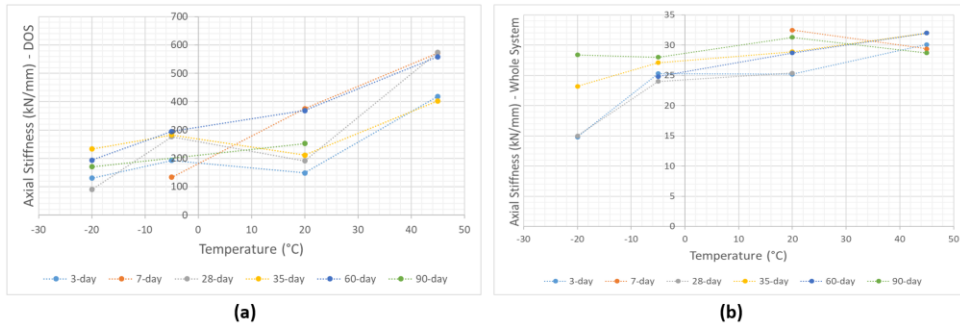


Figure 4-36. Axial stiffness plotted against temperature: (a) DOS – rebar; (b) Conventional instruments – Whole system

4.6.4 DOS Performance in Cold Temperatures

All monitoring instrumentation installed on the FGRB specimens' operating temperature range specifications had been verified to include the testing temperatures of this study, as seen in Table 4-13. Every ϵ DOS and T DOS was confirmed to be operational prior to specimen assembly, however, several ϵ DOS were found to either be partially or wholly non-functional during testing setup (majority from P20 condition) thus, strain profiles did not always include the entire embedment length and/or only had data from only one side of the rebar specimen which is still quite telling. The main cause of these sensor failures has been assessed to be the looping groove at the tail end of the rebar. The low temperature likely caused the fiber optic to become more brittle and affected the minimum operating radius and DOS failure.

Table 4-13. Summary of monitoring instrumentation operating temperature ranges

Instrument	Details	Operating Temperature (°C)
Strain Gauge ¹	N11-FA-5-120-11	-30 to +80 ²
Sensing Fiber	Corning® SMF-28e+	-60 to +85 ³
	SM1550P Fiber Polyimide	-190 to +350 ⁴
Termination Fiber	FG125LA Coreless	-40 to +85 ⁵
LC Connection	Patch Cable	-20 to +70 ⁶

¹ Mounting adhesive (M-Bond 200) operating temperature range works (Micro Measurements, 2014)

² SHOWA Measuring Instruments, 2022

³ Corning, 2021

⁴ ThorLabs, 2024b

⁵ ThorLabs, 2024a

⁶ Fiber Instrument Sales, n.d.

A verification of this DOS technique’s temperature spatial resolution was assessed with selected T DOS data, seen in Figure 4-37. The slopes of the converted temperature change results (Table 4-8) were used to interpolate the timestamps and the average strains along the T DOS were found. The DOS temperature spatial resolution was assessed to be 0.1°C, which is in agreement with the results of Gifford et al. (2005).

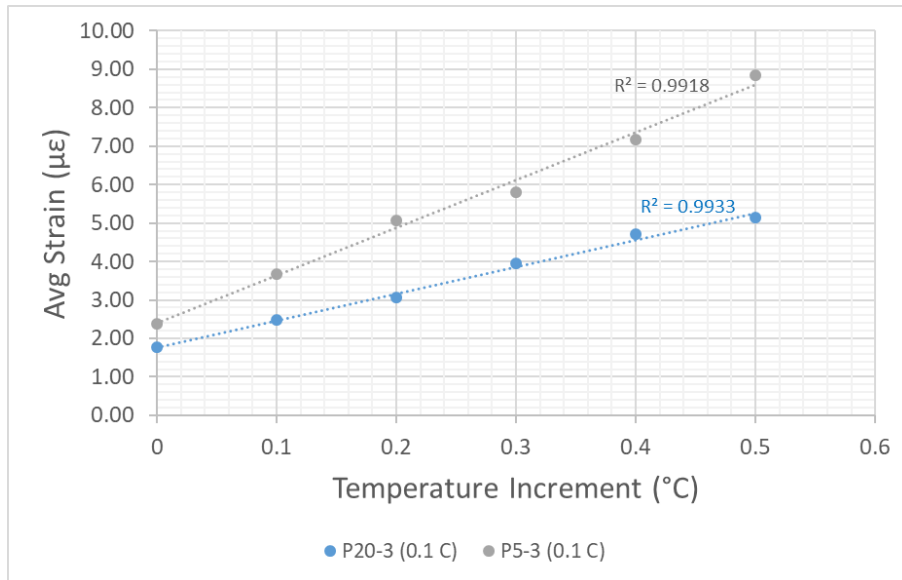


Figure 4-37. DOS temperature spatial resolution verification

4.7 Conclusions

A series of laboratory pull-out tests using DOS were conducted to investigate the effects of permafrost temperature conditions in the specific temperature regime on the performance and capacity development of FGRBs. General trends of strain distribution found that specimens cured at -20°C experienced higher strains along the embedment length compared to those cured at -5°C for the same duration of time and at the same applied load. As well, at the same load, shorter curing duration specimens generally experienced higher strains than the longer curing specimens in the -5°C condition, trends at -20°C cure condition were not as consistent due to higher variations in grout UCS. Therefore, for underground projects, in -5°C permafrost conditions considerations for incremental loading of the support systems in the short curing duration should be made during the design process and this study found that capacity results stabilized at 35-day cure. In -20°C conditions, the grout mixture used in this study was not specifically designed for this temperature, however, it was able to hydrate and gain sufficient strength. The capacity of the specimens also stabilized at 35-day cure but were 10% less than in the -5°C condition. The much colder temperatures pose a challenge for the grouting of FGRBs as the UCS of the Nordic grout was affected by the curing temperature,

as well, mixture procedures and consistency significantly impact the grout. Regression analysis concluded a positive correlation of grout UCS on the capacity of the FGRB, while cure duration was not a significant predictor. Axial stiffness of the rebar and whole support system were used for further analysis and comparisons. Grout UCS and mean bond strength were compared and MLR results determined that the former was a more significant predictor of axial stiffness of the rebar, whereas, neither are statistically significant in predicting whole system axial stiffness. Temperature was found to have positive correlation with axial stiffness (both), thus, as the curing temperature decreases, generally, so does the axial stiffness, which in turn affects the displacements of the support systems. The DOS technique was able to capture continuous strain profiles in cold temperatures and act as an effective temperature monitor for such specimens, with the spatial resolution assessed as 0.1°C. However, the sensor operation life and length were affected by the very cold curing temperatures and removal of the loop is recommended. Additional testing should be conducted in the future in order to verify the failure mechanism(s) associated with pull-out testing in cold temperatures with boreholes prepared with increased roughness.

Acknowledgments: The authors would like to acknowledge support from the Royal Military College of Canada, the RMC Green Team, Sika Canada Inc., the Department of National Defense, and the Natural Sciences and Engineering Research Council.

Conflicts of Interest: The authors declare no conflicts of interest.

5 Investigating the Effects of Geothermally Active Temperature Conditions on Fully Grouted Rock Bolts with Distributed Fiber Optic Sensors

This chapter consists of the journal article that is planned to be submitted to a peer-reviewed journal. This article describes the methodology and testing scheme, along with presenting selected results of the laboratory testing related to high temperature curing conditions.

Article

Investigating the Effects of Geothermally Active Temperature Conditions on Fully Grouted Rock Bolts with Distributed Fiber Optic Sensors

Chuyue (Chelsey) Guo ¹, Kieran Moore ¹ and Nicholas Vlachopoulos ¹

¹ Department of Civil Engineering, Royal Military College of Canada, Kingston, Ontario, K7K7B4, Canada

Abstract: A series of laboratory pull-out tests were conducted on fully grouted rock bolt (FGRB) specimens cured at specific temperature range as well as for different durations in order to study the effects of temperature on their performance, behaviours and capacity development. 20M rebar specimens at 1.3 m embedment length were used with 0.4 water-to-cement ratio (w/c) Portland cement (PC) that was used as grout and a confining steel pipe representative of granite. Two temperatures (20°C and 45°C) were explored to investigate the effects of geothermally active (i.e. hot) temperature conditions on FGRBs. Distributed fiber optic sensors (DOS) were employed to provide a continuous strain profile (with a spatial resolution of 0.65 mm) along the entire rebar and observe micro-mechanisms during testing. The specimens cured in 45°C generally resulted in higher grout UCS (in certain cases 50% higher) compared to specimens cured in 20°C; the ultimate capacity was not significantly impacted as the specimens' embedment length allowed full development of the rock bolt's capacity. However, at 3-day cure the 45°C specimen test ended in pull-out in contrast to all other tests for 20°C and 45°C that reached rebar ultimate strength, thus, higher temperatures may affect the initial capacity development of FGRBs. This paper highlights the results of this study and aim to bridge selected gaps in existing literature with a view to aid practitioners.

Keywords: Fully grouted rock bolt; Fiber optic technology; Geothermally active; Hot temperature effects; Stress distribution; Pull-out test

5.1 Introduction

Rock bolting is a common form of ground support in tunnelling and underground excavation projects and forms a zone of reinforcement with a view to maintain the confinement pressure so that the rock mass remains self-supported. Fully grouted rock bolts (FGRBs) are one of the most popular types of rock support due to their versatility and adaptability to a wide range of ground conditions. Increasing global concerns on climate change and the effects of greenhouse gases (GHGs) is pushing industries to more sustainable practices. Approximately 15% of the electrical power produced in Canada is a result of nuclear power generation, with the majority of plants located in Ontario (World Nuclear Association, 2023). The long-term management plan of used nuclear fuel will be containment and isolation within deep geological repositories (Nuclear Waste Management Organization, 2023). Geothermally active temperature conditions can potentially affect the performance of FGRBs. The long-term stability of repositories is vital for health and safety and the performance of FGRBs is key to the stability of such underground works, as well, as mining operations that are pushing deeper and into higher temperatures (such as virgin coal mines (Belle & Biffi, 2018)). The employment of distributed fiber optic sensors (DOS) to capture the mechanical response of FGRBs in pull-out testing provides a continuous strain profile and can also be used to monitor changes in temperature – during construction and during the service life of underground infrastructure. This paper presents relevant background into the research project and select results and analysis from laboratory testing.

5.2 Background

Canada has generated electrical power for over half a century using the CANDU nuclear reactors and a by-product of the process is spent nuclear fuel. CANDU fuel, which is the main nuclear fuel in Canada, is a solid that consists of uranium dioxide. Existing used nuclear fuel is temporarily stored at or near power generation sites. The Adaptive Phased Management (APM) is Canada's plan for the long-term management of used nuclear fuel, which will be contained and isolated in a deep geological repository between 500-1000 m below ground (Nuclear Waste Management Organization, 2023). This approach is in-line with best practices of the international community for high-level radioactive waste (HLRW), which require isolation periods of 10^5 to 10^6 years. Deep geological repositories provide a

significant geological barrier for the waste and decrease the risks of future condition changes as the effects of changes decrease with depth (Gibb, 1999). The general design of deep geological repositories includes a series of shafts and tunnels with the containment of the HLRW canisters inside a buffer material (commonly bentonite) and surrounded by the natural geological barrier (i.e. surrounding rock) (King et al, 2017; Xue et al, 2021). An example of such a facility seen in Figure 5-1.

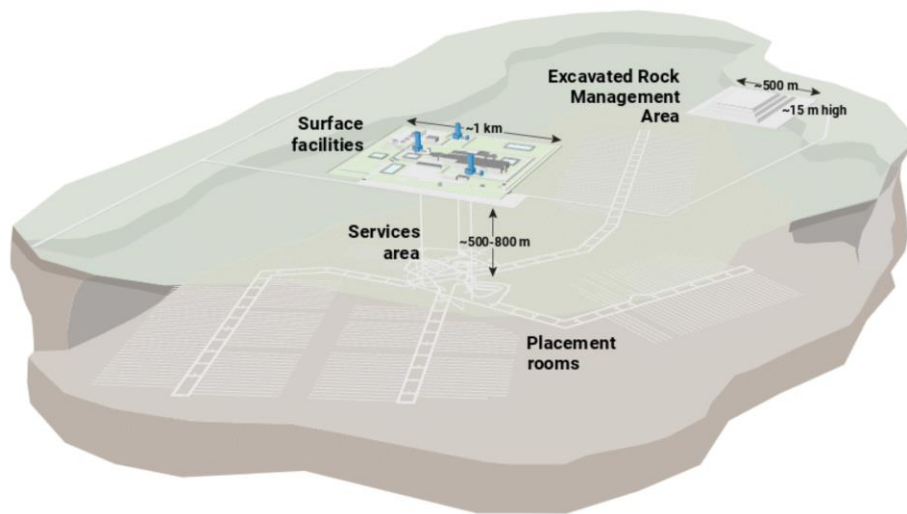


Figure 5-1. Schematic of deep geological repository plan by NWMO (Nuclear Waste Management Organization, 2023)

Xue et al. (2021) presented mathematical models as solutions for temperature development and distribution during the exothermic process of nuclear waste. The typical thermal criterion for peak temperature at the surface of the canister or interior of the buffer material is 100°C in order to control thermal stress and maintain mechanical stability of the repository. The temperature decays exponentially with distance from the canister centre in the local solution and slowly decreases at the global scale. The average temperature first increases with disposal time and then decreases.

A Rock bolt in the most basic form consists of a plain steel rod that is mechanically or chemically anchored into the rock mass on one end and a faceplate and nut on the other (Vlachopoulos et al, 2018). As seen in Figure 5-2, the rock bolt transfers the load from the unstable region (pink zone) close to the excavation, past the boundary of instability, to the more stable rock mass (or ground) further at

depth (grey zone) (Vlachopoulos, 2017). FGRBs create a bond between the rock mass and reinforcement element along the entire length of the bolt, providing an extended shear surface for load transfer along the support element (Signer, 1990).

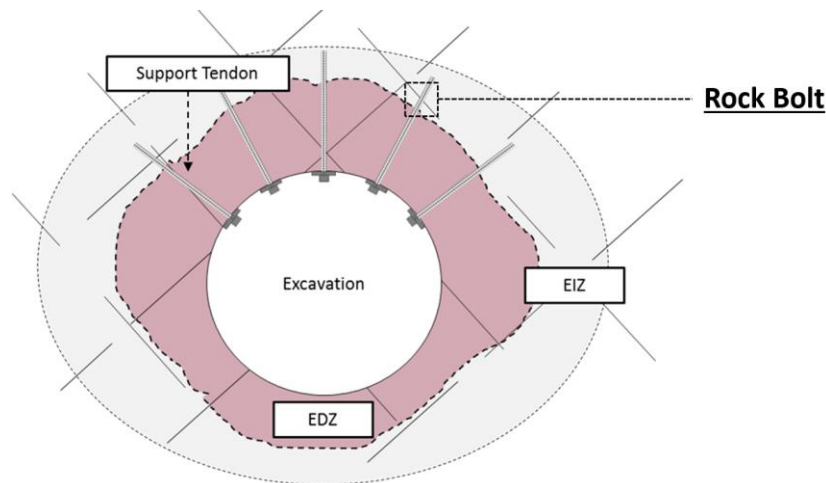


Figure 5-2. Load transfer mechanism of rock bolts (modified after Vlachopoulos, 2017)

Pull-out tests are one of the most common methods of quantifying the performance of rock bolts. The distribution of axial stresses in the bolt and bolt-grout interface resemble an exponential decay curve for full length specimens (Serbousek & Signer, 1987). Various laboratory and field investigations have been conducted to form analytical models with a view to improve the understanding and describe the behaviours of FGRBs (Farmer, 1975; Benmokrane et al, 1995; Li & Stillborg, 1999; Cai et al, 2004; Ren et al, 2010; Ma et al, 2013). However, a full range understanding of the geo-mechanical response of FGRBs still does not exist due in part to past technological limitations of monitoring instrumentation and, specifically, their lack of spatial resolution. Historical research has typically employed discrete monitoring techniques such as strain gauges (SGs), dial gauges, and linear variable displacement transducers (LVDT) (Signer, 1990; Farmer, 1975). Strain profiles between sensing points must be interpolated, thus, any localized phenomenon in between these monitored points may be missed. Continuous strain monitoring has been achieved using a distributed fiber optic sensors (DOS) technique developed by the research group of the authors, achieving a spatial resolution of 0.65 mm (Vlachopoulos et al, 2014; Vlachopoulos et al, 2018). The technique leverages Rayleigh Optical Frequency Domain Reflectometry (ROFDR). When light is sent through an optical fiber, an index profile is created. Rayleigh

backscattering results from random variations in the profile with the scatter amplitude being a function of the distance along the fiber. External factors, such as strain and temperature, cause a spectral shift that can then be calibrated for use as a distributed sensor (Gifford et al, 2005). The use of DOS captures geo-mechanisms associated with axial loading. As well, its use improves conformance as compared to SGs since the fiber is embedded into the rock bolt and does not affect the bolt-grout interface.

The existing research into the effects of geothermal temperatures on FGRB behaviour is limited. Lahouar et al. (2017) presented a study on resin anchors at high temperatures and outlined the non-conservative design issues with existing codes. Although this study was not rock bolt specific, its results can provide insight into the chemical reactions of grouted members to temperature. Li et al. (2017b) tested specimens of 1000 mm embedment lengths at 20°C, 35°C, and 50°C. The rate of exponential decay of axial force and shear stress decreases along the embedment length as temperature increased, with the slowest being at 50°C. However, with an increase in temperature, the maximum shear stress on the bolt-grout interface decreased and its distribution along the embedment length became more uniform thus, concluding that FGRBs are not greatly impacted by geothermal activity. Wang et al. (2018) and Li et al. (2017a) tested short embedment lengths of 100 mm with cement grouts from 20°C to 70°C to study the effects of high temperatures and roughness. Both studies concluded an influence on the pull-out strength of FGRBs with an initial increase between 20°C and 35°C, then a decrease between 50°C and 70°C. Roughness also had an influence on pull-out strength of grout materials. In addition, Li et al. (2017b) through regression analysis proposed the relationship between temperature and ultimate strength followed a cubic polynomial function. All aforementioned studies utilized conventional instrumentation in order to monitor their test setups and specimens.

5.3 Methodology

A series of laboratory pull-out tests were conducted in order to study the effects of a geothermally active temperature condition on FGRBs and understand the development of FGRB capacity overtime in these conditions. A set of specimens cured at 20°C (control) and a set of specimens cured at 45°C were tested. Pull-out tests and grout properties tests were conducted at 3, 7, 28, 35, 60, and 90 days. This study was conducted concurrently to a cold temperature investigation (detailed in a separate paper) to better understand a wide spectrum of

temperature effects on FGRBs. The specimens were instrumented with DOS and cured in temperature-controlled chambers. The most recent preparation and testing procedure that is highlighted herein is a summation of the iterative development process from the author's research group (Forbes, 2015; Cruz, 2017; O'Connor, 2020; Moore, 2021). The methodology was modified in order to monitor strain and temperature changes of the FGRB specimens continuously along the entire embedment length simultaneously during testing.

5.3.1 Rebar Bolt Preparation

20M 400W (\varnothing 19.05 mm) rebar at 1600 mm lengths were procured from Kimco Steel Sales Ltd. Two diametrically opposing grooves (3 mm x 4 mm) were machine grooved into the bars by a local machine shop. The size of the grooves were increased from those previously used by previous investigations by group members in order to install two sets of DOS, one for temperature monitoring and one for strain monitoring. Moore (2021) relocated the grooving to the longitudinal ribs instead of the transverse ribs with a view to improve conformance by decreasing impacts on mechanical interlock and load transfer. As such, this grooving orientation was also followed for this investigation as seen in Figure 5-3. The bars and grooves were cleaned prior to DOS installation using a drill with a wire cup brush attachment, steel brush, acetone, and compressed air for rust and debris removal. Prototype testing was completed as proof-of-concept testing for the new DOS configuration and confirmation of rebar material properties. These results are found in Table 5-1 and were comparable to literature values for mild steel and those of past group members (Cruz, 2017; Moore, 2021).

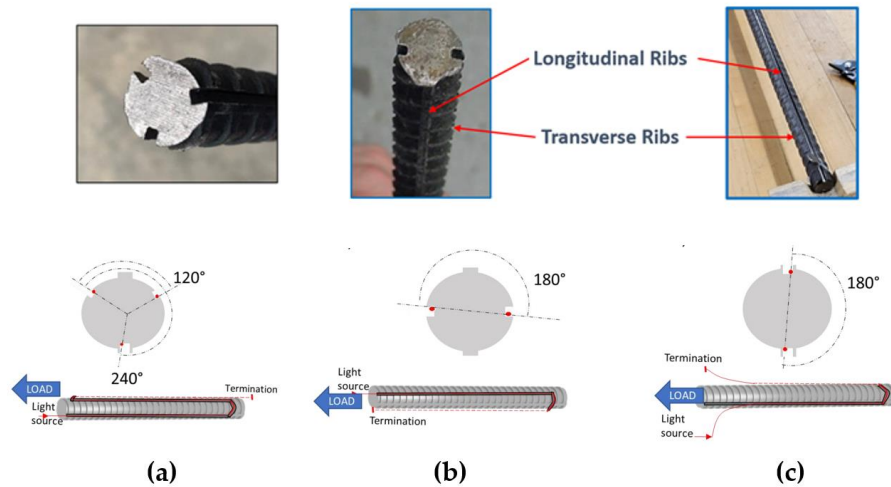


Figure 5-3. Location of machined grooves: (a) Three groove orientation; (b) Diametrically opposing grooves along transverse ribs; (c) Diametrically opposing grooves along longitudinal ribs (modified after Moore, 2021)

Table 5-1. Summary of materials testing results of the rebar

Material Property	Test Result (MPa)	Test Result (kN)
Yield Strength	460	120
Ultimate Strength	658	172
Modulus of Elasticity	200,000	-

5.3.2 DOS Installation

Two DOS were installed: 1. ϵ DOS in order to monitor the rebar strain profile during loading; and 2. T DOS in order to specimen monitor temperature change along the profile of the specimen during testing. The sensing fiber optic had been an acrylate coated fiber that had a 50 mm transition zone for strain pickup (Moore, 2021). A new polyimide coated fiber optic was tested the during prototype phase as they are considered to have immediate pickup (Weisbrich et al, 2020). Guo et al. (2023) details the investigation and results of prototype testing, the acrylate fiber was continued to be used for the ϵ DOS due to the looping requirement (i.e. to be able to monitor the strain on both sides of the entire length of the rock bolt with a single sensor) and the polyimide fiber was calibrated and used for the T DOS. The ϵ DOS

was installed as a sensing loop in order to average out any in plane bending that may have occurred during pull-out testing, with two de-bonded zones in the initial 25 mm of the embedment length. The T DOS was installed as a single sensing length that was de-bonded along the entire embedment length and anchored at the termination end, such that the strain in the rebar would not be collected by the temperature sensor. Care was taken to ensure both DOS were fully embedded into the grooves in order to not affect the bolt-grout interface and the DOS were bonded to the rebar bolt using a proprietary bonding adhesive. Positioning markers were keyed-in using a heated flathead screwdriver. The final DOS configuration is shown in Figure 5-4.

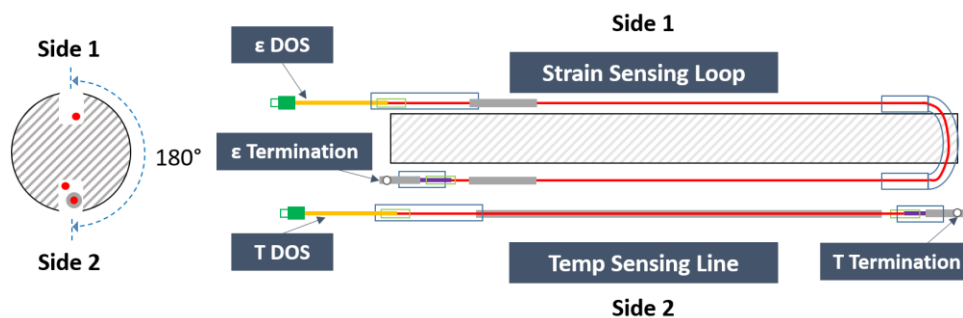
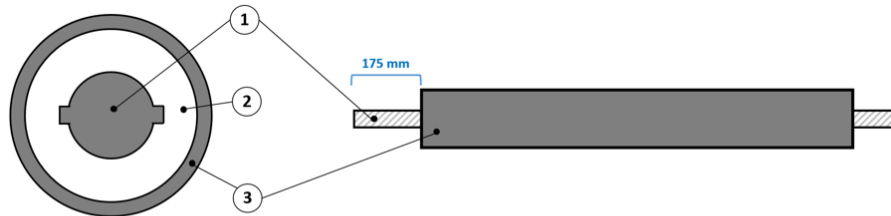


Figure 5-4. DOS configuration in diametrically opposing grooves

5.3.3 Specimen Assembly and Grouting

A total of 24 FGRB specimens were assembled according to the schematic seen in Figure 5-5 and the schedule in Table 5-2 in the laboratory. The FGRB specimen naming convention included a letter and numbers. The first letter was 'C' for control and 'G' for geothermally active (or hot) condition, followed by the numbers representing the curing temperature followed by the curing duration. The 12 FGRB specimens utilized in this cold temperature study were the ones labelled with prefix 'C' and 'G'. An embedment length of 1300 mm and a radial confinement pressure of a granitic rock (approx. 3000 MPa/mm used in this investigation as calculated using thick wall cylinder theory (Hyett et al, 1992) were achieved using schedule 80 1¼" nominal steel pipes. Pipes were refinished using a lathe in order to square the ends. Two N11-FA-10-120-11 or N11-FA-5-120-11 SGs were mounted on the pipes at 50 mm from top of the pipe to monitor the dilation during testing. The strain

gauges (SGs) were aligned perpendicular to the axial loading and positioned over the transverse ribs on diametrically opposing sides.



NTS

1: 20M 400W Rebar (\varnothing 19.05 mm, L 1600 mm)

2: PC 0.4 w/c ratio; Nordic 0.29 w/c ratio

3: 1¼" Sch 80 Steel Pipe (\varnothing_{out} 42.2 mm ; \varnothing_{in} 32.5 mm, L 1300 mm)

Figure 5-5. Schematic of FGRB specimen

Table 5-2. Specimens preparation schedule (24 total specimens)

Cure Time (days)	Number of Specimens ¹	Type of Grout	Name of Specimens
3	4	Nordic (cold) / PC (hot)	P20-3, P5-3, C20-3, G45-3
7	4	Nordic (cold) / PC (hot)	P20-7, P5-7, C20-7, G45-7
28	4	Nordic (cold) / PC (hot)	P20-28, P5-28, C20-28, G45-28
35	4	Nordic (cold) / PC (hot)	P20-35, P5-35, C20-35, G45-35
60	4	Nordic (cold) / PC (hot)	P20-60, P5-60, C20-60, G45-60
90	4	Nordic (cold) / PC (hot)	P20-90, P5-90, C20-90, G45-90

Since the grout was to be pumped into the specimen during the grouting process, a hole was drilled and tapped to fit a ½" hose barb, seen in Figure 5-6. An optimal location of the grouting hole was assessed to confirm that the pipe would

not fail at higher loads due to the reduced pipe area and balance grouting requirements. The strain profile from the most similar sized pipe used by Moore (2021) was used to find the probable stresses at different distances along the pipe. The location was determined to be 80 mm from top of pipe. The rebar had painters tape wrapped around and above the start of the embedment length in order to protect the DOS from the new grout capping method. Adhesive-lined heavy-duty heat shrink tubing was used to seal the confinement pipe during grouting, the painters tape prevented the adhesive from melting to the DOS protective coating and also acted as a reference point during pull-out testing. Prior to installation, the ϵ DOS and T DOS for each rebar bolt were verified to be operational.

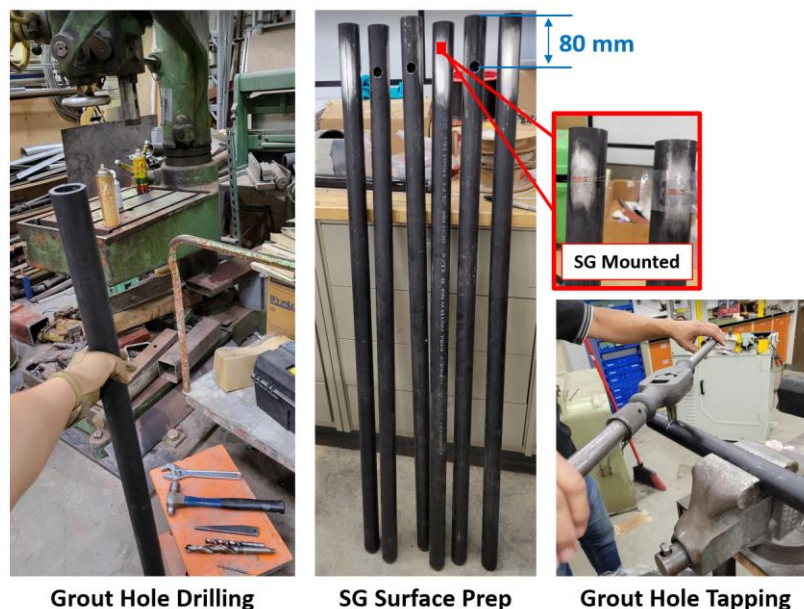


Figure 5-6. Confinement pipe preparations

The specimens were installed into the grouting racks vertically with the top (pull end) at the bottom of the rack, this orientation ensured that the grout would be flush with the top of the confinement pipe (Figure 5-7). The pipes were levelled using a torpedo level. A ½" hose barb was installed and sealed using plumbers putty as the connection point for the grout pump. The monitoring instrumentation wires were secured around hooks to protect during transport and grouting. The G45 specimens (heater room set to 45°C), grout test cylinder moulds, grouting tools and buckets were conditioned in the curing environment for at least 24 hours prior to

grouting. The C20 specimens (ambient 20°C) were conditioned in laboratory condition, thus, only requiring the ϵ DOS to be installed. The grout was a Portland Cement (PC) that was locally available (Ciment Québec Type 1 GU) mixed to 0.4 water-cement (w/c) ratio with a hand mixer in batches with sufficient amounts of grout for the specimen and corresponding strength test cylinder moulds. This w/c ratio has been typically used by the author's research group and within the optimum w/c ratio range in literature to balance grout strength and pumpability (Hyett et al, 1992; Kilic et al, 2002). The grout was placed into the pump's hopper, levels were maintained in order to avoid introducing voids into the pump, and the pump was washed and drained between batches. All specimens were externally vibrated along the entire specimen length to eliminate any potential air voids. The grout was filled to within 1-2 mm of the top of the pipe and a piece of cardboard was placed inside to centre the rebar as the grout set.

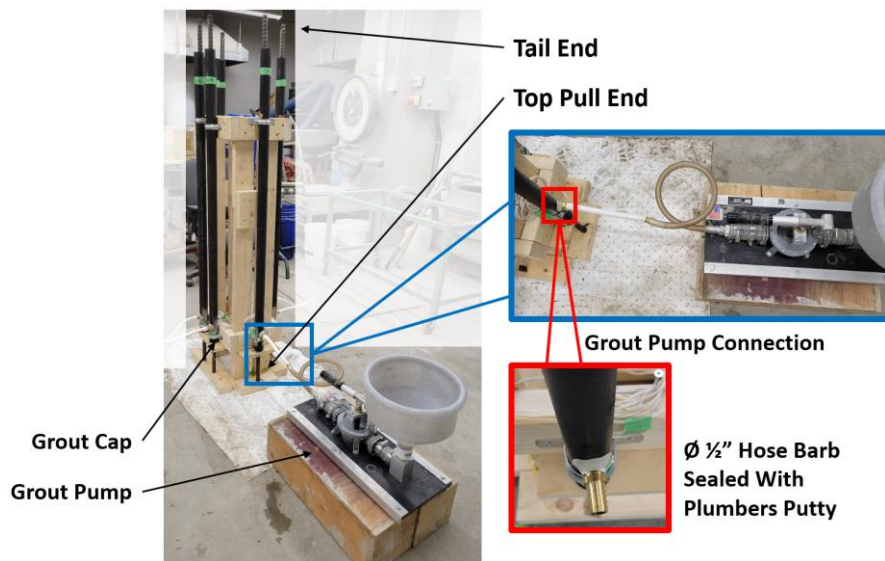


Figure 5-7. FGRB Specimen installation in grouting rack with grout pump

For the 45°C curing specimens, extra care was taken to prevent excess evaporation during grout curing as seen in Figure 5-8. The exposed ends of the confinement pipes were wrapped with several layers of painters' tape and the grout strength test cylinders were covered with sheets of vapour barrier.



Figure 5-8. Evaporation protection of FGRB specimen ends and grout cylinders

The temperatures of the G45 curing chamber was verified throughout the entire test period of 90 days with a Traceable® Extra-Long-Stem thermometer and had a variation of $\pm 1^{\circ}\text{C}$. The C20 condition was monitored with a Traceable® Thermo-Hygrometer for temperature and humidity. The laboratory ambient temperature had a variation of $\pm 2^{\circ}\text{C}$ and humidity range of 33-56%. There were two power outages (2-4 hours) and a campus maintenance power shutdown of 8 hours during the testing period.

Prior to pull-out testing, the grout cap and hose barb were removed and the G45 specimens were wrapped with a thermal-reflective blanket (pre-conditioned in the heater room) to reduce the changes in temperature during testing. Any grout outside of the tail end of the pipe was chipped off. The heat shrink tubing cap method had sealed the end of the pipe and around the rebar, which resulted in a flat and flush grout surface, an improved finish from past capping methods.

5.4 Laboratory Testing Program

The series of pull-out tests were conducted within the RMC structures laboratory on the 12 instrumented FGRB specimens. The tests were performed using a 322.41

MTS with a capacity of 500 kN outfitted with the testing rig and monitoring setup. This set-up can be seen in Figure 5-9. This test rig is the same as has been used by previous investigations conducted by the author’s research group and is representative of full-scale anchorage length axial loading (Cruz, 2017; O’Connor, 2020; Moore, 2021). In addition, a series of material testing were conducted to quantify the material properties of the grout and confirm the properties of the rebar (as described previously). The proof-of-concept investigation and results are presented in Guo et al. (2023). Each FGRB specimen had grout strength test cylinders casted and cured for their corresponding durations and tested for uniaxial compressive strength (UCS) testing and splitting tensile strength (STS) testing. A total of 36 UCS tests and 36 STS tests were completed using a 300,000 lbs RIEHLE Testing Machine.

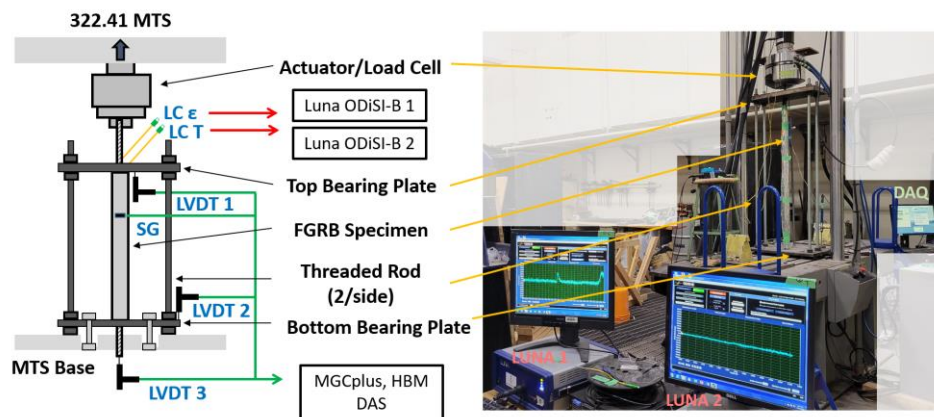


Figure 5-9. Laboratory pull-out test assembly and monitoring setup

5.4.1 Monitoring Program

The FGRB specimen was placed between a 1.5” top steel bearing plate and 1” bottom steel bearing plate, affixed by four 1” coarse threaded rods and nuts. The top plate was lifted and lowered using a lifting contraption placed over the MTS actuator and the bottom plate was mounted to the MTS base using four ¾” bolts. Two LVDTs were mounted on independent retort stands to monitor any movement in the bearing plates during testing. A third LVDT with a washer attached to its tip was placed under the MTS on an independent retort stand to monitor the free tail-end of the rock bolt in order to monitor any potential slip in the rebar. The two SGs

mounted to the confinement pipe were connected to a quick connect junction box. The conventional instrumentation was connected to the DAQ (MGCplus, HBM Catman). The ϵ DOS and T DOS were connected via to two extension boxes to 2 independent units with one channel, Luna ODiSI-B analyzers. The monitoring instrumentation settings, locations, and measurement uncertainties are detailed in Table 5-3, Table 5-4, and Figure 5-10. All monitoring instruments were calibrated prior to testing commencing. The testing machines were professionally calibrated by VACS Calibrations between 14-15 August 2023. For pull-out testing, the DAQ and two Luna analyzers were synchronized by simultaneously starting data collection. Specimen loading started at 1 mm/min and increased to 2 mm/min at approximately 130-140 kN.

Table 5-3. Sensor details and locations

Instrumentation	Range	Location	Measured Parameter
Load Cell	500 kN	MTS	Applied Load
Actuator	250 mm	MTS	Stroke
LVDT 1	150 mm	Top Bearing Plate	Displacement
LVDT 2	200 mm	Bottom Bearing Plate	Displacement
LVDT 3	250 mm	Under MTS / Rebar Tail	Displacement
SG 1	10 mm	Confinement Pipe	Radial Dilation
SG 2	10 mm	Confinement Pipe	Radial Dilation
ϵ DOS	-	Rock Bolt	Rebar Strain
T DOS	-	Rock Bolt	Rebar Temperature
MGCplus	-	Analyzer	Time
Luna ODiSI-B	-	Analyzer	Time

Table 5-4. Sensor settings and uncertainties

Instrumentation	Analyzer	Uncertainty ¹	Connection / Sampling Rate
Load Cell	DAQ MGCplus	0.244%	Ch 1-1
Actuator	DAQ MGCplus	2.5%	Ch 1-2
LVDT 1	DAQ MGCplus	0.65%	Ch 1-4
LVDT 2	DAQ MGCplus	0.65%	Ch 1-3
LVDT 3	DAQ MGCplus	0.65%	Ch 1-5
SG 1	DAQ MGCplus	2.2%	Ch 2-1
SG 2	DAQ MGCplus	2.2%	Ch 2-2
ε DOS	Luna ODiSI-B	25 με	Luna 1
T DOS	Luna ODiSI-B	25 με	Luna 2
GW Instek DC power Supply	-	0.5%	-
MGCplus	-	0.000001 s	1 Hz
Luna ODiSI-B	-	0.37 s	1 Hz

¹ Listed uncertainties are provided specifications (modified after O'Connor, 2020; Moore 2021)

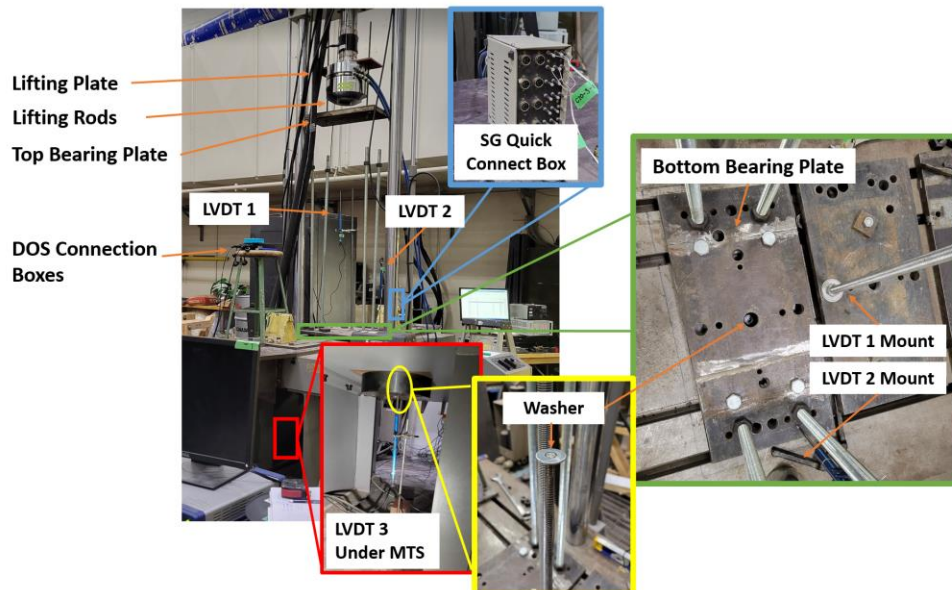


Figure 5-10. Test setup instrumentation details

5.4.2 Testing Scheme

The pull-out testing was conducted following the testing scheme of the hot specimens outlined in Table 5-2, with the aim of exploring the effects of curing temperature and capacity development of FGRBs subject to geothermally active temperature conditions. Two temperatures (20°C and 45°C) and short (3 days) to long (90 days) curing durations were tested. Two cold temperatures were also investigated concurrently with this study, presented in a separate article. Rehearsals were completed prior to the testing began in order to optimize setup procedures and time the process. Since temperature was the main factor being studied, the aim was to minimize changes to the test specimen's temperature. The times improved from 20-25 minutes to 10-15 minutes from the time the specimen was removed from the heating curing chamber to the time that the test specimen was connected to all of the sensors after several practices. In order to minimize setup times and specimen temperature changes, a test DOS was created to ensure that the Luna analyzers were operational and recognizing sensors, as various issues had been experienced during prototype testing and specimen preparation.

5.4.3 Grout Strength Testing

Grout strength testing was conducted for all specimens in order to quantify the grout properties for each FGRB over time and under each curing condition. The cylinders were cast at the same time as the grouting of the FGRB specimens. The cylinders corresponded with the grout utilized in each FGRB specimen. Time was recorded from start of mixing to end of grouting per specimen in order to maintain general consistency between batches. The cylinders were produced in accordance with ASTM C470 (ASTM, 2015) and ASTM C192 (ASTM, 2019) casted in 100mm Ø x 200mm L moulds in two layers. The grout was tested for UCS following the guidelines of ASTM C39 (ASTM, 2021) and STS following the guidelines of ASTM C496 (ASTM, 2017). The average results of the UCS and STS tests for the C20 and G45 conditions are found in Table 5-5 and Table 5-6, respectively. The measured compressive strength results for each series of cylinders were not all within the precision ranges as outlined in the standard. It was noted that the ASTM range corresponds to UCS between 17-35 MPa; generally the compressive strength results were higher. Thus judgements were made in excluding any significant outliers or including based on trend and a slightly bigger acceptance range.

Table 5-5. Summary of PC grout UCS and STS test results in C20 condition

Curing Duration (days)	Average UCS (MPa)	Average STS (MPa)
3	40.9	3.0
7	39.1	2.1
28	42.2	4.1
35	40.8	2.5
60	47.1	3.5
90	54.5	2.6

Table 5-6. Summary of PC grout UCS and STS test results in G45 condition

Curing Duration (days)	Average UCS (MPa)	Average STS (MPa)
3	50.4	2.1
7	60.8	2.2
28	54.1	3.1
35	38.1	3.7
60	59.1	1.9
90	41.0	2.6

5.5 Results

5.5.1 Pull-Out Test Results

The FGRB specimen naming convention included a letter and numbers. The first letter was “C” for control condition and “G” for geothermally active condition, followed by the numbers representing the curing temperature and the curing duration as seen in Table 5-7. The testing age tolerances adhered to ASTM C39 (ASTM, 2021) guidelines with deviations noted outside of the ± 2 hour tolerance for 3-day cure: C20-3 pull-out test and grout UCS tests were 2 hours and G45-3 grout STS test was 3 hours outside of the tolerance. The failure mechanism and load results at end of each pull-out test were observed and recorded in Table 5-7. The tests for C20-28, C20-35, C20-60, and C20-90 were assessed to have been terminated pre-mature with respect to overall rebar tensile failure. All four

specimens had reached ultimate strength of the rebar and upon review of ϵ DOS profiles, the full embedment lengths were not fully activated. In addition, two specimens were observed post-test to have clear rebar necking.

Table 5-7. Pull-Out testing results for C20 and G45 specimens

Specimen	Max Load (kN)	Test End ¹	Notes
C20-3	172.2	Rebar Break	
C20-7	173.0	Rebar Break	Power supply tripped at start of test, LVDT data after 130 kN
C20-28	170.8	Pre-mature	
C20-35	172.8	Pre-mature	Rebar necking observed post-test
C20-60	171.0	Pre-mature	Rebar necking observed post-test
C20-90	170.7	Pre-mature	
G45-3	156.7	Pull-out	
G45-7	171.3	Rebar Break	
G45-28	171.1	Rebar Break	Power supply problems, loading data collected after 120 kN
G45-35	172.6	Rebar Break	
G45-60	173.2	Rebar Break	
G45-90 *	171.8	Rebar Break	

* Entire ϵ DOS not functioning

¹ Observed failure mechanism resulting in ending of testing

The load-displacement curves from the conventional instruments were plotted for each test specimen in order to understand the behaviour of the whole system. The top bearing plate was observed to be yielding during testing. The axial displacement of the system from the MTS actuator stroke was corrected using the displacement captured by the LVDT that was monitoring the top bearing plate and

the elongation of the rebar portion outside of the embedment length. For C20-7 test, the power supply tripped at the start of the test thus LVDT data was not collected until after 130 kN. Therefore, LVDT correction data was estimated based on linear trend line. Similarly G45-28 had power supply issues affecting all loading data until after 120 kN, load time stamps were estimated based on trends of other tests as the loading rate was the same in order to process DOS data. An example from C20 condition is seen in Figure 5-11, the specimen failed by rebar tensile failure. An example from G45 condition is found in Figure 5-12, the specimen test was terminated as stroke continued to increase with minimal load change. Selected LVDTs experienced noise or had power supplies tripped at the start of the test. The majority of tests resembled that of Figure 5-11 with testing ending in rebar tensile failure or termination prior to rebar failure. Some grout mobilization and crushing was observed in post-test analysis.

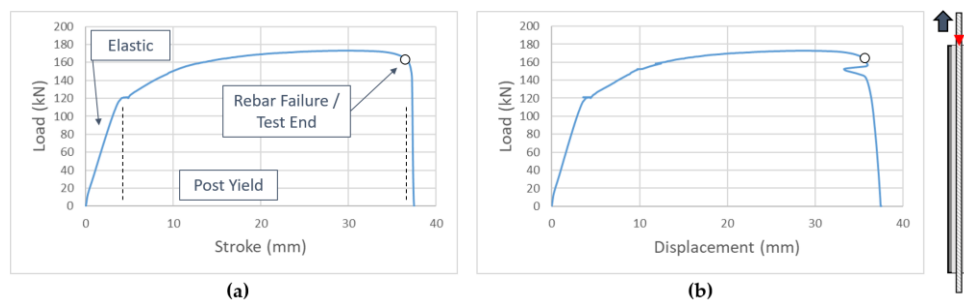


Figure 5-11. Load-Displacement curve from C20-7: (a) Whole system response; (b) Axial displacement corrected for test rig movement and elongation

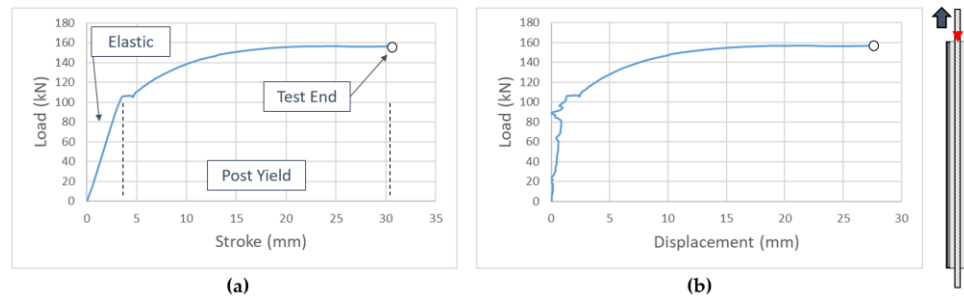


Figure 5-12. Load-Displacement curve from G45-3: (a) Whole system response; (b) Axial displacement corrected for test rig movement and elongation

The ϵ DOS monitored the axial response of the rebar and by using Equation 11, (Cruz, 2017; Moore, 2021) the bolt displacement was calculated along with the strain data. The DOS data began at 75 mm from the borehole collar due to the 50

mm strain pickup transition section and 25 mm de-bonding zones thus the displacement curves were extrapolated in order to determine the displacements at the borehole collar (Figure 5-13).

$$U_x = \sum \left(\frac{\varepsilon_{i+1} + \varepsilon_i}{2} \right) \cdot (x_{i+1} - x_i) \quad (11)$$

where, U_x , is bolt displacement at distance x , ε_i is bolt strain at position i , and x_i , is distance along bolt at position i .

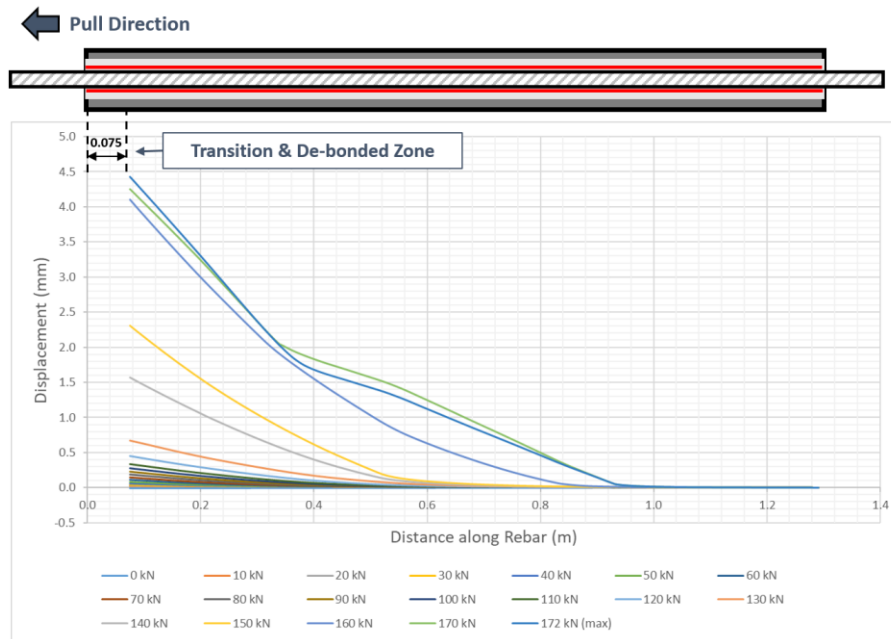


Figure 5-13. C20-7 specimen axial displacement profile

The amount of displacement data was limited to the operational life of the DOS as most of the sensors failed prior to complete material failure, thus, not capturing the full loading sequence. An example that was presented for C20-7 managed to capture the full sequence until the ultimate strength of the rebar was reached. The rebar displacement data was used to generate load-displacement curves for the rock bolt.

The pipe dilation at 50 mm from top of pipe was monitored by two SGs (mounted on diametrically opposing sides) aligned over the transverse ribs. Figure 5-14 is an example of the pipe strains (i.e. confining pressure) as loading increased. Across all 12 specimens (C20 and G45), the highest pipe strain recorded was 1090

$\mu\epsilon$ (measured by SG 1 on C20-3), with majority of tests averaging a maximum of 600-700 $\mu\epsilon$. Thus, concluding that the confinement pipes did not experience significant dilation during testing and pipe failure was not a potential factor, which are in-line with predictions due to the wall thicknesses of the Schedule 80 pipes. Some differences between SG 1 and SG 2 are attributed to alignment and positioning over the rebar ribs.

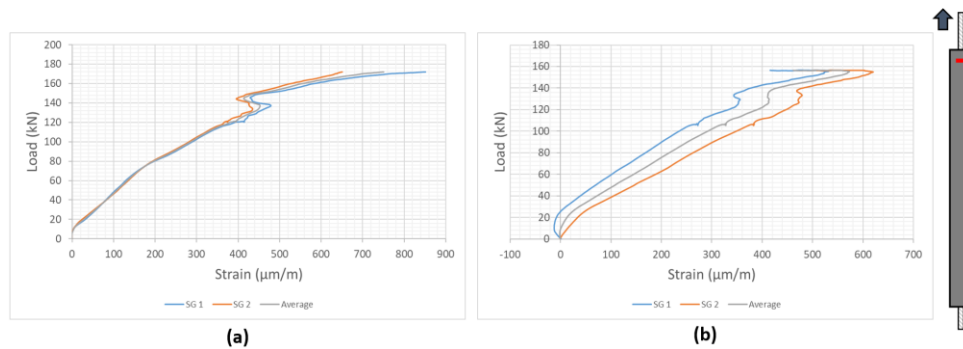


Figure 5-14. Pipe dilation monitoring at 50 mm: (a) C20-7 specimen; (b) G45-3 specimen

After testing concluded, post-test forensics were conducted and specimens were cut open along the longitudinal axis of the pipe in order to evaluate and make observations to provide additional insights and supplement the DOS results. The main observations were of grout crushing, grout shearing, grout voids, and minimal slip. An example of a cut open specimen is presented in Figure 5-15. Most specimens did not have significant voids, thus the grouting method was effective. The presence of voids or de-bonding can also be observed on the ϵ DOS profiles as extended zones of plateaus throughout loading, which was the case in the G45-60 specimen.

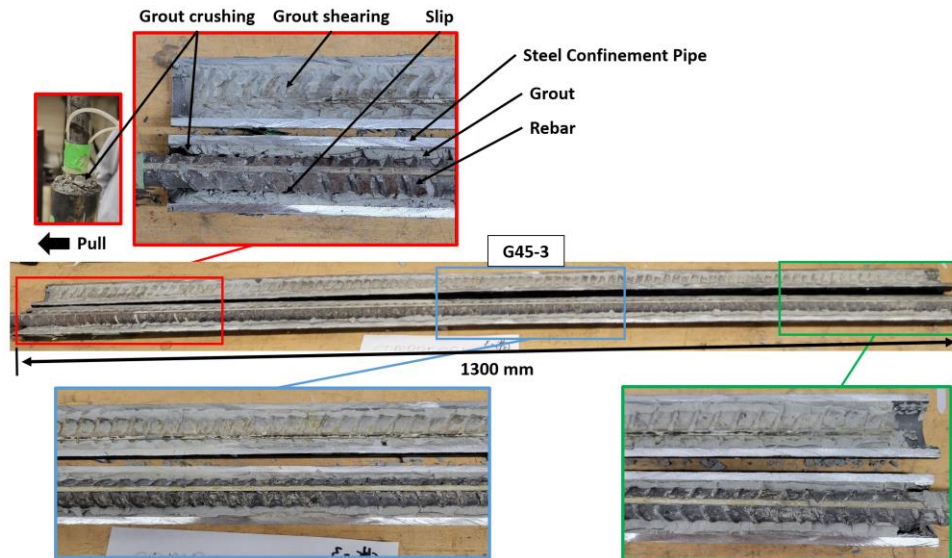


Figure 5-15. G45-3 specimen cut open for post-test evaluations

5.5.2 Strain Profiles

The strain measurements captured by the ϵ DOS for each specimen were plotted as continuous strain profiles along the length of the rock bolt sensing length, analyzed and presented at 10 kN loading increments (example in Figure 5-16). The strains captured on the two sides of the rebar were averaged using Equation 12 in order to remove any bending experienced by the bolt during pull-out testing. The strains displayed at the start of the 75 mm transition and de-bonded zones are the calculated theoretical strains based on the effective cross-sectional rebar area and confirmed rebar Young's Modulus (200 GPa) during materials testing.

$$\epsilon_y = \frac{\epsilon_y^{side\ 1} + \epsilon_y^{side\ 2}}{2} \quad (12)$$

The strain profiles were corrected for any excess noise as required that were picked up by the DOS analyzer. As well, for the G45 specimens, the strains were corrected for temperature change that was captured by the ϵ DOS as the specimens cooled during testing. The average of the T DOS captured strains at each loading increment were added back into the strain profile. Most sensors failed after the yield point and prior to end of testing thus, full loading profiles were not captured, however, the majority was. The premature failure was attributed to the location of

the DOS termination being in the actuator grip thus experiencing significantly higher strains than the embedded portions.

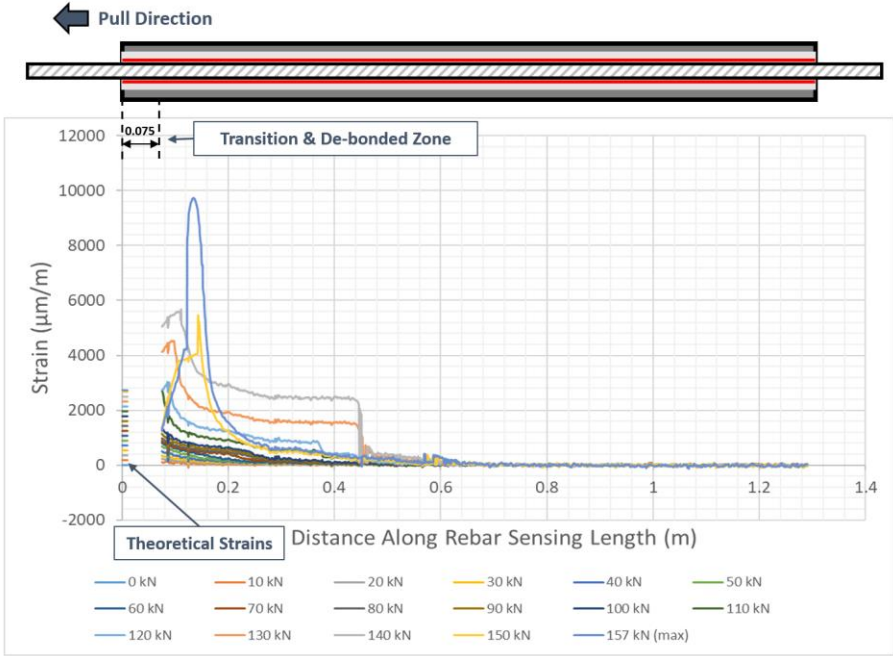


Figure 5-16. G45-3 specimen strain profile along rebar bolt during pull-out testing

Figure 5-17 shows the strain profiles of two specimens that the DOS fiber optics were intact and were operational during the testing in order to capture the entire loading sequence until rebar ultimate strength in both curing conditions. The transition from the elastic stage to the plastic behaviour as loading increased can be monitored as continuous profiles along the entire embedment length. In the elastic stage, the exponential decay in the strain profiles are observed. The plastic behaviour changes drastically as the full capacity of the bolt was developed at higher loads.

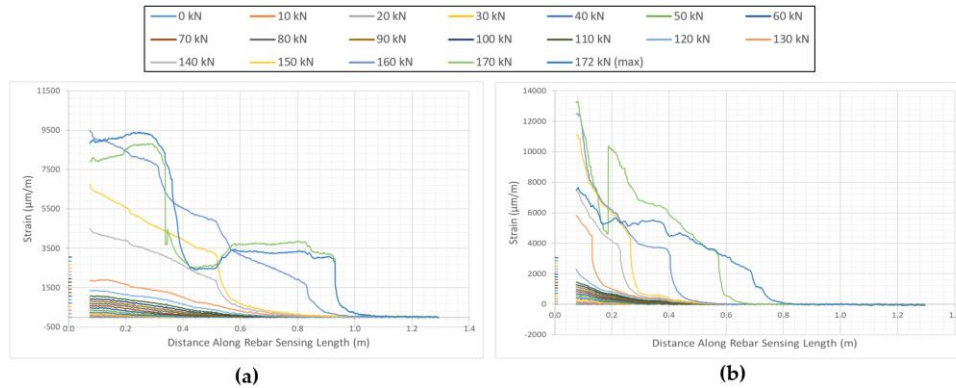


Figure 5-17. Strain profiles over entire loading sequence: (a) C20-7; (b) G45-35

The temperature change was calculated from the measured strain using the conversion factor in Equation 13, resulting from temperature calibration of the T DOS sensing fiber.

$$\Delta T = 8.49 \cdot \varepsilon_{y,t} \quad (13)$$

where, ΔT , is absolute temperature change and $\varepsilon_{y,t}$ is strain due to temperature change. The temperature change during the pull-out test was calculated at 30 second intervals and plotted in Figure 5-18. Several T DOS began to capture strain due to the bolt loading at a singular point as seen in Figure 5-19, likely, due to pinching or lifting at the entry of the de-bonding stainless steel tubing. Any results affected by rebar loading were removed and extrapolation was used to calculate any gaps in the data. The temperature change for G45 specimens is presented in Table 5-8 between the specimens removal from the curing chamber until reaching maximum load during testing. The rates of temperature change (i.e. slope) were calculated from the change in temperature graphs for each specimen, which collected data once pull-out testing began. The transport and set-up times were recorded and pre-test temperature change was estimated using the same slope, this was considered a conservative approach as the MTS would have exposed the specimens to warmer ambient temperatures with the hydraulics.

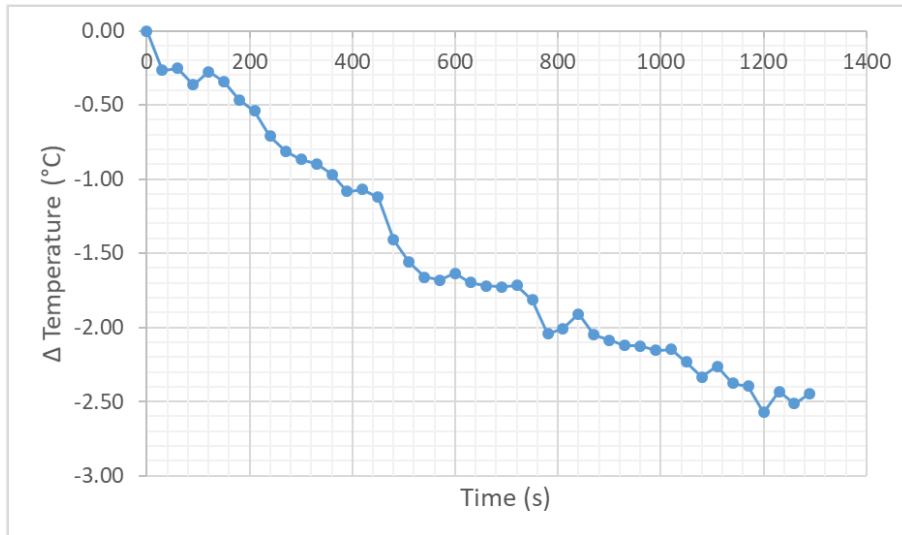


Figure 5-18. G45-28 specimen temperature change during pull-out testing

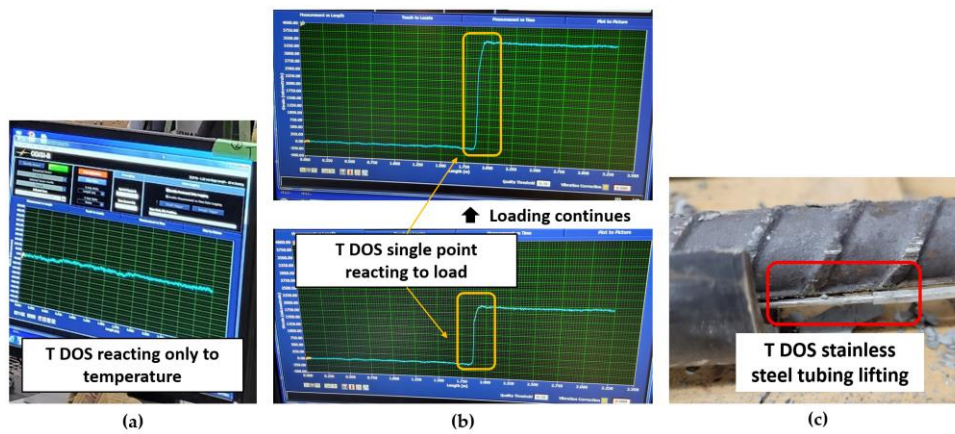


Figure 5-19. Reaction of T DOS: (a) Only reacting to temperature change; (b) Reacting to rebar loading; (c) Post-test observation of T DOS stainless steel tube lifted out of groove

Table 5-8. G45 specimen temperature change results

Specimen	Slope (°C/s)	Time to Max Load (s)	ΔT Test (°C)	Pre-Test Time (s)	ΔT Pre-Test (°C)	ΔT Total (°C)
G45-3	-0.0022	1150	-2.5	1080	-2.4	-4.9
G45-7 *	-0.0022	1246	-2.7	1620	-3.6	-6.3
G45-28	-0.0022	727	-1.6	1200	-2.6	-4.2
G45-35	-0.0023	1028	-2.4	720	-1.7	-4.0
G45-60 **	-0.0022	824	-1.8	1140	-2.5	-4.3
G45-90 **	-0.0022	991	-2.2	840	-1.8	-4.0

* T DOS reacted to loading from start of test (used G45-3 data)

** T DOS not functioning properly (used G45-3 data)

5.5.3 Grout Strength Development

The specimens grout strength was quantified through UCS and STS testing, each specimen had a total of 6 cylinders (3 per test) casted during grouting. The results of the testing are presented as strength development curves in Figure 5-20. The lines connecting the points in the (b) plot is not for the purpose of interpolation but to be indicative of general trends between the conditions and make observations easier. Generally, the UCS results of both increased with curing time and the compressive strength of the G45 condition were higher than that of C20, notably, in the shorter and mid curing durations. In the long 60-90 days, the C20 UCS gained similar strength to the G45 specimen. The STS trends were less consistent for both, however, they were comparable in tensile strength through all curing durations between the temperatures.

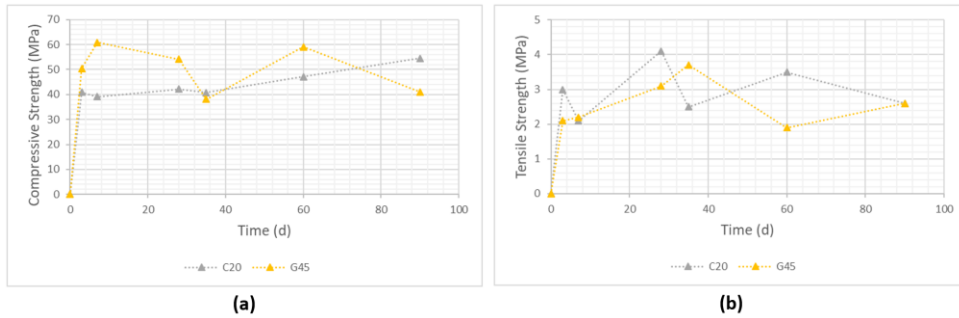


Figure 5-20. Grout strength development curves: (a) UCS; (b) STS

5.6 Discussion

Using DOS technology, the behaviours of the FGRBs during pull-out testing was monitored at the micro-scale with a spatial resolution of 0.65 mm. The specimens generally experienced the failure mechanisms of: (1) rebar tensile failure and (2) bolt-grout interface failure. The first mechanism involves the embedment length being adequate to develop the full capacity of the bolt thus, once applied loads reached ultimate tensile capacity of the rebar, it ruptures. The second mechanism has two types of failure mechanisms – dilation slip and grout shearing (Figure 5-21). At high confinement pressure, dilation is resisted and grout shearing occurs. However, at lower confinement the lateral movement results in volumetric increase at the bolt-grout interface induces bolt movement over the grout ridges referred to as dilation slip (Vlachopoulos et al, 2018). From post-test forensics, grout shearing was the main observation in G45-3 that had ended in pull-out.

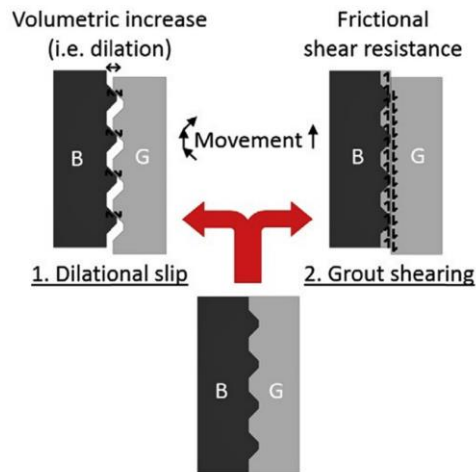


Figure 5-21. Bolt-grout interface failure mechanisms (Vlachopoulos et al, 2018)

Selected observations were made of grout mobilization in the specimens at the end of pull-out testing. An example of this is shown in Figure 5-22. The smooth steel pipe interior may not have had adequate surface texture to provide proper mechanical interlock. The top portions of the system was subjected to the most stress thus, as the shear stress increased, the shear strength of the interface was exceeded and mechanical interlock threshold was surpassed. Incrementally friction was activated until the grout was fully mobilized. The friction within the system was adequate to prevent failure at the grout-pipe interface from impacting the overall test results.

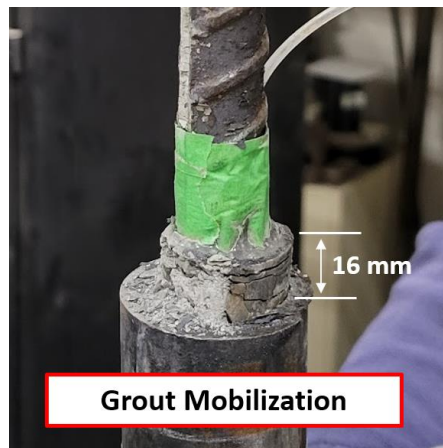


Figure 5-22. Grout mobilization observed in C20-35 specimen

5.6.1 Strain Profile Comparisons

The strain profiles and mobilized embedment length of each specimen were compared within their own curing conditions in order to observe trends as curing duration increased. The G45-90 specimen's ϵ DOS was fully non-functional after testing setup so could not be compared. Examples at low (20 kN) and high (100 kN) loads for C20 and G45 are seen in Figure 5-23 and Figure 5-24, respectively. For both conditions, the strain profiles observed had exponential decay along the embedment length, which is in-line with the expected behaviour of FGRBs. The mobilized embedment lengths increased with loading. The 3-day curing duration specimen in both conditions generally experienced the highest strains at different loading increments.

The critical embedment length is the minimum length that expends all bolt tensile capacity and is a key component to determining the design length of rock bolts. The critical embedment length can be systematically evaluated through monitoring the bolt's complete strain profile to determine where the stress distribution attenuates to zero (Cruz, 2017). The yield critical embedment lengths for the C20 and G45 conditions were determined as a whole for all their respective specimens at 120 kN (Rebar F_y) since the design and application of FGRBs would not exceed the bolt's yield strength. As seen in Figure 5-25, the yield critical embedment length for the C20 condition was 1.0 m and for the G45 condition was 0.60 m.

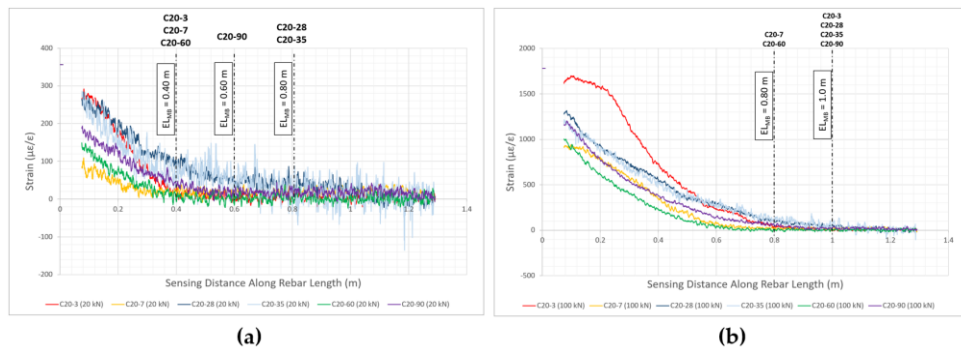


Figure 5-23. C20 Condition comparison of strain profiles and mobilized embedment length: (a) at 20 kN; (b) at 100 kN

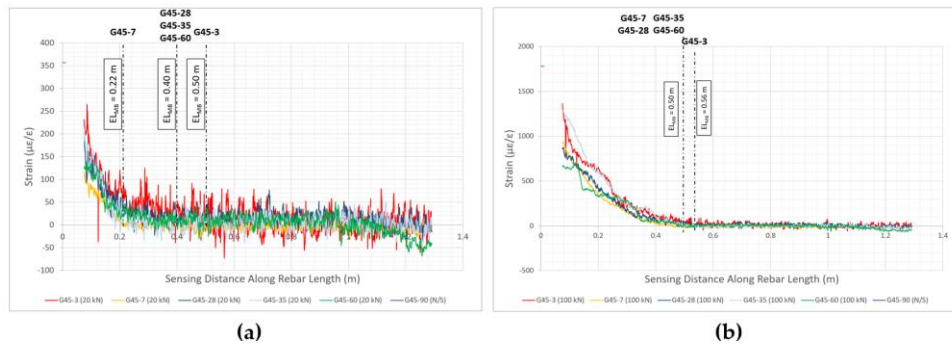


Figure 5-24. G45 Condition comparison of strain profiles and mobilized embedment length: (a) at 20 kN; (b) at 100 kN

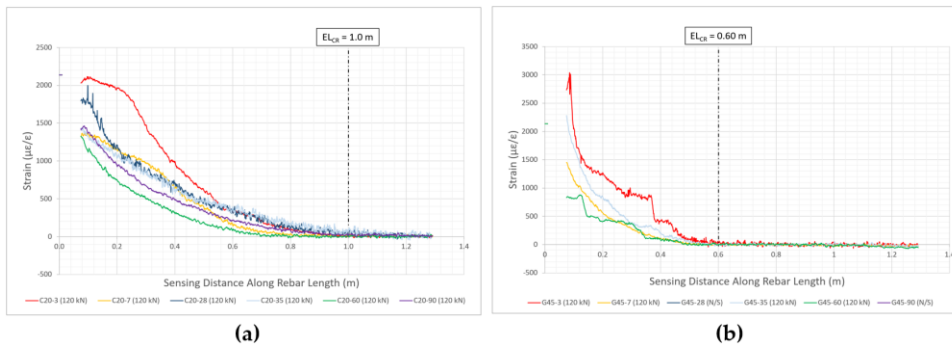


Figure 5-25. Critical embedment length at 120 kN: (a) C20; (b) G45

The strain profiles between the two conditions were compared, examples at 28- and 35- day curing are shown in Figure 5-26. In general across all specimens, the G45 specimens experienced lower strains at the same distance along the rebar when compared to the C20 specimens at the same curing duration and applied load. Strain attenuation (i.e. mobilized embedment lengths) was also more rapid in the G45 specimens compared to the C20 specimens. These results indicate that the bond performance and load transfer are improved in the G45 condition, thus, potentially shorter rock bolt lengths could be employed compared to C20 condition (i.e. only temperature varies).

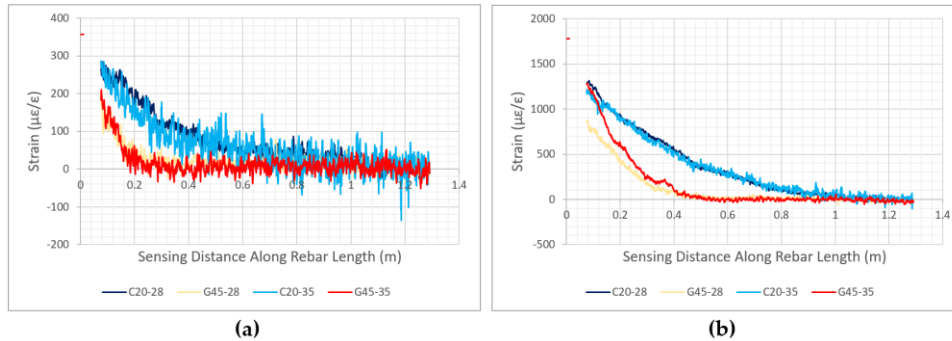


Figure 5-26. Comparison of strain profiles between C20 and G45 at 28-day and 35-day cure: (a) at 20 kN; (b) at 100 kN

5.6.2 Capacity Development

The maximum loads of the specimens were compared with curing temperature as well as curing duration in order to assess the capacity development in the C20 and G45 conditions. Since all but one specimen in both conditions reached ultimate strength of the bolt, the plot in Figure 5-27 includes temperatures from the permafrost conditions that were investigated concurrently with this study (detailed in a separate article) as the extended temperature range provides a more complete picture of temperature effects. All variables, except for curing temperature and type of grout, were the same in both investigations. There is a general increase in capacity as the temperature changes from cold (below freezing) curing conditions to the C20 condition. The 3-day capacity curve has the most variation across the curing durations and may be due to the short time for curing and support system stabilizing. As duration increases to 90 days, the systems across all conditions generally achieve similar ultimate capacities.

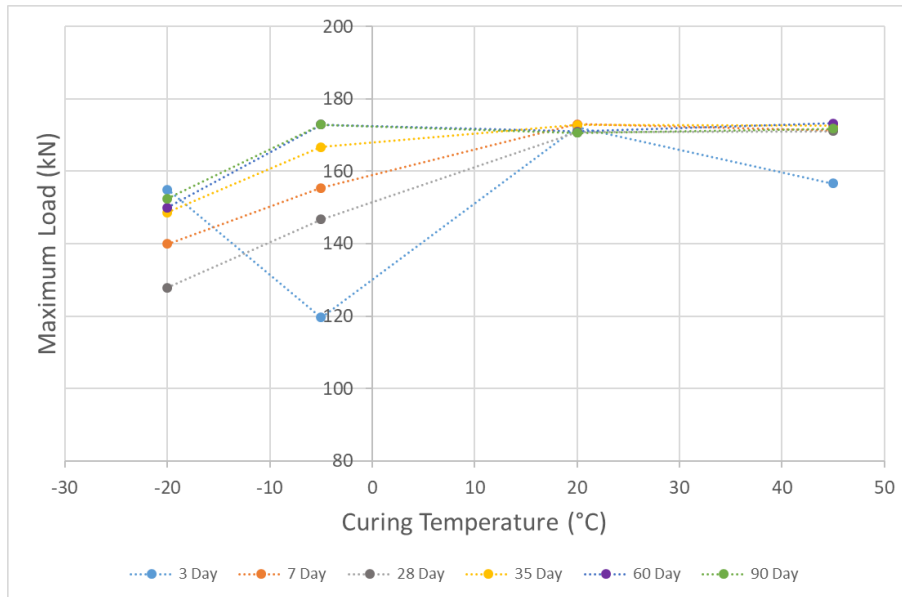


Figure 5-27. Maximum load vs curing temperature

Figure 5-28 compares maximum load to curing duration, which has no correlation. The only specimen of interest was the G45-3 as it failed by pull-out rather than rebar rupture. The effect of grout UCS was considered, however, from the grout UCS development curve, the 3-day strength of the G45 condition was comparable to some of the longer curing durations. Potentially, the high heat affects the initial short-term capacity development of FGRBs, thus, initial incremental loading of the system would need to be considered as compared to the C20-3 specimen that was able to fully develop the full capacity of the bolt.

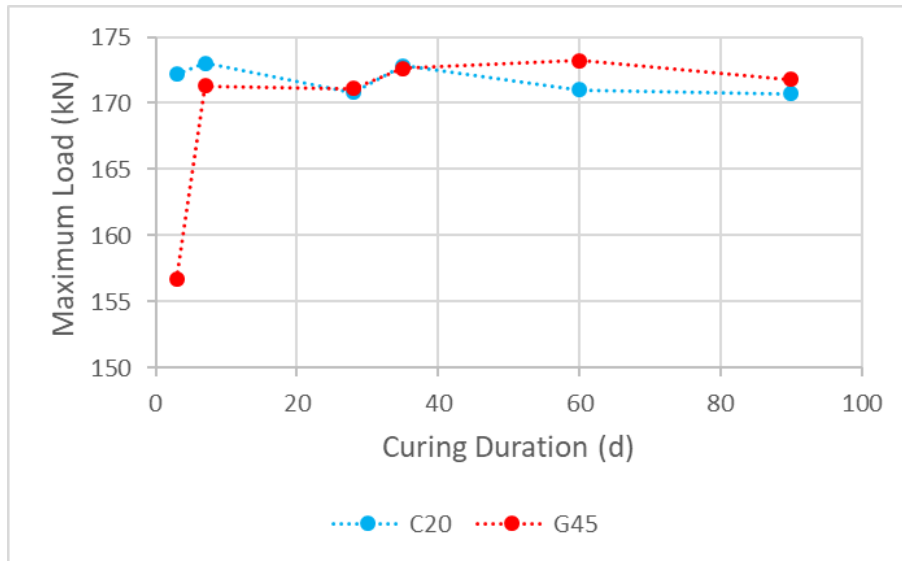


Figure 5-28. Maximum load vs curing duration

Observations comparing the grout UCS and curing duration concluded that they do not significantly impact the results, in order to confirm statistical significance, Multiple Linear Regression (MLR) analysis was completed using an open-source analysis software JASP version 0.18.3.0 (JASP Team, 2024). The R^2 indicates the amount of variance that can be predicted by the independent variable of the model (Gross-Sampson, 2024), the p-value indicates statistical significance (typically 0.05) (Alexopoulos, 2010). The coefficients specify whether there is a positive or negative correlation between the variables and how the dependent variables change when the independent variable changes, unstandardized coefficients are associated with one unit change whereas standardized coefficients are associated with one standard deviation change. The results in Table 5-9 confirm that there was low correlation between these two factors and the maximum load of the test results, and neither were significant predictors. Thus at the same w/c ratio of PC grout, even with G45 condition resulting in higher grout UCS, in some cases 50% higher than C20 at same curing duration, it did not affect the results overall so long as there is sufficient embedment length to develop the capacity.

Table 5-9. MLR coefficients of curing time and grout UCS on max load

Model H ₁	R ²	Unstandardized	Standard Error	Standardized	t	p
(Intercept)	0.13	173.33			21.15	<.001
Cure Time		-0.11	0.17	-0.21	-0.67	0.53
Grout UCS		0.04	0.04	0.31	0.99	0.35

5.6.3 Axial Stiffness

Further analysis was completed to determine the factors affecting the system. Axial stiffness was determined for each specimen as a whole system, as well as, the rebar bolt using the quasi linear portion of the load-displacement curves from the conventional instruments and the ϵ DOS. Table 5-10 presents the results with axial stiffness derived from the conventional system accounting for the whole support system and axial stiffness from the DOS of only the rebar, hence, the order of magnitude difference, which was also seen in the axial stiffness results of Cruz (2017). The whole system corrected accounts for adjusting the axial displacement (i.e. actuator stroke) with the LVDT monitoring the top plate as well as elongation calculations for the portion of the rebar outside of the embedment length. For comparisons, axial stiffness of the whole system was used. In initial comparisons of the axial stiffness, the range of results for the G45 condition were on average 50% higher than that of the C20 condition for the rebar but similar when considering the whole system.

The axial stiffness was compared against grout UCS, mean bond strength, and yield critical embedment length (taking the average of the specimens) as seen in Figure 5-29. The data sets are comprised of singular measurements at each curing duration, therefore, the confidence interval (alpha 0.05) displayed in the (b) plot is based on the mean values of axial stiffness and grout UCS per curing condition (i.e. P20, P5, C20, and G45); the purpose is to present the data variation within the curing condition. The comparison of critical embedment length includes the permafrost conditions in order to have more data points for effective analysis as the critical lengths were determined per condition. The mean bond strength was calculated using Equation 14.

$$s = \frac{P_{max}}{\pi d_b L_e} \quad (14)$$

where, s , is the mean bond strength, P_{max} , is the load at pull-out, d_b , is the bolt diameter, and L_e , is the embedment length. MLR analysis of grout UCS and mean bond strength were completed for axial stiffness – DOS (Table 5-11) and for axial stiffness – whole system (Table 5-12). The correlation of Grout UCS and mean bond strength with axial stiffness – DOS was low, however the former was a higher predictor than the latter when considering only the rebar. The correlation with axial stiffness – whole system was not significant, both factors were not reasonable predictors when considering all components. Regression analysis of axial stiffness – DOS and yield critical embedment length for the whole spectrum of temperature conditions found a negative correlation, however, was not statistically significant ($R^2 = 0.74$, $p = 0.14$) between the factors. However when considering the whole system, there was not a significant correlation and had low statistical significance ($R^2 = 0.28$, $p = 0.47$).

Table 5-10. Axial stiffness

Specimen	Axial Stiffness (kN/mm) – DOS ¹	Axial Stiffness (kN/mm) - Whole System ²	Axial Stiffness (kN/mm) - Whole System Corrected ²
C20-3	148.6	25.2	86.0
C20-7	375.1	32.5	-
C20-28	191.6	25.4	40.7
C20-35	211.5	28.9	100.6
C20-60	368.7	28.7	134.4
C20-90	252.3	31.3	39.5
G45-3	418.8	30.1	83.6
G45-7	572.6	29.4	82.4
G45-28	574.6	-	-
G45-35	402.7	32.0	40.0
G45-60	558.5	32.0	40.4
G45-90	-	28.7	40.0

¹ Blank entries due to ϵ DOS not functioning

² Blank entries due to missing data from DAQ or LVDT malfunctions

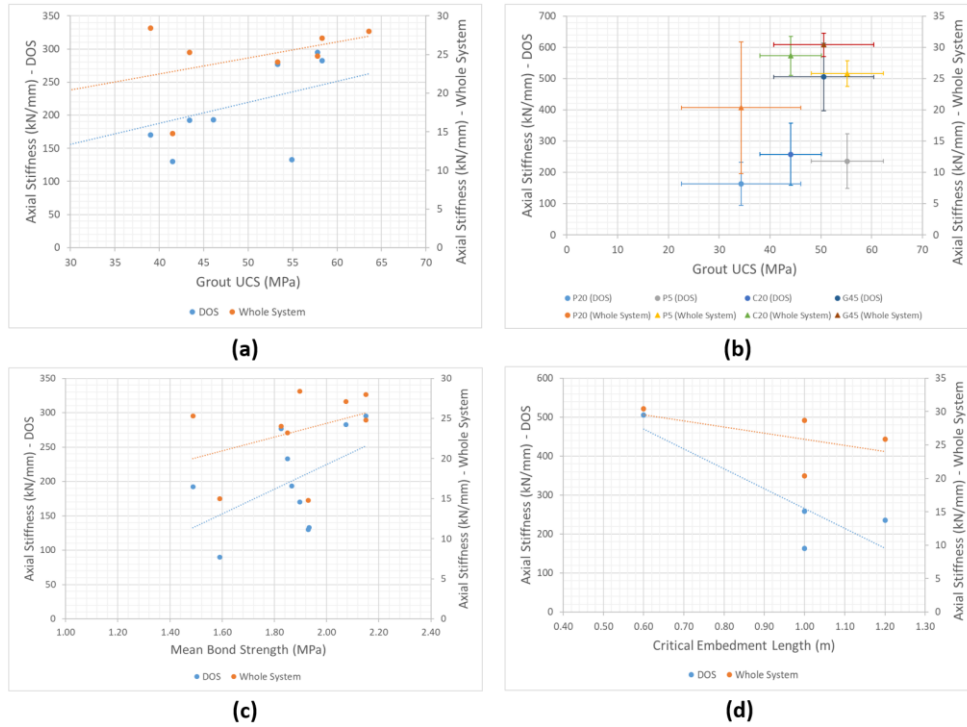


Figure 5-29. Axial stiffness comparisons: (a) Grout UCS; (b) Confidence interval (alpha 0.05); (c) Mean bond strength; (d) critical embedment length

Table 5-11. MLR coefficients of grout UCS and mean bond strength on axial stiffness - DOS

Model H ₁	R ²	Unstandardized	Standard Error	Standardized	t	p
(Intercept)	0.45	-412.58	1580.92		-0.26	0.80
Grout UCS		12.73	4.99	0.68	2.55	0.03
Mean Bond Strength		81.48	716.27	0.03	0.11	0.91

Table 5-12. MLR coefficients of grout UCS and mean bond strength on axial stiffness – whole system

Model H ₁	R ²	Unstandardized	Standard Error	Standardized	t	p
(Intercept)	0.07	22.42	33.38		0.67	0.52
Grout UCS		0.08	0.11	0.27	0.76	0.47
Mean Bond Strength		1.57	15.05	0.04	0.10	0.92

The effects of temperature and curing duration compared against axial stiffness are seen in Figure 5-30, full temperature spectrum included Linear regression found positive correlation of axial stiffness (both) with temperature as the R² values for each curing duration was between 0.70-0.96 and p values between 0.03-0.14. The curing durations that observed the highest correlation and were statistically significant for axial stiffness – DOS were 7-day and 60-day. The curing durations that observed the highest correlation and were statistically significant for axial stiffness – whole system were 35-day and 60-day. The 7-day specimen for the whole system was removed from the analysis due to a lack of data. Therefore, as the curing temperature decreases, generally, so does the axial stiffness of the support system, which in turn affects the displacements that would be observed at the boundaries of underground excavations.

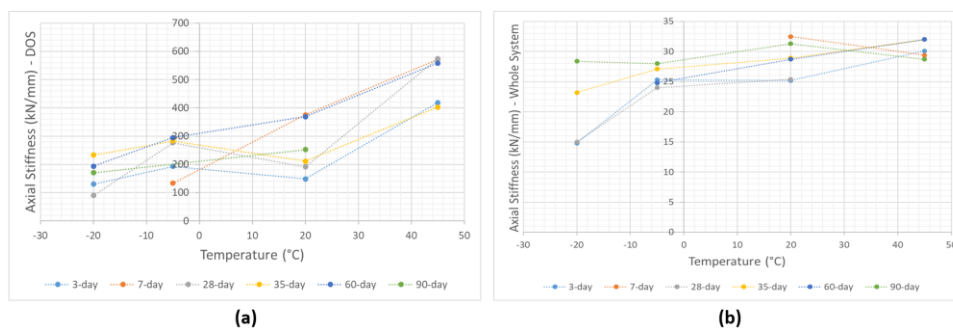


Figure 5-30. Axial stiffness plotted against temperature: (a) DOS – rebar; (b) Conventional instruments – Whole system

5.6.4 DOS Performance in High Temperatures

All monitoring instrumentation installed on the FGRB specimens' operating temperature range specifications had been verified to include the testing temperatures of this study, as seen in Table 5-13. Every ϵ DOS and T DOS was confirmed to be operational prior to specimen assembly. There was only one ϵ DOS that did not function during testing and three of the T DOS malfunctioned, these issues were likely associated to installation problems rather than temperature effects.

Table 5-13. Summary of monitoring instrumentation operating temperature ranges

Instrument	Details	Operating Temperature (°C)
Strain Gauge ¹	N11-FA-5-120-11	-30 to +80 ²
Sensing Fiber	Corning® SMF-28e+	-60 to +85 ³
	SM1550P Fiber Polyimide	-190 to +350 ⁴
Termination Fiber	FG125LA Coreless	-40 to +85 ⁵
LC Connection	Patch Cable	-20 to +70 ⁶

¹ Mounting adhesive (M-Bond 200) operating temperature range works (Micro Measurements, 2014)

² SHOWA Measuring Instruments, 2022

³ Corning, 2021

⁴ ThorLabs, 2024b

⁵ ThorLabs, 2024a

⁶ Fiber Instrument Sales, n.d.

A verification of this DOS technique's temperature spatial resolution was assessed with selected T DOS data, seen in Figure 5-31. The slopes of the converted temperature change results (Table 5-8) were used to interpolate the timestamps and the average strains along the T DOS were found. The DOS temperature spatial resolution was assessed to be 0.1°C, which is in agreement with the results of Gifford et al. (2005).

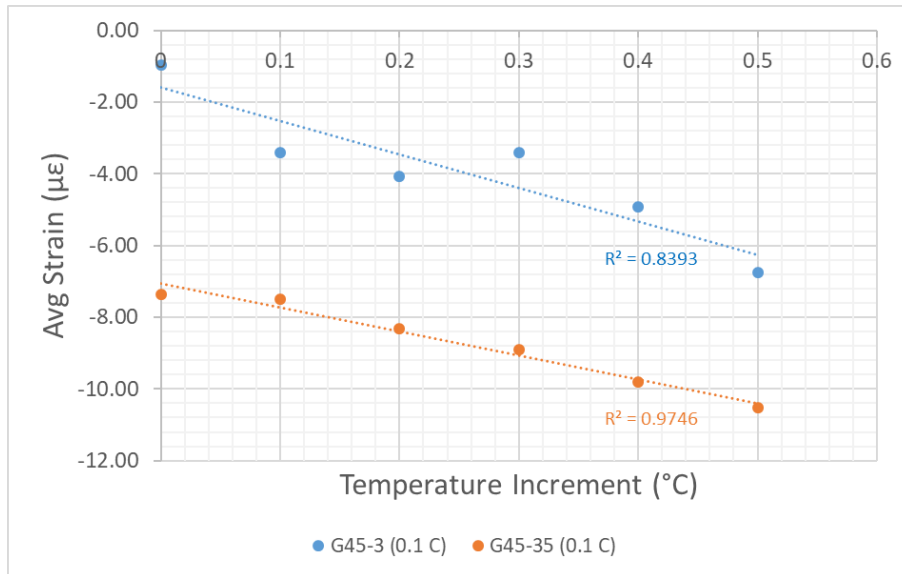


Figure 5-31. DOS temperature spatial resolution assessment

5.7 Conclusions

A series of laboratory pull-out tests using DOS were conducted to investigate the effects of geothermally active temperature conditions in the specific temperature regime on the performance and capacity development of FGRBs. Generally, in both 20°C and 45°C conditions, the 3-day cure specimens experienced the highest strains at the same distance along the rebar bolt compared to the specimens that were cured longer. The increase in temperature resulted in higher grout UCS at 45°C. As well, at all curing durations, the 45°C condition specimens experienced lower strains and profiles attenuated faster resulting in shorter mobilized and critical embedment lengths as compared to those cured at 20°C. All specimens at 20°C curing duration were able to fully develop the capacity of the bolt with sufficient embedment length, reaching ultimate rebar capacity. However, at 45°C, the 3-day curing duration was found to be the most affected in terms of ultimate capacity as it failed by pull-out as compared to all other curing durations that reached ultimate bolt strength. Thus, considerations should be made when loading the system to prevent high loads in geothermal conditions in the initial short-term until the support has stabilized. The evaporation prevention methods were beneficial to prevent the development of excess voids in the 45°C curing conditions. Regression

analysis did not find significant correlation of grout UCS and curing duration on the capacity of the FGRBs as sufficient embedment length was provided. Axial stiffness of the rebar and whole support system were used for further analysis and comparisons. When compared to grout UCS and mean bond strength, axial stiffness generally had low correlation and MLR analysis determined no statistical significance (except for grout UCS and rebar axial stiffness). Temperature was found to have positive correlation with axial stiffness (both), thus, as the curing temperature decreases, generally, so does the axial stiffness, which in turn affects the displacements of the support systems. The DOS technique was able to capture continuous strain profiles in high temperatures and act as an effective specimen temperature monitor, with a temperature spatial resolution of 0.1°C. Additional testing at higher temperatures should be conducted in the future in order to observe further geothermal impacts, as well, the boreholes should be prepared with attention to roughness in order to enhance the grout-pipe interface.

Acknowledgments: The authors would like to acknowledge support from the Royal Military College of Canada, the RMC Green Team, Sika Canada Inc., the Department of National Defense, and the Natural Sciences and Engineering Research Council.

Conflicts of Interest: The authors declare no conflicts of interest.

6 Summary of Main Findings

6.1 Introduction

The methodologies and selected test results from the permafrost condition and the geothermally active condition were presented in Chapter 4 and Chapter 5, respectively. This chapter summarizes the main findings from both articles and provides overall findings across the whole test temperature spectrum, and major contributions. Figure 6-1 provides a summary of this investigation's testing program.

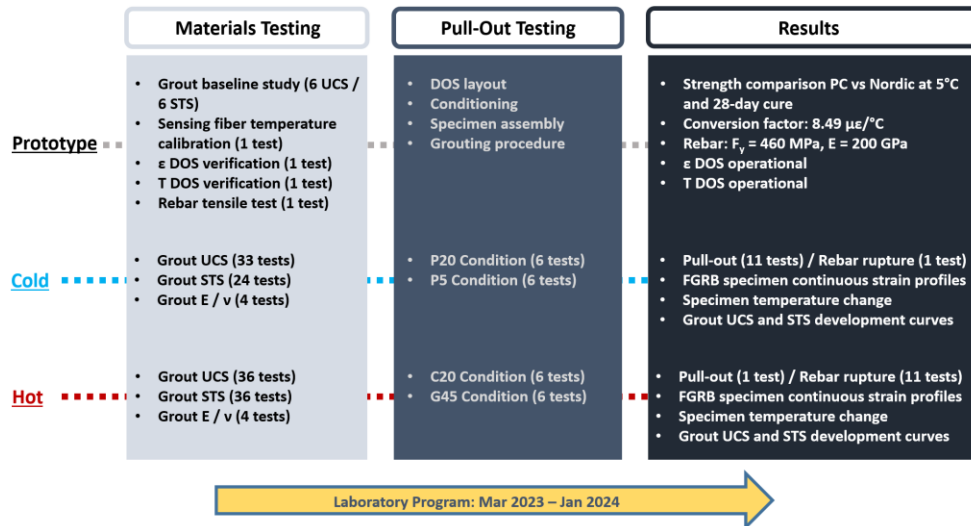


Figure 6-1. Summary of laboratory testing program

6.2 Permafrost Temperature Effects

Two permafrost temperature conditions (-5°C and -20°C) were tested and 12 FGRB specimens (6 per temperature) were cured from 3 to 90 days. Pull-out tests were conducted in the lab to study the geo-mechanical response of FGRBs under axial loading. The monitoring instrumentation included conventional instruments that monitored the whole system reaction and DOS technique that captured continuous

strain profiles of the rebar rock bolt and the internal specimen temperature change. The following are the main findings of the testing:

1. Grout UCS development curves demonstrated an increase and stabilization overtime and that Nordic grout compressive strength was significantly impacted by curing temperature. Although the grout had been designed for -10°C , it managed to hydrate and gain sufficient strength in -20°C conditions. Care must be taken to maintain workability of the grout due to fast setting rate as it considerably impacts strength results;
2. Grout STS development curves demonstrated that the tensile strength of the Nordic grout was not impacted as much by curing temperature compared to compressive strength, however, at -20°C the strength development was not as consistent as -5°C ;
3. All but one specimen failed by pull-out. The main failure mechanisms experienced during the pull-out tests were failure at the bolt-grout interface and failure at the grout-pipe interface. Only one specimen (P5-90) failed by rebar tensile failure inside the embedment length. The smoothness of the steel confinement pipes did not provide adequate mechanical interlock between the grout and pipe, added roughness to this boundary would be beneficial;
4. The results from rebar bolt strain monitoring included the following:
 - a. As load increased, mobilized embedment lengths increased in all specimens;
 - b. Strain profiles resembled exponential decay along the embedment length until full embedment length was activated;
 - c. In the P5 condition, the shorter curing duration specimens experienced higher strains at the same distance along the bolt compared to the longer curing durations with the same applied load;
 - d. In the P20 condition, strain trends were less consistent due to greater variations in the grout UCS; and,

- e. Comparing the two conditions, the P20 specimens generally experienced higher strains at same distance compared to the P5 specimens at the same curing duration and applied load.
5. In the P5 condition at 90 days, the specimen was able to fully develop the capacity of bolt (load capacity increased by 45% from 3-day cure and 11% from 7-day). By contrast, the P20 condition did not have a significant capacity change over the 90 days (load capacity decreased by 2% from 3-day cure and increased by 9% from 7-day cure);
 6. The capacity of the specimens in both curing conditions stabilized at 35-day cure but P20 specimens ultimate capacity was 10% less than in the -5°C condition;
 7. Maximum load versus curing duration curves notably resembled grout UCS curves as well. Multiple Linear Regression (MLR) analysis was completed using an open-source analysis software JASP version 0.18.3.0 (JASP Team, 2024) to statistically determine the significance of impact. It was determined that grout UCS was a positive predictor and that cure time was not a significant predictor;
 8. Axial stiffness of whole system (conventional instruments) and axial stiffness of rebar (DOS) were used for further analysis with respect to the grout UCS and mean bond strength, with the former having a more positive correlation to the DOS results;
 9. DOS was able to capture continuous strain profiles but was impacted by the cold temperatures causing several partial or whole ϵ DOS gaps in the data collection, which have been attributed to the looping at the tail end of the rebar;
 10. Use of de-bonding zones at the pull-end of the bolt for the ϵ DOS were effective in terms of prolonging the operational life of the sensors past yield of rebar, however, the location of the DOS termination inside the MTS grips caused, in selected cases, premature failure of the fiber optic;

11. DOS was effective at monitoring the internal temperature change, however, pinching or lifting of the de-bonding tubing caused the T DOS to react to loading in most specimen at high loads;
12. For underground projects, in -5°C permafrost conditions considerations for incremental loading of the support systems in the short curing duration should be made during the design process, whereas, in -20°C permafrost conditions pose more significant impacts on strength development and consistency of results; and,
13. Additional testing should be conducted in order to verify the failure mechanism(s) of pull-out testing in cold temperatures with boreholes prepared with increased roughness.

6.3 Geothermally Active Temperature Effects

Two temperatures (20°C and 45°C) were tested to investigate the effects of geothermally active conditions and 12 FGRB specimens (6 per temperature) were cured from 3 to 90 days. Pull-out tests were conducted in the lab to study the geo-mechanical response of FGRBs under axial loading. The monitoring instrumentation included conventional instruments that monitored the whole system reaction and DOS that captured continuous strain profiles of the rebar bolt and internal specimen temperature change. The following are the main findings of the testing:

1. Grout UCS development curves demonstrated a more consistent increase in compressive strength for PC grout cured under 20°C conditions and slightly less consistency at 45°C. Generally, grout cured in 45°C had higher UCS results (up to 50%) than at 20°C. The care taken to prevent excess evaporation at 45°C conditions was effective as significant grout voids due to evaporation were not observed;
2. Grout STS development curves demonstrated that the tensile strength of PC was not impacted as much by curing temperature compared to compressive strength, however, the development was not as consistent in both conditions;

3. All but one specimen failed by rebar tensile failure. The embedment length was adequate to develop the full capacity of the bolt. Only one specimen (G45-3) failed by pull-out, failure at the bolt-grout interface. Some grout mobilization was observed in specimens post-test, additional roughness to the inside of the confinement pipes would be beneficial;
4. The results from rebar bolt strain monitoring included the following:
 - a. As load increased, mobilized embedment lengths increased in all specimens;
 - b. Strain profiles resembled exponential decay along the embedment length;
 - c. In both conditions, the 3-day cure specimen experienced the highest strains at the same distance compared to other specimens in the same curing temperature with the same applied load. For example, in the C20 condition, C20-3 experienced an increase in strain of 70-190% from that of C20-7 at a distance of 75 mm along the rebar (at loads ranging from 20-100 kN). In the G45 condition, G45-3 experienced an increase of 35-190% compared to G45-7 at a distance of 75 mm along the rebar (at loads ranging from 20-100 kN);
 - d. Comparing the two conditions, the G45 specimens generally experienced lower strains at same distance compared to the C20 specimens at same curing duration and applied load. For example, G45-28 and G45-35 strains were approximately 13% of that experienced by C20-28 and C20-35 at 200 mm from the borehole collar at 20 kN load; and,
 - e. Strain profiles of the G45 specimens attenuated faster than that of C20, shorter mobilized embedment lengths and critical embedment lengths.
5. In terms of the capacity development in C20 condition, all specimens reached ultimate strength of the rebar, in contrast, in the G45 condition the 3-day did not reach the ultimate strength of the rebar while all of the other specimens ended in rebar rupture;

6. Multiple Linear Regression (MLR) analysis was completed to statistically determine the significance of impact found grout UCS and cure time were not significant predictor with adequate embedment length;
7. Axial stiffness of whole system (conventional instruments) and axial stiffness of rebar (DOS) were used for further analysis to grout UCS and mean bond strength. Both factors were not significant with respect to the whole system, however, grout UCS was more correlated with rebar;
8. DOS was able to capture continuous strain profiles in the high temperature conditions with only one non-operational ϵ DOS in the G45-90 specimen;
9. Use of de-bonding zones at the pull-end of the bolt for the ϵ DOS were effective to prolong the operational life of the sensors past the yield of rebar, however, the location of the DOS termination inside the MTS grips caused premature failure;
10. DOS was effective at monitoring the internal temperature change, however, pinching or lifting of the de-bonding tubing caused the T DOS to react to loading in most specimen at high loads;
11. For underground projects, the geothermally active conditions potentially affect the initial short-term behaviour of FGRBs thus initial incremental loading of the system would need to be considered; and,
12. Additional testing at higher temperatures should be conducted in order to observe further, potential geothermal impacts.

6.4 Whole Temperature Spectrum

The following include general findings across the whole testing spectrum:

1. Capacity development across the whole spectrum found that as temperature increased (especially under cold conditions) and with curing duration (lesser impact), the capacity of FGRBs increased;

2. The 3-day capacity curve had the most variation and may be attributed to the short cure time thus, the support system is still stabilizing;
3. At the 90-day curing duration, the specimens across all conditions generally achieved similar ultimate capacity, with P20 being the lowest;
4. Regression analysis of axial stiffness rebar found a negative correlation with critical embedment length across the temperature spectrum, more temperature conditions would improve statistical significance;
5. Linear regression found positive correlation to both axial stiffness with temperature in each curing duration; and
6. Regression analysis found that change in temperature during testing did not significantly impact results.

6.5 Major Contributions

The following are the major contributions of the author's research endeavour:

1. Refinement of DOS technique. Confirmed methodology to protect DOS and monitor strain profile over full spectrum of specimen loading. Expanded on previous members' de-bonding zone strategy, however, found the limitation to be the location of the DOS termination. This was a result of a shorter pull-end of rebar to fit the termination of a second DOS. The de-bonding method should be continued in future research and increase of pull-end or a non-bonded termination that can be removed from rebar groove during testing;
2. Temperature calibration of fiber optic. The use of glycol bath for temperature calibration of fiber optics was an effective method as the bath provided a stable environment at each temperature increment to capture strain profile. Conversion factor from strain to absolute temperature change was determined;

3. Temperature DOS. The methodology developed in this investigation utilizing DOS (that was isolated from the effects of rebar loading) to monitor specimen temperature change along the entire length of the specimen was effective. The temperature spatial resolution of this DOS technique was assessed to be 0.1°C, which was in agreement with existing literature. However, prevention of lifting at front end during high loads needs to be further explored;
4. Exploration of new polyimide coated fiber optic. The polyimide coated fiber optic saw improvements in capturing strain profiles and reduced/eliminated the pickup transition section. However, the increased brittleness requires sensing lines rather than sensing loops. Data analyzers with multi-channels would allow for full use of this type of fiber;
5. Cement grout in temperature study. Tested a new cementitious grout for this research group for cold temperature curing. The grout was effective and gained sufficient strength even at temperatures much lower than its design / performance range. Use of PC grout at high temperatures was effective so long as evaporation prevention techniques are employed;
6. Effect of temperature on FGRBs. A rigorous laboratory investigation was completed on a very wide range of temperatures to study their effects on the performance of FGRBs in these environments. Various trends and factors were found to be higher or low predictors. The 3-day curing duration was the most unstable at the temperature extremes thus, loading of the system in the initial short-term should be incremented; and,
7. Existing literature. There are limited existing temperature studies on FGRBs, with more studies found in the high temperatures. The testing conditions differ significantly to make effective comparisons with this project's results. There was the general agreement of an initial increase in strength after 20°C and can be concurred with the higher grout UCS results and lower strains experienced by the specimens in the G45 condition and shorter mobilized embedment lengths. More temperatures should be explored in order to confirm when a decrease would be seen and the effects on the strain profile of the rebar, as existing literature has found a decrease in ultimate pull-out loads from 50°C to 70°C. This study has added

onto the limited literature on temperature and FGRBs, especially, in permafrost conditions as no directly comparable studies were readily found.

6.6 Summary of Research Group Objectives and Findings

This investigation into the effects of temperature on the geo-mechanical response of axially loaded FGRBs utilizing DOS technology has contributed to the research endeavours of the author’s research group to study the behaviours of ground support elements using DOS. An updated summary of past and current members’ Masters Thesis projects are found in Table 6-1, Table 6-2, and Table 6-3.

Table 6-1. Updated summary of research group Master’s Degree Thesis objectives

Masters Thesis	Research Objectives
Forbes (2015)	<ul style="list-style-type: none"> • Determine most appropriate commercially available optical strain sensing technology for monitoring support elements • Develop technique to apply chosen system for rock bolts and forepoles • Verify the capability of the optical technique
Cruz (2017)	<ul style="list-style-type: none"> • Develop lab testing scheme to monitor fully grouted rock bolts (FGRB) under axial load • Critical embedment length • Loading mechanisms • Failure mechanisms
O’Connor (2020)	<ul style="list-style-type: none"> • DOS as internal (rebar) and external (confining pipe) sensor • Effects of grout type • Effects of embedment length • Effects of radial stiffness of confining material

Masters Thesis	Research Objectives
Moore (2021)	<ul style="list-style-type: none"> • Further refine and understand limitations of DOS technique • Effects of rib spacing • Effects of grout annulus
Guo (2024)	<ul style="list-style-type: none"> • Improve upon DOS technique and modify to include continuous temperature change monitoring • Explore new polyimide coated fiber optic • Effects of permafrost (cold) and geothermally active (hot) conditions • Investigate cement types for temperature range

Table 6-2. Updated summary of research groups investigations

Masters Thesis	Investigation
Forbes (2015)	<ul style="list-style-type: none"> • Fiber Bragg grating • Brillouin distributed sensing • Rayleigh Optical Frequency Domain Reflectometry (ROFDR) • Technique development • Rock bolt and forepole testing
Cruz (2017)	<ul style="list-style-type: none"> • Confining material: Concrete • Borehole diameters: 31 and 41 mm • Grout: Cement and resin • Changes in embedment length, borehole diameter, and grout type
O'Connor (2020)	<ul style="list-style-type: none"> • Confining material: Various materials (steel, aluminum, PVC, concrete cylinder) • Grout: Cement and resin

Masters Thesis	Investigation
Moore (2021)	<ul style="list-style-type: none"> • Confining material: Steel pipe (various sizes) • Grout: Cement • Rib spacing: 14, 28, 41, 54, and 68 mm • Grout annulus: 7.7, 9.9, 14, 22.8 mm
Guo (2024)	<ul style="list-style-type: none"> • Confining material: 1¼" Schedule 80 steel pipe • Grout: Cement (PC and Nordic) • Temperatures: -20°C, -5°C, +20°C, +45°C • Curing Durations: 3, 7, 28, 35, 60, and 90 days

Table 6-3. Updated summary of research groups thesis conclusions

Masters Thesis	Conclusion
Forbes (2015)	<ul style="list-style-type: none"> • ROFDR was chosen • Continuous sensing at low cost • Reliability and accuracy verified in situ at an operational coal mine • DOS was a feasible sensing solution for ground support elements and should be used in-situ
Cruz (2017)	<ul style="list-style-type: none"> • Larger borehole diameter improved system capacity • Embedment length was most significant factor, capacity increased with length • Resin grout generally had higher capacity
O'Connor (2020)	<ul style="list-style-type: none"> • Grout type was major factor for critical embedment length and bond strength • Increase in embedment length increased both, increase was not proportional • Confinement materials did not have correlations to either

Masters Thesis	Conclusion
Moore (2021)	<ul style="list-style-type: none"> • Rib spacing had significant effect on rock bolt behaviour (stiffness, load to fully mobilize embedment length, bond performance, load transfer, peak and residual strength, etc.) • Grout annulus effects were not consistent
Guo (2024)	<ul style="list-style-type: none"> • Curing temperature had effect on strain distributions along rebar bolt • Grout UCS was affected by temperature and contributed to capacity development in FGRB specimens • Curing duration had impact (lesser than former factors) on FGRB capacity, notably for stabilization of the systems as the initial 3 days had the least consistent results • DOS was effective at monitoring specimen temperature change, with a spatial resolution of 0.1°C

7 Conclusions and Recommendations

7.1 Conclusions

A rigorous laboratory testing scheme was developed and a series of 24 FGRB laboratory pull-out tests were conducted (and related material testing) in order to investigate the effects extreme temperature conditions on the behaviour of FGRBs, as well as, capacity development over time within these environments. The use of the state-of-the-art DOS technology for specimen strain and temperature monitoring was proven effective and continues to address spatial limitation problems that plagues industry in this regard. Overall, the main failure mechanism observed in permafrost conditions was bolt pull-out due to the bolt-grout interface failure and contribution of grout mobilization from grout-pipe (rock) failure. In geothermal conditions, the main failure mechanism observed was tensile failure of the rebar rock bolt. The short-term (3-day) curing duration posed the most inconsistencies for capacity as the systems had not yet stabilized. With adequate embedment length, all conditions ultimately achieved similar capacities in the long-term (90 days). The continuous strain monitoring provided comparisons and trend development of strain profiles in/between each curing condition. Two types of grout were tested and both of their compressive strength results were affected by curing temperature. The grouting process was effective in minimizing grout voids in the specimens and different procedural considerations were determined for the different conditions. Further exploration with more temperature conditions would provide a more wholesome picture of temperature effects on FGRBs.

7.2 Future Recommendations

The results of this study, as well as, past members of this research group have contributed to enhancing the understanding of FGRBs and incrementally extending the utility of this method by improving it and utilizing it in an assortment of relevant scenarios. Previous members investigated the effects of confining medium, embedment length, grouting materials, rib spacing, and grout annulus, and this most recent study adds temperature to the research group's endeavours. This project has bridged selected research gaps and provided insight into the topic, warranting further investigation. The following recommendations are suggested:

1. Expand temperature study to more test conditions in order to assess higher temperature effects. Monitor strains during curing process in temperature conditions to observe what is happening. It is recommended to add internal roughness by threading or grooving the first 25-50 mm of the confinement pipes to prevent grout mobilization and potential failure at the grout-pipe interface affecting results. Re-assess cold temperature conditions and evaluate if roughness improves bonding of the grout and pull-out testing results. Also repeating the tests in all conditions will provide validation for results;
2. Use of multi-channel LUNA analyzers in order to remove the DOS looping requirement, which was the weak point that had caused the ϵ DOS to have gaps in its data acquisition. Also the polyimide coated fiber optic could then be used, which would improve results with immediate strain pickup;
3. If any DOS termination is located on the pull-end of the rebar, then the rebar distance before the borehole collar should be at least 500 mm in order to provide an adequate distance from the MTS grip and prevent premature DOS failure. Alternatively, have the termination be detachable from the rebar and set on top of the top bearing plate during testing;
4. The 1.5" thick top bearing plate began to yield during pull-out testing (which was captured and accounted for in the analysis), which the plate thickness had already been increased from past projects by the previous member's setup. If similar length specimens are to be studied, a minimum 2" thick plate would be recommended;
5. Use of stainless steel tubing was effective for de-bonding zones, however, the lifting or pinching caused issues for the DOS. Increasing the lengths of the tubing and adding extra epoxy overtop could potentially reduce such issues or explore other de-bonding materials for this purpose; and,
6. Another factor that could be explored with available equipment in the RMC Structures lab would be the response of FGRBs to dynamic loads that could be experienced in underground mining operations or due to seismic activity.

8 References

- AdvancedPhotonix. (n.d.). ODiSI-B Optical Distributed Sensor Interrogator [online]: Available from https://www.advancedphotonix.com/wp-content/uploads/2016/07/ODB5_DataSheet_Rev13_020217.pdf
- Alexopoulos, E.C. (2010). Introduction to Multivariate Regression Analysis, *Hippokratia*, 14(1), 23-28.
- Arioglu, N., Canan Girgan, C., & Arioglu, E. (2006). Evaluation of Ratio between Splitting Tensile Strength and Compressive Strength for Concretes up to 120 MPa and its Application in Strength Criterion, *ACI Materials Journal*, 103(1), 18-24.
- ASTM. (2013). *Standard Test Method for Rock Bolt Anchor Pull Test D4435-13e1*. ASTM International.
- ASTM. (2015). *Standard Specification for Molds for Forming Concrete Test Cylinders Vertically C470*. ASTM International.
- ASTM. (2017). *Standard Test Method for Splitting Tensile Strength of Cylindrical Concrete Specimens C496*. ASTM International.
- ASTM. (2019). *Standard Practice for Making and Curing Concrete Test Specimens in the Laboratory C192*. ASTM International.
- ASTM. (2021). *Standard Test Method for Compressive Strength of Cylindrical Concrete Specimens C39*. ASTM International.
- ASTM. (2022). *Standard Test Method for Static Modulus of Elasticity and Poisson's Ratio of Concrete in Compression C469*. ASTM International.
- Aziz, N., Jalaifar, H., & Conclaves, J. (2006). *Bolt Surface Configurations and Load Transfer Mechanism* [2006 Coal Operators' Conference, University of Wollongong].
- Bednarek, L. & Majcherczyk, T. (2020). An Analysis of Rock Mass Characteristics that Influence the Choice of Support. *Geomatics and Engineering*, 21(4), 371-377. <https://doi.org/10.12989/gae.2020.21.4.371>
- Belle, B. & Biffi, M. (2018). Cooling Pathways for Deep Australian Longwall Coal Mines of the Future. *International Journal of Mining Science and Technology*, 28, 865-875. <https://doi.org/10.1016/j.ijmst.2018.02.001>
- Benmokrane, B., Chennouf, A., & Mitri, H. (1995). Laboratory Evaluation of Cement-Based Grouts and Grouted Rock Anchors. *International Journal of*

- Rock Mechanics and Mining Sciences & Geomechanics Abstracts*, 32(7), 633-642.
- Björnfot, F. & Stephansson, O. (1984). Interaction of Grouted Rock Bolts and Hard Rock Masses at Variable Loading in a Test Drift of the Kiirunavaara Mine, Sweden. *Rock bolting: Theory and application in mining and underground construction*, 1st Edition. Routledge.
- Blanco Martín, L., Tijani, M., & Hadj-Hassen, F. (2011). A New Analytical Solution to the Mechanical Behaviour of Fully Grouted Rockbolts Subjected to Pull-out Tests. *Construction and Building Materials*, 25, 749-755.
- Bobet, A. & Einstein, H.H. (2011). Tunnel Reinforcement with Rock Bolts. *Tunnelling and Underground Space Technology*, 26(1), 100-123. <https://doi.org/10.1016/j.tust.2010.06.006>
- Brady, B.H.G. & Brown, E.T. (2004). *Rock Mechanics for Underground Mining, Third Edition*. Kluwer Academic Publishers.
- Cai, Y., Esaki, T., & Jiang, Y. (2004). An Analytical Model to Predict Axial Load in Grouted Rock Bolt for Soft Rock Tunnelling. *Tunnelling and Underground Space Technology*, 19(6), 607-618. <https://doi.org/10.1016/j.tust.2004.02.129>
- Cao, C., Nemcik, J., Aziz, N., & Ren, T. (2012). *Failure Modes of Rock Bolting* [2012 Coal Operators' Conference, University of Wollongong].
- Ciment Québec. (n.d.). General Use Cement – Typical Analysis Certificate.
- Corning. (2021). Corning® SMF-28e+ Product Information [online]: Available from <https://www.corning.com/media/worldwide/coc/documents/Fiber/PI-1463-AEN.pdf>
- Cruz, D.F. (2017). *The Geomechanical Response of Axially Loaded Fully Grouted Rock Bolts Utilizing Fibre Optics Technology* [Master's Thesis, Royal Military College of Canada]. Kingston: Department of Civil Engineering.
- Cruz, D.F., Vlachopoulos, N., & Forbes, B.J. (2016). *The Geo-Mechanical Response of Axially Loaded Rock Bolts using Fiber Optic Technology* [XV Colombian Geotechnical Congress & II International Specialized Conference of Soft Rocks, Cartagena].
- Farmer, I.W. (1975). Stress Distribution along a Resin Grouted Rock Anchor. *International Journal of Rock Mechanics and Mining Sciences & Geomechanics Abstracts*, 12(11), 347-35. [https://doi.org/10.1016/0148-9062\(75\)90168-0](https://doi.org/10.1016/0148-9062(75)90168-0)

- Fiber Instrument Sales. (n.d.). FIS Stock Fiber Optic Patchcords [online]: Available from <https://www.fiberinstrumentsales.com/specs/Patch-Cable.pdf>
- Forbes, B.J. (2015). *The Application of Distributed Optical Sensing for Monitoring Support in Underground Excavations* [Master's Thesis, Queen's University]. Kingston: Department of Geological Sciences & Geological Engineering.
- Forbes, B., Vlachopoulos, N., & Hyett, A.J. (2018). The application of distributed optical strain sensing to measure the strain distribution of ground support members, *Facets*, 3(1).
- Freeman, T.J. (1978). The Behaviour of Fully-Bonded Rock Bolts in the Kielder Experimental Tunnel. *Tunnels and Tunnelling International*, 10(5), 37-40.
- Frenelus, W., Peng, H., & Zhang, J. (2022). An Insight from Rock Bolts and Potential Factors Influencing Durability and the Long-Term Stability of Deep Rock Tunnels. *Sustainability*, 14(7), 10943. <https://doi.org/10.3390/su141710943>
- Gibb, F.G.F. (1999). High-temperature, very deep, geological disposal: a safer alternative for high-level radioactive waste?. *Waste Management*, 19, 207-211.
- Gifford, D.K., Soller, B.J., Wolfe, M.S., & Froggatt, M.E. (2005). Distributed Fiber-Optic Temperature Sensing using Rayleigh Backscatter. *ECOC 2005*.
- Government of Canada. 2022. Arctic and Northern Policy Framework. <https://www.rcaanc-cirnac.gc.ca/eng/1560523306861/1560523330587>
- Gross-Sampson, M.A. (2024). Statistical Analysis in JASP: A guide for students. Available at: <https://jasp-stats.org/wp-content/uploads/2024/03/Statistical-Analysis-in-JASP-2024.pdf>
- Guo, C., Moore, K.S., & Vlachopoulos, N. (2023). *The Effects of Temperature on the Axial Response of Fully Grouted Rock Bolts Utilizing Distributed Fiber Optic Sensors* [GeoSaskatoon 2023, Saskatoon].
- He, L., An, X.M., & Zhao, Z.Y. (2014). Fully Grouted Rock Bolts: An Analytical Investigation. *Rock Mechanics and Rock Engineering*, 48(3), 1181-1196. <https://doi.org/10.1007/s00603-014-0610-0>
- Hoek, E. (2007). *Practical Rock Engineering*. Rocscience Inc.
- Hoek, E. & Wood, D.F. (1987). Support in Underground Hard Rock Mines. *Underground Support Systems*, 35, 1-6.
- Hoek, E., Kaiser, P.K., & Bawden, W.F. (2000). *Support of Underground Excavations in Hard Rock*. CRC Press.

- Huang, G. (2021). *Performance of Calcium Sulfoaluminate Cement-based Mixtures Used for Permafrost Regions* [PhD Thesis, University of Alberta]. Edmonton: Department of Civil and Environmental Engineering.
- Hyett, A.J., Bawden, W.F., & Reichert, R.D. (1992). The Effect of Rock Mass Confinement on the Bond Strength of Fully Grouted Cable Bolts, *International Journal of Rock Mechanics and Mining Sciences & Geomechanics Abstract*, 29(5), 503-524. [https://doi.org/10.1016/0148-9062\(92\)92634-0](https://doi.org/10.1016/0148-9062(92)92634-0)
- JASP Team. (2024). JASP (Version 0.18.3) [Computer software]. Available at: <https://jasp-stats.org/>
- Jenness, J.L. 1949. Permafrost in Canada. *Arctic*, 2(1), 13-27.
- Johnston, G.H. & Ladanyi, B. (1972). Field Tests of Grouted Rod Anchors in Permafrost. *Canadian Geotechnical Journal*, 9(2), 176-194.
- Kilic, A., Yasar, E., & Celik, A.G. (2002). Effect of Grout Properties on the Pull-out Load Capacity of Fully Grouted Rock Bolt. *Tunnelling and Underground Space Technology*, 17, 355-362.
- King, F., Hall, S.D. & Keech, P.G. (2017). Nature of the near-field environment in a deep geological repository and the implications for the corrosion behaviour of the container. *The International Journal of Corrosion Processes and Corrosion Control*, 52, 25-30.
- King A Sika Company. (n.d.). Nordic Cable CT Technical Data Sheet.
- Lahouar, M.A., Caron, J., Pinoteau, N., Forêt, G., & Benzarti, K. (2017). Mechanical Behaviour of Adhesive Anchors under High Temperature Exposure: Experimental Investigation. *International Journal of Adhesives and Adhesion*, 78, 200-211. <https://doi.org/10.1016/j.ijadhadh.2017.07.004>
- Li, B., Qi, T., Wang, Z., & Yang, L. (2011). Back Analysis of Grouted Rock Bolt Pullout Strength Parameters from Field Tests. *Tunnelling and Underground Space Technology*, 28, 345-349. <https://doi.org/10.1016/j.tust.2011.11.004>
- Li, C. & Håkassan, U. (1999). Performance of the Swellex Bolt in Hard and Soft Rocks. *Rock Support and Reinforcement Practice in Mining, 1st Edition* [Edited A.G. Thompson]. Routledge.
- Li, C. & Sillborg, B. (1999). Analytical Models of Rock Bolts. *International Journal of Rock Mechanics and Mining Sciences*, 36(8), 1013-1029. [https://doi.org/10.1016/S1365-1609\(99\)00064-7](https://doi.org/10.1016/S1365-1609(99)00064-7)

- Li, C.C. (2010). A New Energy-Absorbing Bolt for Rock Support in High Stress Rock Masses. *International Journal of Rock Mechanics and Mining Sciences*, 47(3), 396-404. <https://doi.org/10.1016/j.ijrmmms.2010.01.005>
- Li, C.C., Kristjansson, G., & Høyen, A.H. (2016). Critical Embedment Length and Bond Strength of Fully Encapsulated Rebar. *Tunnelling and Underground Space Technology*, 59, 16-23. <https://doi.org/10.1016/j.tust.2016.06.007>
- Li, F., Jin, H., Hu, D., Wang, B., & Jia, Y. (2017a). Influence of Temperature and Roughness of Surrounding Rocks on Mechanical Behavior of Rock Bolts. *Soil Dynamics and Earthquake Engineering*, 103, 55-63. <https://doi.org/10.1016/j.soildyn.2017.09.011>
- Li, F., Quan, X., Jia, Y., Wang, B., Zhang, G., & Chen S. (2017b). The Experimental Study of the Temperature Effect on the Interfacial Properties of Fully Grouted Rock Bolt. *Applied Science*, 7, 327. <https://doi.org/10.3390/app7040327>
- Li, Y.Z. & Ingason, H. (2014). *Maximum Ceiling Temperature in a Tunnel Fire SP Report 2010:51* [SP Technical Research Institute of Sweden].
- Ma, S., Nemcik, J., & Aziz, N. (2013). An Analytical Model of Fully Grouted Rock Bolts Subjected to Tensile Load. *Construction and Building Materials*, 49, 519-526. <https://doi.org/10.1016/j.conbuildmat.2013.08.084>
- Mark, C., Compton, C.S., Oylar, D.C., & Dolinar, D.R. (2002). *Anchorage Pull Testing for Fully Grouted Roof Bolts* [21st International Conference on Ground Control in Mining, West Virginia University].
- Micro Measurements. (2014). M-Bond 200 Strain Gauge Adhesive [online]: Available from https://docs.micro-measurements.com/?id=6671&_ga=2.51895470.603289743.1666273322-318736113.1666273322
- McTyer, K. (2020). *The Effect of Elevated Temperature on Resin-anchored Rock Bolts* [2020 Coal Operators' Conference, University of Wollongong].
- Morris, E.F. (1970). *Evaluation of Cement Systems for Permafrost* [99th Annual Meeting of American Institute of Mining, Metallurgical, and Petroleum Engineers].
- Moore, K.S. (2021). *The Effects of Rib Spacing and Grout Annulus on the Geomechanical Response of Axially Loaded Fully Grouted Rock Bolts Utilizing Distributed Fiber Optic Technology* [Master's Thesis, Royal Military College of Canada]. Kingston: Department of Civil Engineering.

- Moore, K.S. & Vlachopoulos, N. (2021). *Utilizing a Fiber Optic Methodology to Capture the Axial Response of Rib Spacing Effects on Grouted Rock Bolts* [GeoNiagara 2021].
- Moosavi, M., Jafari, A., & Khosravi, A. (2003). Bond of Cement Grouted Reinforcing Bars under Constant Radial Pressure. *Cement & Concrete Composites*, 27, 103-109.
<https://doi.org/10.1016/j.cemconcomp.2003.12.002>
- Natural Resources Canada. (2016). Permafrost, Atlas of Canada, 5th Edition.
<https://open.canada.ca/data/en/dataset/d1e2048b-ccff-5852-aaa5-b861bd55c367>
- Nuclear Waste Management Organization. (2023). Canada's Plan – Adaptive Phased Management. <https://www.nwmo.ca/en/Canadas-Plan/About-Adaptive-Phased-Management-APM>
- NWT & Nunavut Chamber of Mines. (2022). Mines Actively Producing in the NWT and Nunavut. <https://www.miningnorth.com/our-industry#:~:text=In%20the%20NWT%2C%20we%20have,the%20Mary%20River%20iron%20mine.https://www.miningnorth.com/mines>
- O'Connor, T.P. (2020). *The Geo-Mechanical Response of Axially Loaded Fully Grouted Rock Bolts Utilizing Distributed Fiber Optic Technology* [Master's Thesis, Royal Military College of Canada]. Kingston: Department of Civil Engineering.
- O'Connor, T.P., Vlachopoulos, N., Forbes, B., & Diederichs, M. (2020). *Grout Comparison for Fully Grouted Rock Bolts Using Distributed Fiber Optic Sensors* [54th U.S. Rock Mechanics/Geomechanics Symposium].
- Oke, J., Vlachopoulos, N., & Diederichs, M.S. (2014). Numerical analyses in the design of umbrella arch systems. *Journal of Rock Mechanics and Geotechnical Engineering*, 6(6), 546-546.
<http://dx.doi.org/10.1016/j.jrmge.2014.09.005>
- Peck, R.B. (1969). Advantages and Limitations of the Observational Method in Applied Soil Mechanics. *Geotechnique*, 19(2), 171-187.
<https://doi.org/10.1680/geot.1969.19.2.171>
- Peng, S. & Tang, D. (1984). Roof Bolting in Underground Mining: A State-of-the-art Review. *International Journal of Mining Engineering*, 2(1), 1-42.
- Pinazzi, P.C., Spearing, A.J.S., Jessu, K.V., Singh, P., & Hawker, R. (2020). Mechanical Performance of Rock Bolts under Combined Load Conditions.

- International Journal of Mining Science and Technology*, 30(2), 167-177.
<https://doi.org/10.1016/j.ijmst.2020.01.004>
- Potvin, Y., & Nedin, P. (2003). *Rockfalls and surface support in Australian underground hard rock mines* [J. Hadigeorgiou (Ed.), 3rd International Seminar on Surface Support Liners: Thin Spray-on Liners, Shotcrete and Mesh (Quebec City, Canada ed., Vol. n/a, pp. Section 1, 1-14), Universite Laval].
- Ren, F.F., Yang, Z.J., Chen, J.F., & Chen, W.W. (2010). An Analytical Analysis of the Full-range Behaviour of Grouted Rockbolts Based on a Tri-linear Bond-slip Model. *Construction and Building Materials*, 24(3), 361-370.
<https://doi.org/10.1016/j.conbuildmat.2009.08.021>
- Reny, S., Cruz, J.P., & Clements, W. (2019). Developments of New Cementitious Grout for Permafrost Conditions. *Ground Support*.
- Serbousek, M.O. & Signer, S.P. (1987). Linear Load-Transfer Mechanics of Fully Grouted Roof Bolts. *Bureau of Mines Report of Investigations 9135*. United States Department of the Interior.
- SHOWA Measuring Instruments Inc. (2022). Types and Specifications of Strain Gages [online]: Available from http://www.showa-sokki.co.jp/english/products_e/strain_gage_e/strain_gage_config_e.htm
- Signer, S.P. (1990). Field Verification of Load Transfer Mechanics of Fully Grouted Roof Bolts. *US Bureau of Mines (1903)*.
- Singh, B. & Goel, R.K. (1999). *Rock Mass Classification: A Practical Approach to Civil Engineering*. Elsevier Science Ltd.
- Stille, H. (1992). Keynote Lecture: Rock Support in Theory and Practice. *Rock Support in Mining and Underground Construction [Edited P.K. Kaiser & D. McCreath]*. CRC Press.
- Thompson, A.G. & Villaescusa, E. (2014). Case Studies of Rock Reinforcement Components and Systems Testing. *Rock Mechanics and Rock Engineering*, 47, 1589-1602. <https://doi.org/10.1007/s00603-014-0583-z>
- ThorLabs. (2024a). Coreless Termination Fiber [online]: Available from https://www.thorlabs.com/newgrouppage9.cfm?objectgroup_id=7948&pn=FG125LA
- ThorLabs. (2024b). Polyimide-Coated Single Mode Fiber [online]: Available from https://www.thorlabs.com/newgrouppage9.cfm?objectgroup_id=13401&pn=SM1550P

- Vlachopoulos, N. (2017). Sensing the Ground: The use of Distributed Optical Sensing for Monitoring the Ground as well as for Support in Underground Excavations [PowerPoint Slides]. University of Toronto.
- Vlachopoulos, N. (2022). *Eupalinos Tunnel - First Tunnel to be Excavated Simultaneously from Both Ends in the 6th Century B.C.* [GeoCalgary 2022, Calgary].
- Vlachopoulos, N., Carrapatoso, C., Holt, S.W., Cruz, D., & Forbes, D. (2020). An Investigation into Support Interaction of Ground Support through Numerical Modelling and Laboratory Testing. *Geotechnical and Geological Engineering*, 38, 5719-5736. <https://doi.org/10.1007/s10706-020-01389-0>
- Vlachopoulos, N., Cruz, D., & Forbes, B. (2018). Utilizing a Novel Fiber Optic Technology to Capture the Axial Responses of Fully Grouted Rock Bolts. *Journal of Rock Mechanics and Geotechnical Engineering*, 10(2), 222-235. <https://doi.org/10.1016/j.jrmge.2017.11.007>
- Vlachopoulos, N. & Diederichs, M.S. (2009). Improved Longitudinal Displacement Profiles for Convergence Confinement Analysis of Deep Tunnels. *Rock Mechanics and Rock Engineering*, 42, 131-146.
- Vlachopoulos, N., Diederichs, M.S., & Marinou, P. (2013). Tunnel Behaviour Associated with Weak Alpine Rock Masses of the Driskos Twin Tunnel System, Egnatia Odos Highway. *Canadian Geotechnical Journal*, 50(1), 91-120. <https://doi.org/10.1139/cgj-2012-002>
- Vlachopoulos, N., Forbes, B., Oke, J., & Hyett, A. (2014). *The Development of a Technique in order to Measure the Distributed Optical Sensing of a Forepole temporary support element employed within an Umbrella Arch System* [EUROCK, International Symposium, Vigo, Spain].
- Wang, B., Guo, X., Li, F., Hu, D., & Jia, Y. (2018). Mechanical Behavior of Rock Bolts under a High Temperature Environment. *International Journal of Rock Mechanics and Mining Sciences*, 104, 124-130. <https://doi.org/10.1016/j.ijrmms.2018.01.026>
- Wang, J., Apel, D.B., Dyczko, A., Walentek, A., Prusek, S., Xu, H., & Wei, C. (2022). Analysis of the Damage Mechanism of Strainbursts by a Global-Local Modeling Approach. *Journal of Rock Mechanics and Geotechnical Engineering*. <https://doi.org/10.1016/j.jrmge.2022.01.009>
- Wang, X., Liu, C., Liu, S., Yan, C., Zhang, J., & Li, H. (2020). Compressive Strength of Pile Foundation Concrete in Permafrost Environment in China. *Construction*

- and Building Materials*, 247.
<https://doi.org/10.1016/j.conbuildmat.2020.118431>
- Weisbrich, M., Holschemacher, K., & Bier, T. (2020). Comparison of different fiber coatings for distributed strain measurement in cementitious matrices. *Journal of Sensors and Sensor Systems*, 9(2), 189–197.
- Windsor, C.R. & Thompson, A.G. (1993). Rock Reinforcement – Testing, Design and Evaluation. *Comprehensive Rock Engineering, Principles, Practice & Projects, Vol. 4 [Edited J.A. Hudson]*. Pergamon Press.
- World Nuclear Association. (2023). How can nuclear combat climate change?. <https://world-nuclear.org/nuclear-essentials/how-can-nuclear-combat-climate-change.aspx>
- Xue, Y., Sun, D., & Wang, L. (2021). An analytical solution of temperature in a nuclear waste repository. *Annals of Nuclear Energy*, 163.
- Yazici, S. & Kaiser, P.K. (1992). Bond Strength of Grouted Cables. *International Journal of Rock Mechanics and Mining Sciences & Geomechanics Abstracts*, 29(3), 279-292. [https://doi.org/10.1016/0148-9062\(92\)93661-3](https://doi.org/10.1016/0148-9062(92)93661-3)
- Zhang, K., Zhang, G., Hou, R., Wu, Y., & Zhou, H. (2014). Stress Evolution in Roadway Rock Bolts During Mining in a Fully Mechanized Longwall Face, and an Evaluation of Rock Bolt Support Design. *Rock Mechanics and Rock Engineering*, 48, 333-344.
- Zhang, W., Wang, L., Song, Y., & Tan, Y. (2021). Experimental Study on the Mechanical Properties of Grouted Rock Bolts Subjected to Sulfate Attack and Freeze-thaw Cycling. *Construction and Building Materials*, 291.
<https://doi.org/10.1016/j.conbuildmat.2021.123391>

Appendix A Specimen Results

This appendix presents the results for each FGRB specimen. Each specimen includes load-displacement curve, DOS strain profile, axial displacement, pipe dilation monitoring, and specimen temperature change.

P20 Condition Specimens:

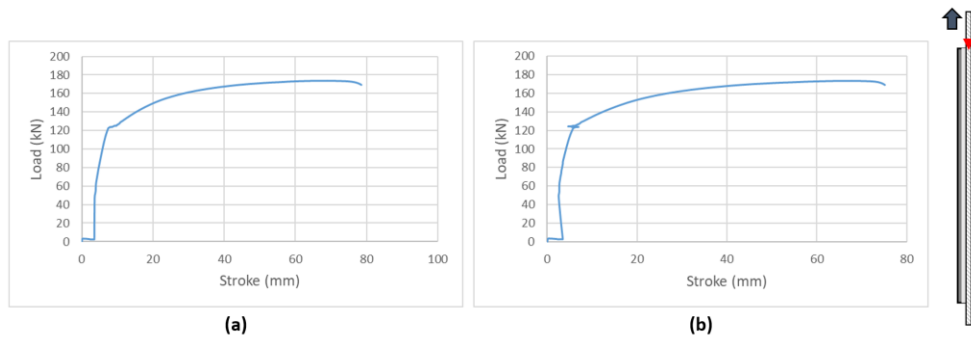


Figure A-1. Load-Displacement curve from P20-3: (a) Whole system response; (b) Axial displacement corrected for test rig movement and elongation

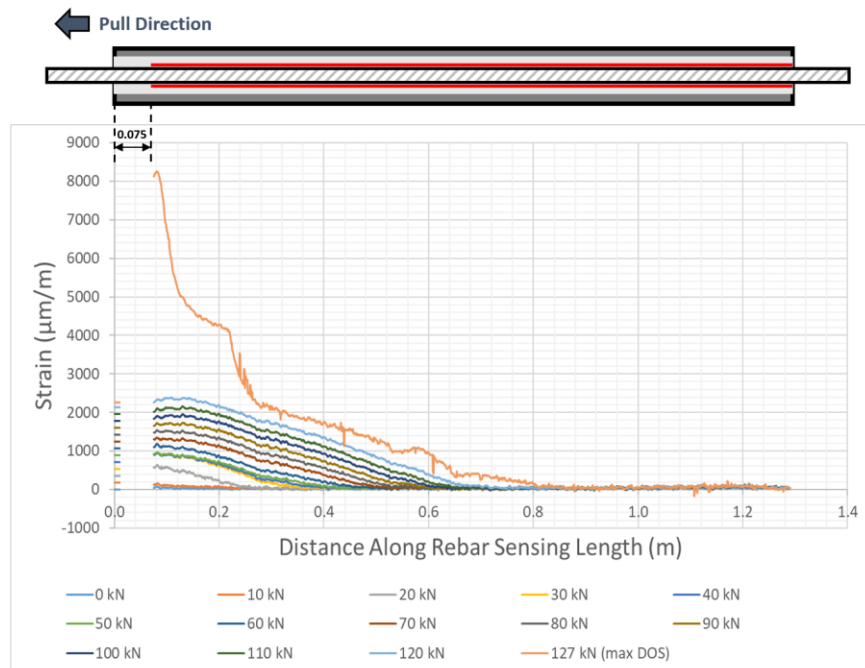


Figure A-2. P20-3 specimen strain profile along rebar bolt during pull-out testing

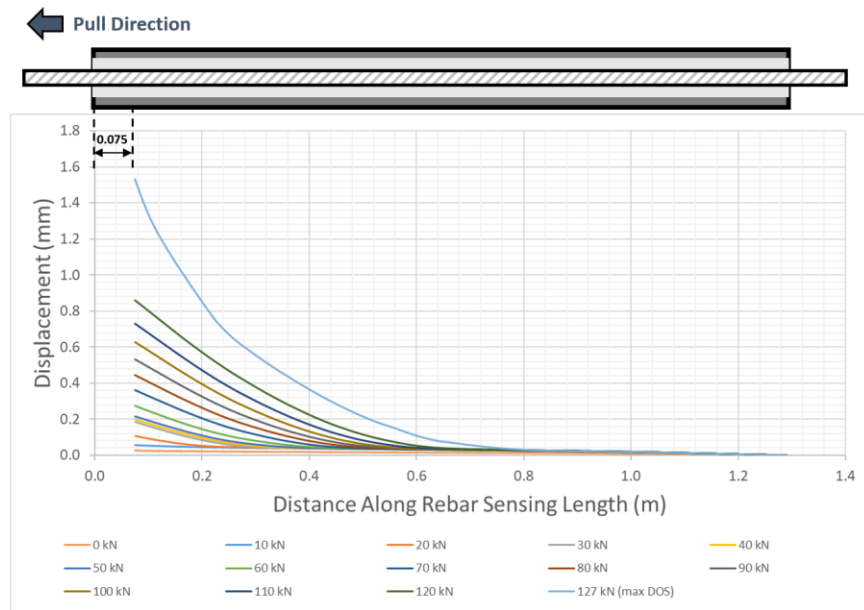


Figure A-3. P20-3 specimen axial displacement profile

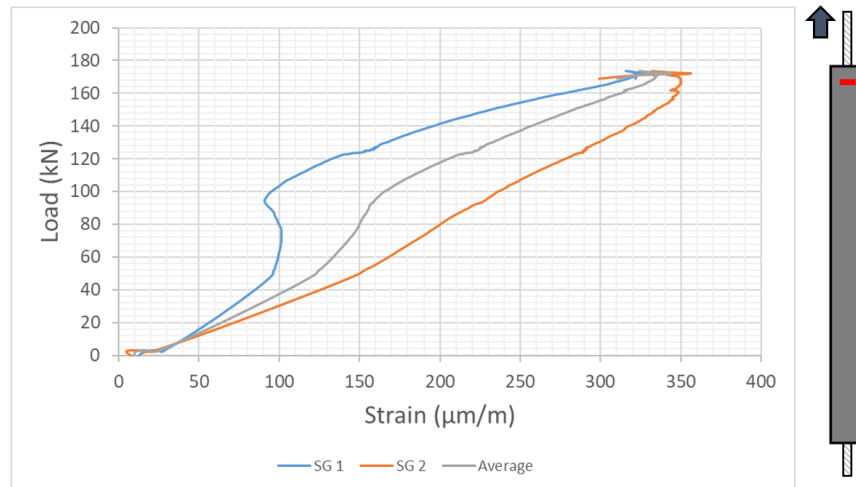


Figure A-4. P20-3 specimen pipe dilation monitoring at 50 mm

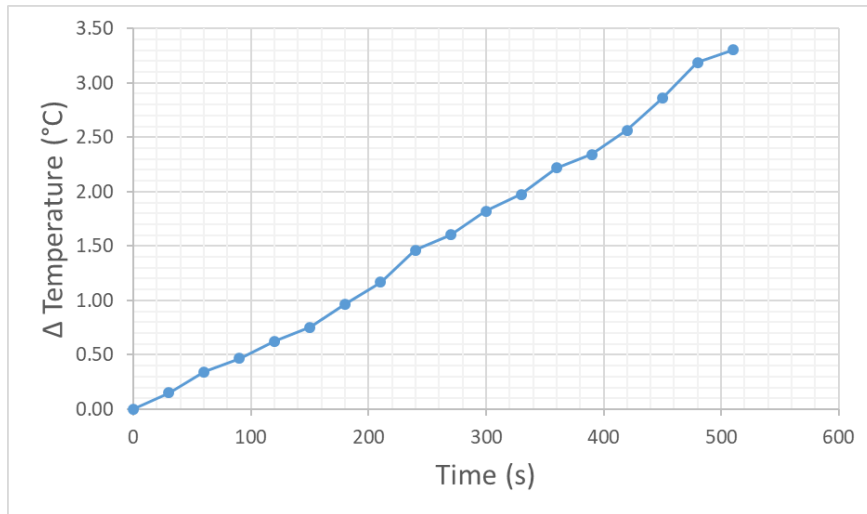


Figure A-5. P20-3 specimen temperature change during pull-out testing

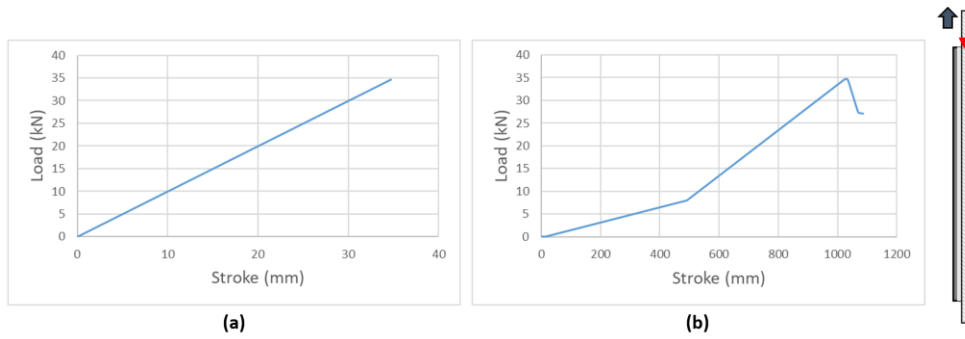


Figure A-6. Load-Displacement curve from P20-7 [DAQ malfunction resulted in inaccurate load recording]: (a) Whole system response; (b) Axial displacement corrected for test rig movement and elongation

P20-7 ϵ DOS failure – No strain profile

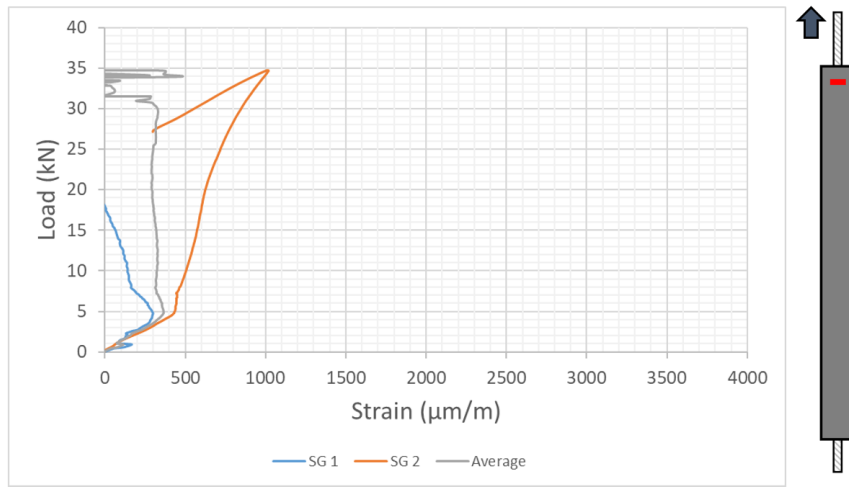


Figure A-7. P20-7 specimen pipe dilation monitoring at 50 mm [[DAQ malfunction resulted in inaccurate load recording]: SG 1 failure during testing

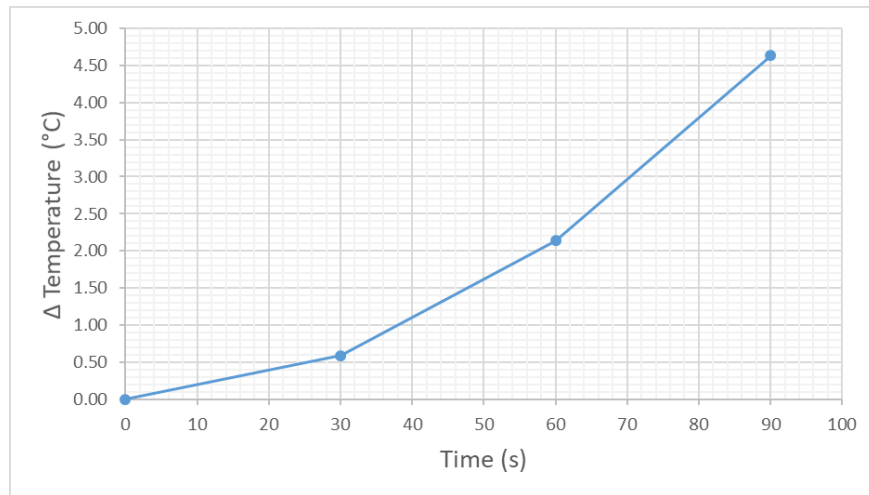


Figure A-8. P20-7 specimen temperature change during pull-out testing

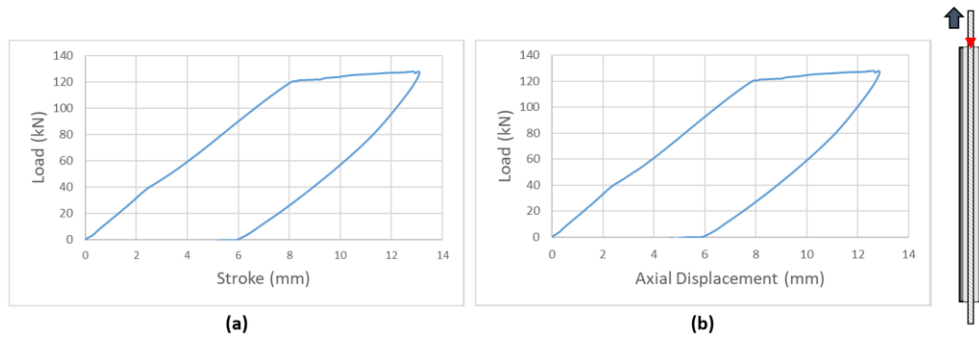


Figure A-9. Load-Displacement curve from P20-28: (a) Whole system response; (b) Axial displacement corrected for test rig movement and elongation

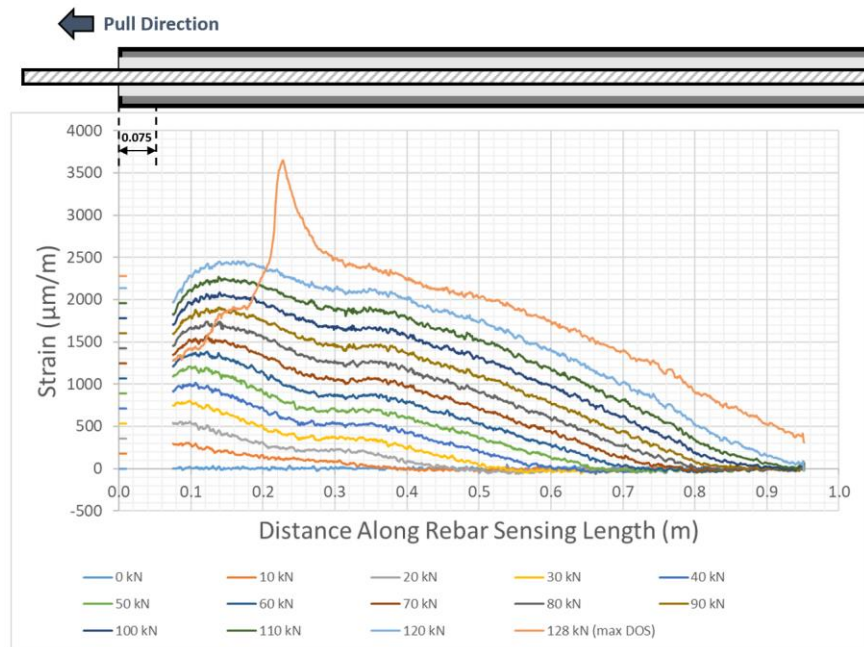


Figure A-10. P20-28 specimen strain profile along rebar bolt during pull-out testing [partial length]

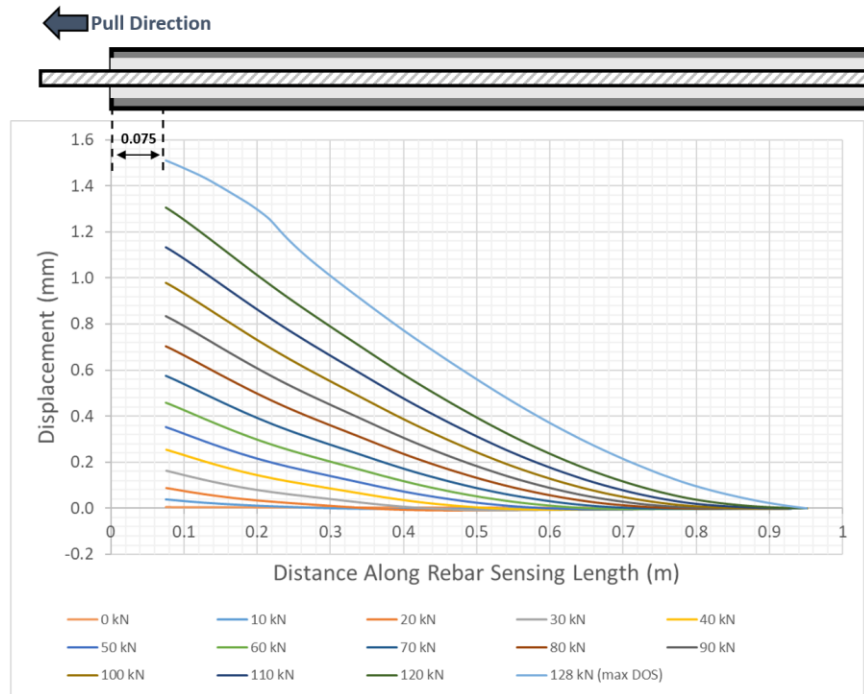


Figure A-11. P20-28 specimen axial displacement profile [partial length]

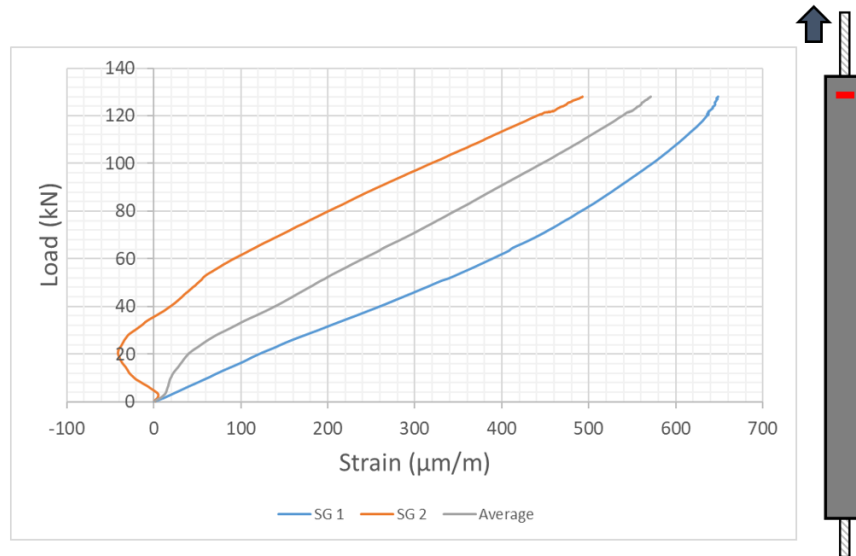


Figure A-12. P20-28 specimen pipe dilation monitoring at 50 mm

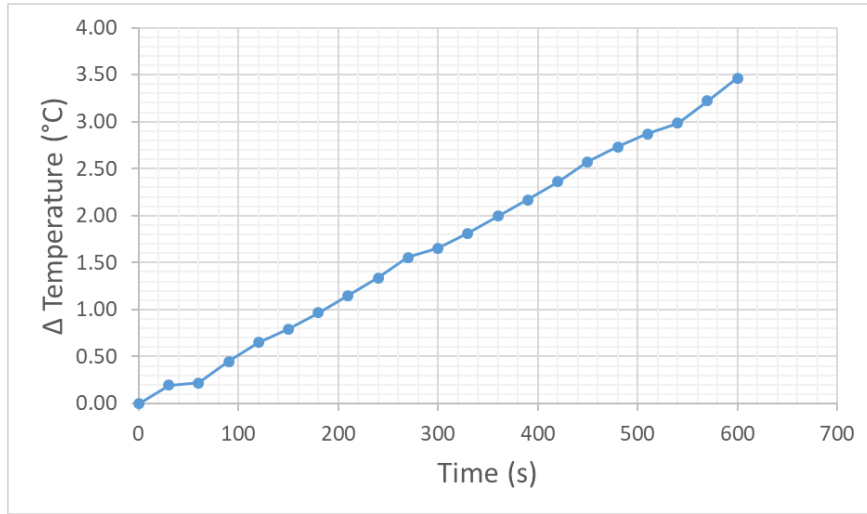
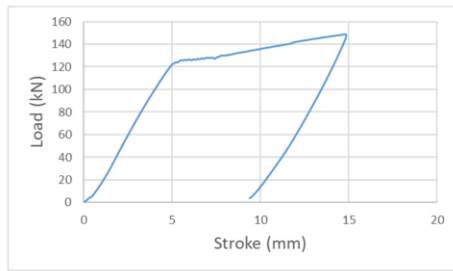


Figure A-13. P20-28 specimen temperature change during pull-out testing



(a)

(b)



Figure A-14. Load-Displacement curve from P20-35: (a) Whole system response; (b) Axial displacement corrected [LVDT malfunction]

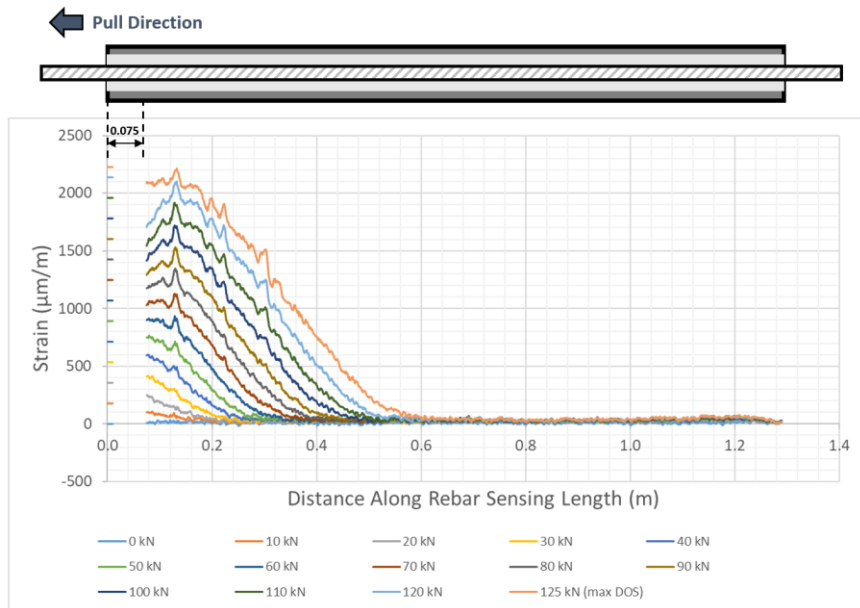


Figure A-15. P20-35 specimen strain profile along rebar bolt during pull-out testing

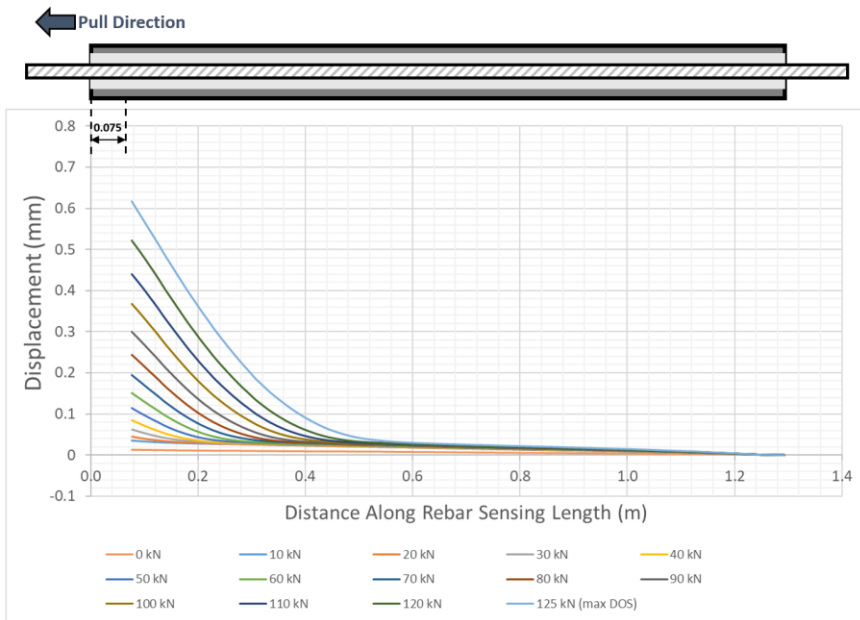


Figure A-16. P20-35 specimen axial displacement profile

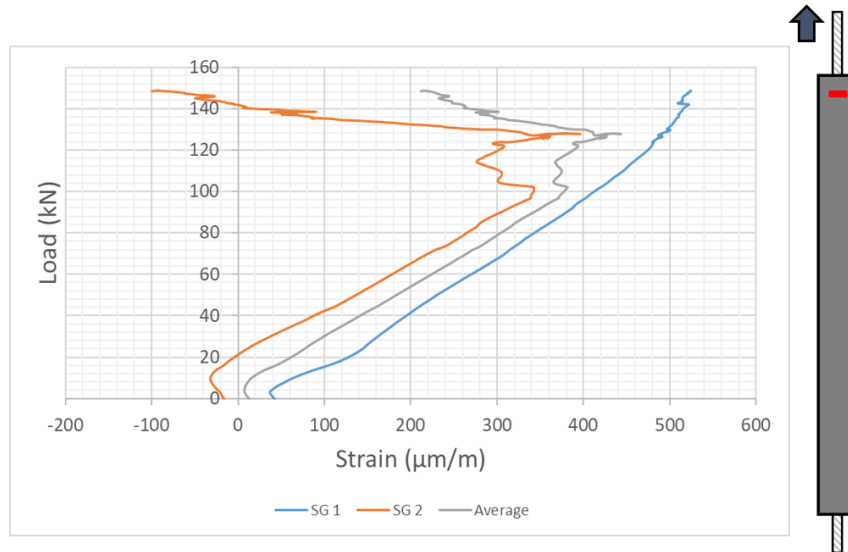


Figure A-17. P20-35 specimen pipe dilation monitoring at 50 mm

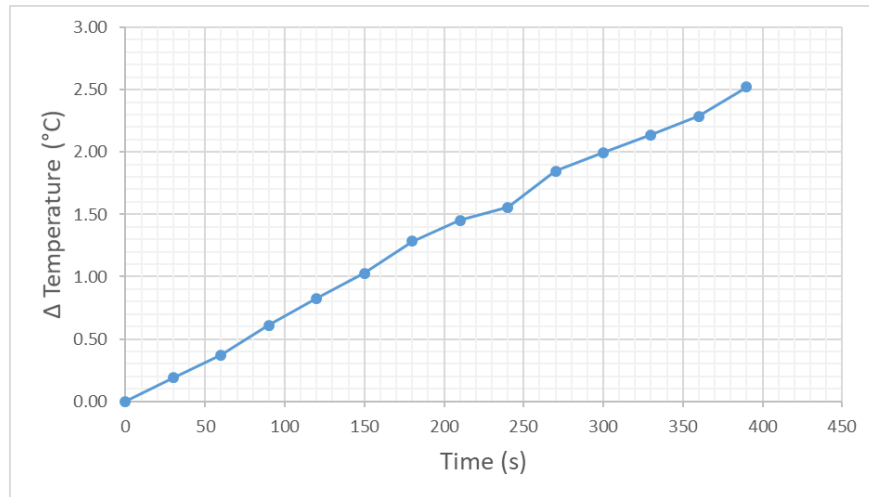


Figure A-18. P20-35 specimen temperature change during pull-out testing

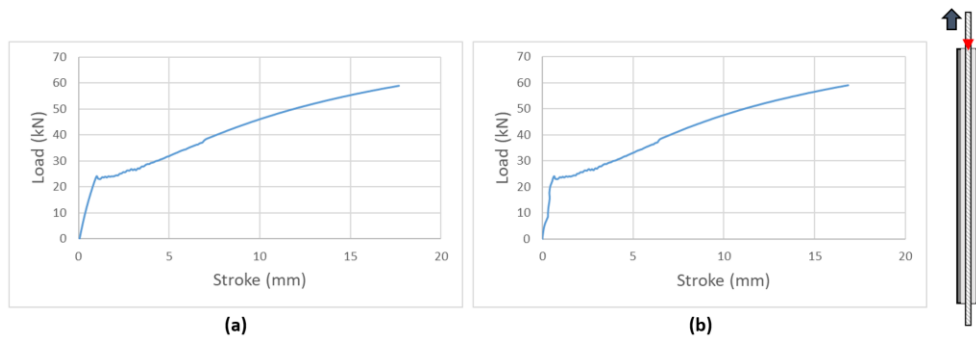


Figure A-19. Load-Displacement curve from P20-60 [DAQ malfunction resulted in inaccurate load recording]: (a) Whole system response; (b) Axial displacement corrected for test rig movement and elongation

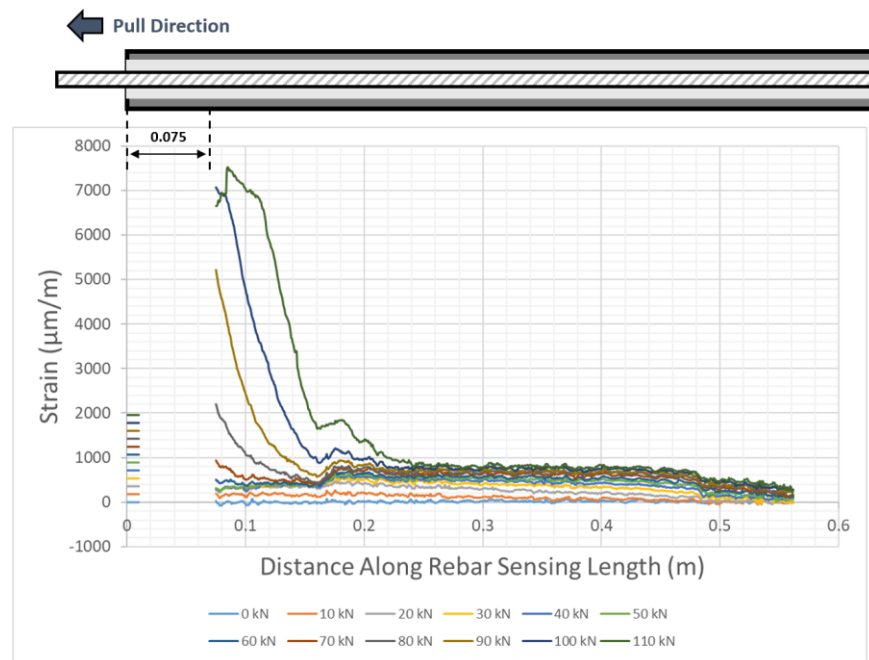


Figure A-20. P20-60 specimen axial displacement profile [partial length]

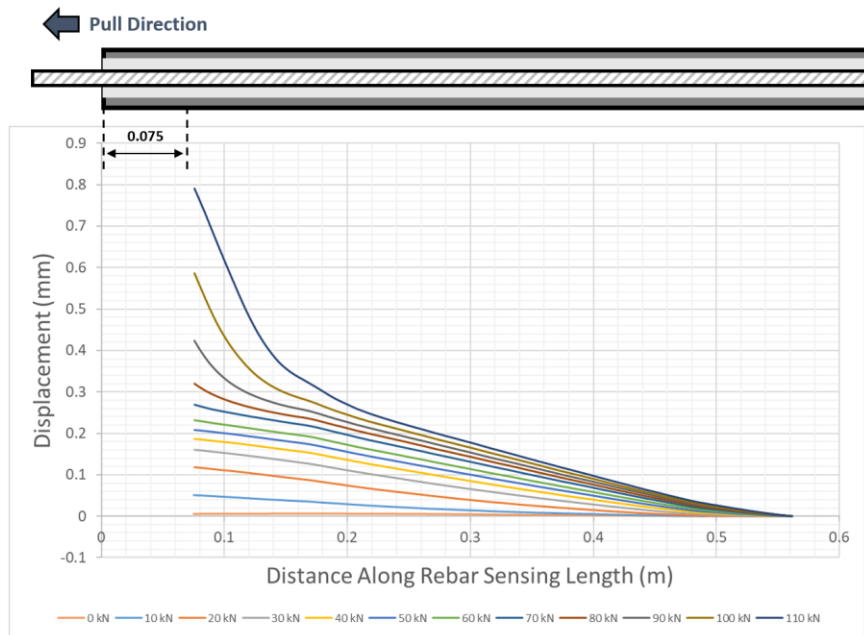


Figure A-21. P20-60 specimen axial displacement profile [partial length]

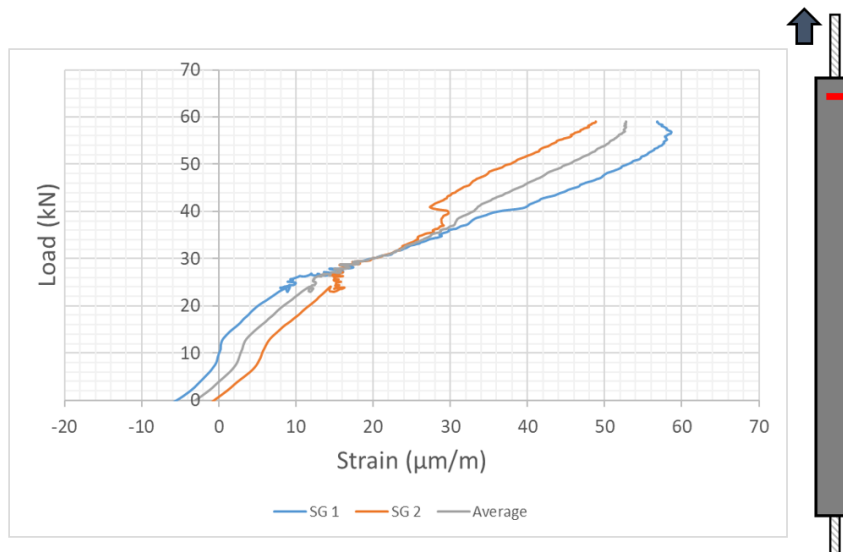


Figure A-22. P20-60 specimen pipe dilation monitoring at 50 mm [DAQ issues]

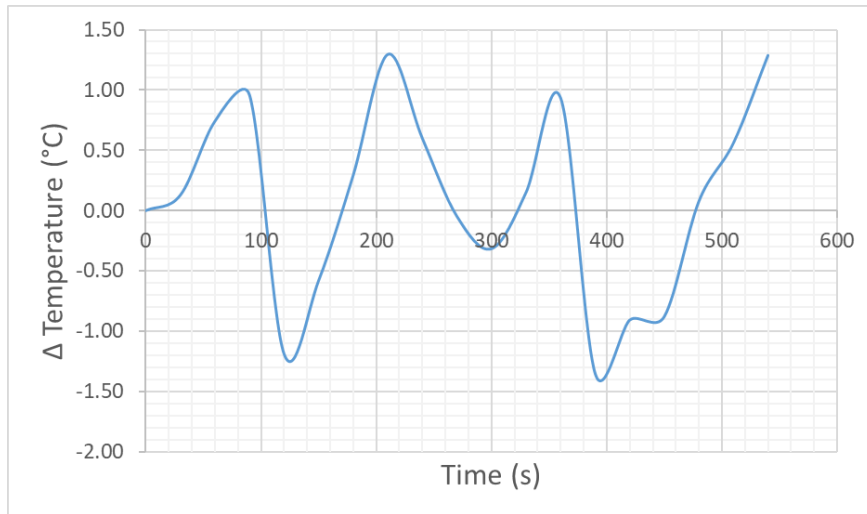


Figure A-23. P20-60 specimen temperature change during pull-out testing [T DOS malfunction]

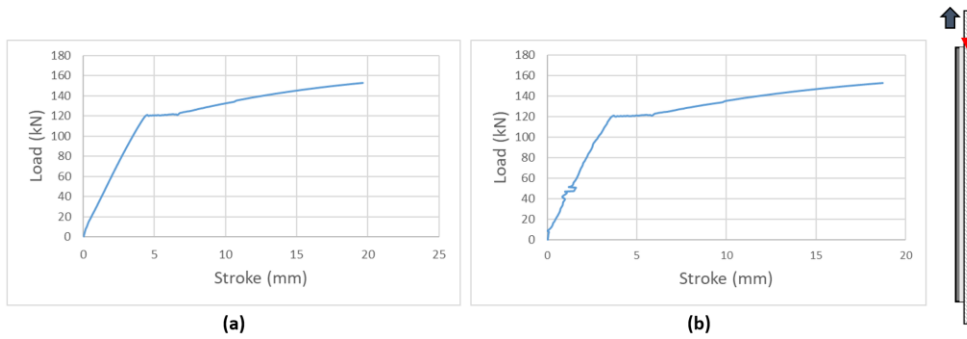


Figure A-24. Load-Displacement curve from P20-90: (a) Whole system response; (b) Axial displacement corrected for test rig movement and elongation

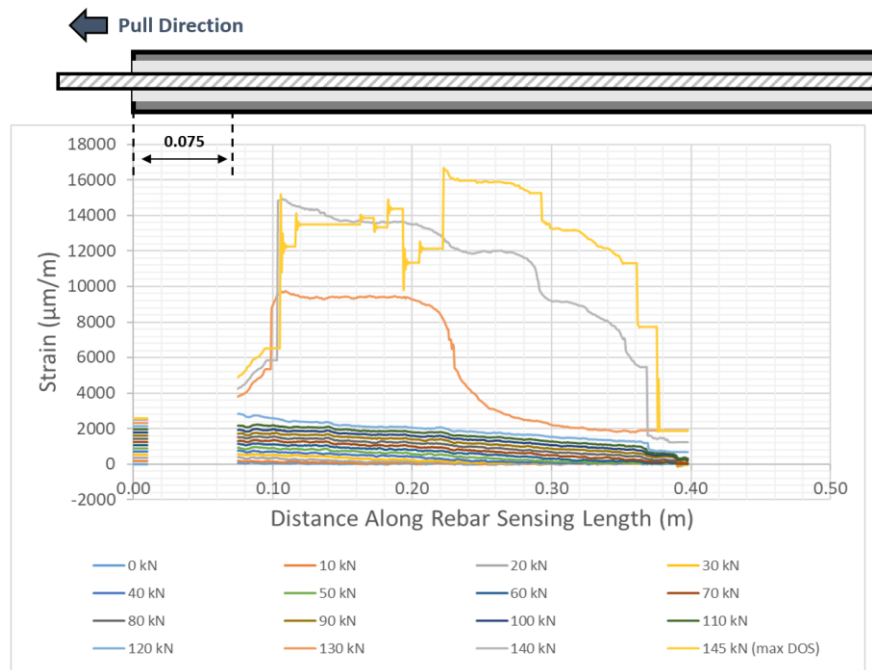


Figure A-25. P20-90 specimen strain profile along rebar bolt during pull-out testing [partial length]

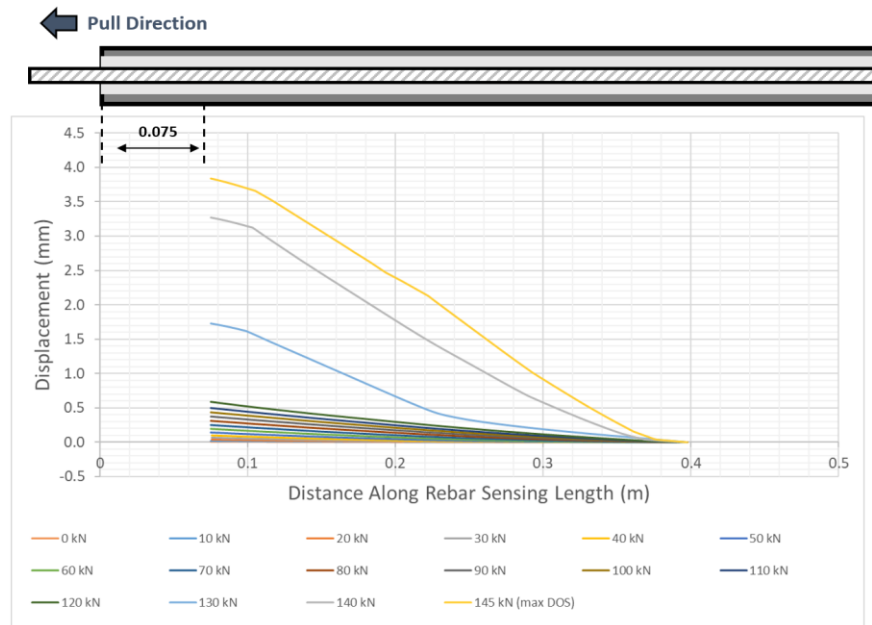


Figure A-26. P20-90 specimen axial displacement profile [partial length]

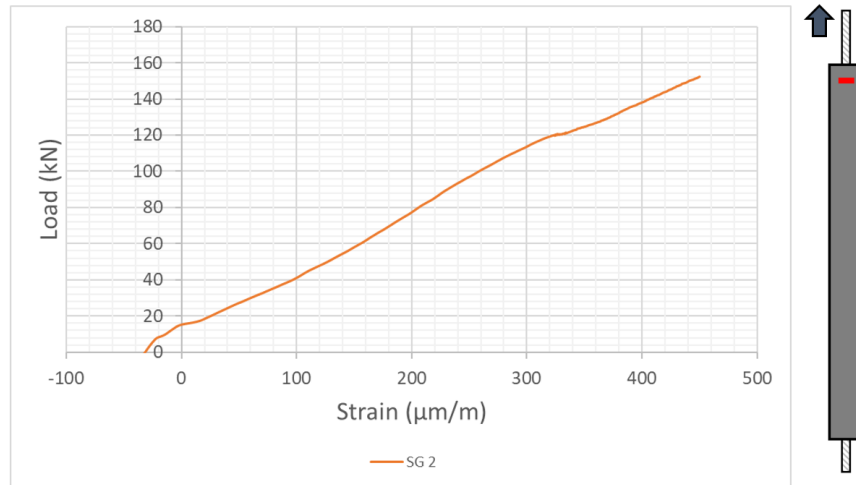


Figure A-27. P20-90 specimen pipe dilation monitoring at 50 mm: SG 1 failure

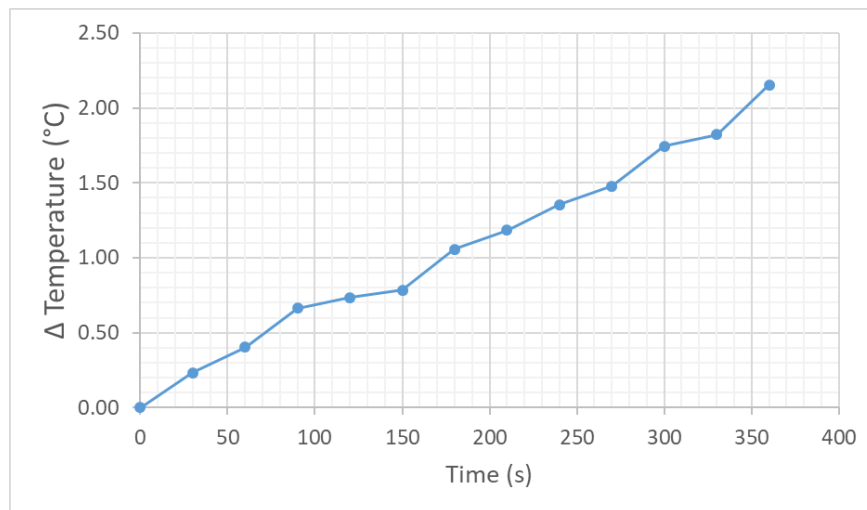


Figure A-28. P20-90 specimen temperature change during pull-out testing

P5 Condition Specimens:

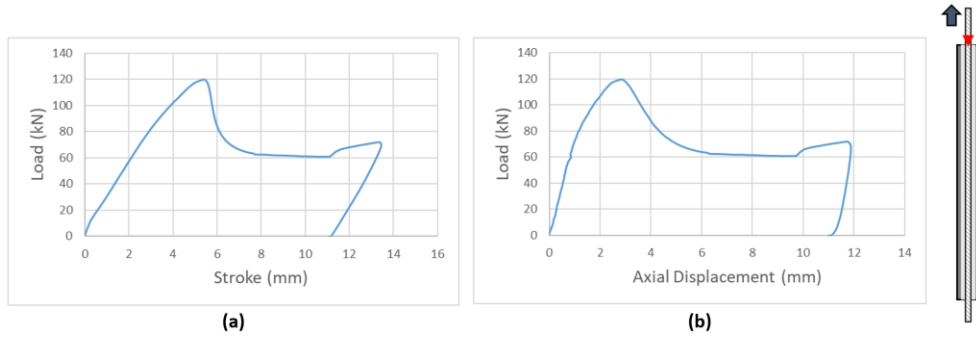


Figure A-29. Load-Displacement curve from P5-3: (a) Whole system response; (b) Axial displacement corrected for test rig movement and elongation

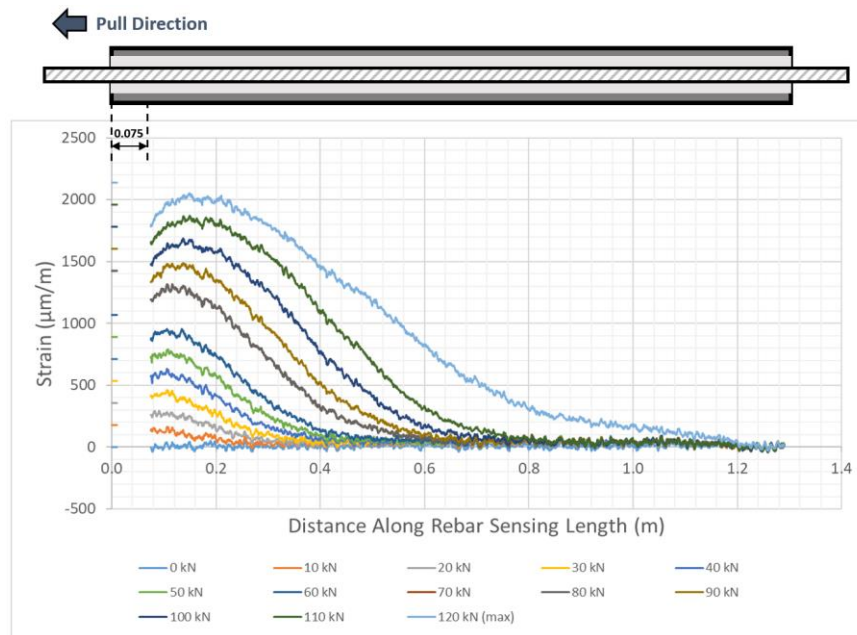


Figure A-30. P5-3 specimen strain profile along rebar bolt during pull-out testing

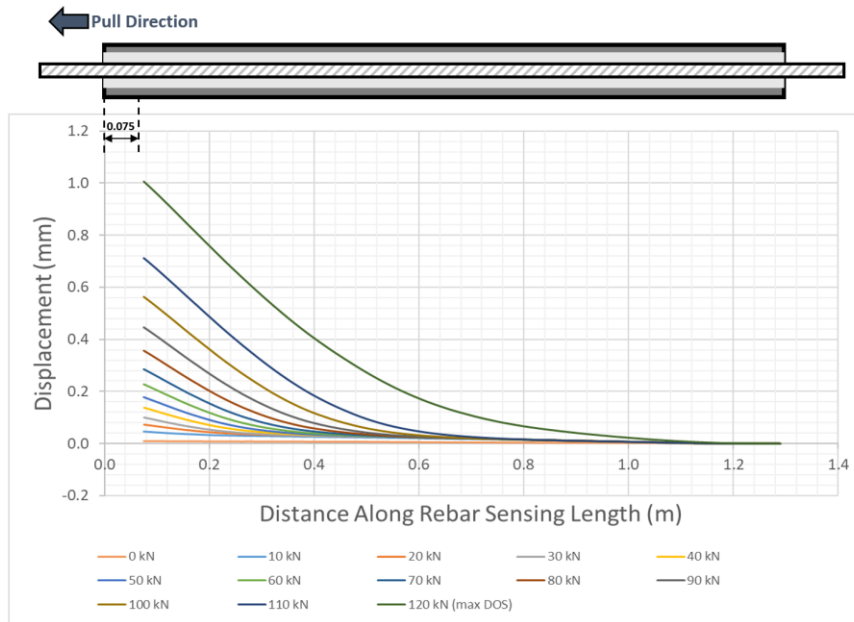


Figure A-31. P5-3 specimen axial displacement profile

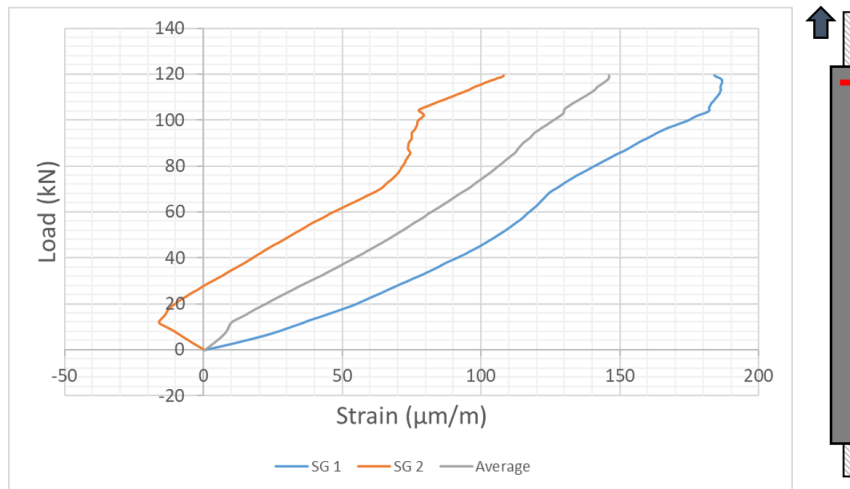


Figure A-32. P5-3 specimen pipe dilation monitoring at 50 mm

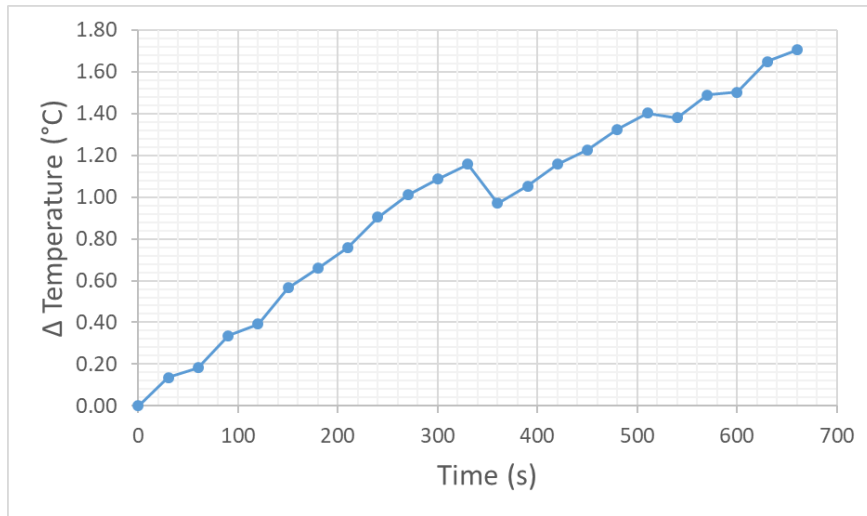
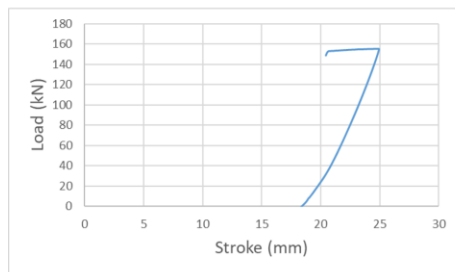


Figure A-33. P5-3 specimen temperature change during pull-out testing



(a)

(b)



Figure A-34. Load-Displacement curve from P5-7 [DAQ collection overload]: (a) Whole system response; (b) Axial displacement corrected [DAQ malfunction]

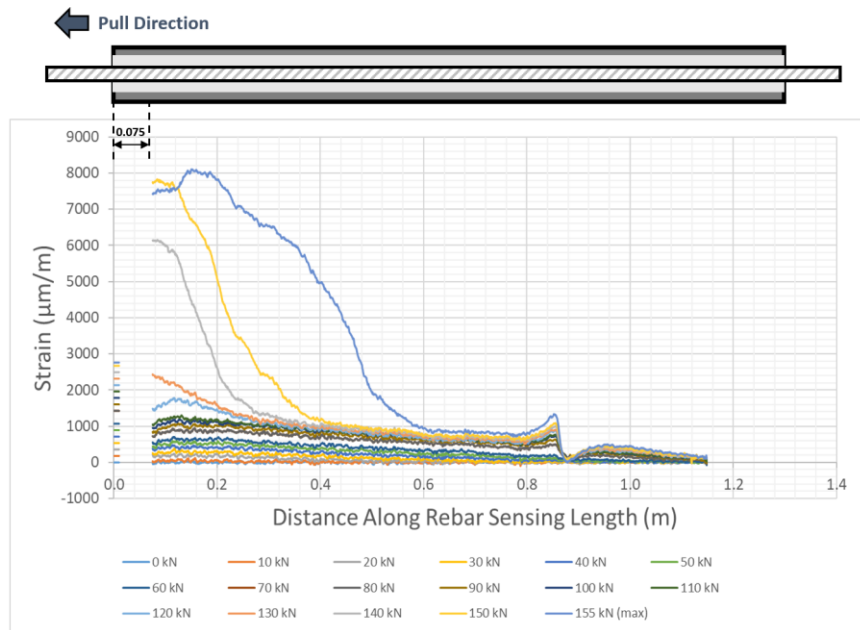


Figure A-35. P5-7 specimen strain profile along rebar bolt during pull-out testing [partial length]

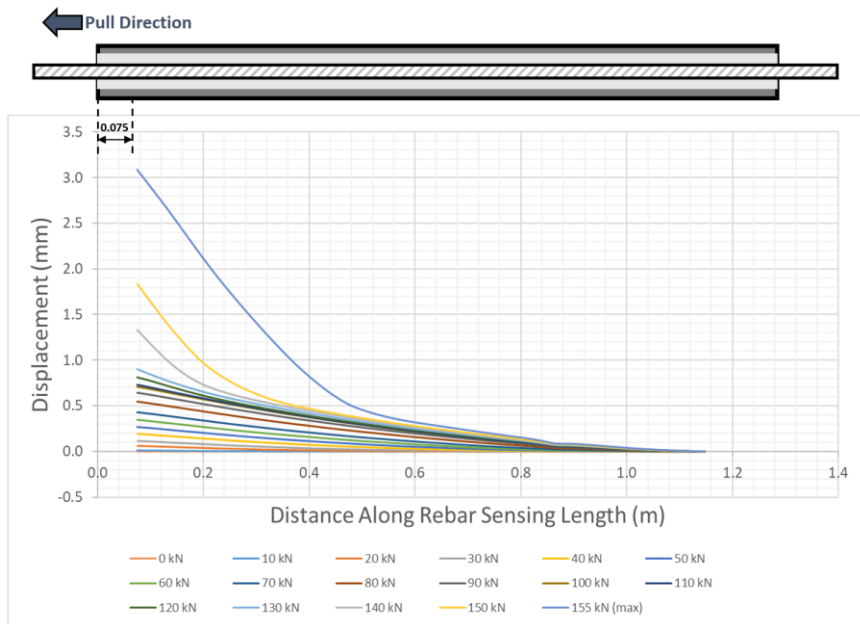


Figure A-36. P5-7 specimen axial displacement profile [partial length]

P5-7 Pipe strain no data due to DAQ overload

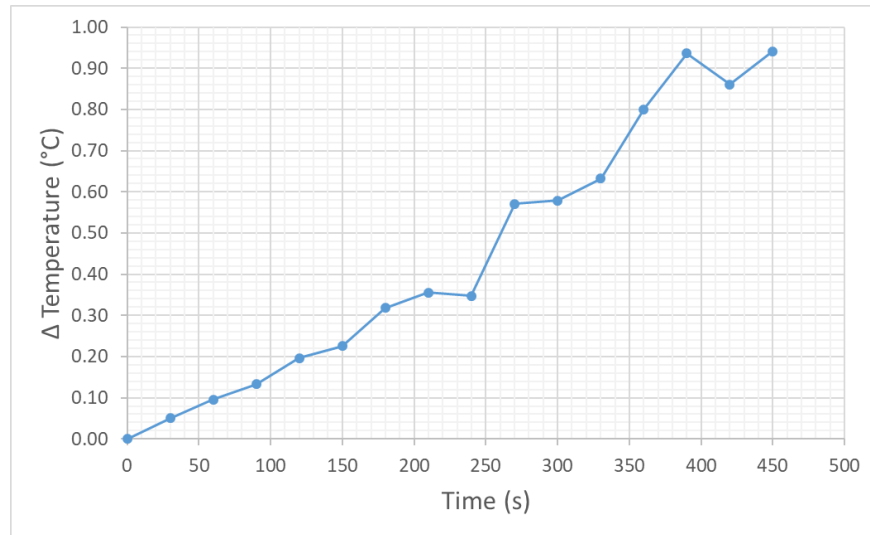
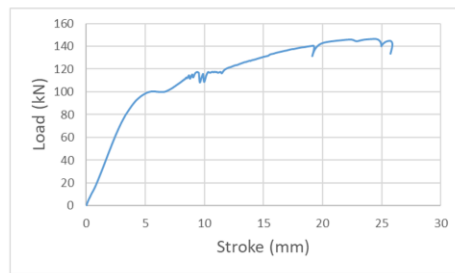
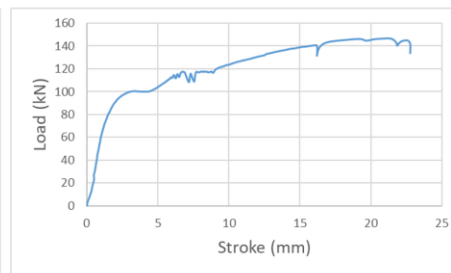


Figure A-37. P5-7 specimen temperature change during pull-out testing



(a)



(b)



Figure A-38. Load-Displacement curve from P5-28: (a) Whole system response; (b) Axial displacement corrected for test rig movement and elongation

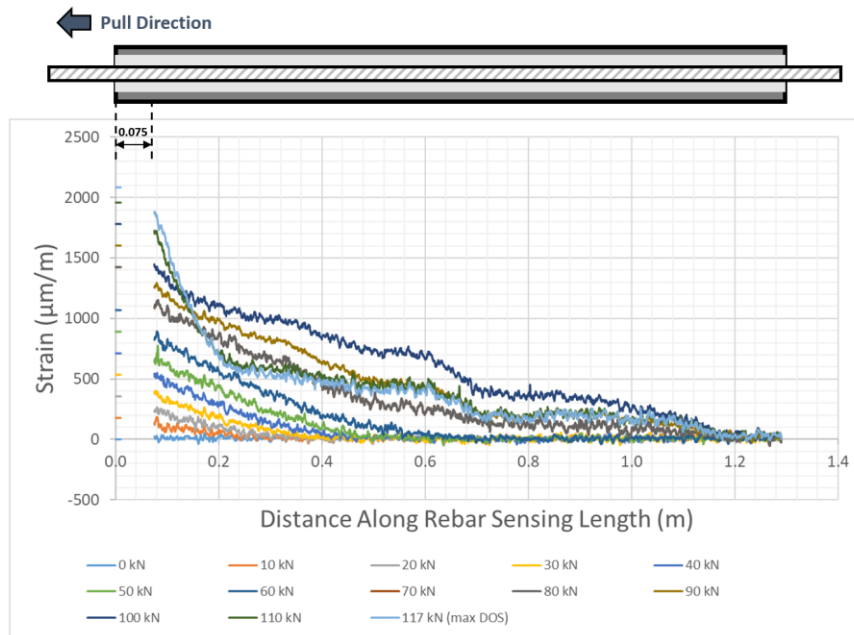


Figure A-39. P5-28 specimen strain profile along rebar bolt during pull-out testing

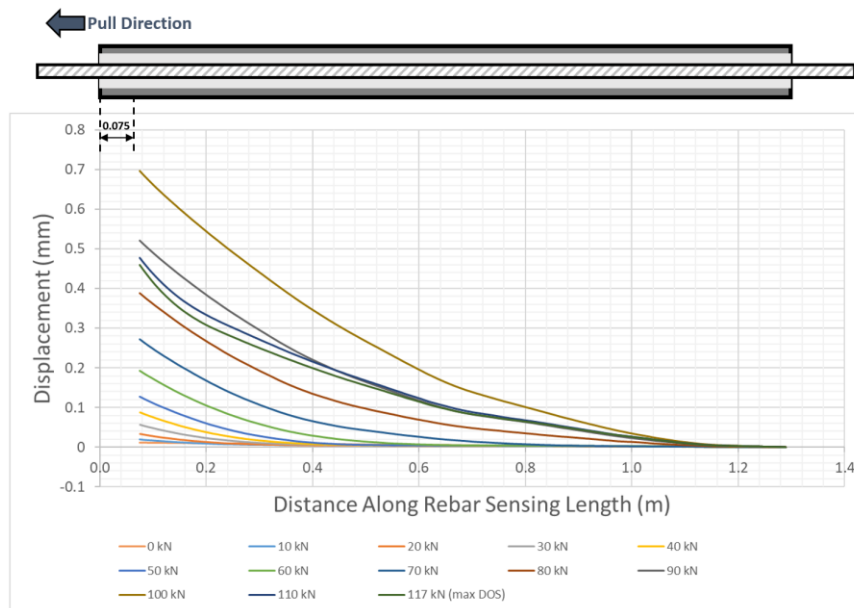


Figure A-40. P5-28 specimen axial displacement profile

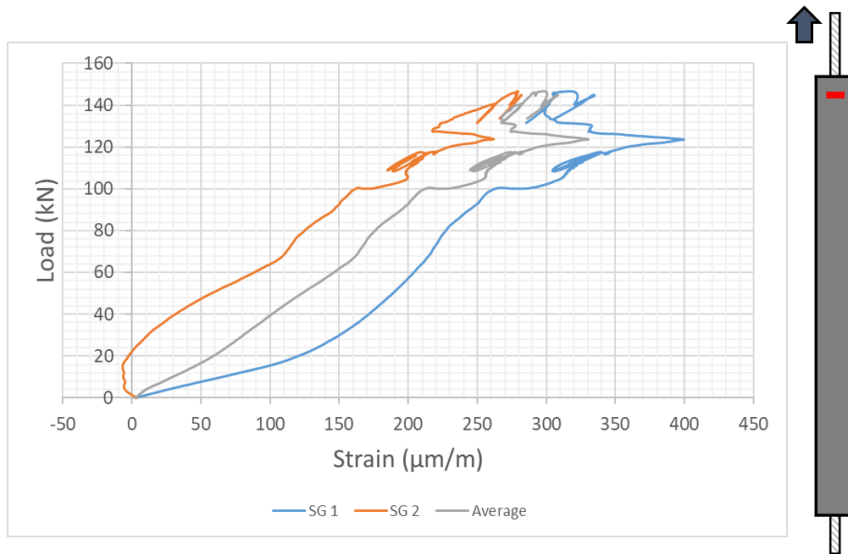


Figure A-41. P5-28 specimen pipe dilation monitoring at 50 mm

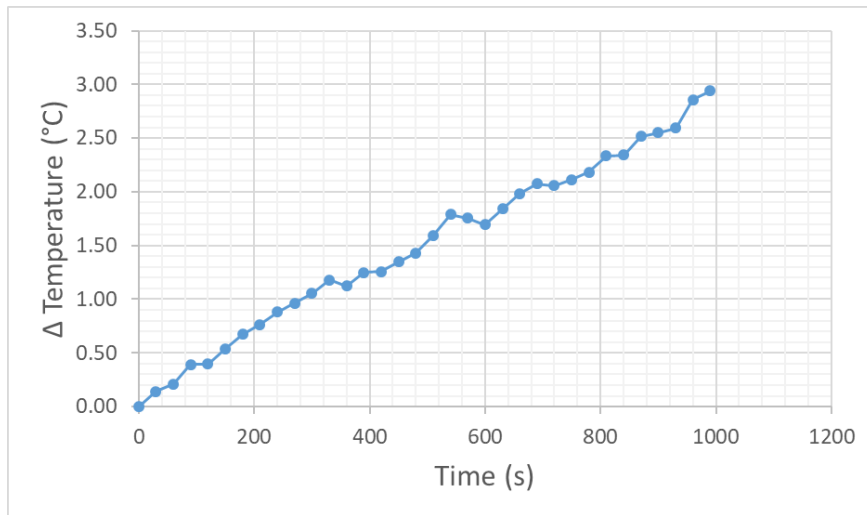


Figure A-42. P5-28 specimen temperature change during pull-out testing

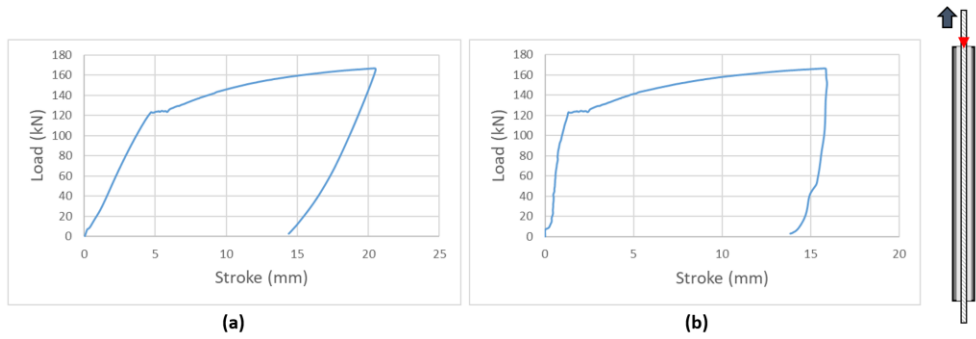


Figure A-43. Load-Displacement curve from P5-35: (a) Whole system response; (b) Axial displacement corrected for test rig movement and elongation

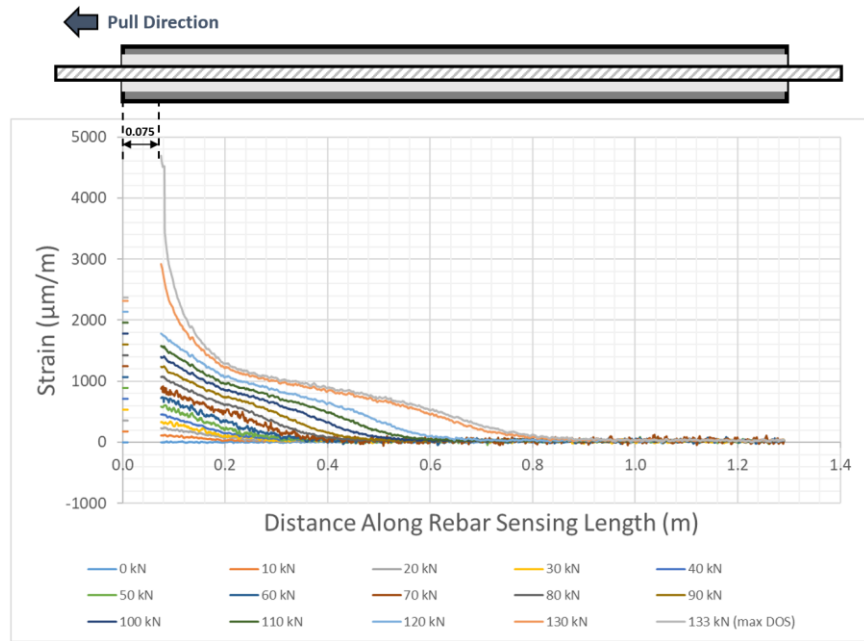


Figure A-44. P5-35 specimen strain profile along rebar bolt during pull-out testing

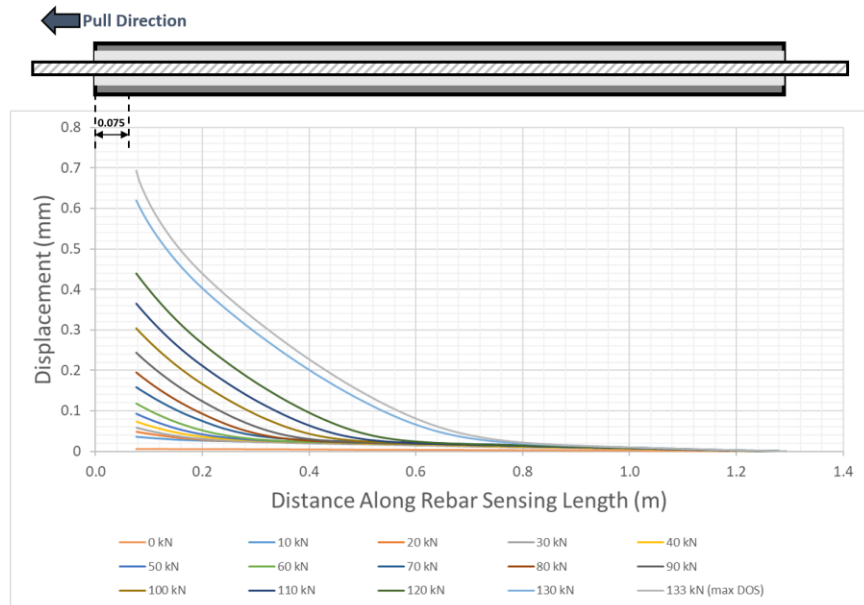


Figure A-45. P5-35 specimen axial displacement profile

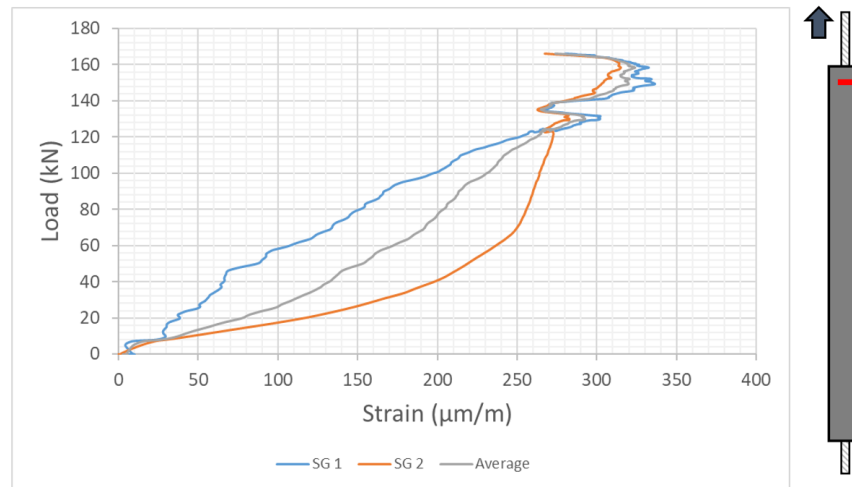


Figure A-46. P5-35 specimen pipe dilation monitoring at 50 mm

P5-35 T DOS malfunction

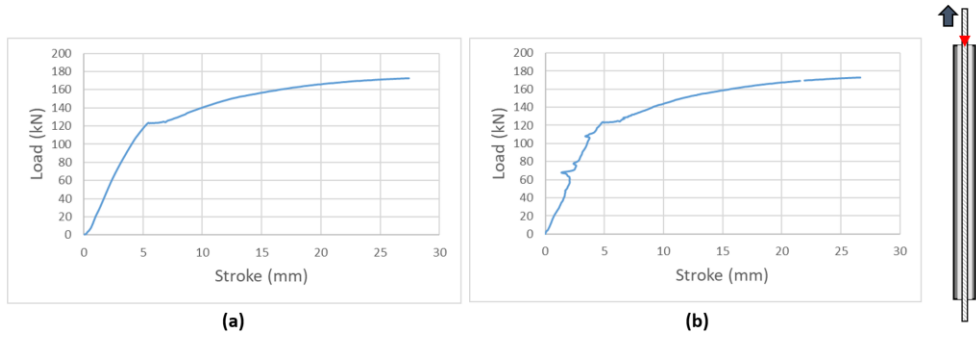


Figure A-47. Load-Displacement curve from P5-60: (a) Whole system response; (b) Axial displacement corrected for test rig movement and elongation

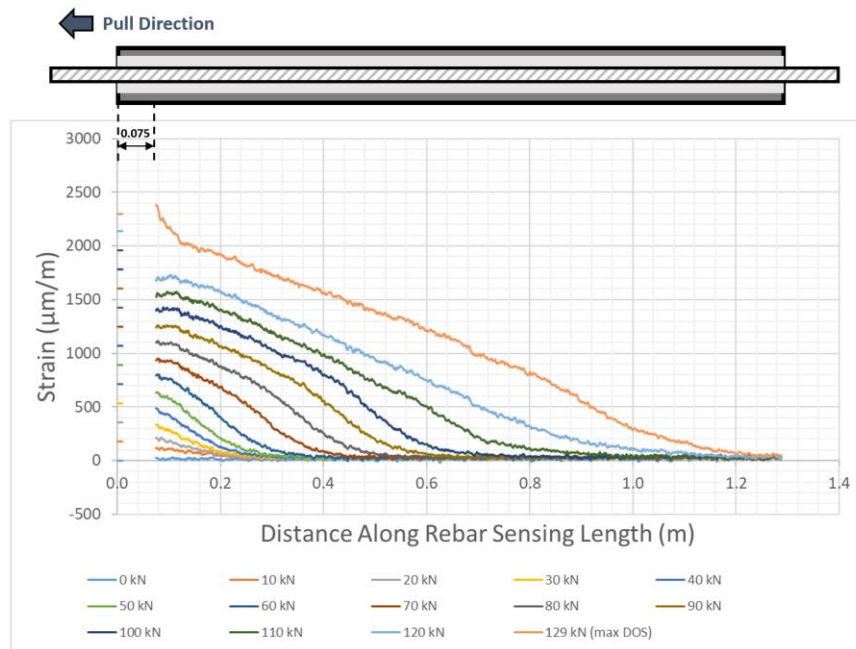


Figure A-48. P5-60 specimen strain profile along rebar bolt during pull-out testing

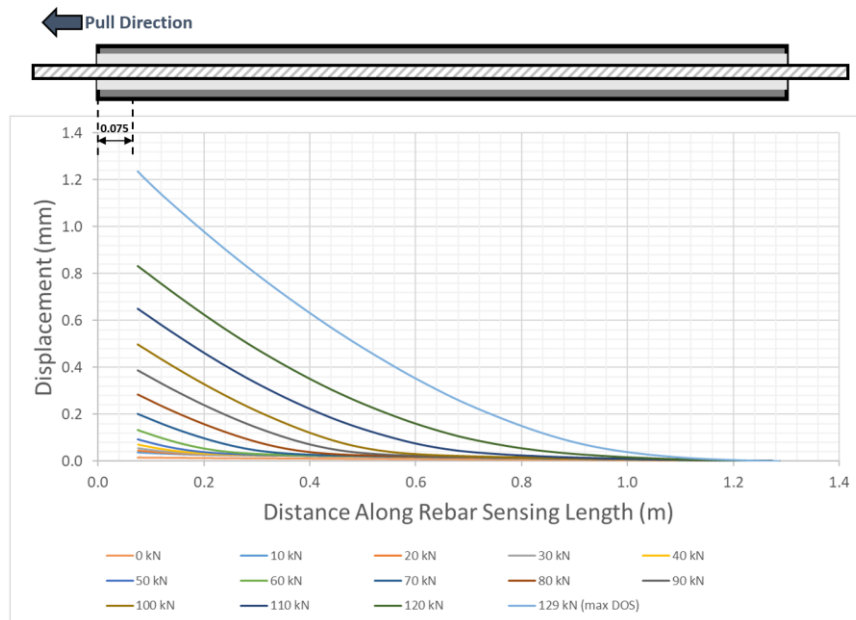


Figure A-49. P5-60 specimen axial displacement profile

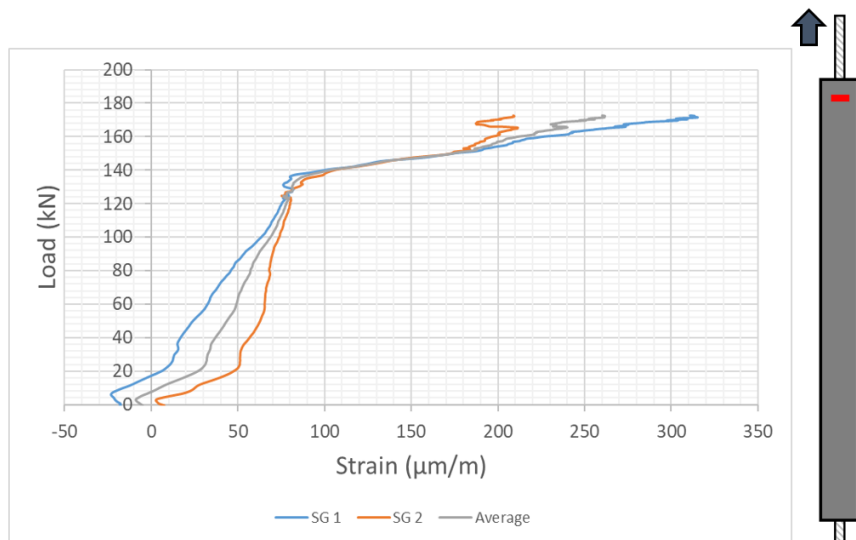


Figure A-50. P5-60 specimen pipe dilation monitoring at 50 mm

P5-60 T DOS malfunction

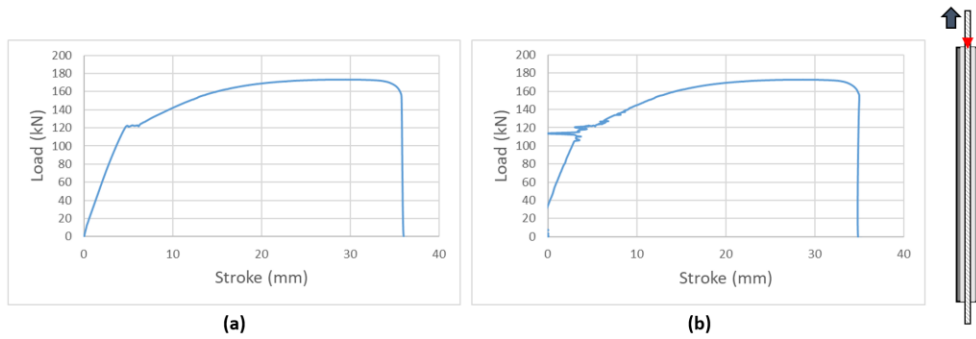


Figure A-51. Load-Displacement curve from P5-90: (a) Whole system response; (b) Axial displacement corrected for test rig movement and elongation [LVDT malfunction]

P5-90 ϵ DOS failure

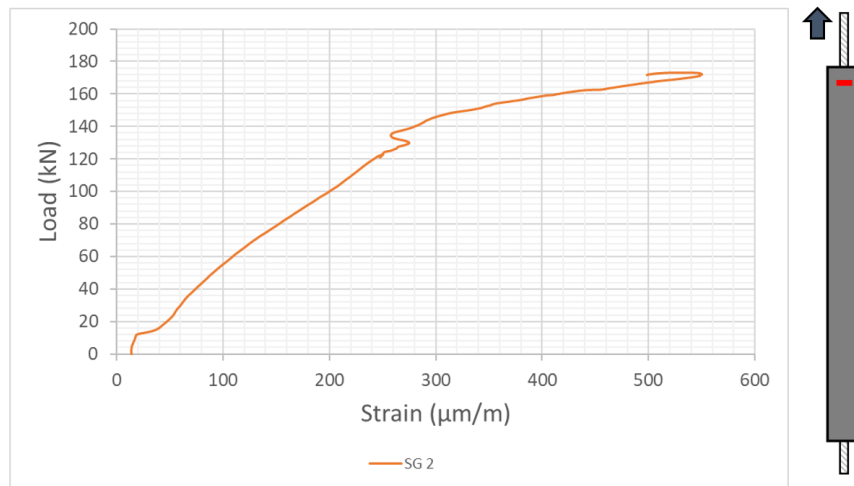


Figure A-52. P5-90 specimen pipe dilation monitoring at 50 mm

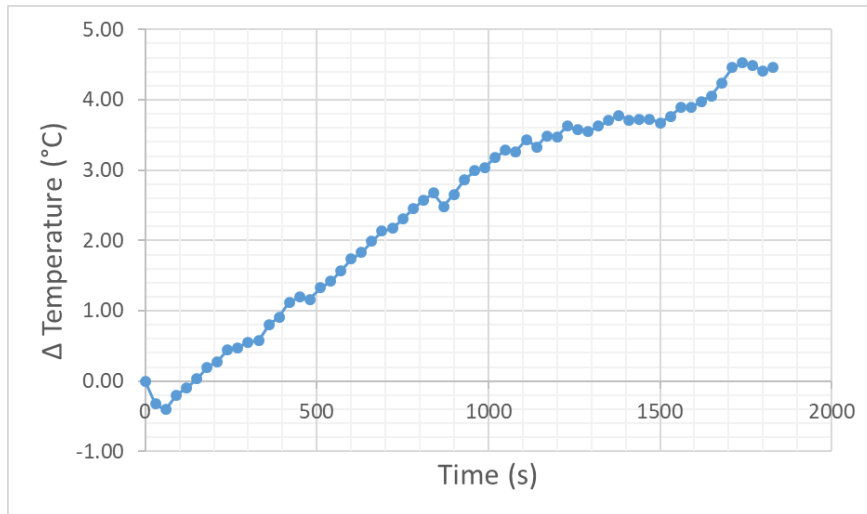


Figure A-53. P5-90 specimen temperature change during pull-out testing

C20 Condition Specimens:

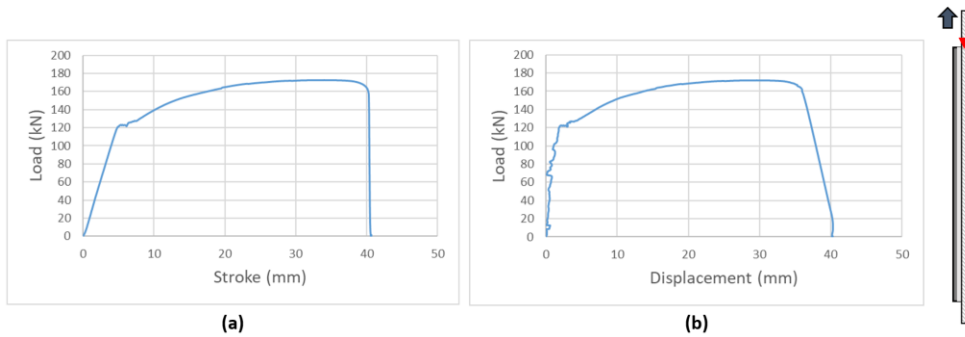


Figure A-54. Load-Displacement curve from C20-3: (a) Whole system response; (b) Axial displacement corrected for test rig movement and elongation

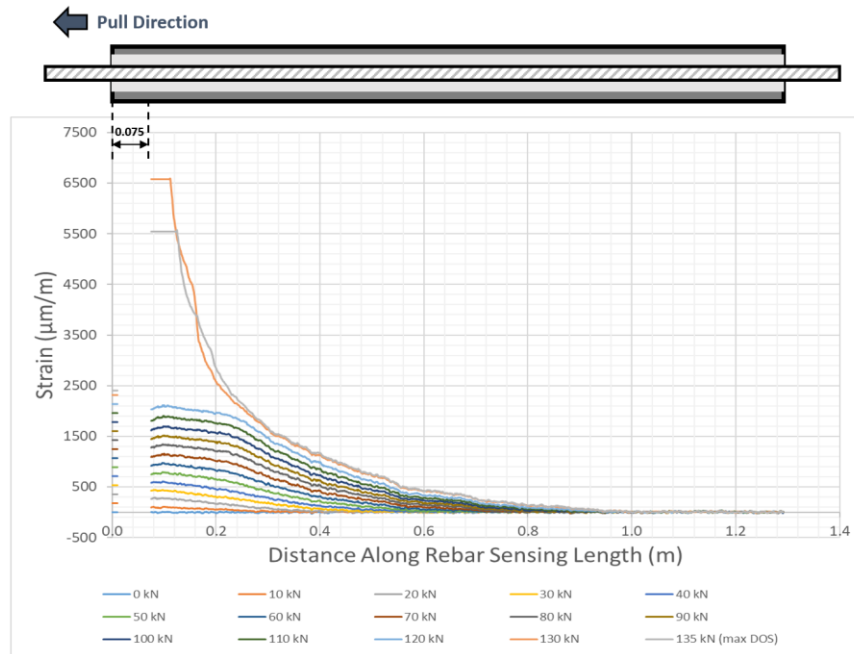


Figure A-55. C20-3 specimen strain profile along rebar bolt during pull-out testing

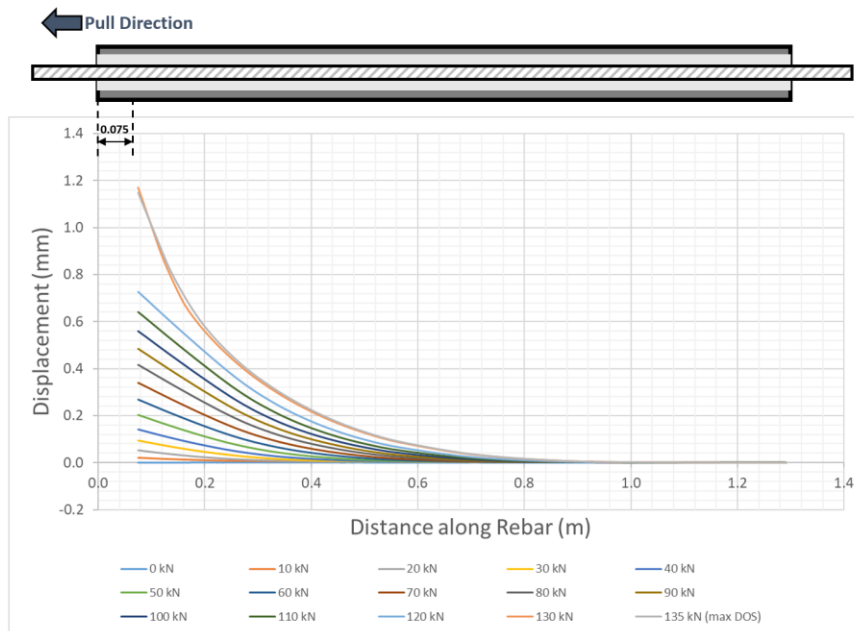


Figure A-56. C20-3 specimen axial displacement profile

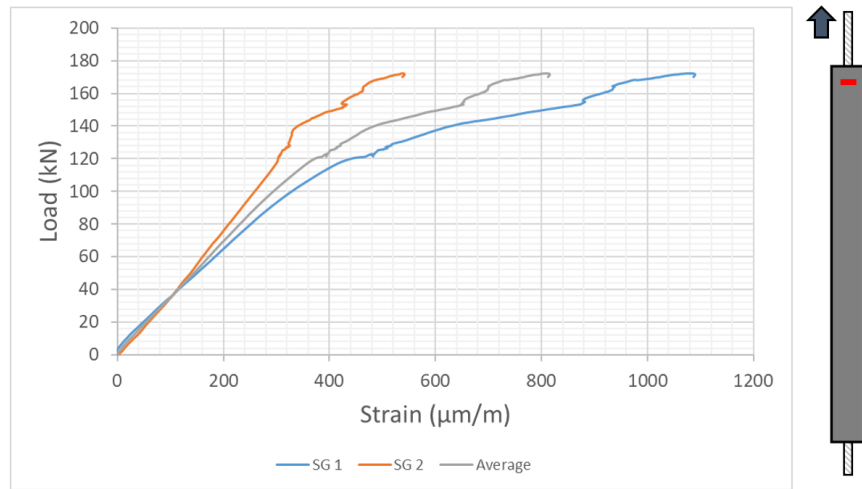


Figure A-57. C20-3 specimen pipe dilation monitoring at 50 mm

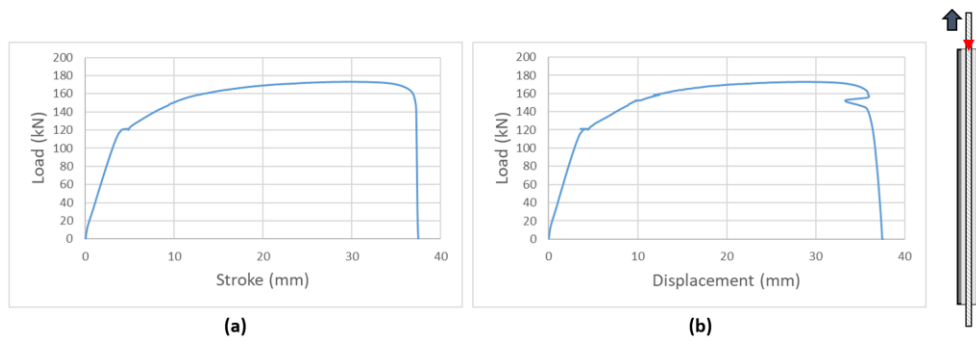


Figure A-58. Load-Displacement curve from C20-7: (a) Whole system response; (b) Axial displacement corrected for test rig movement and elongation

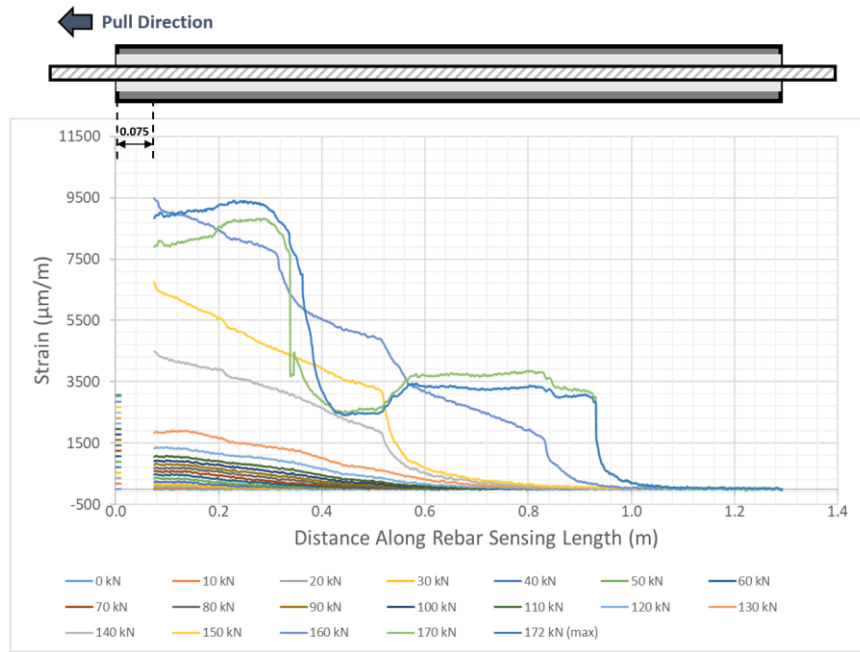


Figure A-59. C20-7 specimen strain profile along rebar bolt during pull-out testing

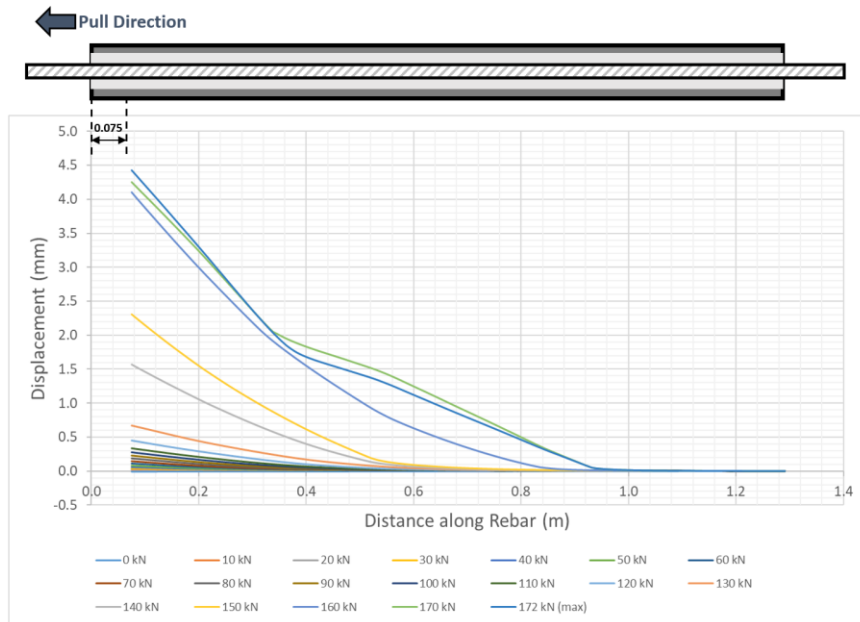


Figure A-60. C20-7 specimen axial displacement profile

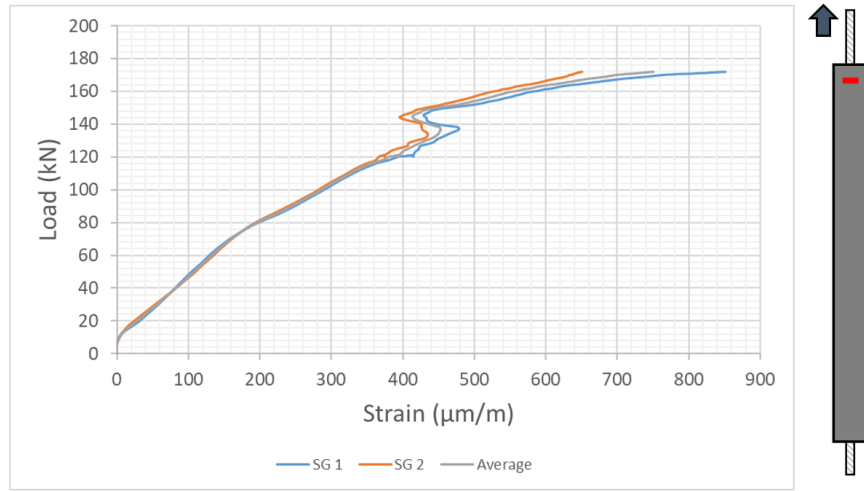


Figure A-61. C20-7 specimen pipe dilation monitoring at 50 mm

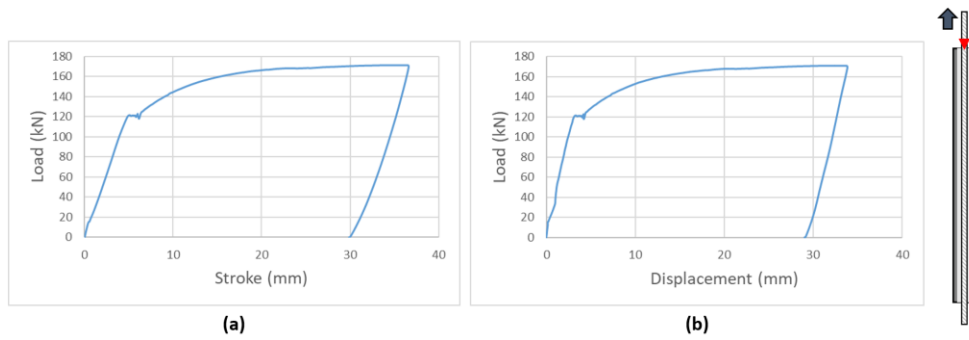


Figure A-62. Load-Displacement curve from C20-28: (a) Whole system response; (b) Axial displacement corrected for test rig movement and elongation

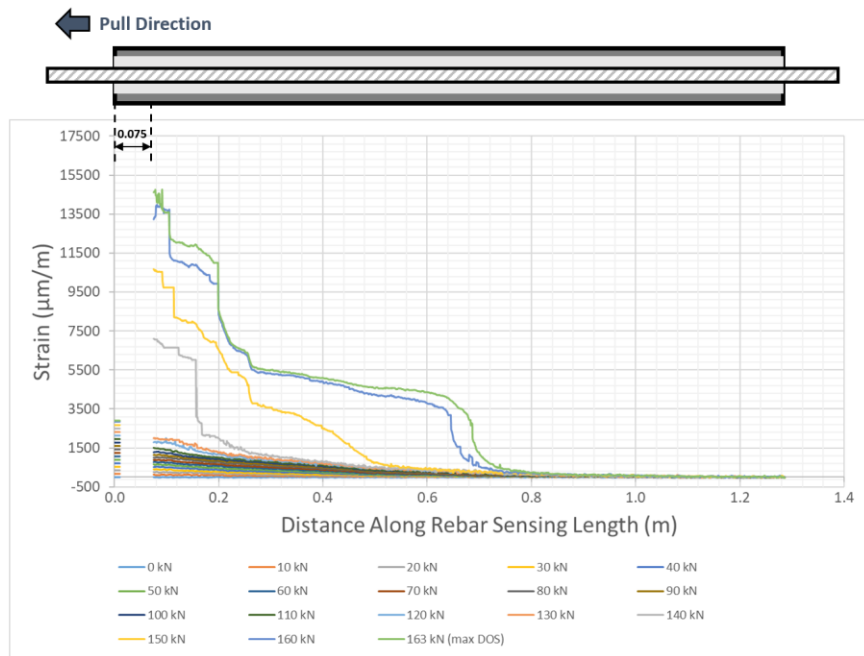


Figure A-63. C20-28 specimen strain profile along rebar bolt during pull-out testing

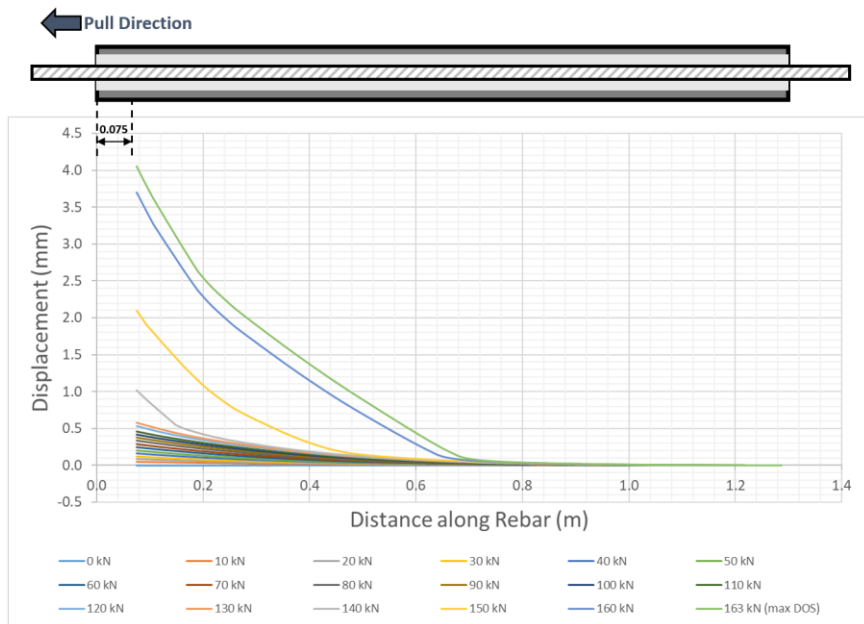


Figure A-64. C20-28 specimen axial displacement profile

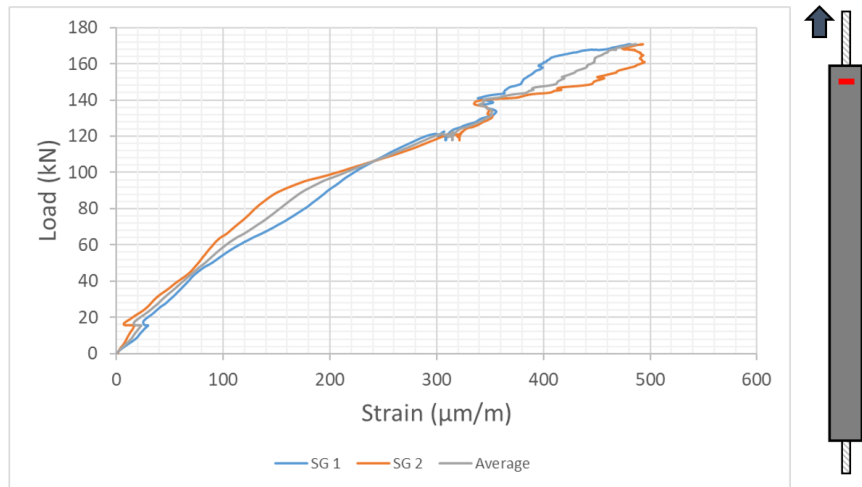


Figure A-65. C20-28 specimen pipe dilation monitoring at 50 mm

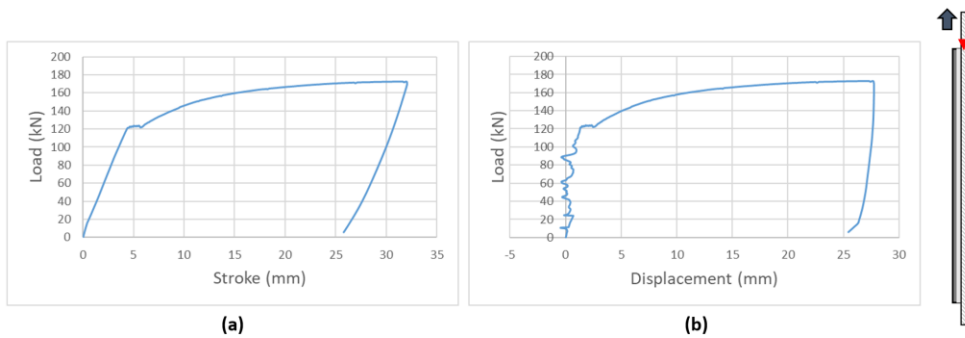


Figure A-66. Load-Displacement curve from C20-35: (a) Whole system response; (b) Axial displacement corrected for test rig movement and elongation

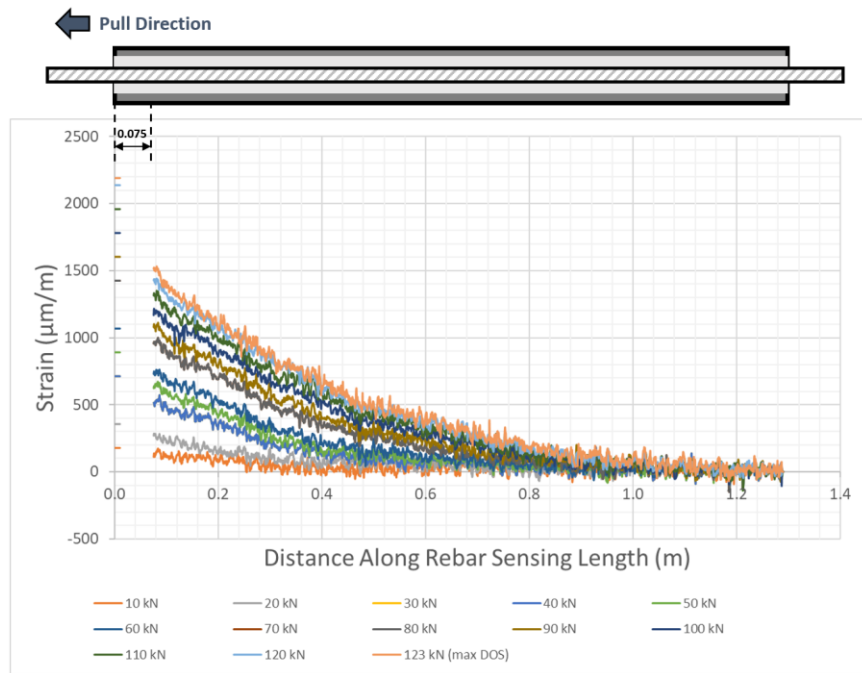


Figure A-67. C20-35 specimen strain profile along rebar bolt during pull-out testing

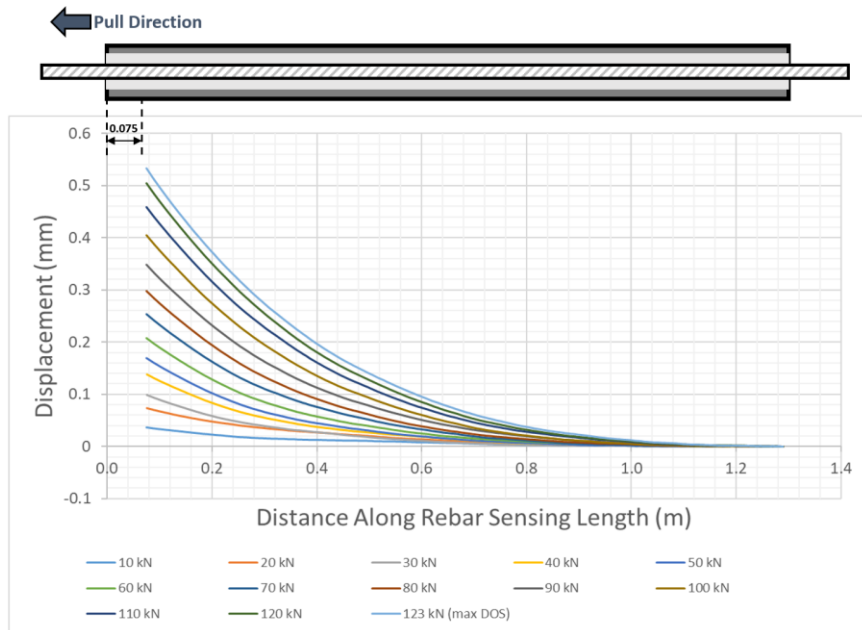


Figure A-68. C20-35 specimen axial displacement profile

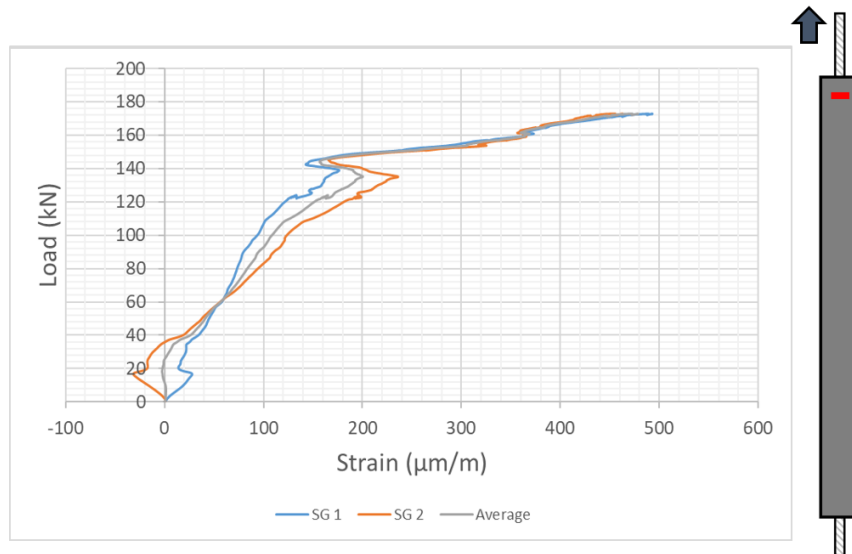


Figure A-69. C20-35 specimen pipe dilation monitoring at 50 mm

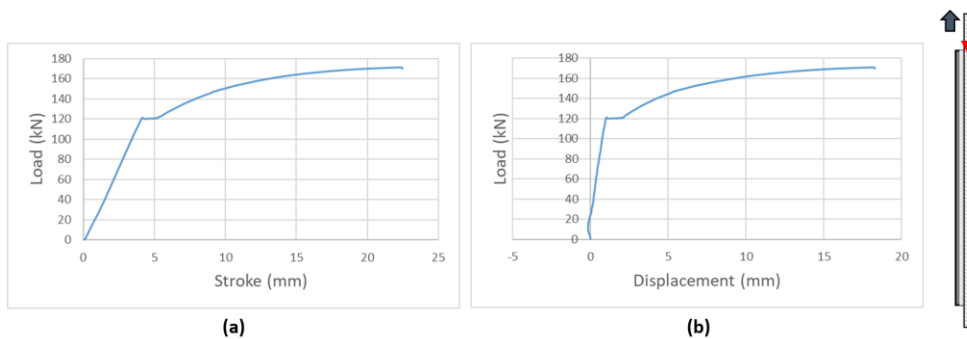


Figure A-70. Load-Displacement curve from C20-60: (a) Whole system response; (b) Axial displacement corrected for test rig movement and elongation

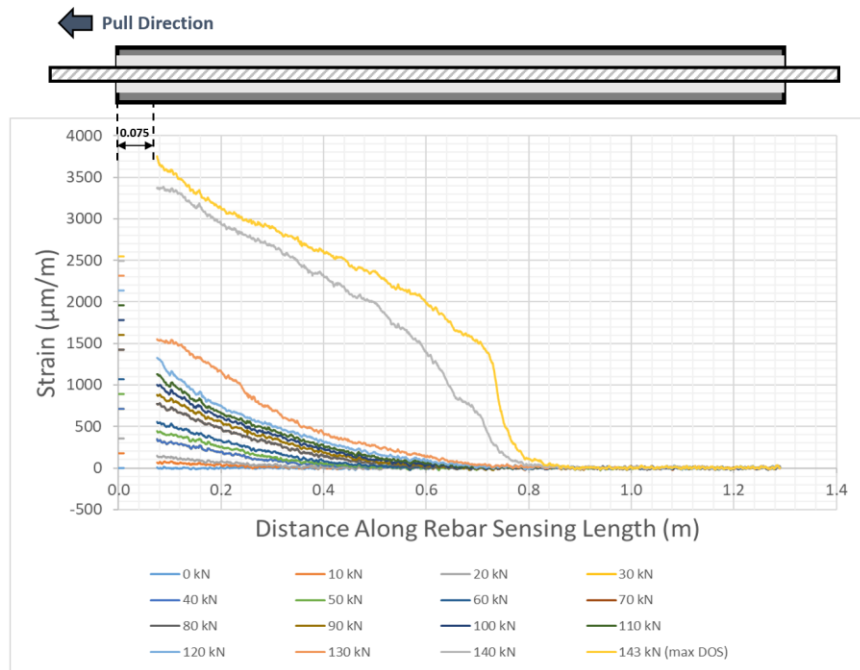


Figure A-71. C20-60 specimen strain profile along rebar bolt during pull-out testing

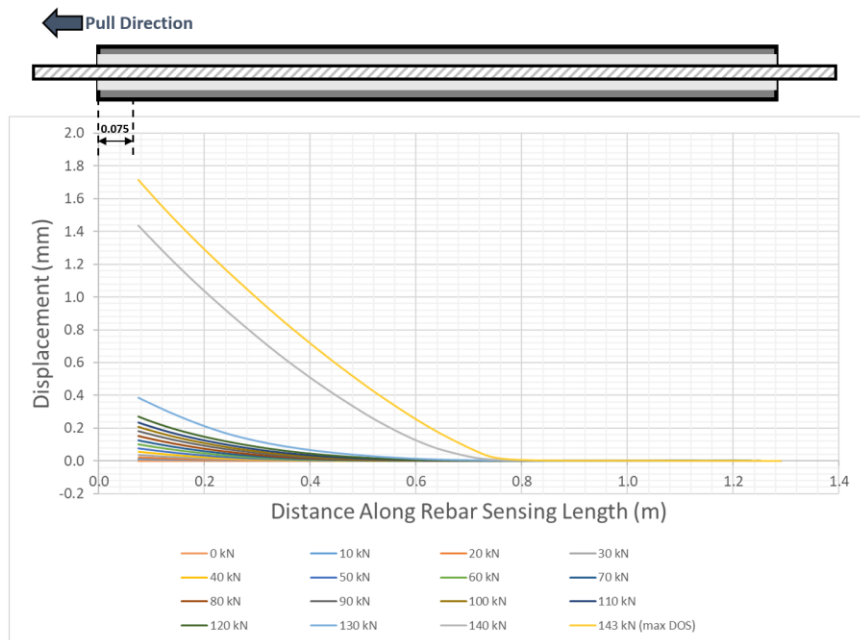


Figure A-72. C20-60 specimen axial displacement profile

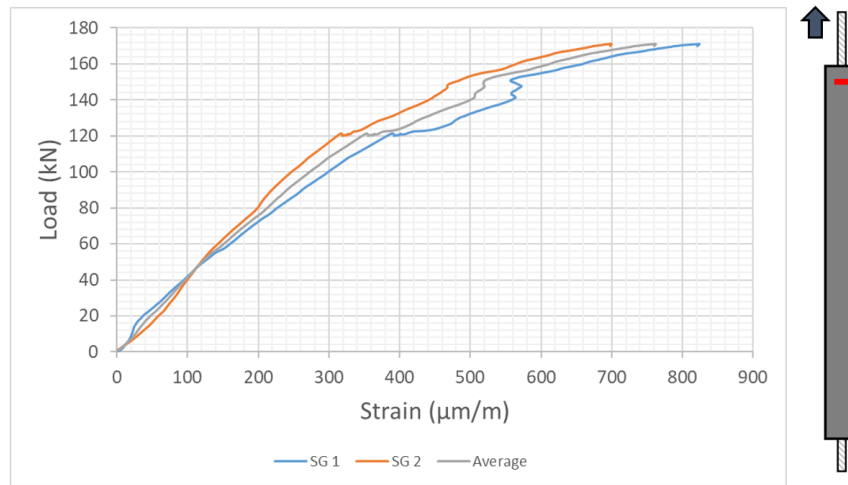


Figure A-73. C20-60 specimen pipe dilation monitoring at 50 mm

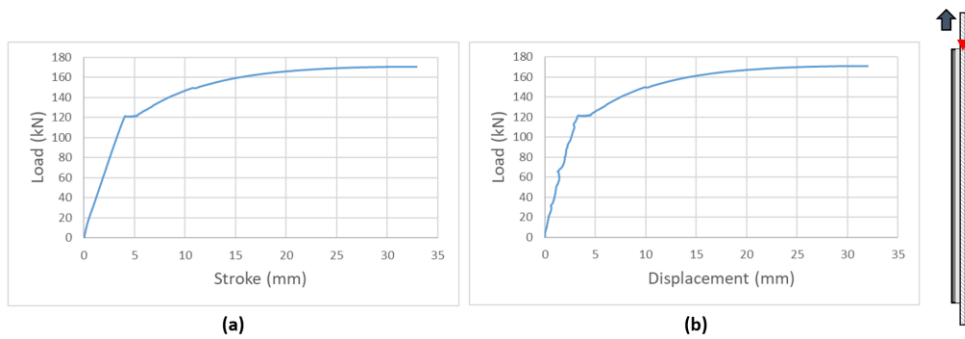


Figure A-74. Load-Displacement curve from C20-90: (a) Whole system response; (b) Axial displacement corrected for test rig movement and elongation

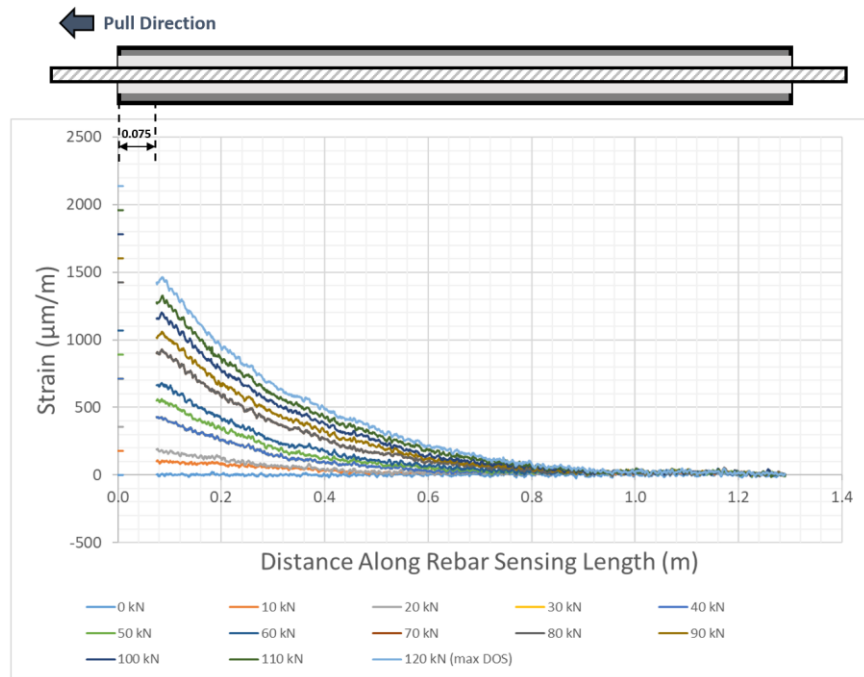


Figure A-75. C20-90 specimen strain profile along rebar bolt during pull-out testing

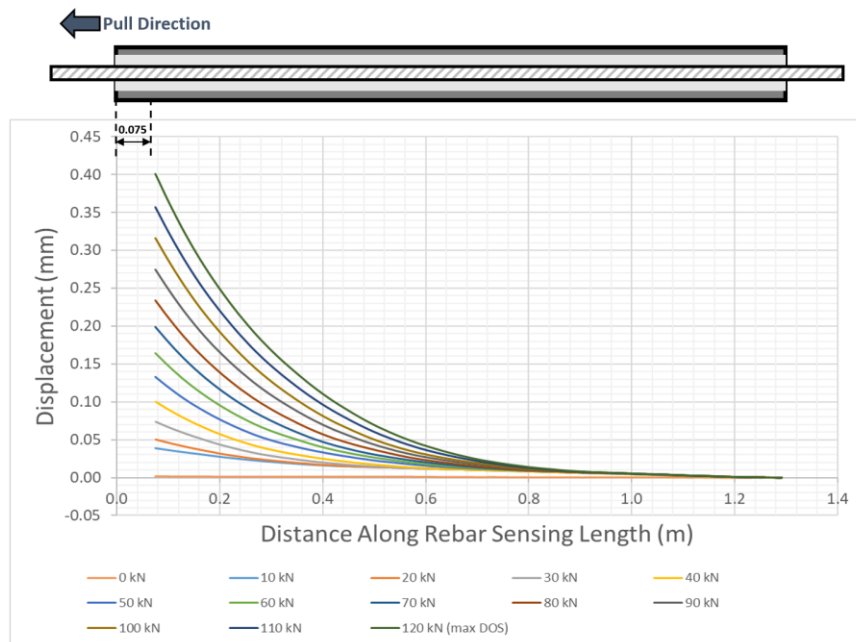


Figure A-76. C20-90 specimen axial displacement profile

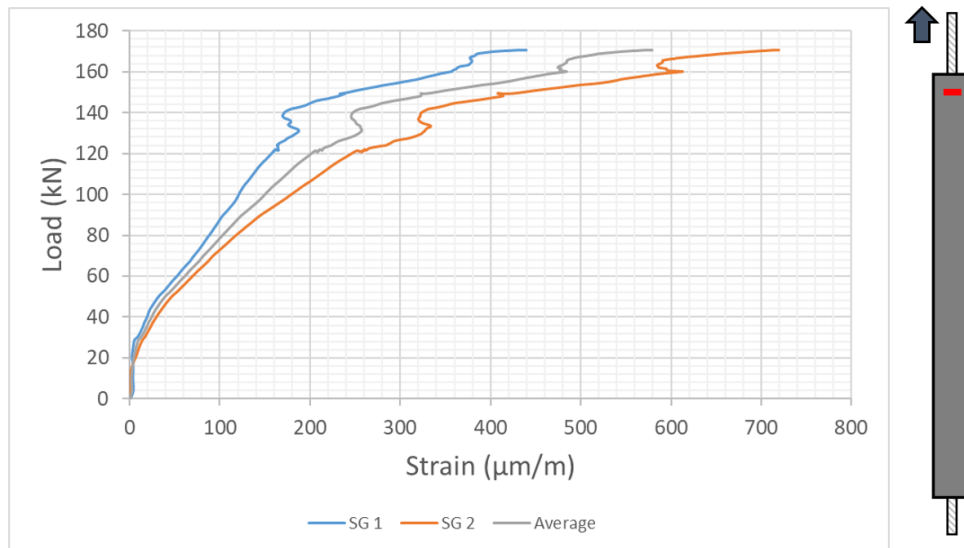


Figure A-77. C20-90 specimen pipe dilation monitoring at 50 mm

G45 Condition Specimens:

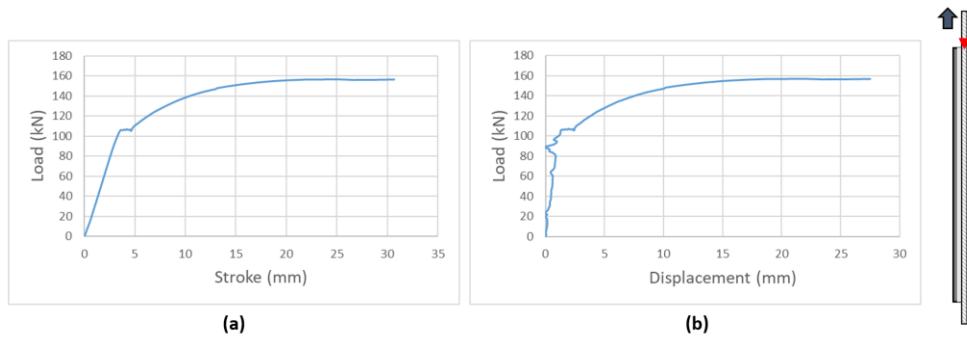


Figure A-78. Load-Displacement curve from G45-3: (a) Whole system response; (b) Axial displacement corrected for test rig movement and elongation

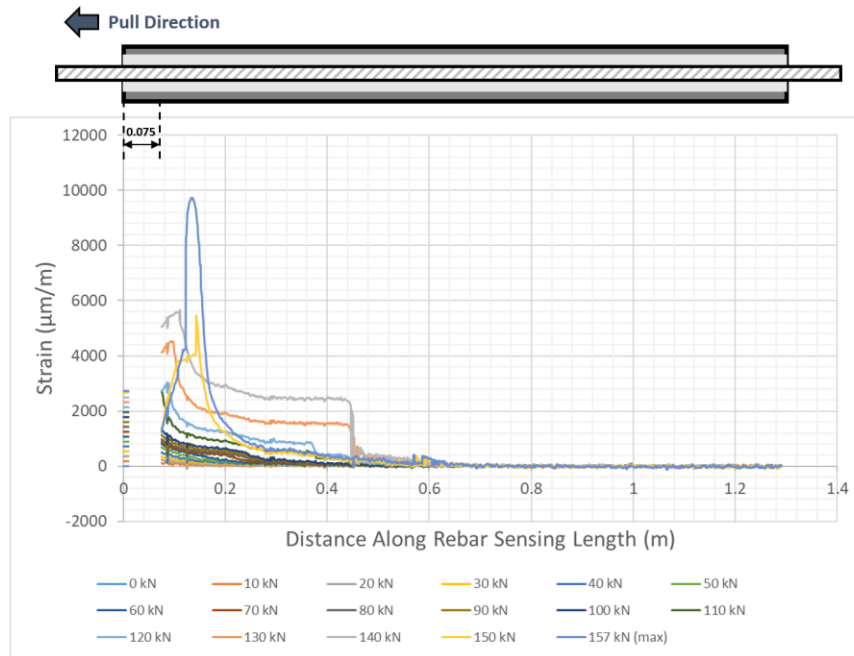


Figure A-79. G45-3 specimen strain profile along rebar bolt during pull-out testing

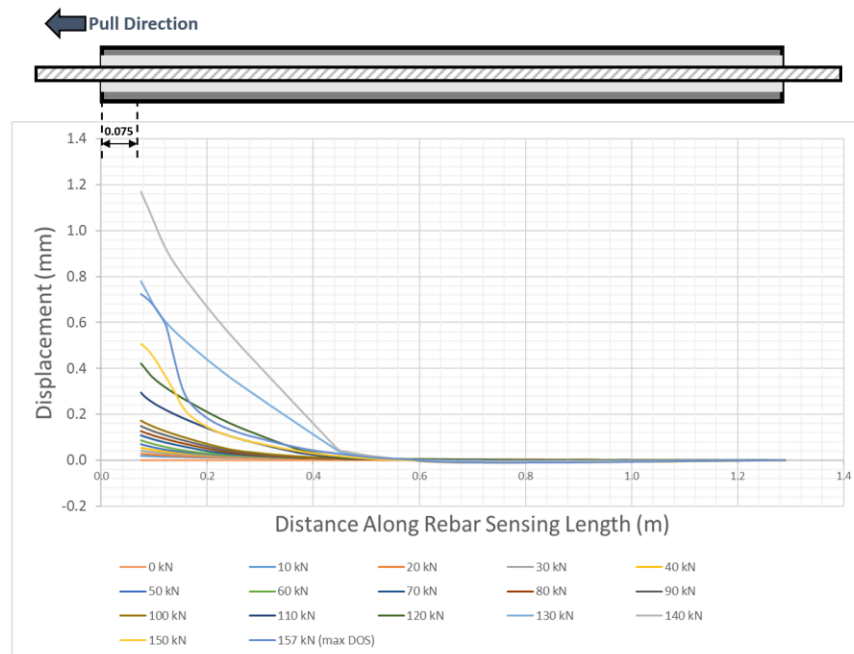


Figure A-80. G45-3 specimen axial displacement profile

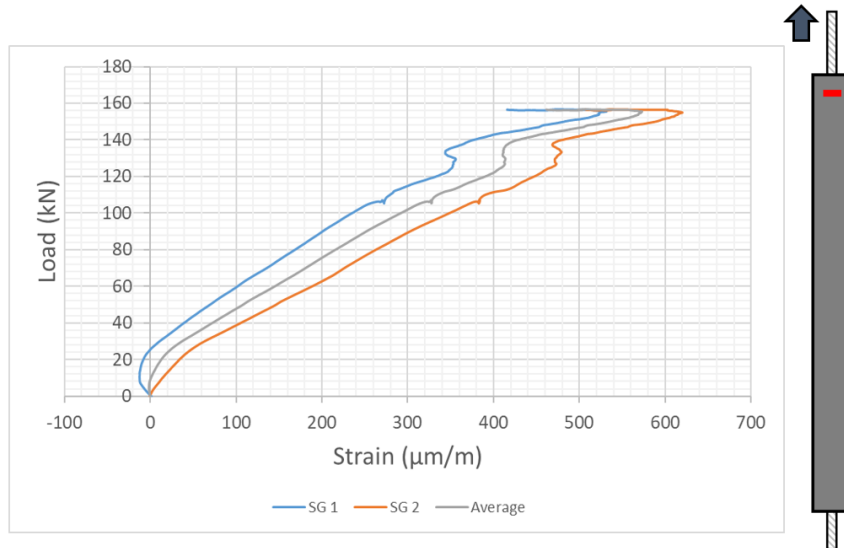


Figure A-81. G45-3 specimen pipe dilation monitoring at 50 mm

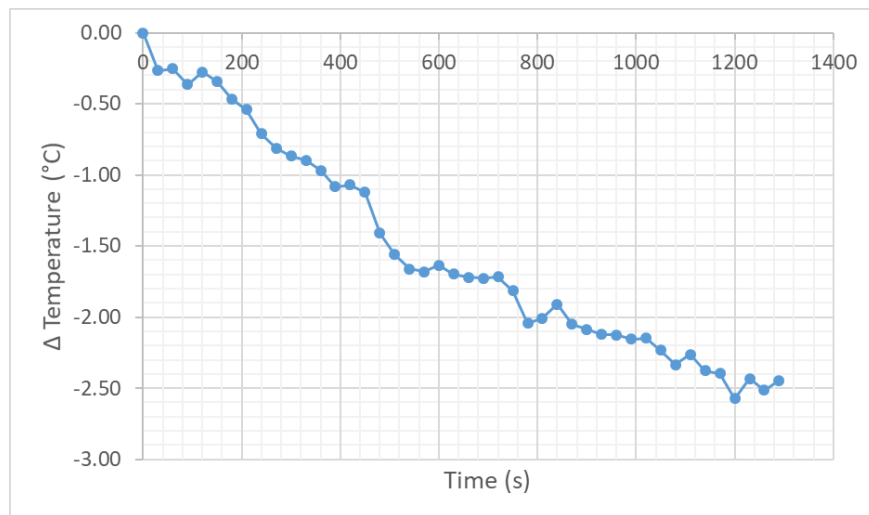


Figure A-82. G45-3 specimen temperature change during pull-out testing

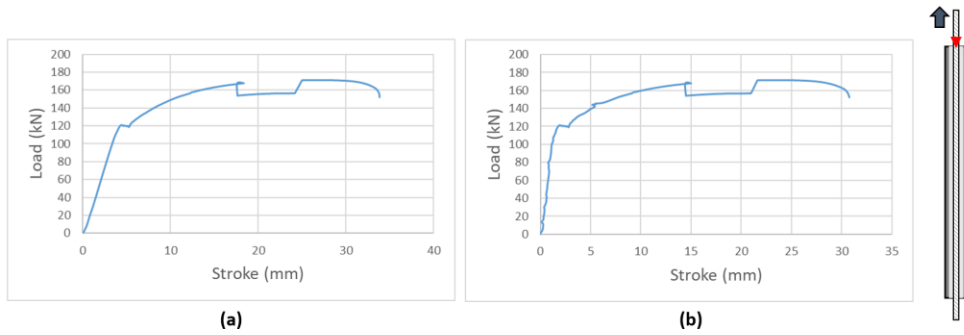


Figure A-83. Load-Displacement curve from G45-7 [MTS grip slipped during loading]: (a) Whole system response; (b) Axial displacement corrected for test rig movement and elongation

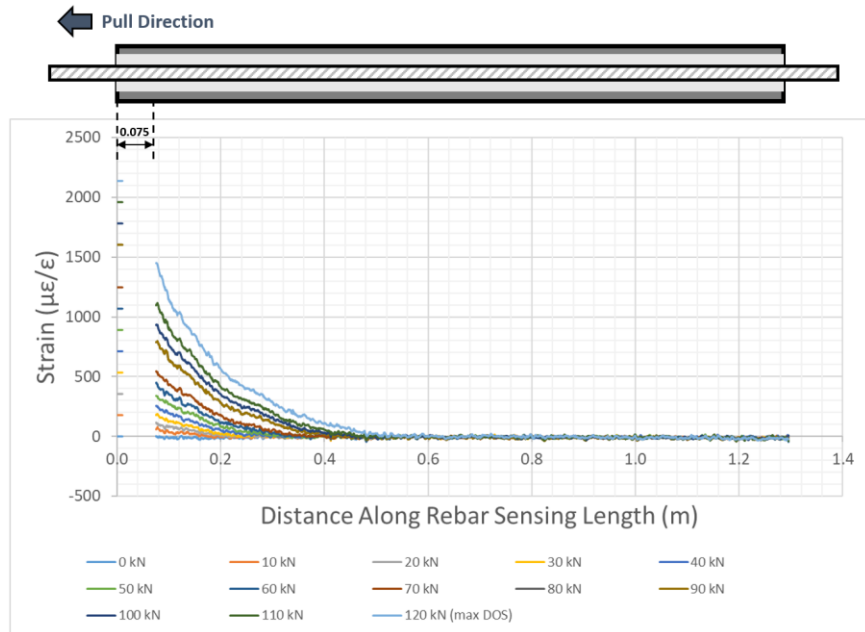


Figure A-84. G45-7 specimen strain profile along rebar bolt during pull-out testing

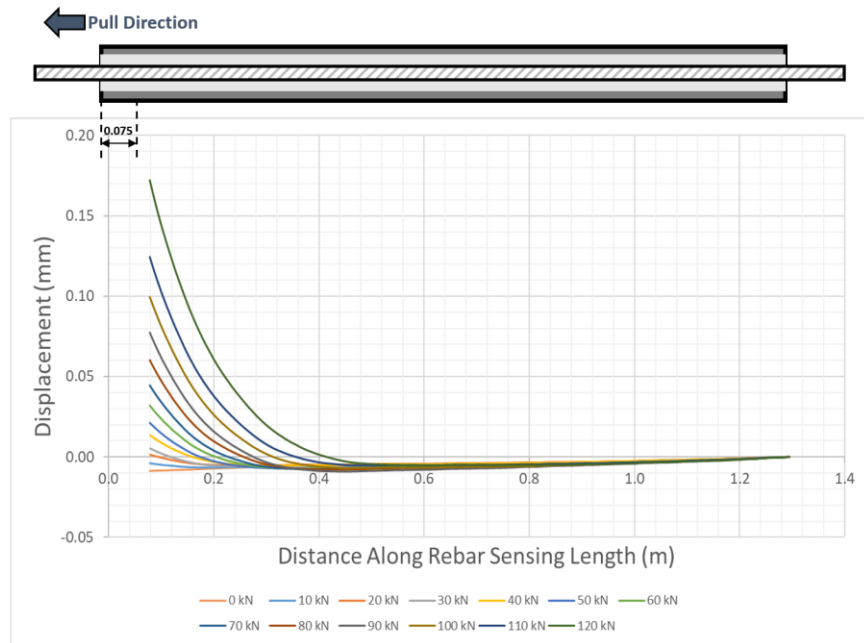


Figure A-85. G45-7 specimen axial displacement profile

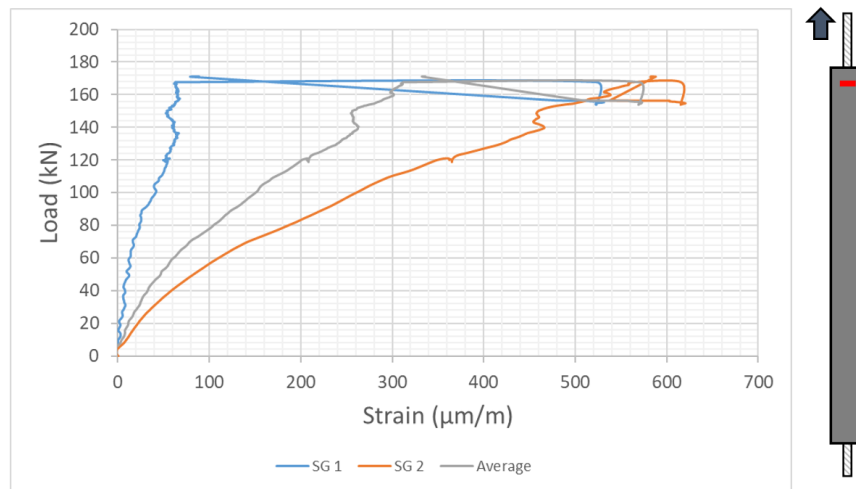


Figure A-86. G45-7 specimen pipe dilation monitoring at 50 mm

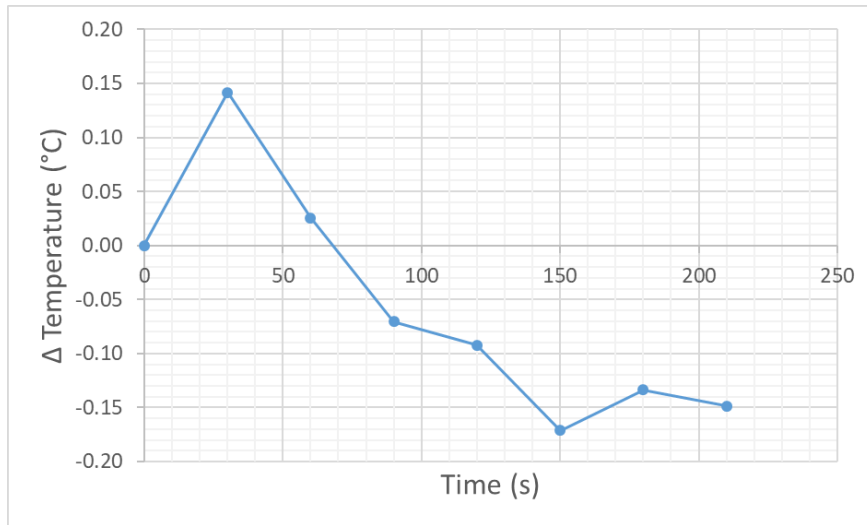


Figure A-87. G45-7 specimen temperature change during pull-out testing

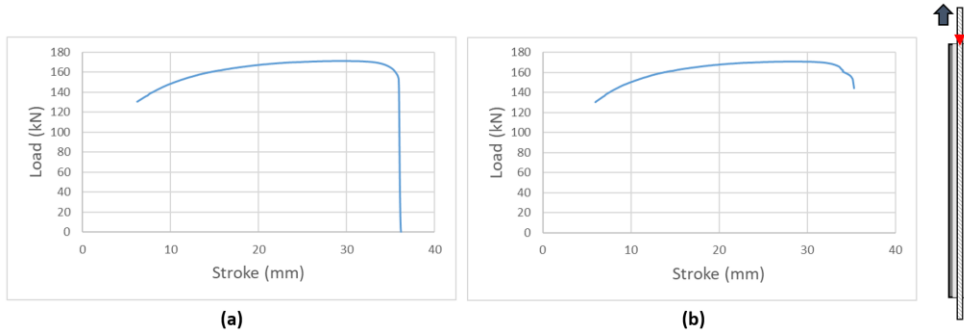


Figure A-88. Load-Displacement curve from G45-28 [Power supply tripped]: (a) Whole system response; (b) Axial displacement corrected for test rig movement and elongation

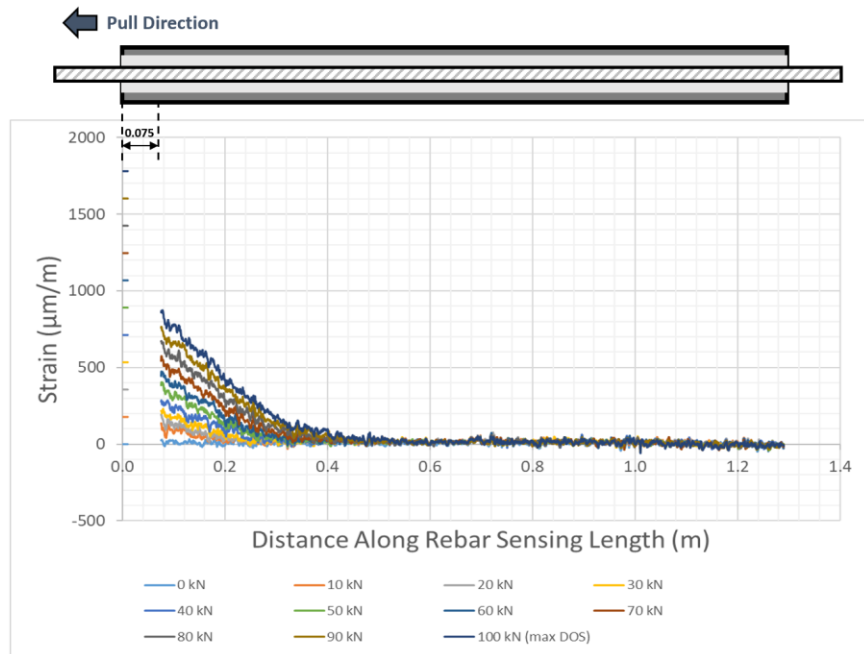


Figure A-89. G45-28 specimen strain profile along rebar bolt during pull-out testing

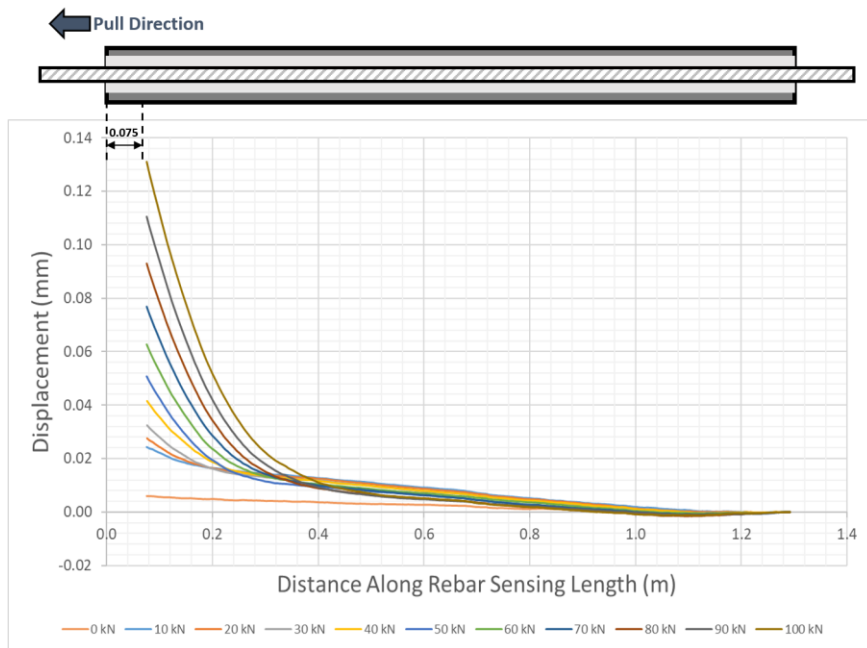


Figure A-90. G45-28 specimen axial displacement profile

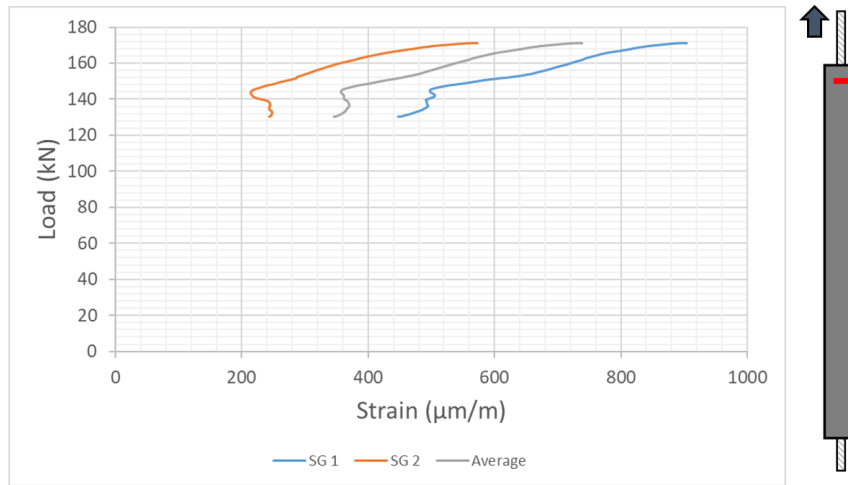


Figure A-91. G45-28 specimen pipe dilation monitoring at 50 mm

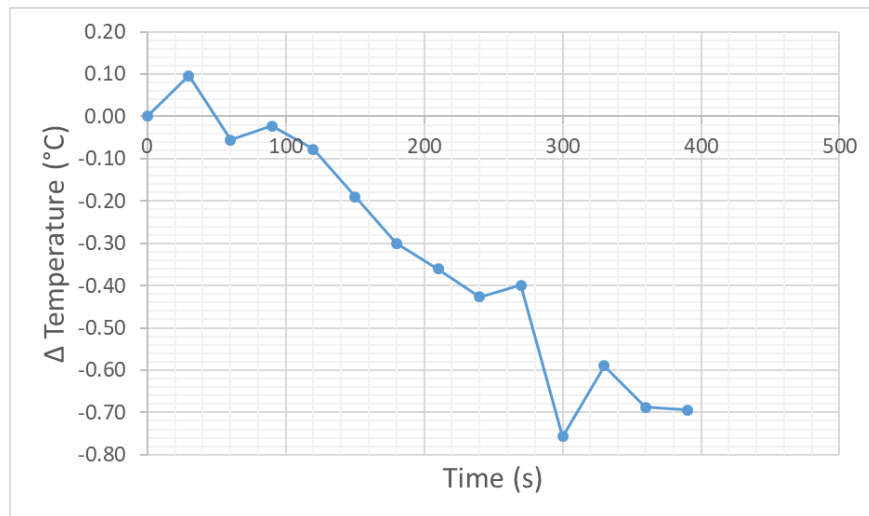


Figure A-92. G45-28 specimen temperature change during pull-out testing

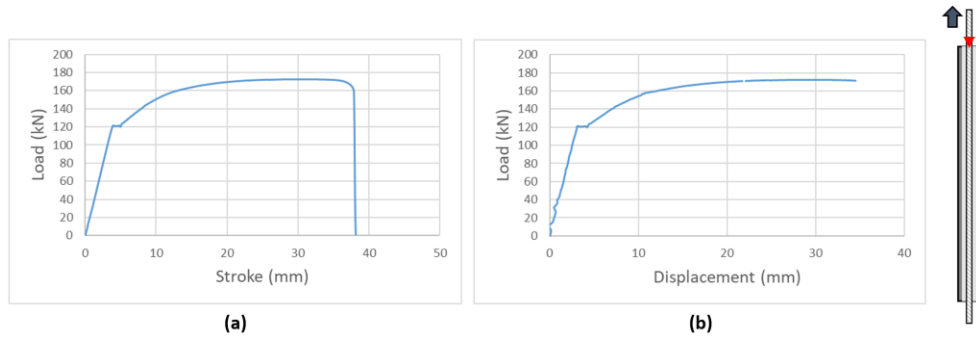


Figure A-93. Load-Displacement curve from G45-35: (a) Whole system response; (b) Axial displacement corrected for test rig movement and elongation

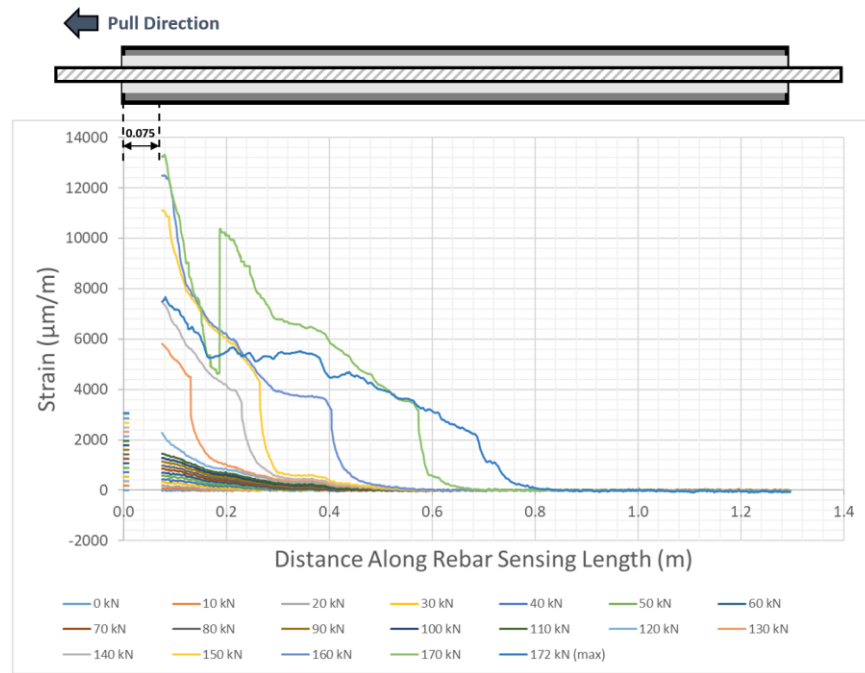


Figure A-94. G45-35 specimen strain profile along rebar bolt during pull-out testing

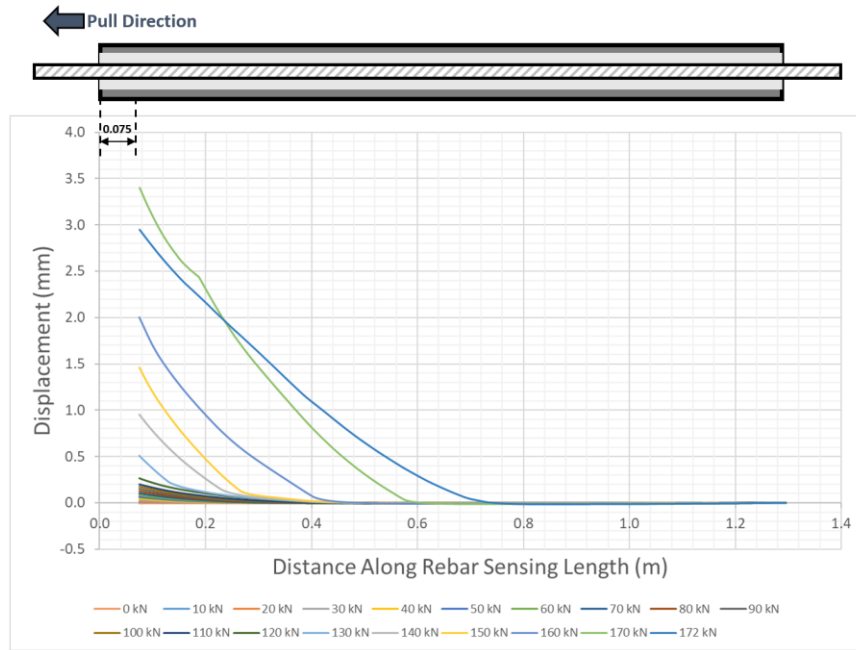


Figure A-95. G45-35 specimen axial displacement profile

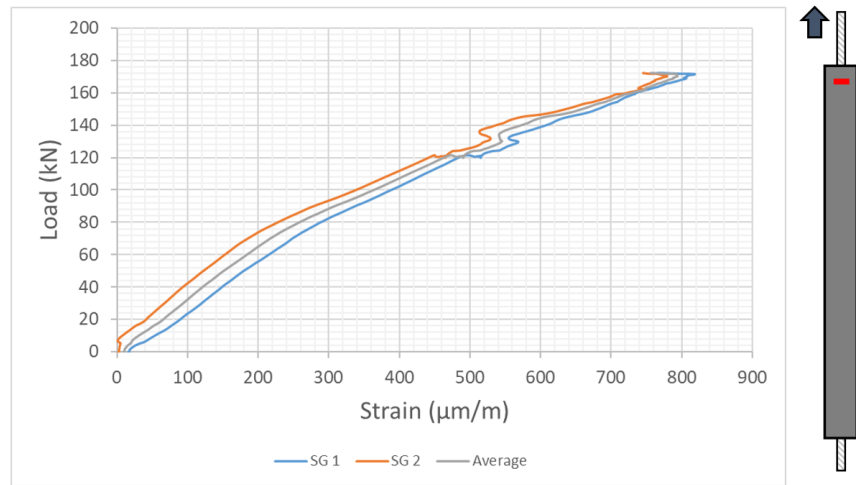


Figure A-96. G45-35 specimen pipe dilation monitoring at 50 mm

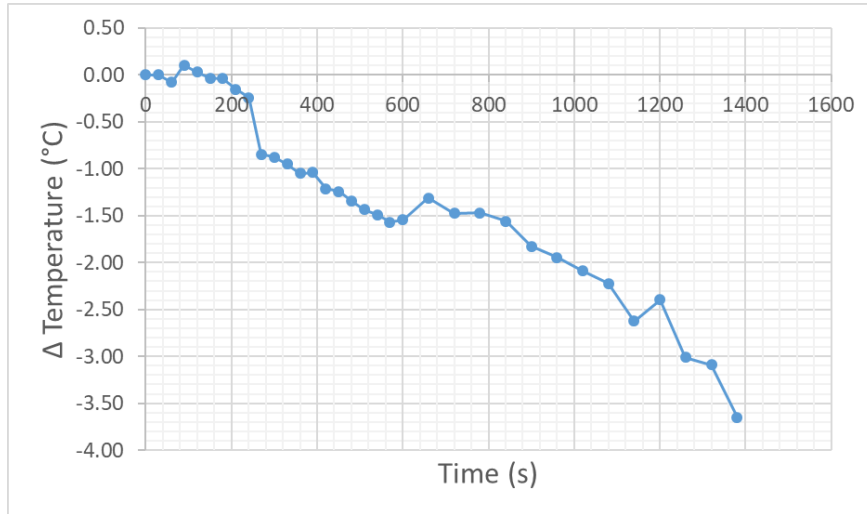
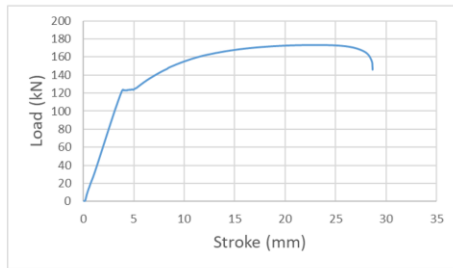
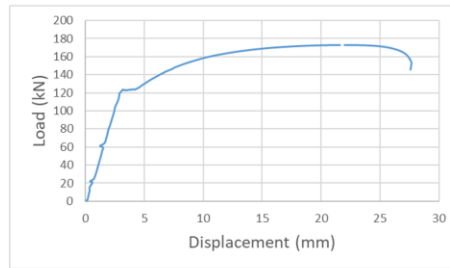


Figure A-97. G45-35 specimen temperature change during pull-out testing



(a)



(b)



Figure A-98. Load-Displacement curve from G45-60: (a) Whole system response; (b) Axial displacement corrected for test rig movement and elongation

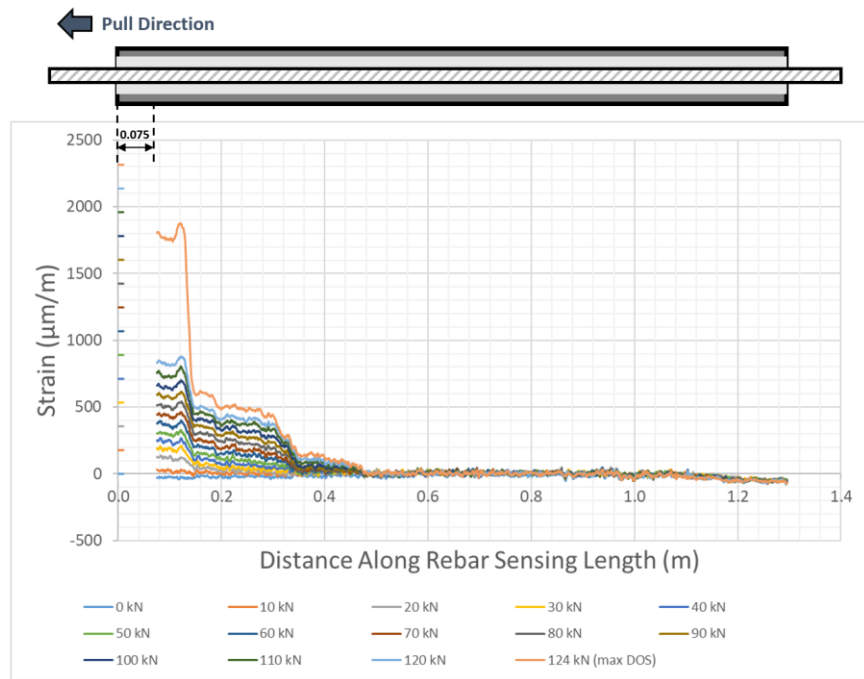


Figure A-99. G45-60 specimen strain profile along rebar bolt during pull-out testing

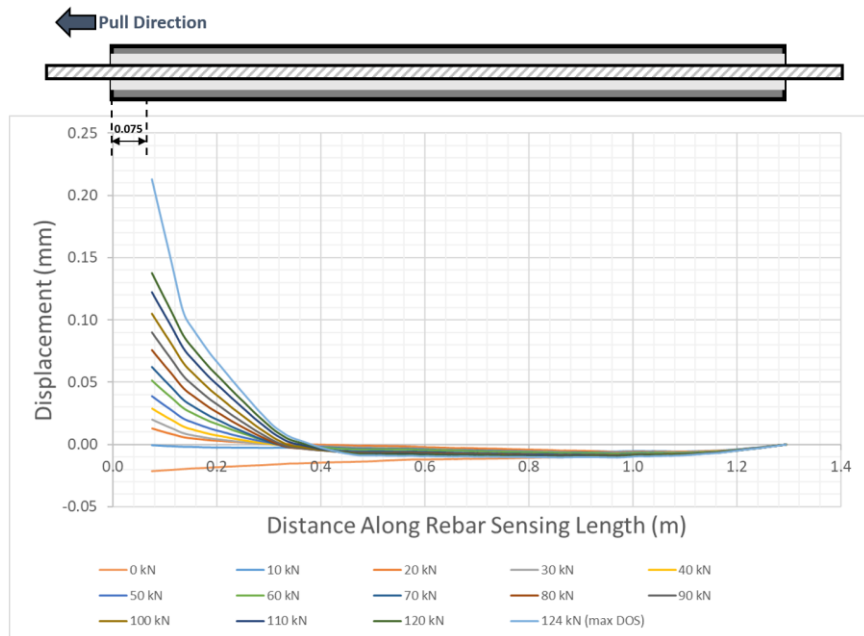


Figure A-100. G45-60 specimen axial displacement profile

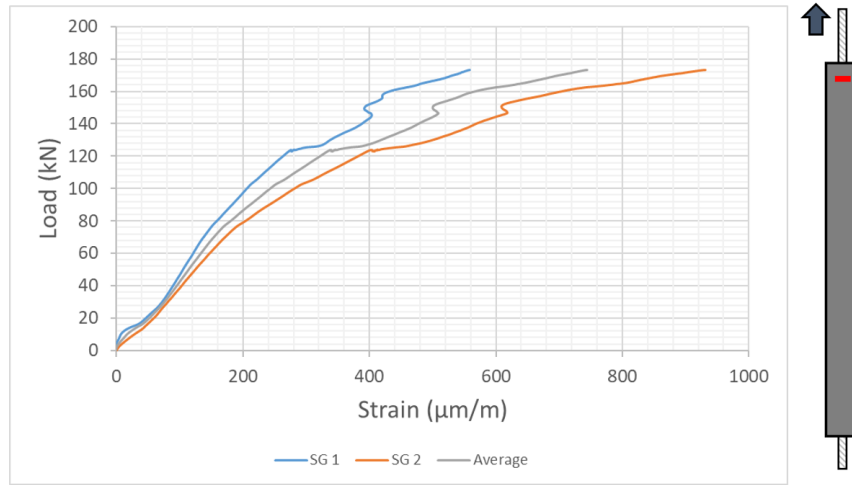


Figure A-101. G45-60 specimen pipe dilation monitoring at 50 mm

G45-60 T DOS malfunction

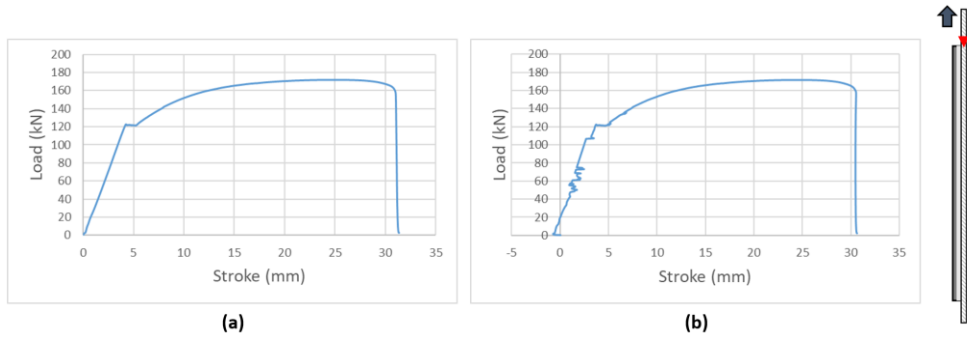


Figure A-102. Load-Displacement curve from G45-90: (a) Whole system response; (b) Axial displacement corrected for test rig movement and elongation

G45-90 ε DOS failure

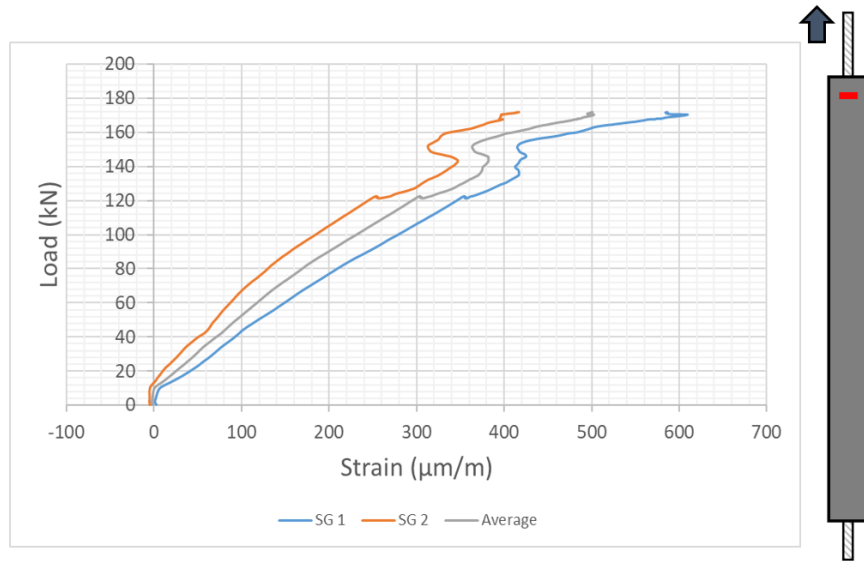


Figure A-103. G45-90 specimen pipe dilation monitoring at 50 mm

G45-90 T DOS malfunction

Appendix B Comparisons & Miscellaneous

This appendix presents the results comparisons, other testing results, and photos.

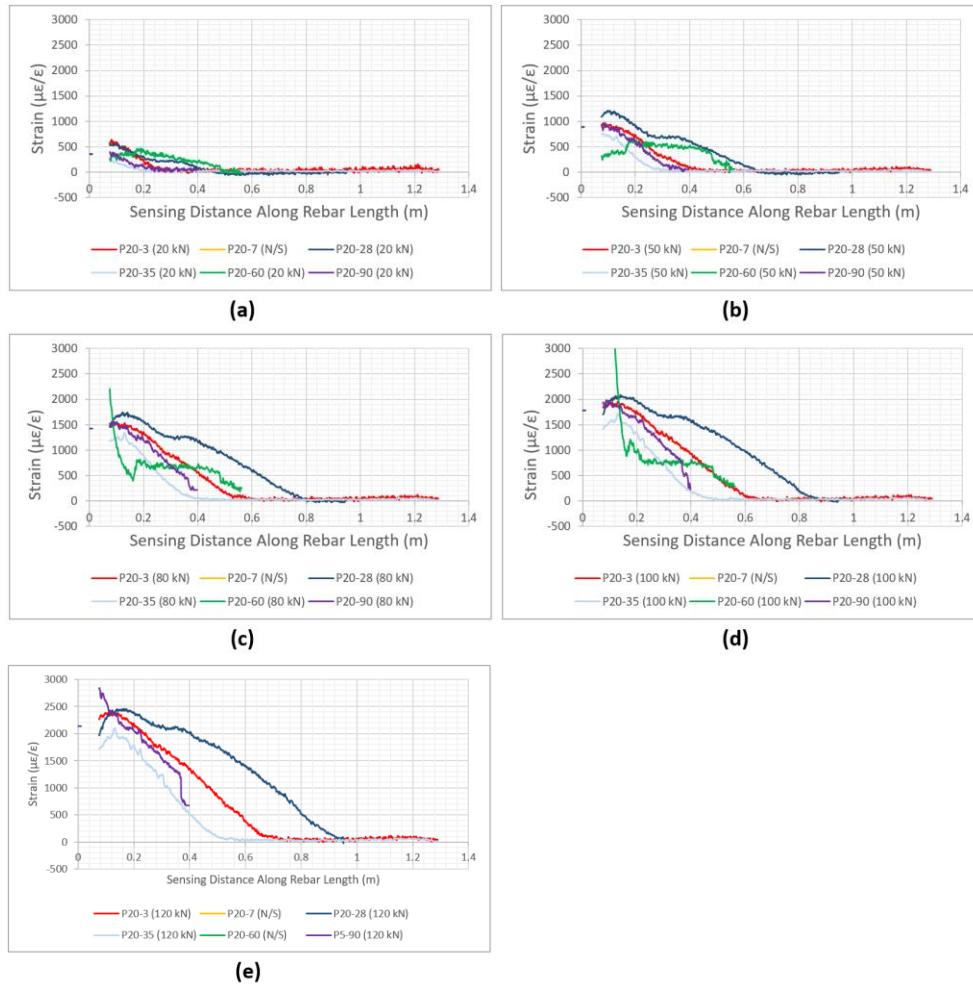


Figure B-1. P20 condition specimens strain profile comparisons at different loads: (a) 20 kN; (b) 50 kN; (c) 80 kN; (d) 100 kN; (e) 120 kN

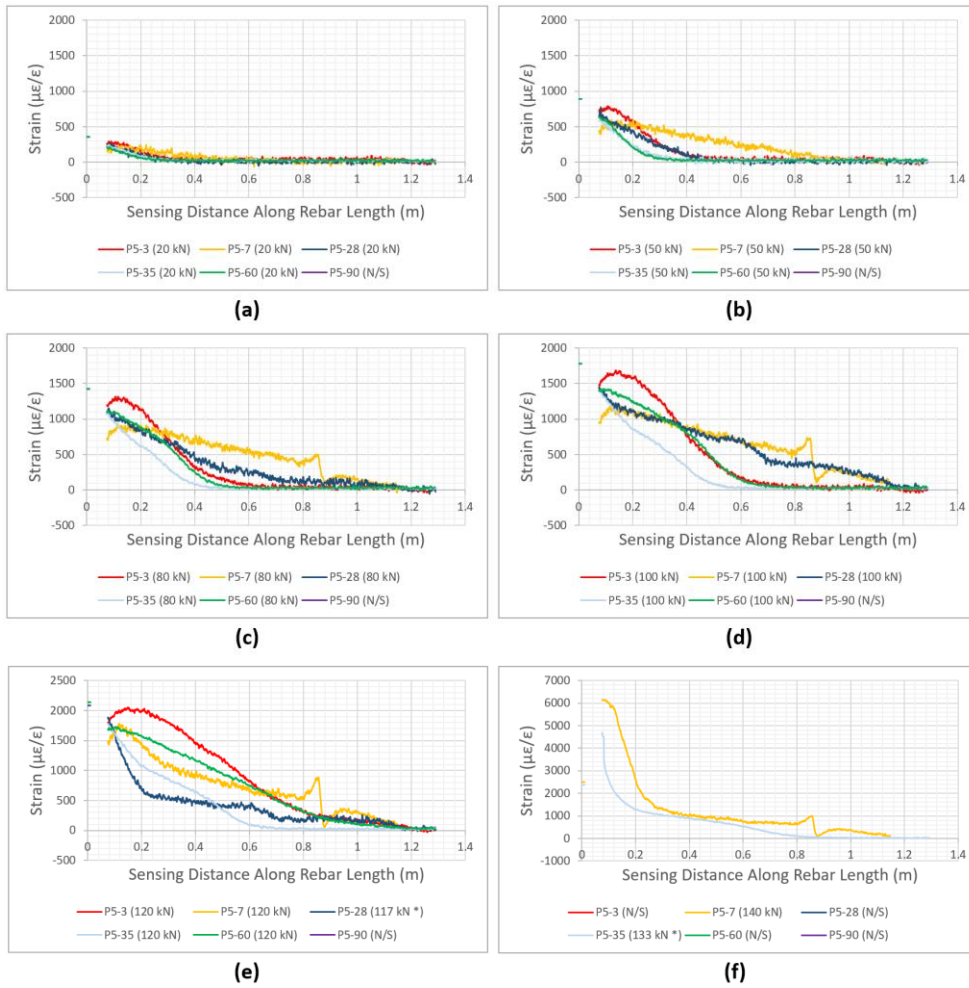


Figure B-2. P5 condition specimens strain profile comparisons at different loads: (a) 20 kN; (b) 50 kN; (c) 80 kN; (d) 100 kN; (e) 120 kN; (f) 140 kN

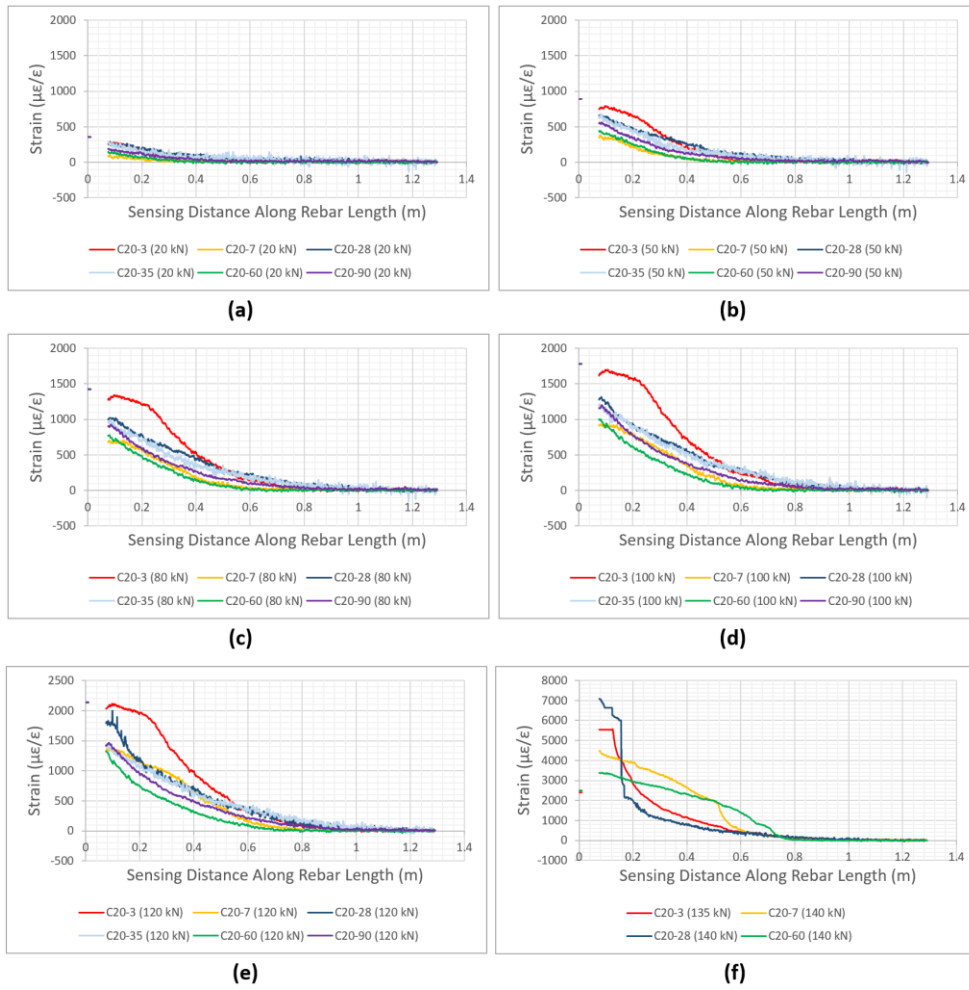


Figure B-3. C20 condition specimens strain profile comparisons at different loads: (a) 20 kN; (b) 50 kN; (c) 80 kN; (d) 100 kN; (e) 120 kN; (f) 140 kN

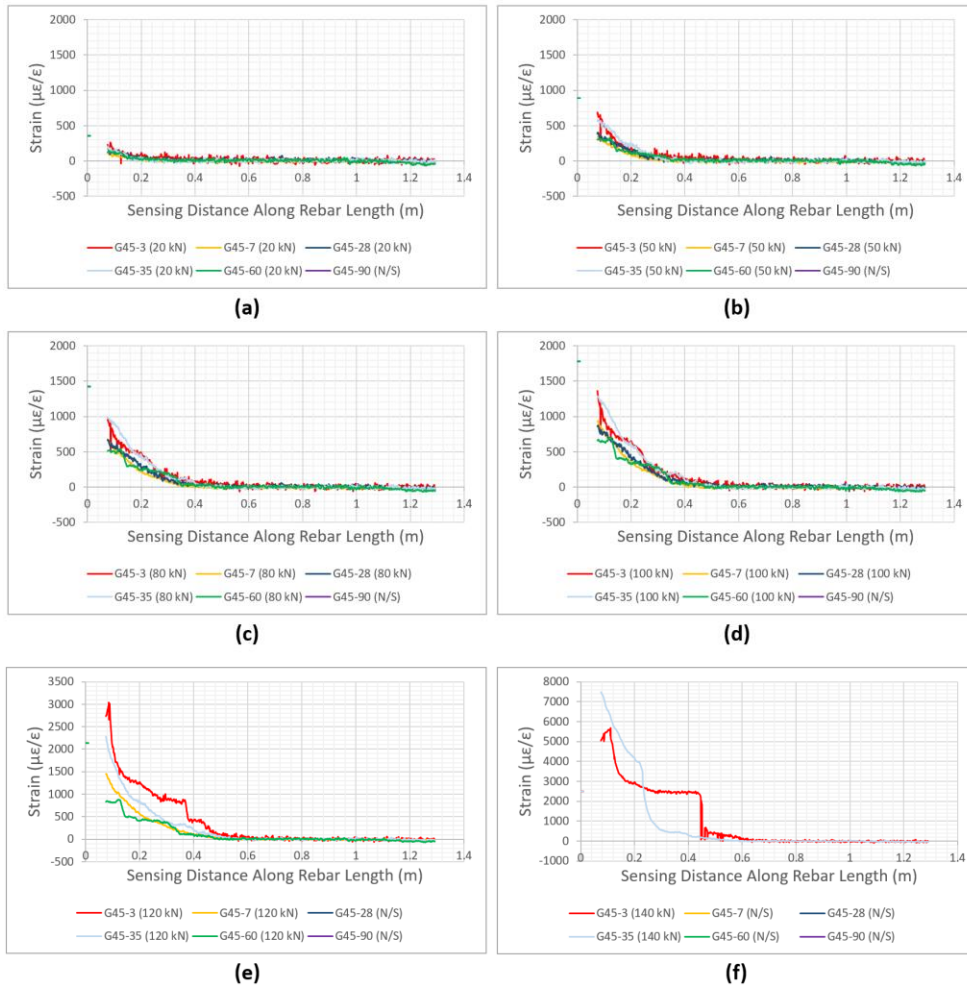


Figure B-4. G45 condition specimens strain profile comparisons at different loads: (a) 20 kN; (b) 50 kN; (c) 80 kN; (d) 100 kN; (e) 120 kN; (f) 140 kN

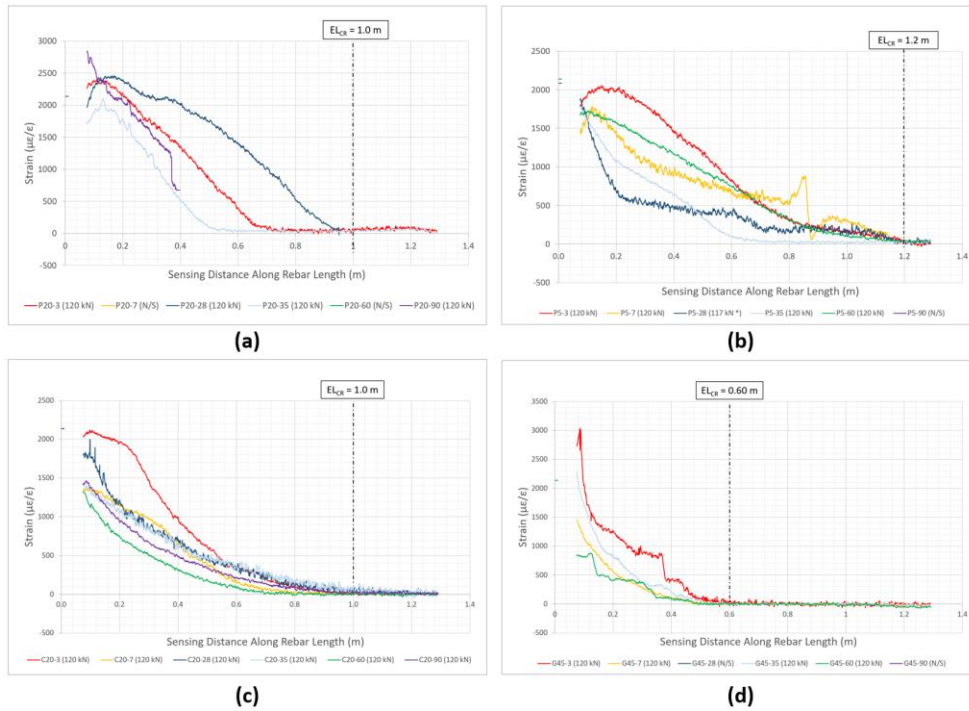


Figure B-5. Critical embedment length comparisons: (a) P20; (b) P5; (c) C20; (d) G45

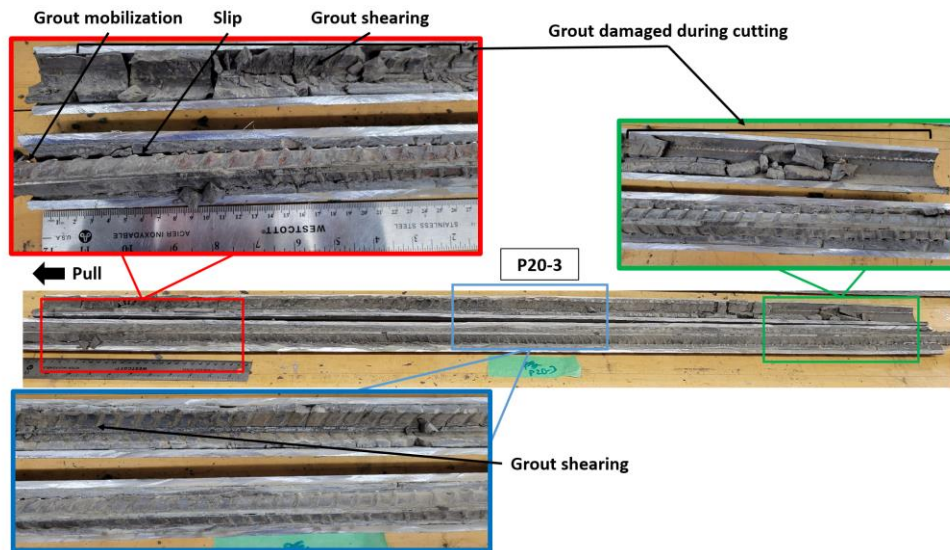


Figure B-6. P20-3 specimen post-test forensics

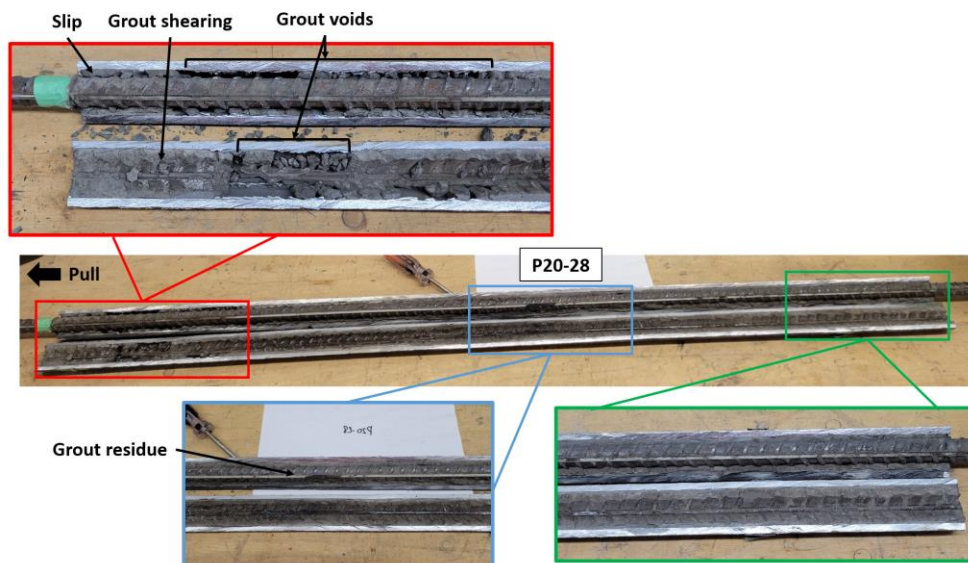


Figure B-7. P20-28 specimen post-test forensics

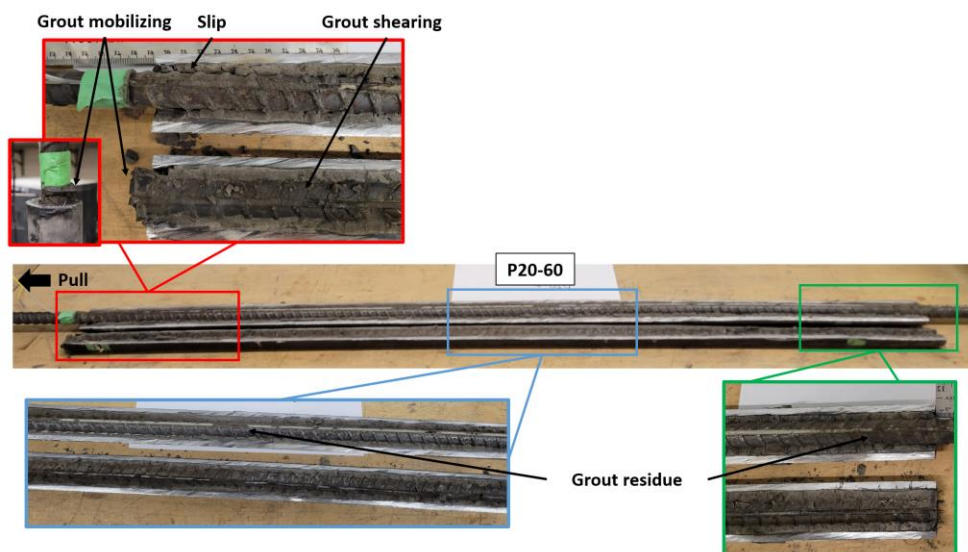


Figure B-8. P20-60 specimen post-test forensics

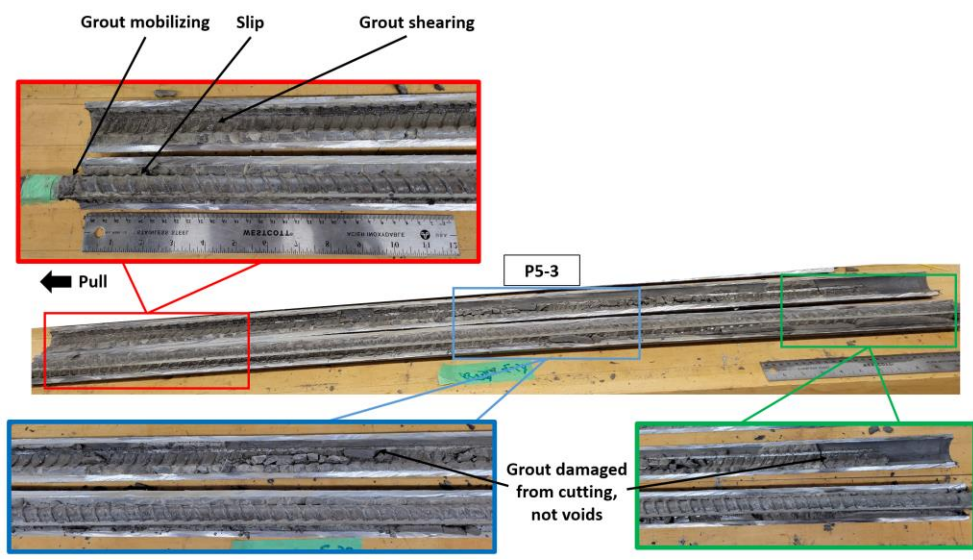


Figure B-9. P5-3 specimen post-test forensics

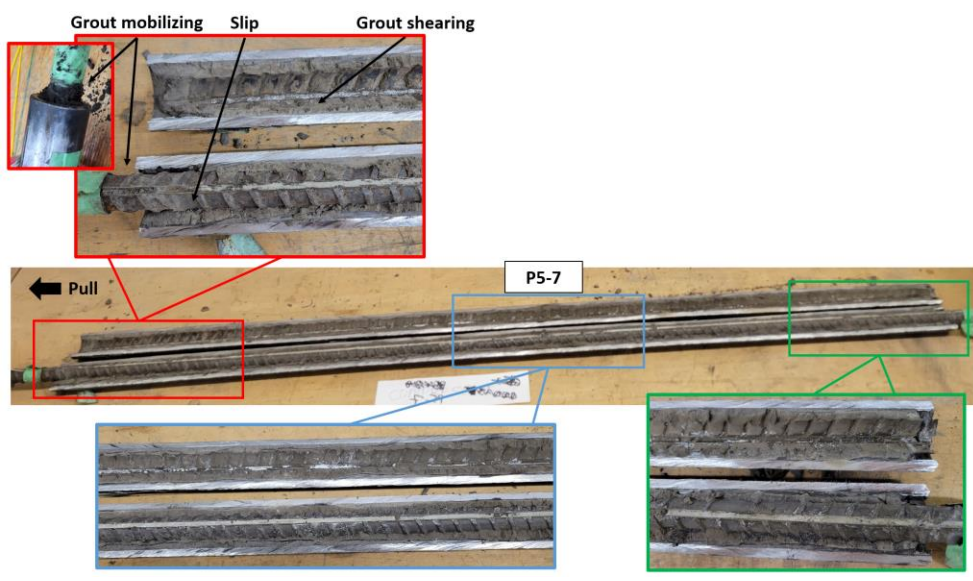


Figure B-10. P5-7 specimen post-test forensics

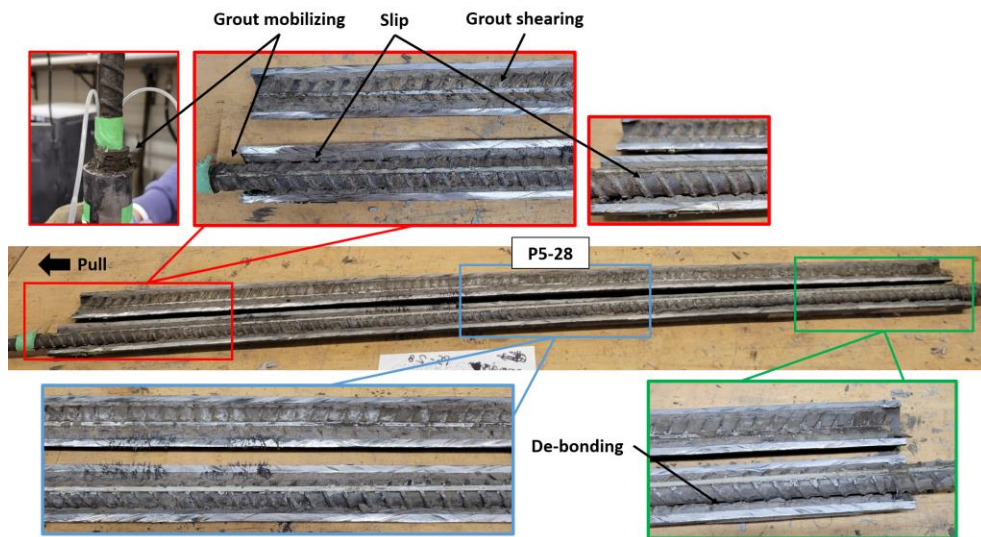


Figure B-11. P5-28 specimen post-test forensics

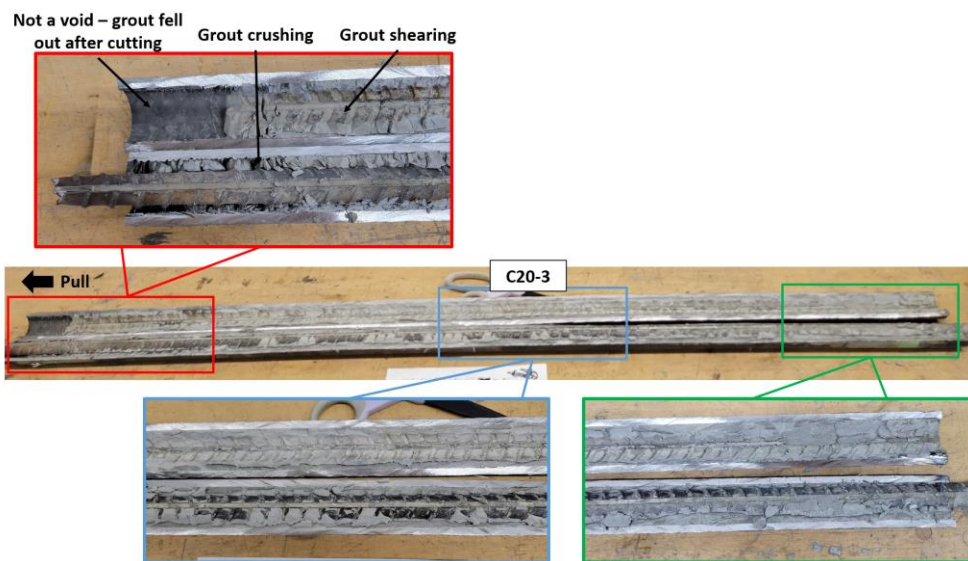


Figure B-12. C20-3 specimen post-test forensics

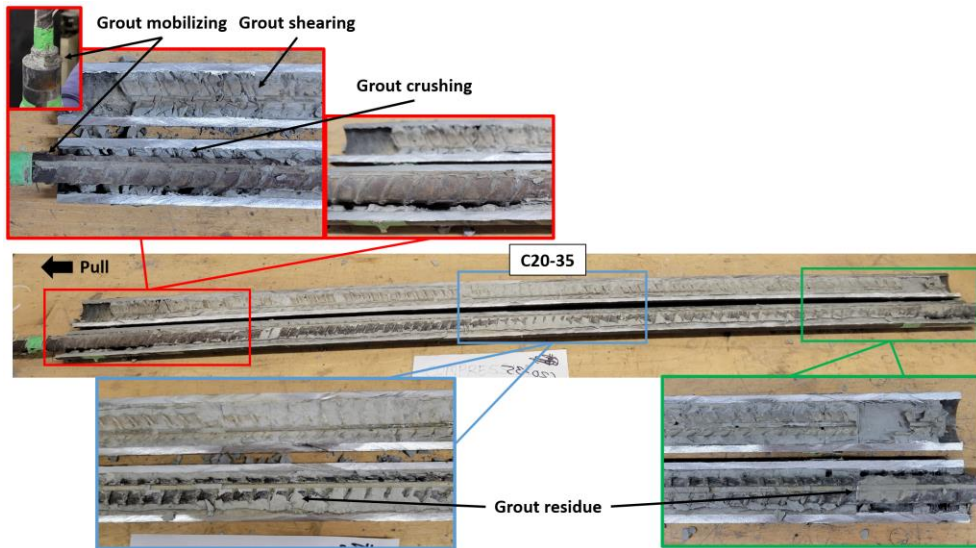


Figure B-13. C20-35 specimen post-test forensics

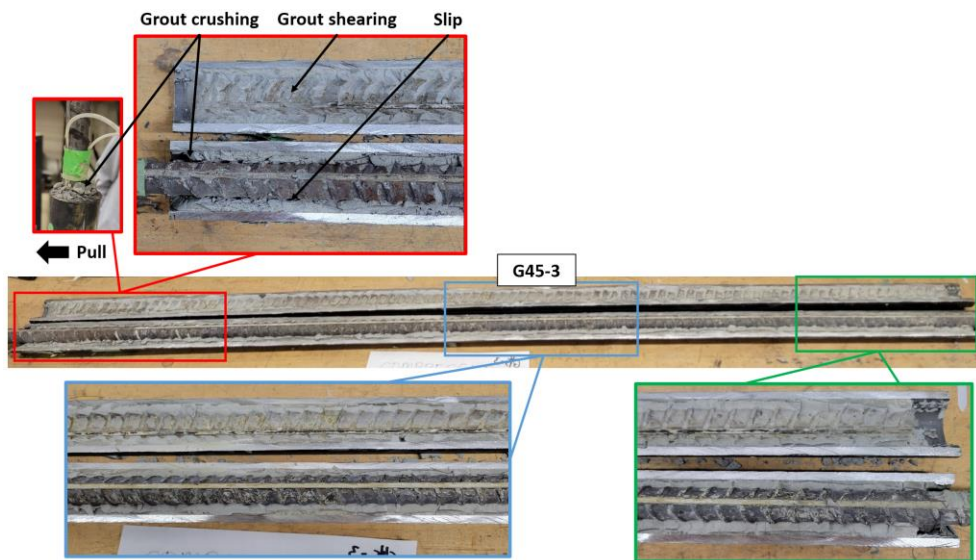


Figure B-14. G45-3 specimen post-test forensics

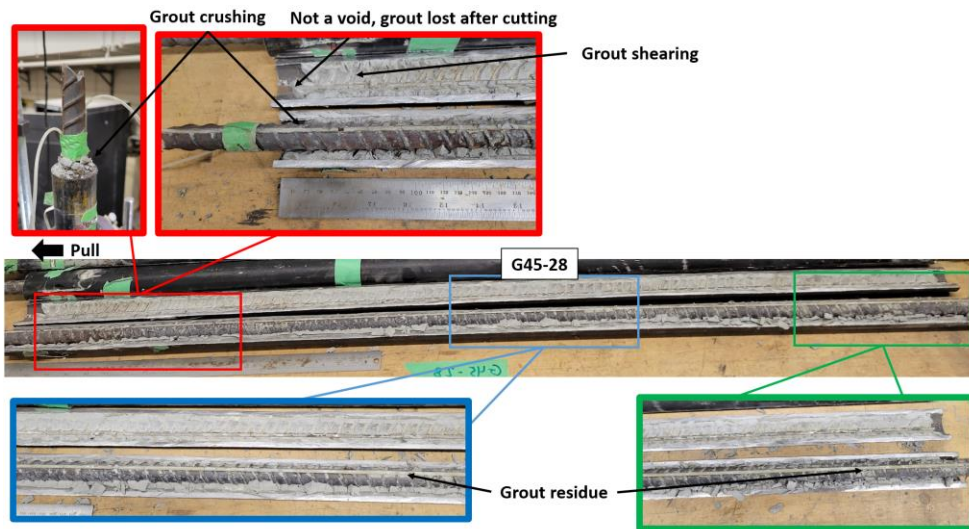


Figure B-15. G45-28 specimen post-test forensics

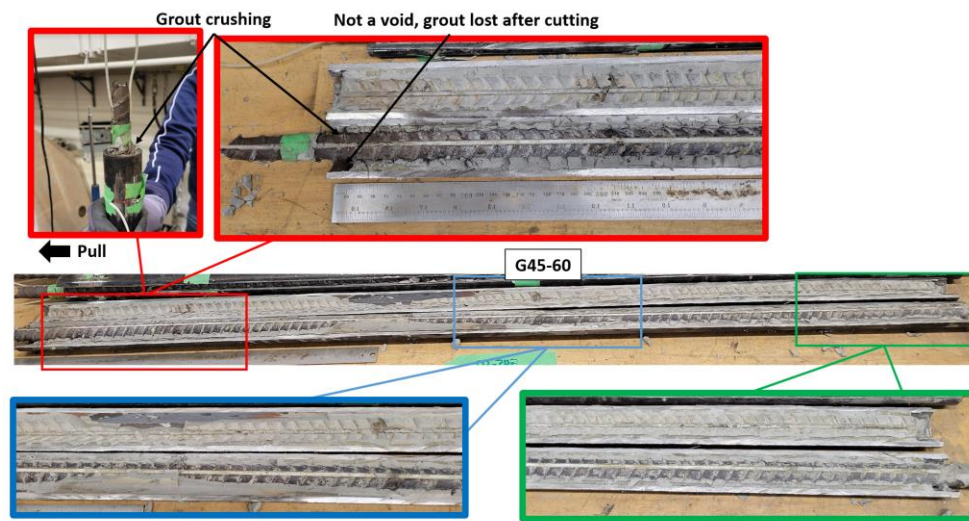


Figure B-16. G45-60 specimen post-test forensics